Dosimetry with the Dosepix detector in pulsed high dose rate photon fields

Dosimetrie mit dem Dosepix-Detektor in gepulsten Photonenfeldern mit hohen Dosisleistungen

der Naturwissenschaftlichen Fakultät
der Friedrich-Alexander-Universität Erlangen-Nürnberg
zur

Erlangung des Doktorgrades Dr. rer. nat.

vorgelegt von

Patrick Hufschmidt

Als Dissertation genehmigt
von der Naturwissenschaftlichen Fakultät
der Friedrich-Alexander-Universität Erlangen-Nürnberg
Tag der mündlichen Prüfung: 08.07.2022

Vorsitzender des Promotionsorgans: Prof. Dr. Wolfgang Achtziger

Gutachter/in: Prof. Dr. Gisela Anton
Prof. Dr. Christoph Hoeschen

Abstract

Dosepix is a pixelated semiconductor-based hybrid photon detector designed for dosimetry measurements. 16×16 pixels with two different pixel sizes are realized on a 300 µm thick silicon sensor. Each pixel can detect single photons and acquire the corresponding deposited energy individually. The Dosepix detector can be operated in different data acquisition modes. Two of them are used in this thesis for dose measurements. A dosemeter consisting of three Dosepix detectors with different metal filters is used in the experiments. The filters alter the impinging photon spectrum that is then acquired by each detector. This increases the energy information about the initial spectrum and enables the dosemeter to perform dosimetry in photon fields with energies up to 1.3 MeV. Test measurements are performed to investigate the detector concerning different calibration methods and adjustable measurement parameters. The performance of the Dosepix dosemeter using the spectroscopic photon-counting mode fulfills the legal requirements for new personal dosemeters. Quantities like the energy of the applied X-ray spectrum or the applied dose rate are tested. For the energy dependence, the personal dose equivalents $H_\mathrm{p}(10)$ and $H_\mathrm{p}(0.07)$ are investigated. The maximum applied dose rate that produces a response that is still within the required limits is over 100 times higher than the mandatory value. The behavior of the Dosepix detector changes with the applied dose rate due to pile-up in the pixel electronics. The effects pile-up can have on a dose measurement depend on the energy distribution of the initial spectrum. This dependence is examined for several unfiltered X-ray spectra.

The behavior of the Dosepix detector changes significantly in short-pulsed photon fields with high dose rates as they are applied by portable X-ray generators. Characterization measurements with different measurement parameters are performed in such pulsed photon fields to investigate the behavior of the detector. The approach to measuring the dose under these extreme conditions with photon-counting fails. For this case, another method is introduced. A simulation of the data acquisition in an integrating operation mode of the Dosepix detector in these high dose rate photon fields is outlined. A deep learning analysis that uses training data from this simulation is used to estimate the dose quantities $H_\mathrm{p}(10)$ and $H_\mathrm{p}(0.07)$. Different network architectures are investigated concerning their performance on simulated data. Measurements with two portable X-ray generators that apply different photon spectra are performed. For both devices, the selected neural network yields stable results over a wide dose rate range up to about $2.4 \cdot 10^6 \, \frac{\mathrm{Sv}}{\mathrm{h}}$. The deep learning analysis to reconstruct the personal dose equivalent $H_\mathrm{p}(10)$ is tested on short X-ray pulses produced via laser-driven emission. Here, a significant contribution to the dose from electrons occurs. The dose measured with the Dosepix dosemeter is very similar to the dose measured separately with a spectrometer. A coincidental agreement cannot be ruled out since the Dosepix detector was not tested so far in mixed electron / photon fields.

The neural network analysis to estimate the dose in continuous radiation fields, as they are legally required, is tested and shows good results. Almost all tested requirements are fulfilled with the deep learning analysis. This is unexpected since the simulation that generates the training data for the neural network is not designed for continuous radiation. Furthermore, the deep learning analysis, which is performed with an integrating operation mode, is tested with different irradiation times to vary the applied dose. The resulting response is stable over a wide dose range up to 82 mSv, which shows that the performance of the neural network does not depend on the irradiation time.

The experiments and analysis performed in this thesis show that pile-up, as it occurs in pulsed, high dose rate photon fields, has a significant impact on dose measurements. It is shown that a dosemeter based on Dosepix detectors is capable of measuring personal dose equivalents under these extreme conditions. Further research might enable the Dosepix dosemeter to expand its applications beyond personal photon dosimetry and put it to use in other fields of science.

Kurzzusammenfassung

Dosepix ist ein pixelierter, hybrider Halbleiterphotonendetektor, der für Messungen in der Dosimetrie entwickelt wurde. Der 300 µm dicke Siliziumsensor ist in 16×16 Pixel mit zwei verschiedenen Größen unterteilt. Jedes Pixel kann einzelne Photonen und die entsprechende deponierte Energie individuell registrieren. Der Dosepix-Detektor kann in verschiedenen Aufnahmemodi betrieben werden. Zwei davon werden in dieser Arbeit für Dosismessungen benutzt. Ein Dosimeter, das aus drei Dosepix-Detektoren mit unterschiedlichen Metallfiltern besteht, wird in den Experimenten verwendet. Die Filter verändern das auftreffende Photonenspektrum, das dann von den Detektoren gemessen wird. Dies erhöht die Energieinformation über das ursprüngliche Spektrum. Dadurch ist es mit dem Dosimeter möglich, Dosismessungen in Photonenfeldern mit Energien bis zu 1.3 MeV durchzuführen. Testmessungen werden durchgeführt, um den Detektor hinsichtlich verschiedener Kalibrierungsmethoden und einstellbarer Messparameter zu untersuchen. Im spektroskopisch aufgelösten Photonenzählmodus erfüllt das Dosepix-Dosimeter die gesetzlichen Anforderungen für neue Personendosimeter. Es werden Größen wie die Energie des applizierten Röntgenspektrums oder die applizierte Dosisleistung getestet. Die Personendosen $H_\mathrm{p}(10)$ und $H_\mathrm{p}(0,07)$ werden bezüglich ihrer Energieabhängigkeit untersucht. Die maximal applizierte Dosisleistung mit einer Response, die noch innerhalb der geforderten Grenzen liegt, ist mehr als 100-mal höher als der vorgeschriebene Wert. Das Verhalten des Dosepix-Detektors ändert sich mit der applizierten Dosisleistung aufgrund von Pile-up in der Pixelelektronik. Welche Auswirkungen Pile-up auf eine Dosismessung haben kann, hängt von der Energieverteilung des eintreffenden Spektrums ab. Dieser Zusammenhang wird für mehrere ungefilterte Röntgenspektren untersucht.

Das Verhalten des Dosepix-Detektors ändert sich deutlich in Photonenfeldern mit kurzen Pulsen und hohen Dosisleistungen, wie sie von tragbaren Röntgengeneratoren erzeugt werden. Messungen zur Charakterisierung werden in solchen gepulsten Photonenfeldern mit unterschiedlichen Messparametern durchgeführt, um das Verhalten des Detektors zu untersuchen. Die Dosis unter diesen extremen Bedingungen mit dem Photonenzählmodus zu messen, schlägt fehl. Für diesen Fall wird eine andere Methode präsentiert. Eine Simulation der Datenerfassung in Photonenfeldern mit hohen Dosisleistungen mit einem integrierenden Aufnahmemodus des Dosepix-Detektors wird vorgestellt. Eine Deep-Learning-Analyse, die Trainingsdaten aus dieser Simulation verwendet, wird benutzt, um die Dosisgrößen $H_\mathrm{p}(10)$ und $H_\mathrm{p}(0,07)$ zu bestimmen. Verschiedene Netzwerkarchitekturen werden hinsichtlich ihrer Leistungsfähigkeit auf simulierten Daten untersucht. Es werden Messungen mit zwei tragbaren Röntgengeneratoren, die unterschiedliche Photonenspektren erzeugen, durchgeführt. Für beide Geräte liefert das ausgewählte neuronale Netz über einen weiten Dosisleistungsbereich bis etwa $2.4 \cdot 10^6 \, \frac{\mathrm{Sv}}{\mathrm{h}}$ stabile Ergebnisse. Die Deep-Learning-Analyse zur Rekonstruktion der Personendosis $H_\mathrm{p}(10)$ wird in kurzen Röntgenpulsen, die durch lasergetriebene Emission erzeugt werden, getestet. Dabei tritt ein erheblicher Beitrag zur Dosis von Elektronen auf. Die Dosis, die mit dem Dosepix-Dosimeter gemessen wird, stimmt mit der Dosis, die separat mit einem Spektrometer gemessen wird, gut überein. Es kann nicht ausgeschlossen werden, dass die gute Übereinstimmung zufällig zustande kommt, da der Dosepix-Detektor bis jetzt noch nicht in gemischten Elektronen-/Photonenfeldern getestet wurde.

Die Analyse mit dem neuronalen Netzwerk zur Abschätzung der Dosis wird in kontinuierlichen Strahlungsfeldern, wie sie gesetzlich vorgeschrieben sind, getestet und zeigt gute Ergebnisse. Mit der Deep-Learning-Analyse werden fast alle getesteten Anforderungen erfüllt. Dies ist unerwartet, da die Simulation, die Trainingsdaten für das neuronale Netzwerk generiert, nicht für kontinuierliche Strahlung ausgelegt ist.

Weiterhin wird die Deep-Learning-Analyse, die mit einem integrierenden Aufnahmemodus durchgeführt wird, mit unterschiedlichen Bestrahlungszeiten getestet, um die applizierte Dosis zu variieren. Die resultierende Response ist über einen weiten Dosisbereich bis zu 82 mSv stabil, was zeigt, dass die Leistung des neuronalen Netzwerks nicht von der Bestrahlungszeit abhängt.

Die in dieser Arbeit durchgeführten Experimente und Analysen zeigen, dass Pile-up, wie er in gepulsten Photonenfeldern mit hohen Dosisleistungen auftritt, einen signifikanten Einfluss auf Dosismessungen hat. Es wird gezeigt, dass ein Dosimeter, das aus Dosepix-Detektoren besteht, dazu geeignet ist, um unter diesen extremen Bedingungen die Personendosis zu messen. Weitere Forschungen könnten es ermöglichen, den Anwendungsbereich des Dosepix-Dosimeters über die Photonendosimetrie hinaus zu erweitern und in anderen Wissenschaftsbereichen einzusetzen.

Contents

Chapter 1

Introduction

Wilhlem Conrad Röntgen discovered the X-ray radiation in 1895 [1]. Since then, this high energetic part of the electromagnetic spectrum has played a significant role in non-destructive material testing, security, the food industry, and of course, in science. The most important field of application, however, is human medicine. With the first X-ray examination, the meaning of this ground-breaking discovery became clear. Today, using this technology to look inside the human body is well-established and forms a cornerstone of modern medicine. A variety of diseases and injuries can be recognized using X-ray imaging. Besides the pure examination purposes, curative aspects of X-rays are fundamental. Here, oncology benefits the most since X-rays can destroy cancer cells within the irradiated area of the human body.
Although the destructive properties of X-rays or γ-radiation can beneficially be used, it is also the most significant disadvantage of this technology. Unwanted exposure is dangerous, especially since humans cannot sense this kind of radiation. The exposure might therefore be unnoticed. Monitoring exposed personnel is, therefore, necessary and legally required. A passive personal dosemeter, which the person at risk wears, acquires the amount of ionizing radiation over a certain period (usually one month [2]). After that, the dosemeter is read out and provides information about the acquired dose.
This procedure, however, still harbors the risk of harmful exposure, for example, in the case of an accident due to malfunctioning of an X-ray tube or broken shielding. Active personal dosemeters (APDs) provide more immediate information about the acquired dose. In Germany, however, those dosemeters cannot be legally used due to their insufficient accuracy in pulsed photon fields with high dose rates. Such pulsed radiation can lead to a significant underestimation of the applied dose or even a complete failure of the measurement device [3, 4]. However, X-ray applications with such high dose rates (up to 400 $\frac{\mathrm{Sv}}{\mathrm{h}}$ [4]) can occur in the direct beam. The medical sectors of interventional radiology and cardiology are particularly interesting for an immediate dose reading [5].
Besides human medicine, pulsed X-ray radiation frequently occurs in the other application fields mentioned above. Portable X-ray generators are used for non-destructive testing [6] and veterinary medicine [7]. Some of those devices produce X-ray pulses with pulse lengths of 10 ns to 50 ns [8]. The corresponding dose rates can reach up to 10^6 $\frac{\mathrm{Sv}}{\mathrm{h}}$. These high dose rates, which are already orders of magnitudes higher than what can be measured with currently available APDs, are exceeded by dose rates that are produced by X-ray pulses as they occur in some laser facilities. The short bursts generated by laser-induced X-ray emission reach even lower pulse durations. With laser pulses that are only 0.7 ps long, dose rates up to 10 $\frac{\mathrm{GSv}}{\mathrm{h}}$ can occur.

In this thesis, measurements in radiation fields with such high dose rates as they occur in different applications are performed. In doing so, a new kind of APD is used. The Dosepix detector forms the basis of this new kind of APD. Characteristics of this pixelated, photon-counting, semiconductor-based detector concerning its energy calibration are investigated. Further, Its spectrum-dependent response and its behavior in high dose rate photon fields are evaluated. The signals measured by the individual pixels of three Dosepix detectors with metal filters are used to determine different dose quantities. Here, two methods are used. One of those methods is based on a neural network trained with simulated high dose rate photon fields.

Chapter 2

Theoretical background

Contents

In this chapter, the theory and the definitions that are necessary for this thesis are introduced. The X-ray sources used in the experiments are outlined, and the main interaction mechanisms of photons with matter are explained. A brief introduction to the analytical methods that are based on deep learning and neural networks is given. Relevant dosimetric quantities and the associated requirements for a new dosemeter to gain admission are presented. Finally, an overview of currently used dosemeters in the medical sector is given.

2.1 Physical background

2.1.1 Origin of X-rays and γ-radiation

As mentioned above, X-rays and γ-radiation are used in a wide range of scientific fields. Reliable sources of high-energy photons are therefore indispensable. In the following, the sources of X-rays and γ-radiation used in this thesis are introduced.

X-ray tube

One standard device that produces X-ray radiation in a laboratory is an X-ray tube. Fig. 2.1 depicts a schematic of its working principle. Electrons are liberated from the cathode via thermionic emission. These electrons (red) propagate through the evacuated tube in an applied electric field towards the anode. Here, the electrons interact with the anode material [9]. The X-rays (blue) produced in the anode material exit the tube through a thin window. These X-rays are produced in two ways in the material [9, 10]:

- *Bremsstrahlung:* An electron is deflected by the Coulomb field of a nucleus in the anode material. Thereby, the electron loses energy which is emitted in the form of photons. The energy spectrum of these photons is continuous.
- *Characteristic Lines:* An incoming electron ionizes an atom by liberating an electron from an inner shell. This leaves a hole that is filled by an electron of an outer shell. A photon with an energy equal to the difference between the energy levels of the outer and inner shell is emitted. Since the energy levels of the shells are fixed, all emitted photons have the same energy for each transition. The energy transitions are different for each element [11] and are, therefore, characteristic for the anode material. These characteristic photon energies appear as narrow lines in the photon energy spectrum.

Besides the applied voltage U that determines the electric field, the resulting X-ray spectrum is influenced by the anode material, the angle between the anode and the electron beam in the X-ray tube [11], the material and thickness of the exit window, and internal and external filters. External metal filters with specific thicknesses are used to generate standard spectra in, e.g., type test evaluations (see sec. 2.3.2).

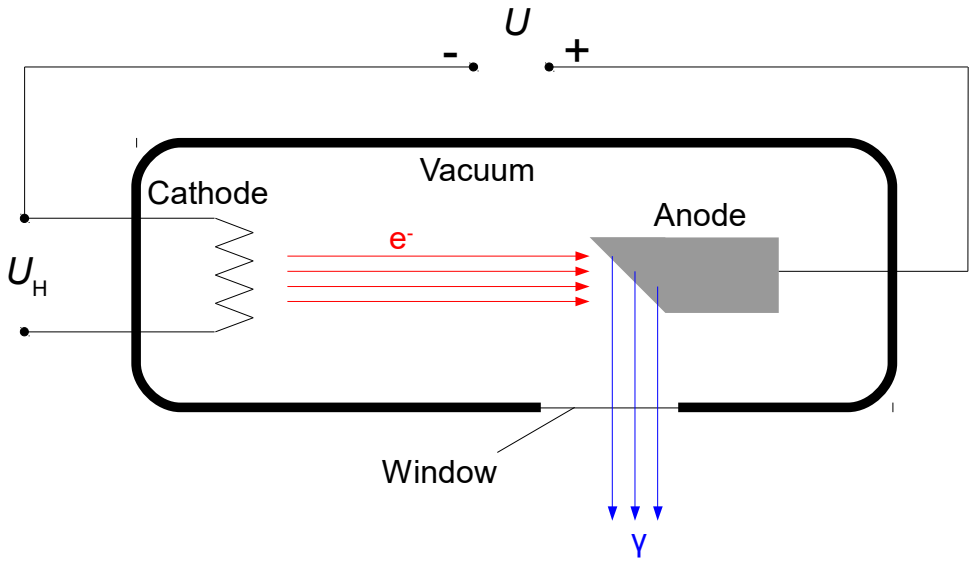

Figure 2.1 Schematic of the working principle of an X-ray tube. Image adapted and modified from [9].

Laser induced X-ray emission

If a high-power laser is focused on a target, hot plasma is formed on its surface. In this plasma, a significant number of energetic electrons (often referred to as „hot“) [12] is produced. These electrons can reach energies in the magnitude of MeV [12]. The electrons interact with the plasma material and generate X-rays via three interaction processes [13]:

- *Bremsstrahlung:* Free electrons in the plasma emit Bremsstrahlung by interacting with the Coulomb potential of other ions. The spectrum of the emitted radiation is, as for the X-ray tube, continuous. The Bremsstrahlung power W_B depends on the electron density n and electron temperature T_e in the produced plasma [13]

$$W_\mathrm{B} \propto n^2 \, T_\mathrm{e}^{\frac{1}{2}}. \tag{2.1}$$

  According to [13], the electron temperature depends on the absorbed laser intensity I_abs via

$$T_\mathrm{e} \approx \left(\frac{I_\mathrm{abs}}{f \, n_\mathrm{e}}\right)^{\frac{2}{3}} \cdot \frac{m^{\frac{1}{2}}}{k_\mathrm{B}}, \tag{2.2}$$

  where $f < 1$ denotes a flux limiter parameter and k_B the Boltzmann constant. Energy loss mechanisms are not included in this expression. It, therefore, tends to overestimate the electron temperature. However, from equ. 2.1 and equ. 2.2 an increasing dependence of the Bremsstrahlung power with the absorbed laser intensity can be derived.

- *Recombination:* Free electrons are captured by an ionized atom and transit into a bound state. Here, the energy E_γ of the emitted photon is described via

$$E_\gamma = E_\mathrm{e} + E_\mathrm{Z}^\mathrm{n}, \tag{2.3}$$

  where E_e is the kinetic energy of the electron and E_Z^n is the energy of the final atomic state with Z the ion charge and n the principal quantum number. Since the kinetic energy of the free electrons in the plasma is continuous, the X-ray spectrum produced by this process is also continuous.

- *Characteristic Lines:* The transition of an electron from an excited bound state to a lower bound state in an atom leads to the emission of an X-ray photon with discrete energy. Therefore, the energy spectrum that originates from this mechanism is not continuous and appears, as for the X-ray tube, as narrow lines in the photon energy spectrum.

Nuclear γ-sources

Besides artificially produced X-ray radiation, γ-radiation from nuclear sources is also commonly used in radiation physics. When a nucleus of a radioactive isotope decays, the residual nucleus can remain in an excited state. When the nucleus transits from this energetically excited state to the ground state, a γ-photon can be emitted [14]. Like the characteristic X-ray emission, all photons emitted by the nucleus that undergoes such a transition have the same energy. Therefore, the photon energy spectrum of a γ-source forms narrow characteristic lines in the photon energy spectrum.

2.1.2 Interactions of photons with matter

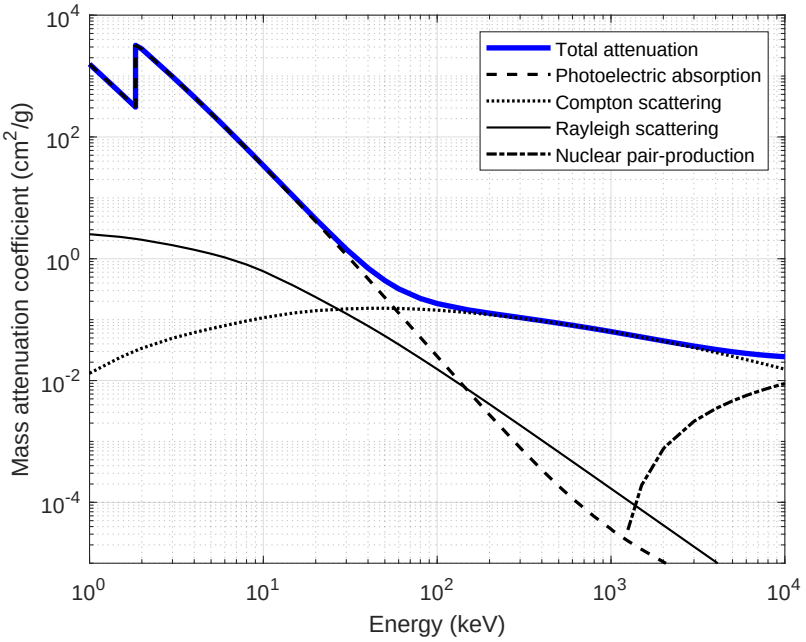

Figure 2.2 Mass attenuation coefficient for photoelectric absorption, Compton scattering, Rayleigh scattering, and nuclear pair-production. Data taken from [15].

Detecting photons and quantifying their energy requires the interaction of the photon with the detector material. The thickness and the density of the material, the photon energy, and the kind of interaction contribute to the number of photons that are absorbed in the detector material. The exponential attenuation law [9]

$$I(E) = I_0(E) \cdot \mathrm{e}^{(-\mu(E)\rho l)} \tag{2.4}$$

describes the radiation intensity $I(E)$ of photons with energy E after the penetration of a material with thickness l and density ρ. $I_0(E)$ is the initial radiation intensity, and $\mu(E)$ the mass attenuation coefficient that depends on the photon energy, the penetrated material, and the kind of interaction. Its unit is given in $[\mu] = \frac{\mathrm{cm}^2}{\mathrm{g}}$. In the case of the Dosepix detector, the sensor consists of 300 µm silicon. Fig. 2.2 shows the mass attenuation coefficient for four kinds of interactions (data taken from [15]) that are explained in the following [10, 11]:

Photoelectric absorption

Photoelectric absorption, also called total absorption, occurs when a bound electron fully absorbs a photon with energy E_γ. If E_γ is higher than the binding energy E_b of the electron to its atom, the electron is emitted with the kinetic energy

$$E_\mathrm{e} = E_\gamma - E_\mathrm{b}. \tag{2.5}$$

The interaction cross-section σ for photoelectric absorption increases with increasing atomic number Z and decreases with increasing photon energy. For $E_\gamma < 100\,\mathrm{keV}$, the relation [11]

$$\sigma \sim \frac{Z^5}{(h\nu)^3} \tag{2.6}$$

holds. Here, ν denotes the frequency of the photon, h the Planck constant, and m_0 the rest mass of an electron. Photoelectric absorption is the dominant process up to photon energies of about 60 keV.

Compton scattering

Compton scattering, also called incoherent scattering, occurs when an incoming photon with energy E_γ transfers part of its energy to a free or only loosely bound electron. The transferred energy results in the kinetic energy E_e of the electron, whereas a second photon is emitted with the residual energy $E_{\gamma'}$

$$E_{\gamma'} = E_{\gamma 0} - E_e. \tag{2.7}$$

Fig. 2.3 depicts the ionization process via Compton scattering. The secondary photon is emitted under the angle φ. Its energy $E_{\gamma'}$ depends on this angle via [11]

$$E_{\gamma'} = \frac{E_\gamma}{1 + \frac{E_\gamma}{m_0 c^2} \cdot (1 - \cos(\varphi))}, \tag{2.8}$$

where m_0 denotes the rest mass of an electron and c the speed of light. $\varphi = 180°$ represents a special case. Here, the maximum energy E_e^{max} is transferred from the initial photon to the electron. Using equ. 2.7 and equ. 2.8, this maximum electron energy is calculated via

$$E_e^{max} = \frac{E_\gamma}{1 + \frac{m_0 c^2}{2E_\gamma}}. \tag{2.9}$$

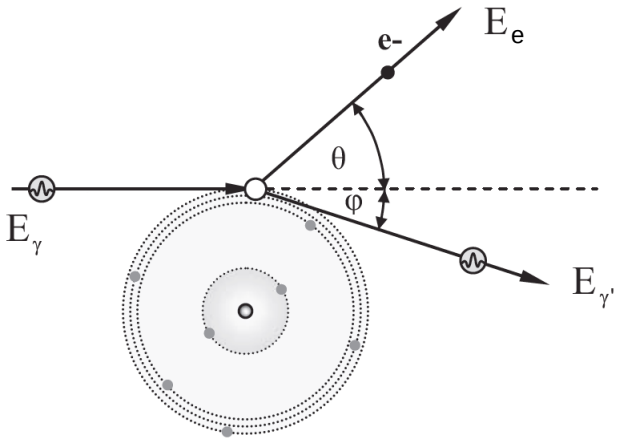

Figure 2.3 Schematic process of Compton scattering. An initial photon with energy E_γ transfers part of its energy E_e to an electron which scattered under the angle Θ. A secondary photon with energy $E_{\gamma'}$ is emitted under the angle φ. Image taken and modified from [10].

Rayleigh scattering

Rayleigh scattering, also called coherent scattering, occurs when an initial photon is scattered from an atom without losing any of its energy. In this case, the whole atom can take the recoil of the photon, and no ionization takes place. Since there is no electron dislodged that might propagate through the detector material, Rayleigh scattering is not detected by the Dosepix detector.

Nuclear pair production

Pair production denotes the process where particles and their anti-particles are created from an initial photon. The initial photon must have an energy E_γ that is higher than the rest energy of the created particles. In the case of an electron-positron pair, E_γ must be at least two times the electron rest energy $E_\gamma > 1022\,\mathrm{keV}$ to create those particles. The process can, for example, take place in the Coulomb field of a nucleus. Since the effect occurs only at energies higher than 1022 keV and can still be neglected for energies of 1.3 MeV, the effects of pair production are not discussed in this thesis.

Within the scope of this work, Compton scattering and photoelectric absorption are the most important interactions. Concerning photons, these interaction types are the only ones that can lead to energy deposition in the sensor material of the Dosepix detector and produce an output signal (neglecting nuclear pair production).

2.2 Deep learning

Determining physical quantities from measurements usually requires precise knowledge about the underlying physics truth. Correlations between the detector output and the measurands can be too complex to be expressed using classical methods, which might therefore fail or provide results with insufficient accuracy. Deep learning methods are applied to make predictions without prior knowledge about these correlations. However, a neural network needs to be provided with a large amount of training data. Therefore, data samples are often generated synthetically. There are many tasks (e.g., classification and denoising) that neural networks can effectively be used for. Since determining a dosimetric quantity requires a numeric value as output, the focus lies on regression [16] in this work. Within this thesis, simulation data samples are used for supervised machine learning. A neural network is provided with known input and corresponding output data throughout the training process. In the following, neural networks in general, the training process, and evaluation methods are introduced.

2.2.1 Neural networks

Fig. 2.4 shows the basic architecture of a feed-forward neural network. Such a network is characterized by a data flow from input to output where, e.g., no recursions (feedback connections) take place [16]. It consists of an input layer (blue), one or more hidden layers (yellow), and an output layer (red). Each layer comprises several neurons. Each neuron j is associated with a value z_j, the so-called activation of the j^{th} neuron.

It depends on the activations of the i^{th} neurons in the prior layer. z_j is calculated via [17]

$$z_j = \Phi\left(\sum_i^N w_{j,i}\, z_i + b_j\right), \tag{2.10}$$

where $w_{j,i}$ is a weight that is associated with the connection between neuron i and neuron j. N denotes the total number of neurons in the layer. b_j is a bias that is associated with the j^{th} neuron and is added to the sum. Φ is the so-called activation function. Various activation functions can be used. Two examples of common activation functions are [17]

$$\Phi_{sig}(x) = \frac{1}{1+e^{-x}}, \tag{2.11}$$

and

$$\Phi_{tanh}(x) = \tanh(x). \tag{2.12}$$

A very prominent activation function is the so-called *rectified linear unit* [16] (ReLU). It is defined as

$$\Phi(x) = \max(0, x). \tag{2.13}$$

The neural network is provided with input data for the first layer, from which the neural network predicts one or more output values y_k at the output layer. In a network, where every neuron of a layer is connected to every neuron of the subsequent layer, the layers are called fully connected.

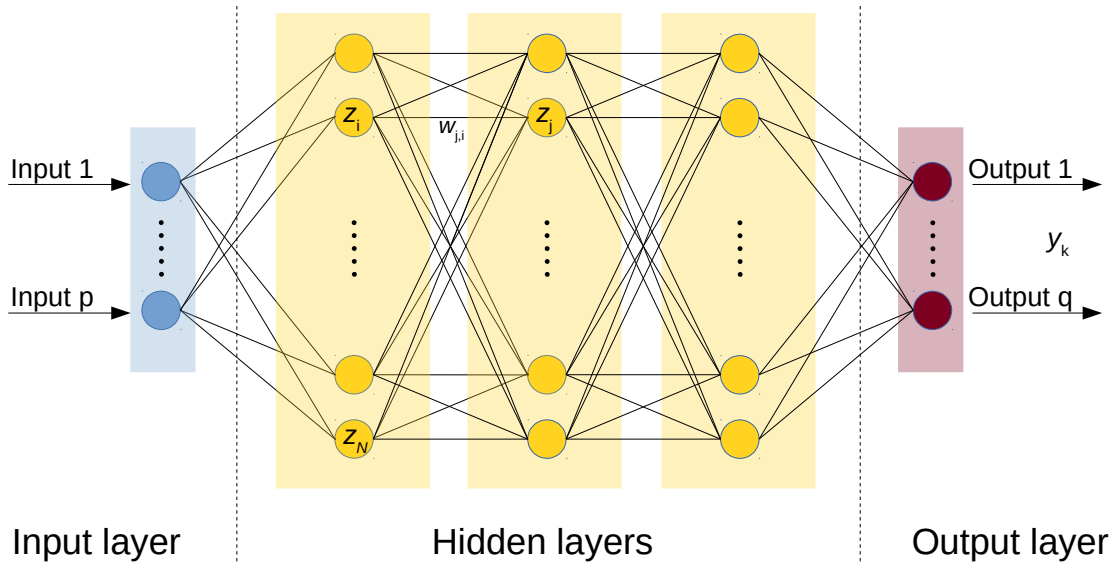

Figure 2.4 Architecture of a feed-forward neural network. It consists of an input layer, one or more hidden layers, and an output layer. Each layer consists of individual neurons that are connected layer-wise. The connections are associated with weights and biases. The image is adapted and modified from [17].

2.2.2 Learning process

The following explanation of the learning process is taken from [17]. The actual true output values (labels) y need to be known for the training process in supervised learning. The loss L is a measure of the deviation between predicted outputs y_k and labels y. The predicted outputs correspond to input values. The loss function is defined to optimize weights w and biases b. A common choice for the loss function is the mean squared error (MSE), defined as

$$L = \frac{1}{2\,n} \sum_{s}^{n} |y(s) - y_k(s)|^2, \tag{2.14}$$

where n denotes the number of training samples, s an individual training sample, $y(s)$ the labels, and $y_k(s)$ the predicted outputs of s. Basically, any differentiable function can be used to determine L. A reasonable choice strongly depends on the kind of problem (e.g., classification or regression). The goal of the learning process is to adjust w and b such that L is minimized. This optimization is realized using backpropagation. In doing so, it is important to understand how L changes with variations of w and b. A notation that simplifies the argument in the activation function in equ. 2.10 is introduced

$$a_j = \sum_{j} w_{j,i}\, z_i. \tag{2.15}$$

Biases can be included in the sum by using an extra neuron and weight with an activation fixed at +1. This allows the explanation of backpropagation without an explicit discussion of b. From equ. 2.10 and equ. 2.15 follows

$$z_j = \Phi(a_j). \tag{2.16}$$

The change of L with $w_{j,i}$ can be expressed via

$$\frac{\partial L}{\partial w_{j,i}} = \frac{\partial L}{\partial a_j} \frac{\partial a_j}{\partial w_{j,i}} \tag{2.17}$$

using the chain rule for partial derivatives. One term in equ. 2.17 is evaluated using equ. 2.15

$$\frac{\partial a_j}{\partial w_{j,i}} = z_i \tag{2.18}$$

and the error δ_j is defined as

$$\delta_j = \frac{\partial L}{\partial a_j}. \tag{2.19}$$

Therefore, equ. 2.17 can be written as

$$\frac{\partial L}{\partial w_{j,i}} = \delta_j\, z_i. \tag{2.20}$$

As previously mentioned, the goal of backpropagation is to understand how L changes when w and b are altered. Equ. 2.20 describes this change in terms of a product of the error δ_j and the activation of neuron i.

For the output layer, the error δ_k is calculated using equ. 2.19, where L is expressed as

$$L_s = \frac{1}{2} |y - y_k|^2 = \frac{1}{2} |y - \Phi(a_k)|^2 \tag{2.21}$$

for a single training set s. This leads to

$$\delta_k = \frac{\partial L_s}{\partial a_k} = \Phi(a_k)' \frac{\partial L_s}{\partial y_k} \tag{2.22}$$

with $y_k = z_k$ for the output layer and $\Phi(a_k)'$ the derivative of $\Phi(a_k)$. To calculate the errors for hidden layers, the chain rule is used again

$$\delta_j = \frac{\partial L_s}{\partial a_j} = \sum \frac{\partial L_s}{\partial a_k} \frac{\partial a_k}{\partial a_j}. \tag{2.23}$$

Using equ. 2.15, equ. 2.16, and equ. 2.19 in equ. 2.23 yields the back-propagation formula

$$\delta_j = \Phi'(a_j) \sum_k w_{k,j} \delta_k. \tag{2.24}$$

It is an expression for the errors that are multiplied by the activations of the neurons in the second to last hidden layer depending on the error δ_k. This process is repeated for every layer from back to front in the neural network by applying equ. 2.24 recursively.

The back-propagation algorithm to determine all $\frac{\partial L_s}{\partial w_{j,i}}$ is summarized in the following steps:

- Calculate all a of all neurons in the network by propagating a data sample s through the network using equ. 2.15 and equ. 2.16.
- Obtain L_s and δ_k using equ. 2.21 and equ. 2.22.
- Evaluate equ. 2.24 to calculate all δ_s for all neurons of each hidden layer in the network.
- Apply equ. 2.20 to obtain the required derivatives.

The back-propagation algorithm, as explained above, is applied for all s to calculate the total loss L for all training sets s. The individual derivatives are summed up for a batch B of individual training sets

$$\frac{\partial L_B}{\partial w_{j,i}} = \sum_s \frac{\partial L_s}{\partial w_{j,i}}. \tag{2.25}$$

Each batch denotes a subset of the utilized training samples. For example, gradient descent can be applied to determine the new weights $W_{j,i}$ via

$$W_{j,i} = w_{j,i} - \nu \delta_j \frac{\partial L}{\partial w_{j,i}}, \tag{2.26}$$

where ν is a positive number called the learning rate. It denotes a measure for how much the weights can change their values at each back-propagation process. Here, the mean of $\frac{\partial L_B}{\partial w_{j,i}}$ is used in equ. 2.26. Once all batches have been used to train the network, a so-called *epoch* has passed. Then, the batches are shuffled randomly and the optimization process starts over.

For the calculation of the new weights $W_{j,i}$, different methods, so-called optimizers, can be used. Depending on the optimizer, different parameters like the learning rate are varied during the training to increase efficiency. Within this thesis, only regression networks are used to predict scalar outputs. For optimization, *adaptive moment estimation* (ADAM) [18] is used to train the networks in this thesis.

2.2.3 Evaluation and overfitting

Depending on the architecture of a neural network, the number of free parameters (weights and biases) that are optimized can become significantly larger than the number of individual training samples used to train the network. Therefore, it is possible that weights and biases are adjusted so that the input training data is matched perfectly to the corresponding labels. If predictions made by evaluating the network with unseen data worsen with an increasing number of epochs, this process is called over-fitting. One way to monitor the training and stop it before overfitting occurs is to evaluate a second data set during training. A criterion to abort the training can be that the loss of the second data set has not improved within a fixed number of epochs. This so-called validation data set originates from the same population as the training data but is excluded from the training process [17]. At some point during the training, the loss of the validation data set converges since optimization has reached a local minimum. If overfitting takes place, the validation loss starts to rise again. An approach to finding a network with a good performance on new data is to train and evaluate various networks. The resulting loss on the validation data of the networks is compared, and the network with the smallest loss is selected. This approach is called the *hold out method* [17].

However, there is still the chance that the chosen set of validation data is biased somehow. This is especially then a problem if the validation data set is small. Therefore, a chosen architecture is trained multiple times, where the validation data set is exchanged with an equally sized subset of data from the whole data pool. This procedure is called cross-validation and provides a method to estimate the average test error on the validation data using all data samples from the whole data pool [16].

2.3 Dosimetry

2.3.1 Dosimetric quantities

Different dose quantities are used to estimate the harmfulness of ionizing radiation. A selection of them is listed in the following. The physical quantities are the absorbed dose D, the photon fluence Φ, and the so-called air kerma K_a [19]. Here, the fundamental quantity is the absorbed dose since every radiation effect on the human body is based on radiation absorption. The dose quantities are:

- Absorbed dose defined as [19]

$$D = \frac{\mathrm{d}\bar{\varepsilon}}{\mathrm{d}m}, \tag{2.27}$$

  where $\mathrm{d}\bar{\varepsilon}$ denotes the mean energy imparted to the matter $\mathrm{d}m$ via ionization. Its unit is joule per kilogram, also called *Gray*

$$[D] = 1\,\mathrm{Gy} = 1\,\frac{\mathrm{J}}{\mathrm{kg}}. \tag{2.28}$$

- Photon fluence defined as [11, 19]

$$\Phi = \frac{\mathrm{d}N}{\mathrm{d}A}, \tag{2.29}$$

where $\mathrm{d}A$ is the number of photons on a sphere of cross-sectional area $\mathrm{d}A$. Its unit is

$$[\Phi] = \frac{1}{\mathrm{cm}^2}. \tag{2.30}$$

- Kerma (*kinetic energy released per unit mass*) K defined as [19]

$$K = \frac{\mathrm{d}E_{\mathrm{tr}}}{\mathrm{d}m}, \tag{2.31}$$

where $\mathrm{d}E_{\mathrm{tr}}$ denotes the sum of all initial energies of the charged particles that are generated by irradiation of a volume of matter $\mathrm{d}m$ with uncharged ionizing particles. Its unit is joule per kilogram, also called *Gray*

$$[K] = 1\,\mathrm{Gy} = 1\,\frac{\mathrm{J}}{\mathrm{kg}}. \tag{2.32}$$

- Dose equivalent H defined as [19]

$$H = D \cdot Q, \tag{2.33}$$

where D denotes the absorbed dose at a pre-defined point in tissue and Q is a dimensionless quality factor that is dependent on the linear energy transfer in water. Its unit is joule per kilogram. It is also called *Sievert*

$$[H] = 1\,\mathrm{Sv} = 1\,\frac{\mathrm{J}}{\mathrm{kg}}. \tag{2.34}$$

- Ambient dose equivalent $H^*(d)$ at a point in a radiation field is defined as the dose equivalent that would be produced by the applied radiation field in a depth d of an ICRU sphere [19] filled with ICRU-tissue (density $\rho = 1\,\frac{\mathrm{g}}{\mathrm{cm}^3}$, mass composition: 76.2 % oxygen, 11.1 % carbon, 10.1 % hydrogen and 2.6 % nitrogen [20]). $H^*(d)$ depends on the orientation of the incident radiation field [19]. Its unit is joule per kilogram, also called *Sievert*

$$[H^*(d)] = 1\,\mathrm{Sv} = 1\,\frac{\mathrm{J}}{\mathrm{kg}}. \tag{2.35}$$

- Personal dose equivalent $H_{\mathrm{p}}(d)$ defined as the dose equivalent in a depth of d millimeters in ICRU-tissue [19]. Within this work, especially $H_{\mathrm{p}}(10)$ (so-called deep dose equivalent) and $H_{\mathrm{p}}(0.07)$ (so-called skin entrance dose) are of interest. Its unit is joule per kilogram, also called *Sievert*

$$[H_{\mathrm{p}}(d)] = 1\,\mathrm{Sv} = 1\,\frac{\mathrm{J}}{\mathrm{kg}}. \tag{2.36}$$

- The dose rate $\dot{H}_\mathrm{p}(d)$ is defined as the applied personal dose equivalent in a depth of d per unit of time Δt

$$\dot{H}_\mathrm{p}(d) = \frac{\Delta H_\mathrm{p}(d)}{\Delta t}. \tag{2.37}$$

  A common dimensioning of the unit is Sievert per hour

$$[\dot{H}_\mathrm{p}(d)] = 1\,\frac{\mathrm{Sv}}{\mathrm{h}}.$$

The path length from the surface of an ICRU-tissue medium to a point in a depth d of the medium depends on the incident angle α of an applied radiation field $\mathrm{S}(\alpha)$ (see fig. 2.5). Therefore, a different dose equivalent in a depth d is expected for different α. [19] provides conversion factors that match, for example, $H_\mathrm{p}(d, 0°) \rightarrow H_\mathrm{p}(d, \alpha)$ depending on the incident photon energy. Test measurements for dosemeters are carried out on so-called phantoms, where the dosemeter is mounted onto. The phantom serves as a substitute for the human body and is important since backscattering in tissue significantly influences measurements. There are various kinds of phantoms representing parts of the human body. Each phantom has a different geometry and, therefore, different scattering properties. Within this work, only an ISO water slab phantom (further referred to as slab phantom) [21] is used to determine the dose. This phantom is a $30\,\mathrm{cm} \times 30\,\mathrm{cm} \times 15\,\mathrm{cm}$ container with polymethyl methacrylate (PMMA) walls filled with water. The applied dose $H_\mathrm{p}(d, 0°)$ on a slab phantom can be expressed as a function of the photon energy and the photon fluence. [19] provides conversion factors matching an energy-dependent photon fluence to air kerma $\Phi(E) \rightarrow K_\mathrm{a}$ and air kerma to personal dose equivalent $K_\mathrm{a} \rightarrow H_\mathrm{p}(10, 0°)$ and $K_\mathrm{a} \rightarrow H_\mathrm{p}(0.07, 0°)$.

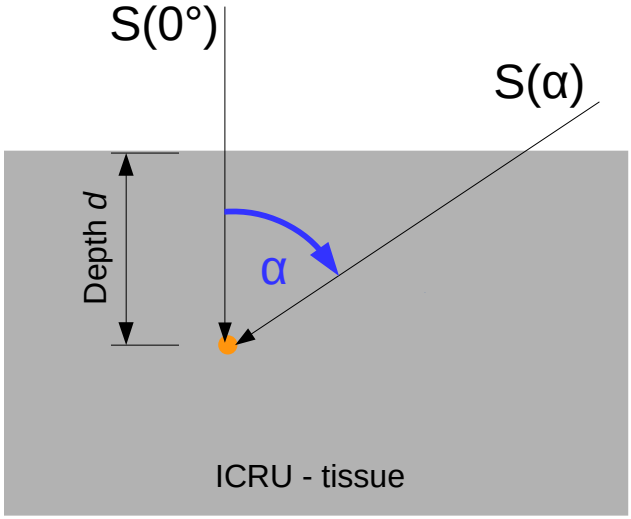

Figure 2.5 Scheme of the angular dependence of the personal dose equivalent. $H_\mathrm{p}(d)$ is defined as the dose equivalent in a depth of d in ICRU-tissue and alters with the path length in the tissue. The path length depends on the incident angle α of an applied radiation field $\mathrm{S}(\alpha)$.

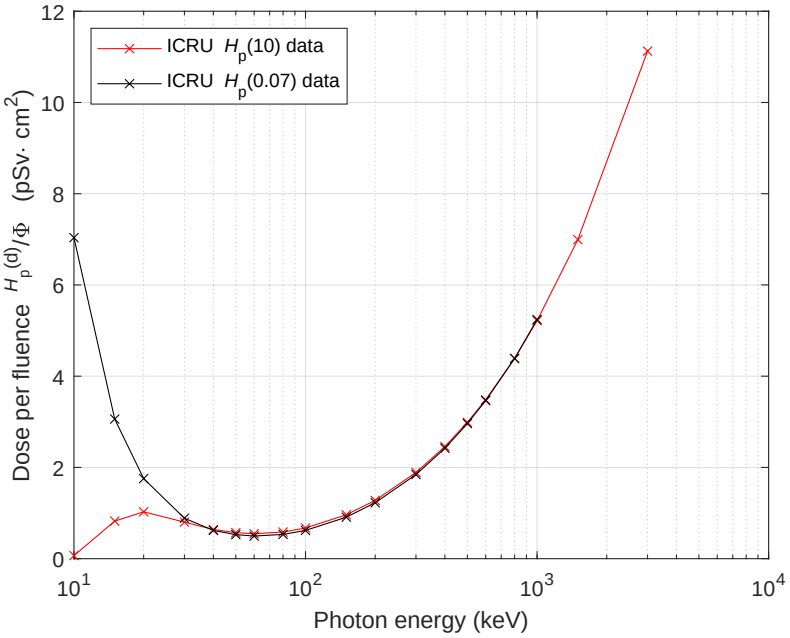

Figure 2.6 Dose per fluence $\frac{H_\mathrm{p}(d)}{\Phi}$ as a function of the energy of the initial photon field for $H_\mathrm{p}(10)$ (red) and $H_\mathrm{p}(0.07)$ (black) for an angle of incidence of 0°. The data is valid for an ISO water slab phantom. The data is taken from [19].

These relations are used to calculate the personal dose equivalent per photon fluence depending on the photon energy. Fig. 2.6 shows this relation for $\frac{H_\mathrm{p}(10,0°)}{\Phi}$ and $\frac{H_\mathrm{p}(0.07,0°)}{\Phi}$ for a slab phantom. The red and black crosses mark the data points extracted from [19] for $H_\mathrm{p}(10, 0°)$ and $H_\mathrm{p}(0.07, 0°)$. A cubic data interpolation [22, 23] is applied (red (black) line in fig. 2.6) since only a few data points are given over a wide energy range. Using this data, $H_\mathrm{p}(10, 0°)$ and $H_\mathrm{p}(0.07, 0°)$ are calculated for known photon spectra depending on the photon fluence.

2.3.2 PTB requirements

Personal dosemeters (active or passive) need to be tested and approved before they can be legally used for radiation protection purposes. National and international standards regulate the requirements for personal dosemeters. In Germany, so-called type tests are performed by the national metrology institute of Germany (***P**hysikalisch-**T**echnische **B**undesanstalt* (PTB) [24]) to evaluate personal dosemeters concerning metrological and non-metrological requirements. For this work, only a selection of the metrological ones is of interest. Tab. 2.1 lists these requirements for $H_\mathrm{p}(10)$ and tab. 2.2 for $H_\mathrm{p}(0.07)$. The limits on the dose rate are usually tested in pulsed radiation fields. An important quantity that is used for evaluation is the response of a dosemeter to an applied radiation field. The response R is defined as the fraction of the measured dose H_mes and the truly applied dose (the reference dose) H_0

$$R = \frac{H_\mathrm{mes}}{H_0}. \tag{2.38}$$

The normalized response R_n is defined as

$$R_n = \frac{R}{R_0}, \tag{2.39}$$

where R_0 denotes the response at a reference value for each measured quantity respectively. The allowed range for R_n is given by the limits f_{min} and f_{max}

$$f_{min} \leq R_n - 1 \leq f_{max}. \tag{2.40}$$

Tab. 2.1 and tab. 2.2 list the nominal range of use, the reference value that is to be used for R_0, and the allowed limits for each quantity for $H_p(10)$ and $H_p(0.07)$.

Quantity	Minimum nominal range of use	Reference value	$f_{min}...f_{max}$
$\overline{E}$ and α	80 keV to 1250 keV and $-60° \leq \alpha + 60°$	662 keV ($\overline{E}$ of ^{137}Cs) and 0°	-29%...+67%
Dose and Dose rate	0.1 mSv to 1 Sv and 0.1 $\frac{\mu Sv}{h}$ to 1 $\frac{Sv}{h}$	1 mSv and 1 $\frac{mSv}{h}$	-13%...+18%
Pulse duration and Peak pulse dose rate	0.1 mSv to 10 s 0 $\frac{Sv}{h}$ to 1 $\frac{Sv}{h}$	Response in continuous radiation	-20%...+20%

Table 2.1: Selection of PTB requirements for personal dosemeters for $H_p(10, \alpha)$ [25]. This table only lists requirements that are relevant to this work.

Quantity	Minimum nominal range of use	Reference value	$f_{min}...f_{max}$
$\overline{E}$ and α	30 keV to 250 keV and $-60° \leq \alpha + 60°$	65 keV ($\overline{E}$ of A-80) and 0°	-29%...+67%
Dose and Dose rate	0.1 mSv to 10 Sv and 0.1 $\frac{\mu Sv}{h}$ to 1 $\frac{Sv}{h}$	3 mSv and 1 $\frac{mSv}{h}$	-13%...+18%
Pulse duration and Peak pulse dose rate	0.1 mSv to 10 s 0 $\frac{Sv}{h}$ to 1 $\frac{Sv}{h}$	Response in continuous radiation	-20%...+20%

Table 2.2: Selection of PTB requirements for personal dosemeters for $H_p(0.07, \alpha)$ [25]. This table only lists requirements that are relevant to this work.

Dose range	$v_{\max}$ (%)
$H_0 < H_u$	15
$1 \cdot H_u \leq H_0 < 11 \cdot H_u$	16 - $\frac{H_0}{H_u}$
$11 \cdot H_u \leq H_0$	5

Table 2.3: Limits $v_{\max}$ on the coefficient of variation [25, 26] for different dose ranges.

In addition to the limits on the normalized response, a maximum variation of the response for several measurements under the same conditions is required. The so-called coefficient of variation is calculated via

$$v = \frac{\sigma(H_{mes})}{\mu(H_{mes})}, \tag{2.41}$$

where $\mu(H_{mes})$ and $\sigma(H_{mes})$ denote the mean and the standard deviation of the measured doses on a series with n independent measurements. The maximum coefficient of variation $v_{\max}$ is defined for three dose ranges [26] (see tab. 2.3). Here, $H_u = 0.1\,\mathrm{mSv}$ for $H_p(10)$ and $H_u = 1\,\mathrm{mSv}$ for $H_p(0.07)$.

Another important quantity that is not part of the PTB requirements, but is still evaluated here, is the relative standard error F^{stat}. It is defined as the fraction of the standard uncertainty of the mean ΔH^{stat} on the dose measurement and the measured dose H_{mes}. Since the measured dose depends on the energy of the applied photon field, the relative statistical error needs to be normalized to a fixed dose value to make different measurements at different energies comparable. Here, the reference dose H_0 is set into relation to a fixed dose of $10\,\mu\mathrm{Sv}$. Therefore, F^{stat} is defined as

$$F^{stat} = \frac{\Delta H}{H_{mes}} \sqrt{\frac{H_0}{10\,\mu\mathrm{Sv}}}. \tag{2.42}$$

The measurements performed to evaluate a proper functioning of a dosemeter are carried out using specified radiation fields. These are generated by applying certain metal filters to an X-ray tube. The so-called A-series (ISO 4037 code: N-series [27, 28]) is used to investigate the energy dependence of the normalized response. Tab. 2.4 lists the filtration and tube parameters for these radiation qualities. In addition to the A-series, the γ-lines of two radioactive sources are used. ^{137}Cs with an energy of 661.7 keV and ^{60}Co with two γ-lines at 1173.2 keV and 1332.5 keV. The mean energy of the ^{60}Co lines is about 1253 keV. X-ray spectra of the so-called RQR-series are used to investigate the normalized response in dependence on the dose rate. Here, only aluminum filters are applied to minimize the reduction of photon flux. This provides a higher maximum dose rate. The C-60 spectrum, which is not necessary to investigate in a type test, is used for additional examination in this work.

IEC 61267 code	PTB code	Tube voltage (kV)	Mean energy (keV)	Total filtration (mm)			
				Al	Cu	Sn	Pb
	A-15	15	12.0	0.5			
	A-20	20	16.4	1.0			
	A-25	25	20.3	2.0			
	A-30	30	24.7	4.0			
	A-40	40	33.3	4.0	0.21		
	A-60	60	47.9	4.0	0.6		
	A-80	80	65.0	4.0	2.0		
	A-100	100	83.1	4.0	5.0		
	A-120	120	101.1	4.0	5.0	1.0	
	A-150	150	120	4.0		2.5	
	A-200	200	166.5	4.0	2.0	3.0	1.0
	A-250	250	210.2	4.0		2.0	3.0
	A-300	300	251.9	4.0		3.0	5.0
	A-350	350	291.2	4.0		4.5	7.0
	A-400	400	330.8	4.0		6.0	10.0
RQR 8		100	50.8	3.36			
RQR 9		120	56.6	3.73			
	C-60	60	38.2	3.9			

Table 2.4: Selection of radiation qualities and their properties [27, 28].

2.3.3 Existing dosemeter systems

Two kinds of dosemeters exist for personal dosimetry: passive and active. Passive dosemeters integrate the dose over a designated period (usually one month) and are then read out manually. Commonly used passive dosemeters are film badges and thermoluminescent dosemeters (TLDs). However, active dosemeters (APDs) are capable of measuring and displaying the personal dose in a matter of seconds. Their detection principle is usually semiconductor-based. Some of the APDs that are used in European hospitals were investigated by the EURADOS working group 12 in [29]. The focus in this work is on the performance of the dosemeters concerning the dose rate in laboratory tests. Tab. 2.5 lists the energy range, the dose range, and the dose rate range the investigated devices are made for. The dosemeter with the highest upper limit for the dose rate is the PM1610A by Polimaster with 12 $\frac{\mathrm{Sv}}{\mathrm{h}}$. However, dose rates in common X-ray examinations usually exceed 100 $\frac{\mathrm{Sv}}{\mathrm{h}}$. The actual performance concerning the dose rate is tested in [29] as well, using two different radiation fields. An RQR 8 spectrum with 10 ms long pulses and continuous radiation from a ^{60}Co source. Fig. 2.7 shows the normalized responses for these spectra for different applied dose rates for each of the investigated dosemeters. The response is normalized to the response at 0.1 $\frac{\mathrm{Sv}}{\mathrm{h}}$ for the RQR 8 spectrum and at 0.01 $\frac{\mathrm{Sv}}{\mathrm{h}}$ for the ^{60}Co source. The red dotted line indicates the specified maximum dose rate. All dosemeters strongly underestimate the dose at dose rates higher than 100 $\frac{\mathrm{Sv}}{\mathrm{h}}$, and most APDs even show a normalized response close to zero. The Dosepix dosemeter that is developed to measure dose rates in the range of several hundred $\frac{\mathrm{Sv}}{\mathrm{h}}$ has already been successfully tested in laboratory conditions at PTB with an RQR 8 spectrum. A measurable energy range of 24.6 keV to 1250 keV [30] and a maximum measurable dose rate of 704 $\frac{\mathrm{Sv}}{\mathrm{h}}$ [31] was achieved within the required limits given by PTB [25]. A further comparison of the performance of the Dosepix dosemeter to the dosemeters listed in tab. 2.5 is given in sec. 7.1.5.

Dosemeter Type	Manufacturer	Detector type	Energy range	Dose range	Dose rate range
EPD Mk2	Thermo Fischer Scientific	Silicon Diode	16 keV to 7 MeV	10 µSv to 10 Sv	0.05 $\frac{\mu Sv}{h}$ to 1 $\frac{Sv}{h}$
DMC 3000	Mirion Technologies	Silicon Diode	15 keV to 7 MeV	1 µSv to 10 Sv	0.1 $\frac{\mu Sv}{h}$ to 10 $\frac{Sv}{h}$
L36	DOSITEC	Silicon Diode	20 keV to 6.2 MeV	10 µSv to 9.99 mSv	10 $\frac{\mu Sv}{h}$ to 9.99 $\frac{mSv}{h}$
DMC 2000 XB	Mirion Technologies	Silicon Diode	20 keV to 6 MeV	1 µSv to 10 Sv	0.1 $\frac{\mu Sv}{h}$ to 10 $\frac{Sv}{h}$
Rad-60SE	Mirion Technologies	Silicon Diode	60 keV to 6 MeV	1 µSv to 9.99 Sv	5 $\frac{\mu Sv}{h}$ to 3 $\frac{Sv}{h}$
AT3509C	Atomtex	Silicon Diode	15 keV to 10 MeV	1 µSv to 10 Sv	0.1 $\frac{\mu Sv}{h}$ to 5 $\frac{Sv}{h}$
PM1621A	Polimaster	Geiger-Müller tube	10 keV to 20 MeV	0.01 µSv to 9.99 Sv	0.01 $\frac{\mu Sv}{h}$ to 2 $\frac{Sv}{h}$
EDM-III	Dosilab	Silicon Diode	20 keV to 6 MeV	1 µSv to 1 Sv	1 $\frac{\mu Sv}{h}$ to 1 $\frac{Sv}{h}$
RaySafe i2	Unfors/RaySafe	Silicon Diode	33 keV to 101 keV	1 µSv to 10 Sv	40 $\frac{\mu Sv}{h}$ to 300 $\frac{mSv}{h}$
PM1610A	Polimaster	Geiger-Müller tube	20 keV to 10 MeV	0.05 µSv to 10 Sv	0.01 $\frac{\mu Sv}{h}$ to 12 $\frac{Sv}{h}$

Table 2.5: Commonly used dosemeters and their specified properties as stated by the manufacturer. The data is taken from [29].

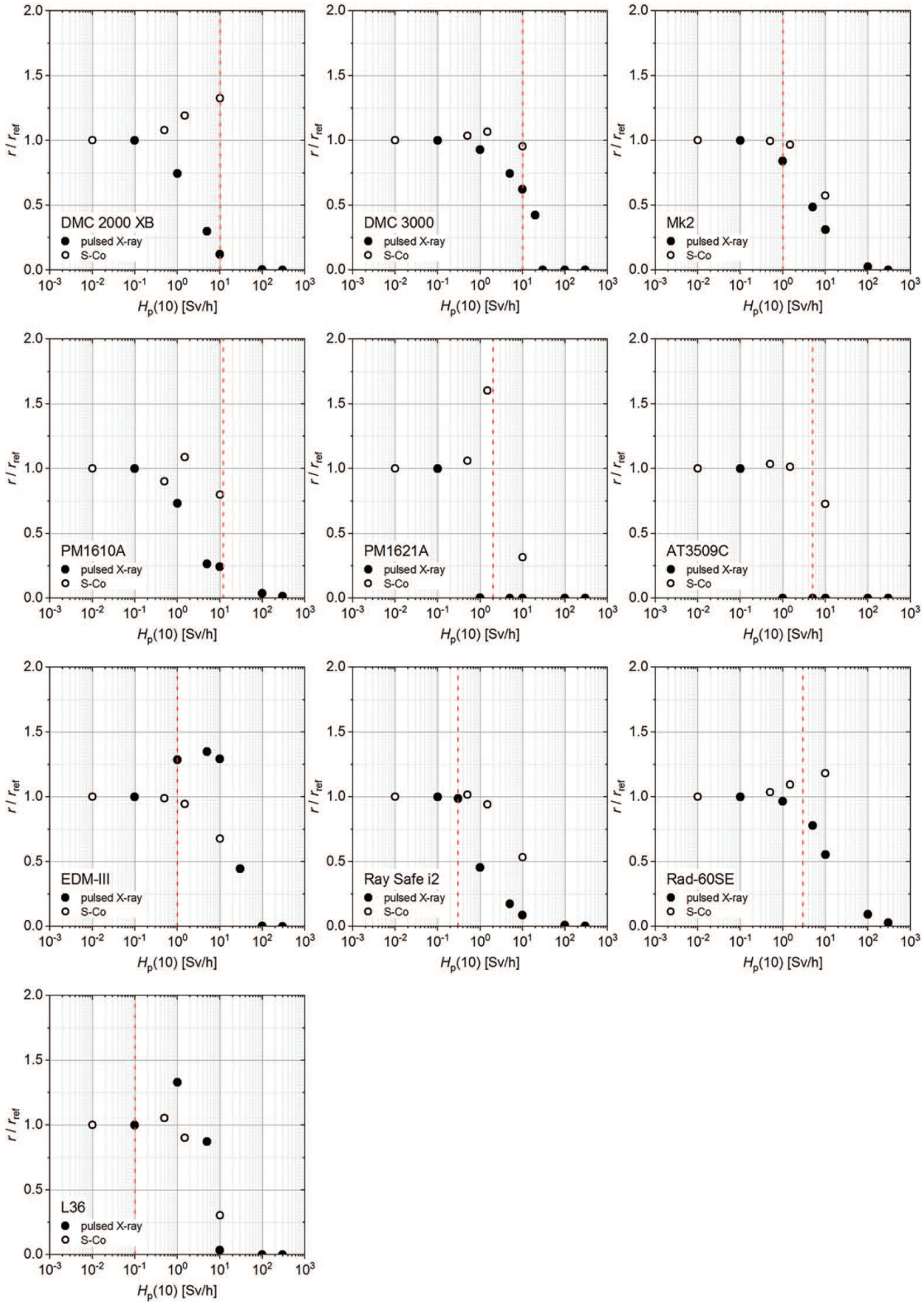

Figure 2.7 Normalized responses for each evaluated APD. The normalization response for pulsed X-rays (RQR 8 spectrum) is 0.1 $\frac{\text{Sv}}{\text{h}}$ and 0.01 $\frac{\text{Sv}}{\text{h}}$ for ^{60}Co. The dotted red line indicates the specified maximum dose rate given by the manufacturer. The images are taken from [29].

Chapter 3

The Dosepix detector

Contents

In this chapter, the Dosepix detector and its layout, signal processing, operation modes, and adjustable measurement parameters are introduced. The setup of the Dosepix dosemeter that consists of three Dosepix detectors is outlined. The occurrence of pile-up and its effect on the data acquisition is discussed. A brief examination of temperature dependence is given. A simulation of the Dosepix dosemeter in X-ray radiation fields is presented. Energy deposition spectra and the accompanying photon detection efficiency from this simulation are outlined.

3.1 Sensor layout

Dosepix is a pixelated semiconductor-based hybrid photon detector that was developed by W. Wong [32] in a collaboration between the *University of Erlangen-Nürnberg*, *IBA-Dosimetry* [33] and the *Medipix-Collaboration* at CERN [34]. Fig. 3.1 shows a schematic of the main elements of its hybrid design. Its segmented sensor consists of 300 µm thick silicon that is p-in-n doped with a total area of about (3.5 mm × 3.5 mm). The sensor resides on top of a readout ASIC (application-specific integrated circuit). The segments (pixels) of the sensor are each connected to a charge processing electronics on the ASIC. The part of the ASIC that is not covered by the sensor (called periphery) contains readout and control circuits. Wire bonds connect the ASIC with a printed circuit board (PCB) for data readout and power supply. Fig. 3.2a shows an image of the sensor and the ASIC that is connected to the PCB via wire bonds. The pixels of the sensor are arranged in a grid of 16 × 16 pixels. Fig. 3.2b shows a schematic of the arrangement. The upper and lower two rows of the matrix consist of pixels with an active area of 55 µm × 55 µm (further referred to as *small pixels*). The remaining pixels have an active area of 220 µm × 220 µm (further referred to as *big pixels*).

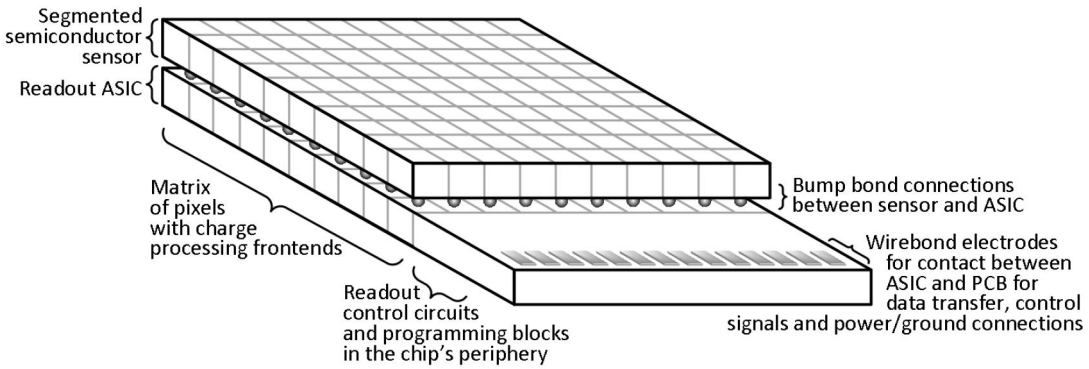

Figure 3.1 Schematic of the main elements of the detector ASIC with sensor. The image is taken from [32].

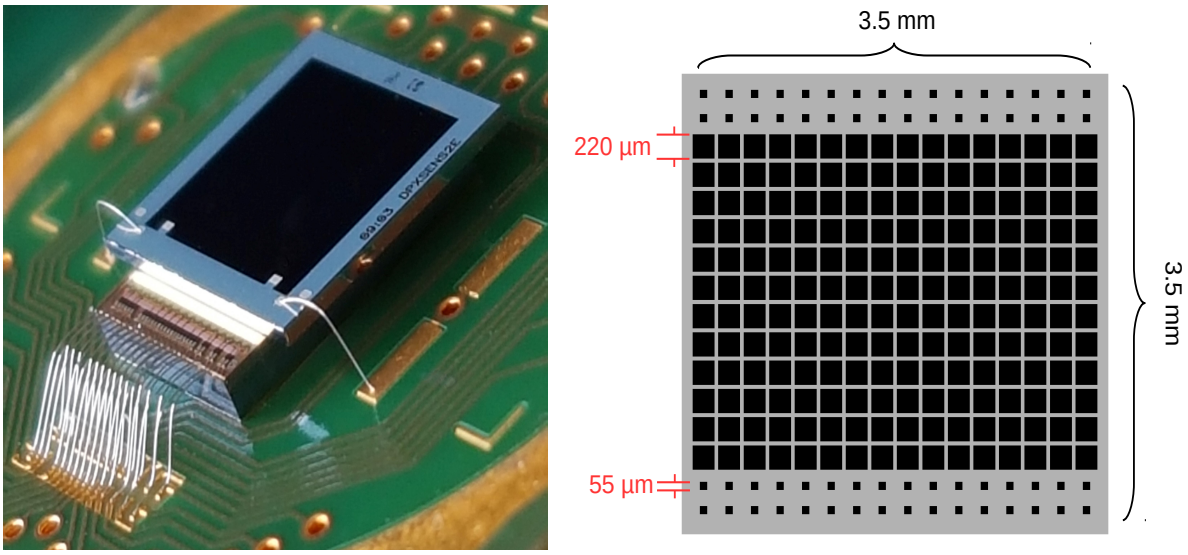

(a) Dosepix detector **(b)** Pixel matrix layout

Figure 3.2 (a): Photo of the Dosepix detector. Wire bonds connect the ASIC to the PCB. (b): Pixel matrix layout of the sensor. The pixel matrix has an edge length of 3.5 mm. Two different pixel sizes with 55 µm (small pixels) and 220 µm (big pixels) are realized.

The setup of the Dosepix dosemeter is chosen as it was established in [35, 36]. The dosemeter consists of three Dosepix detectors that reside on a readout-board (see fig. 3.3). This board is placed in an acrylonitrile butadiene styrene (ABS) plastic box of 12 cm × 12 cm × 3.5 cm. Each detector is covered with a metal filter. The filter on the right-hand side consists of a hollow aluminum cylinder with an aluminum foil of 0.25 mm thickness on top that has an opening above the sensor. This Dosepix detector will further be referred to as *first detector* or *Free*. The Dosepix detector in the middle is covered with a hollow spherical filter made of 2 mm thick aluminum. This detector will further be referred to as *second detector* or *Al*. The Dosepix detector on the left-hand side is covered with a hollow spherical filter made of 1 mm thick β-tin. This detector will further be referred to as *third detector* or *Sn*. Two different sets of filter caps are used. The first measurement is performed with one cylindrical and two hemispheric caps that are taped to the PCB (see fig. 3.4a). These caps are later replaced by a quadratic and two hemispherical caps with an edge on the lower end to hold the filters in place (see fig. 3.4b). The new caps are mechanically more stable than the old ones. The mounts ensure that the caps can be placed at the exact same location on the PCB after removing them. Which set of filters is

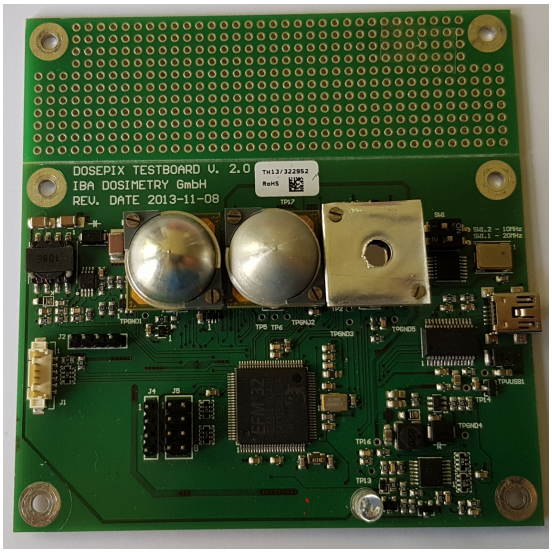

Figure 3.3 Dosepix readout-hardware with filters applied to all three detectors. The filters from left to right: Hemisphere made of tin, hemisphere made of aluminum, foil made of aluminum with an opening above the sensor.

used is pointed out for each particular measurement.

The filter caps are necessary since the measurable energy of a single Dosepix detector is limited to energy values, where the total absorption peak (photopeak) is still measurable. The energy deposition spectra of the three detectors differ due to the filters. The differences between the measured spectra provide information about the initial spectrum. The lower measurable limits vary for each individual detector and pixel and are also dependent on the adjusted measurement parameters (see sec. 3.4). Some pixels are able to measure the photopeak of an iron fluorescence target at about 6.5 keV. These pixels, however, are the minority. Energies above 10 keV are typically measurable for all pixels. The measurement statistics limits the highest energy value at which the photopeak is still measurable. The probability for photoelectric absorption decreases with increasing energy and becomes subdominant in comparison to Compton scattering at about 60 keV in silicon (see fig. 2.2). Here, the highest measured photoabsorption energy from a monoenergetic source is 81 keV from a ^{133}Ba source [37]. With the energy information of three differently filtered Dosepix detectors, dosimetry up to energies of about 1.3 MeV is achievable (see chap. 7).

(a) Filter caps without edges **(b)** Filter caps with edges

Figure 3.4 Different sets of filter caps. (a): Filter caps without edges. These were mounted to the PCB using adhesive tape. (b): Filter caps with edges to mount to the PCB.

3.2 Signal processing

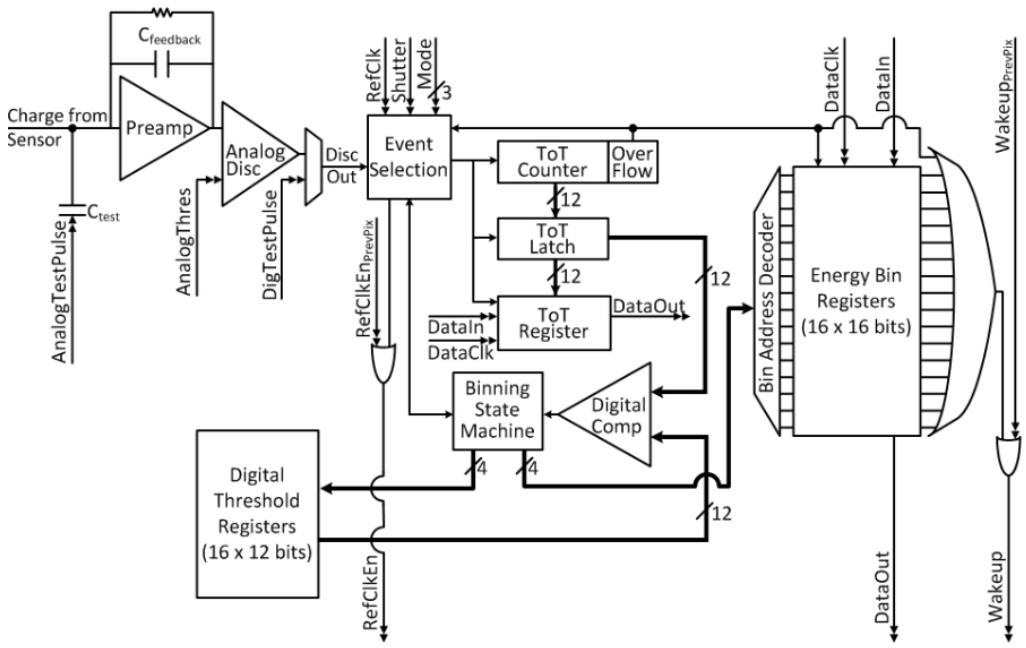

Figure 3.5 Block diagram of the charge processing electronics of a single pixel in Dosimode. Detailed information is given in the text. The image is taken from [32].

An incoming photon can deposit energy in the sensor material via either Compton scattering or photoelectric absorption (see sec. 2.1.2). In both cases, an impinging photon ionizes the sensor material by liberating a Compton- or photoelectron. This electron propagates through the sensor material and creates secondary positive and negative charge carriers. These charges are separated and drifted in the electric field applied between the sensor and the ASIC. The positive charge carriers are collected by the individual readout electronics of each pixel. The amount of liberated charge carriers depends on the energy deposited by the initial electron. Fig. 3.5 shows a block diagram of the pixel electronics that generate the Data output. The analogue charge signal from the sensor is amplified, shaped, and digitized. The digitization process is depicted in fig. 3.6. A discriminator compares the analogue signal to a reference threshold (THL) (dashed gray line). The discriminator output is distributed to the event selection block (see fig. 3.5) and from there to the ToT counter block. If the discriminator output is 1, the clock cycles (blue) of a 100 MHz reference clock are recorded until the discriminator output is 0 again. The number of counted clock cycles is called *Time-over-Threshold* (ToT). It depends on the charge quantity and, therefore, on the energy deposited in the sensor material. The distribution of the ToT and the data output depends on the operation mode of the Dosepix detector. The operation modes are discussed in the following sec. 3.3. Adjustable settings of the ToT acquisition influence the ToT output of the detector as shown in sec. 3.4.

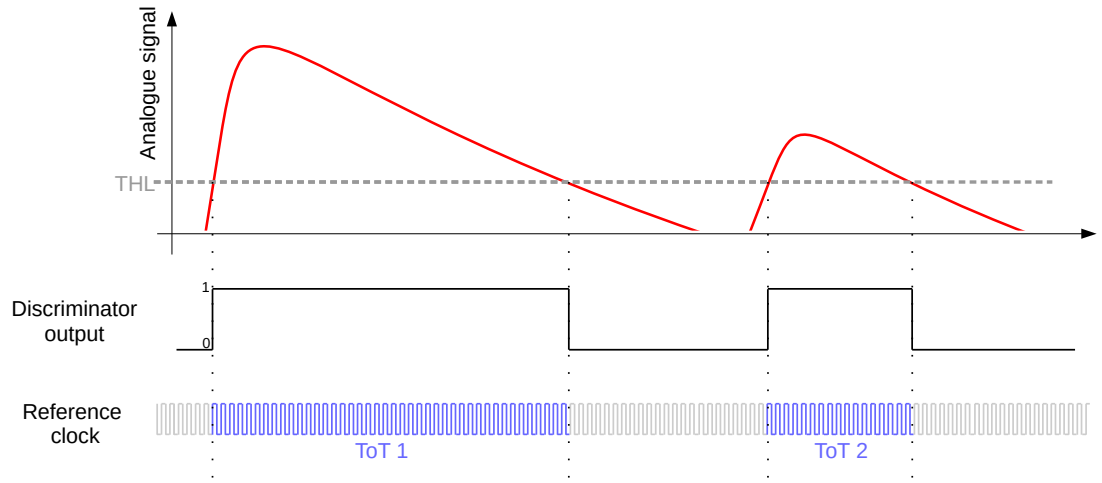

Figure 3.6 Scheme of the signal processing principle. When a charge signal (red) in the pixel electronics exceeds an analogue threshold (dashed gray line), the cycles of a reference clock are counted into a register until the signal undercuts the threshold again. The resulting number of clock cycles is depicted as ToT 1 and ToT 2. The image is adapted and modified from [32].

3.3 Operation modes

The Dosepix detector can take measurements in three different data acquisition modes [32]:

- Energy-binning-mode (further referred to as Dosi-mode, see fig. 3.5): Each individually acquired ToT value is stored in a 12-bit latch and from there distributed to a 12-bit register. By comparing this ToT value to 16 digital thresholds in the Binning State Machine block, the event is directly sorted into one of 16 energy bin registers. Each energy bin has a storage capacity of 16 bits. The digital thresholds are programmable for each pixel individually. The 12-bit register and the 12-bit ToT latch are overwritten with the subsequent ToT value. The last ToT value acquired during the measurement time stays stored in the 12-bit register and is read out when the measurement is finished. The measured data acquired during the adjustable measurement time is read out using a rolling shutter. That means the pixel matrix is read out column-wise, leaving 15 of 16 columns active. This way, consecutive measurements can be performed without dead time. Using the ToT value stored in the 12-bit register, a ToT spectrum can be acquired with several measurements. Although this way of data acquisition is technically not a separate operation mode of Dosepix, it will further be referred to as ToT-mode since it is often used in this work. Fig. 3.7 shows an energy deposition spectrum acquired in ToT-mode (black, left Y-axis). The ToT measured by each big pixel is converted to energy using the energy calibration introduced in sec. 4.2. The large bins (red, right Y-axis) denote the data output when the measurements are performed in Dosi-mode.

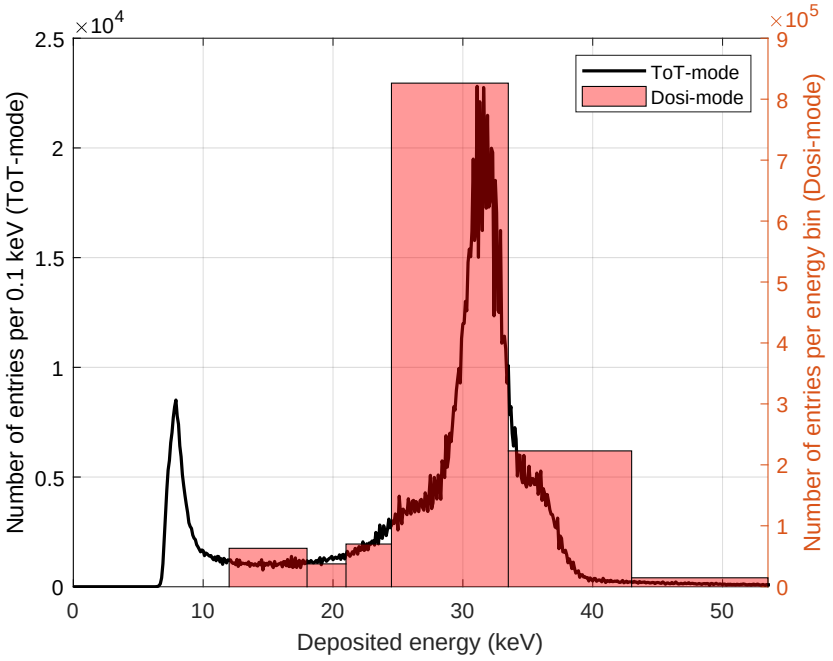

Figure 3.7 Comparison between an energy deposition spectrum of a Ba fluorescence acquired in ToT-mode (black) and the corresponding data output if the data was acquired in Dosi-mode (red).

- Energy integration-mode: While the discriminator output is 1, the clock cycles of the references clock are counted in a 24-bit register. The individual ToT values that correspond to the analogue signals are, therefore, not separated. The ToT of all occurring events during the measurement time is summed up. The value of the 24-bit ToT register of each pixel is given as data output.
- Photon counting-mode: The number of discriminator output pulses are recorded and stored in an 8-bit register. This way, the number of times the threshold is exceeded during the measurement time is counted. A ToT measurement is, therefore, not performed. The value of the 8-bit register of each pixel is given as data output.

3.4 Measurement parameters

Some parameters that specify the ToT acquisition and, therefore, the data output can be modified. The charge from a processed signal is amplified via a charge-sensitive amplifier. The resulting signal is decreased with a constant current. This current is proportional to a current I_{Krum} that is adjustable between 0 nA and 51 nA in steps of 0.2 nA [32]. In addition, I_{Krum} contributes to the leakage current compensation. Fig. 3.8 shows two analogue signals with the same initial charge but different I_{Krum}. The signal with higher I_{Krum} (blue) has a steeper discharge curve than the signal with smaller I_{Krum} (red). The different slopes (m 1 and m 2) result in different decay times and, therefore, different ToTs. ToT 1 is smaller than ToT 2 for the same deposited energy. This results in different ToT spectra. Fig. 3.9 shows five measurements for different I_{Krum} with values between 2.2 nA and 13 nA performed in ToT-mode. The γ-line of an ^{241}Am source at about 60 keV is measured. As expected, the peak of the ^{241}Am source shifts towards smaller ToT values with increasing I_{Krum}. The peak becomes thinner and higher.

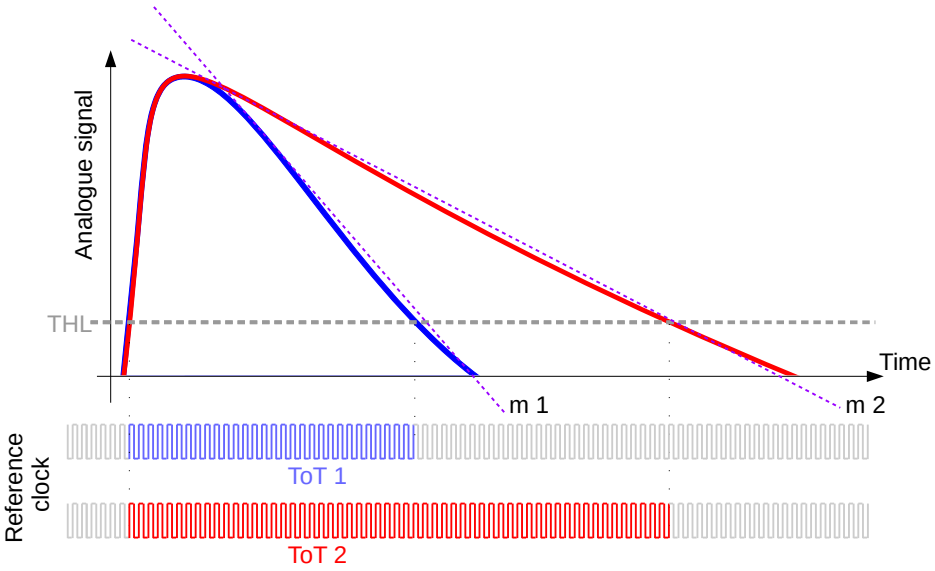

Figure 3.8 ToT acquisition for different I_{Krum}. Measurements with higher I_{Krum} (blue) result in signals with a steeper discharge curves than measurements with lower I_{Krum}. Therefore, the registered ToT is smaller (ToT 1 < ToT 2).

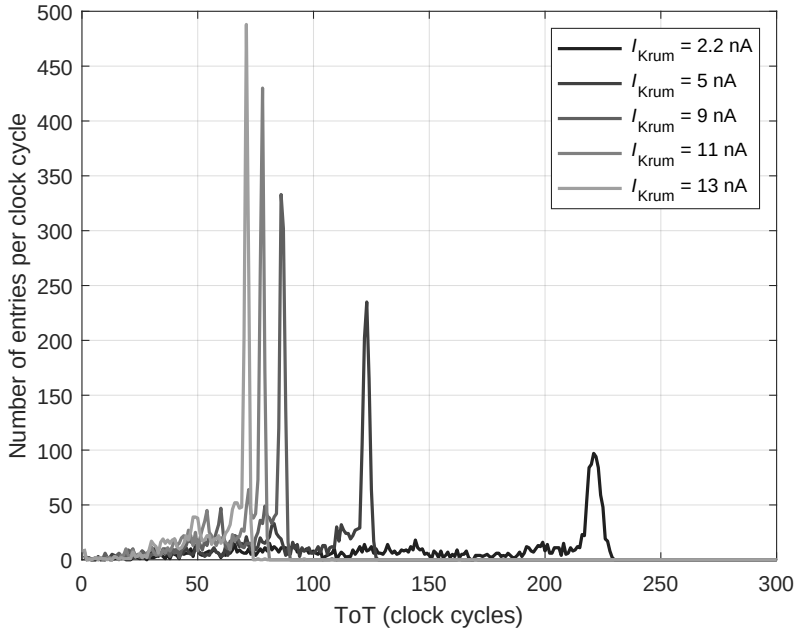

Figure 3.9 Measurements of an ^{241}Am γ-line at about for different I_{Krum}.

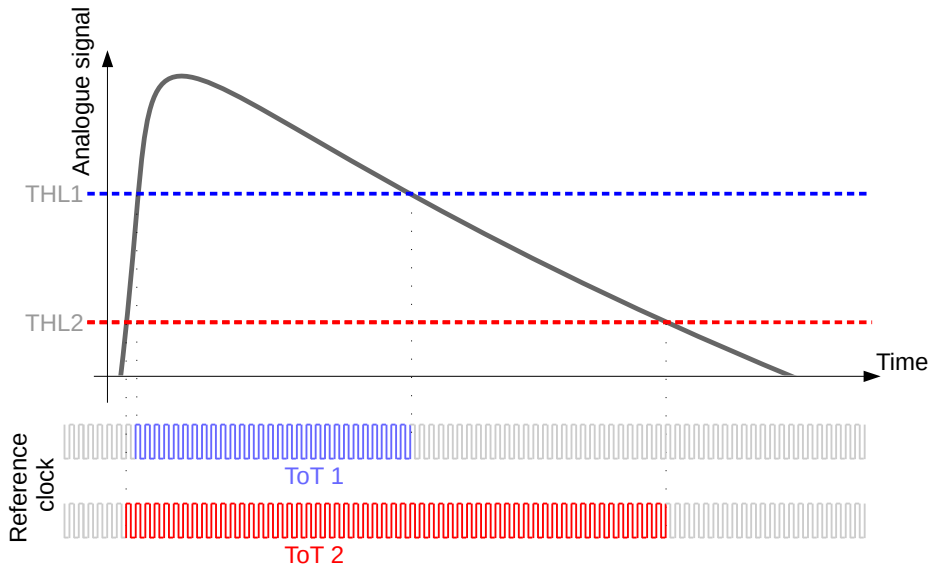

Figure 3.10 ToT acquisition for different threshold levels. Measurements with a higher threshold level (blue) result in smaller ToT values than measurements with a lower threshold level (red) (ToT 1 < ToT 2).

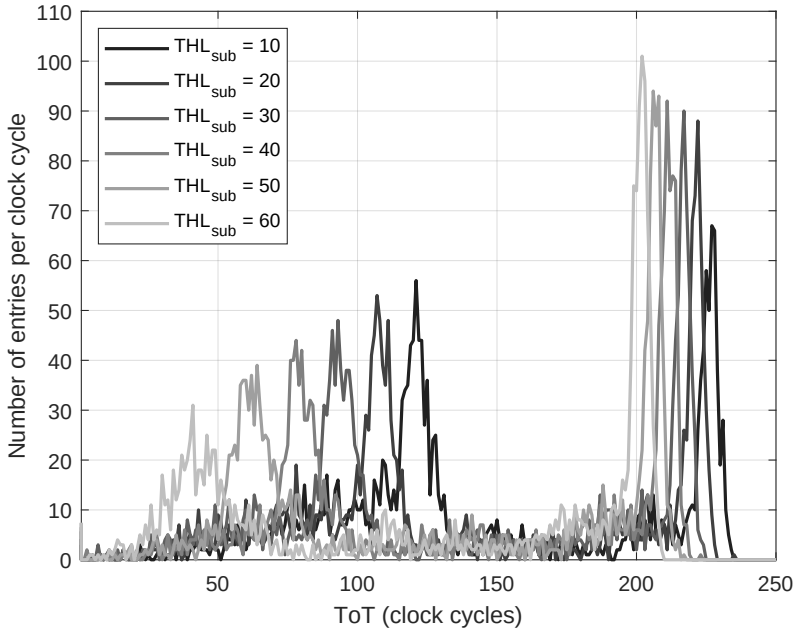

Figure 3.11 Measurements of a ^{241}Am γ-line (peaks at high ToT) and a strontium fluorescence line (peaks at low ToT) for different threshold levels $\mathrm{THL_{sub}}$.

Another adjustable parameter is the analogue threshold level. Fig. 3.10 shows an analogue signal (gray) that is digitized with a high threshold (THL 1, blue) and a low threshold (THL 2, red). In the case of THL 1, the signal exceeds the threshold later and undercuts it earlier than in the case of THL 2. ToT 1 is, therefore, smaller than ToT 2. Fig. 3.11 shows six measurements with different threshold levels $\mathrm{THL}_{\mathrm{sub}}$. The threshold level increases with increasing $\mathrm{THL}_{\mathrm{sub}}$ (a more detailed explanation is given in sec. 4.1). The two prominent peaks in each measurement originate from the γ-line of an ^{241}Am source (peak at high ToT values) at about 60 keV and the most prominent fluorescence lines of a strontium fluorescence target at about 14 keV (peak at low ToT values). As expected, the peaks shift towards lower ToT values with increasing $\mathrm{THL}_{\mathrm{sub}}$. The threshold level corresponds to the minimum energy that can be measured. Therefore, the height of the peak at low ToT values decreases with an increasing threshold level. A further contribution to this decrease is the shape of the ToT-energy calibration curve (see sec. 4.2).

3.5 Pile-up

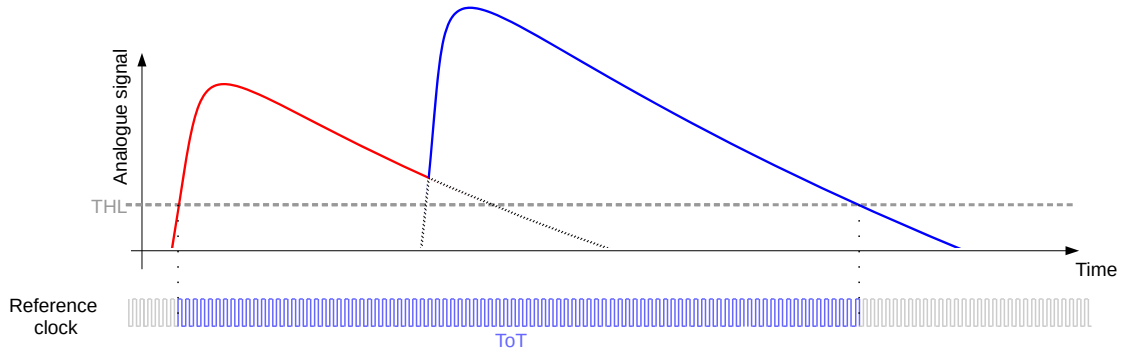

Figure 3.12 Schematic explanation of pile-up. Two signals overlap so the threshold is not undercut after the first (red) signal is decayed. A single ToT value is measured instead of two ToT values.

Pile-up occurs when multiple photons generate charge signals in a pixel within a short time interval. Fig. 3.12 shows two analogue signals that overlap so the analogue signal does not fall below the threshold after the first (red) charge signal is decayed. Instead, the second (blue) charge signal gives rise to the analogue signal again, keeping it above the threshold. The corresponding ToT differs from the sum of the ToTs that each analogue charge signal produces in the case of no pile-up since the slope of the decaying charge signal is dependent on the maximum amplitude [32]. A more detailed examination of the maximum effect pile-up can have on the ToT is given in sec. 5.1. When multiple photons generate charge signals within the rise time of the analogue signal, which is in the range of 500 ns (extracted from a figure in [32], page 132), pile-up necessarily occurs. Therefore, short radiation exposures with pulse durations lower than the rise time always generate pile-up. This special case of pile-up is further referred to as *total pile-up*. In addition, any kind of pile-up complicates and usually prevents the determination of the deposited energy since the model used to transfer deposited energy E to ToT shows the characteristic

$$\mathrm{ToT}(E_1 + E_2) \neq \mathrm{ToT}(E_1) + \mathrm{ToT}(E_2), \tag{3.1}$$

where E_1 and E_2 denote two deposited energies in a pixel. A detailed explanation of the energy calibration procedure with the model is given in sec. 4.2.2.

3.6 Temperature dependence

As with most semiconductor-based detector systems, the behavior of the Dosepix detector depends on its temperature. The effects on measurements were investigated and quantified in a bachelor's thesis performed within the Dosepix workgroup [38]. The leakage current, which is compensated via I_{Krum} during the generation of the voltage signal in the pixel electronics, changes with temperature. As a result, the measured ToT values shift with the temperature. This is problematic if the temperature of the detector during the energy calibration differs strongly from the temperature at which measurements are conducted later. One approach to address this problem is to perform several energy calibrations for different temperatures with the detector. Although Dosepix can measure relative temperatures in units of DAC-values using a built-in temperature sensor, this is not practical. Another possible approach to balance this energy shift is to increase I_{Krum} and, therefore, the leakage current compensation. Fig. 3.13 shows the temperature-dependent shift of the energy deposition as a function of I_{Krum}. The temperature shift decreases with rising I_{Krum}. At $I_{\mathrm{Krum}} = 11\,\mathrm{nA}$ it is almost zero. Therefore, the temperature dependence is neglected for measurements performed with $I_{\mathrm{Krum}} = 11\,\mathrm{nA}$. For measurements performed in integration-mode, a comparison to measurements with other measurement parameters indicates that the temperature dependence is not significant (see sec. 8.1.4). Therefore, the temperature dependence is neglected for measurements performed with $I_{\mathrm{Krum}} = 2.2\,\mathrm{nA}$.

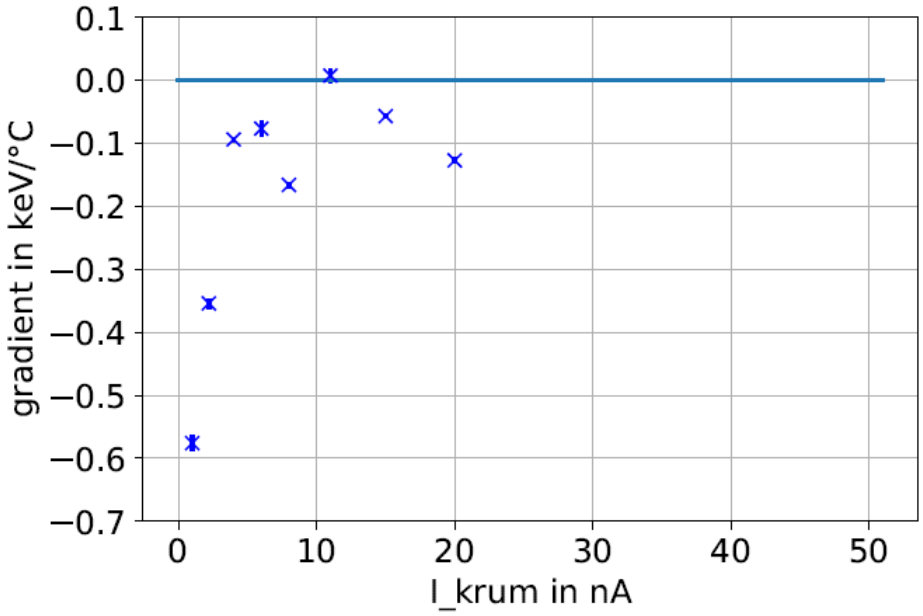

Figure 3.13 Energy shift per 1°C temperature difference as a function of the adjusted I_{Krum}. The image is taken form [38].

3.7 Simulated energy deposition spectra

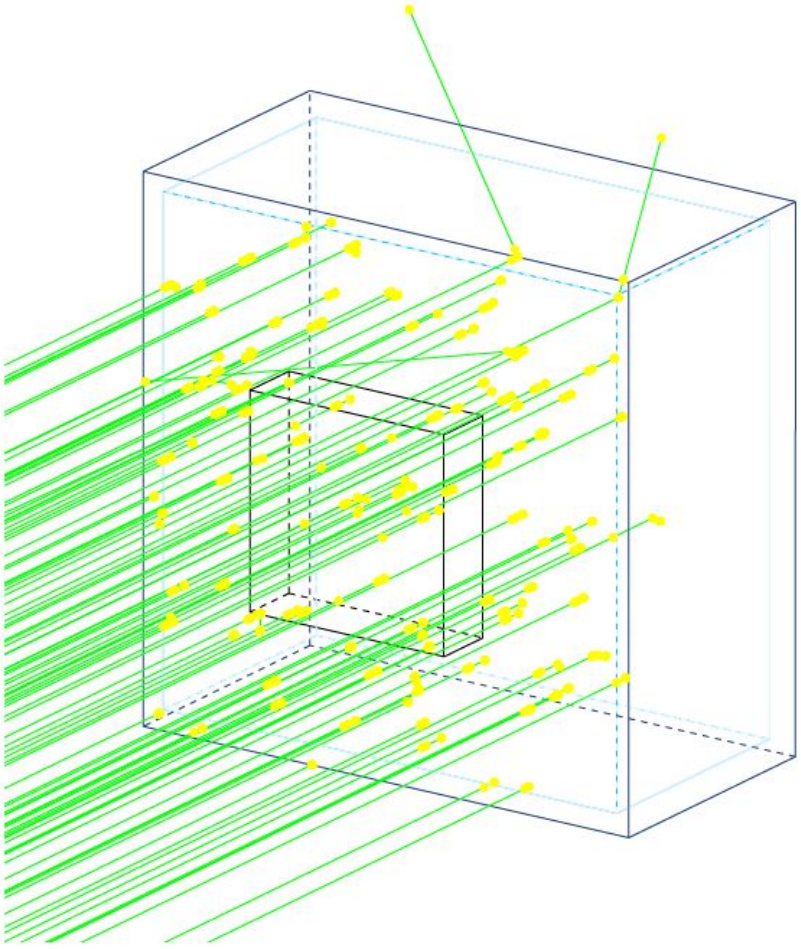

Figure 3.14 Geant4 simulation of the Dosepix dosemeter, depicted by the smaller black box that is attached to an ISO slab phantom that is depicted by the larger black box. The phantom is filled with water in the simulation. The blue box inside the phantom depicts the water level. The green lines indicate the paths of photons that interact with the slab phantom. The photon field is simulated to irradiate the phantom perpendicularly. The image is taken from [39].

The energy deposition spectra provide information about the detector response for an incident photon field. The energy E_j that is deposited in a pixel by a photon with the energy E_i usually differs due to Compton-scattering, Rayleigh-scattering, repulsion, and charge sharing. This statistical process of energy deposition needs to be simulated in a Monte Carlo simulation to gain accurate information about the energy deposition spectra in a single pixel. Such a simulation, where the charge deposition in single pixels is determined, is performed in [39]. The charge deposition can later be linearly converted to deposited energy. The simulation is carried out using Allpix^2 [40], which is a framework for the simulation software GEANT4 [41]. The Dosepix readout-board is geometrically implemented, including the PCBs, circuits, and electronic components. Different materials and material compositions are considered. In the simulation, the readout-board resides in a plastic box that is placed on a slab phantom. Backscattering from the phantom is implemented as well. Fig. 3.14 shows a graphical implementation of the Dosepix dosemeter placed on the slab phantom in the GEANT4 simulation. The green lines indicate photons that undergo an interaction.

The charge deposition of photons in individual pixels is simulated, considering different types of energy-dependent photon interactions with the sensor material and the effects of charge sharing and repulsion. Big and small pixels are simulated separately, where simplifying assumptions concerning the small pixels are made. This, however, is not discussed in detail since only simulations of the big pixels are used in this thesis. Monoenergetic photons and perpendicular irradiation of the frontal surface of the phantom are considered for all simulated radiation fields. Tab. 3.1 lists the energy intervals of the initially simulated photon energies.
Fig. 3.15 shows an example of simulated charge deposition spectra for irradiation with photons of 60 keV. The spectra are shown for the detector without filter (blue), with aluminum filter (red), and with tin filter (black). The bottom X-axis indicates the number of dislodged electrons in the sensor material. The number of electrons generated during the passage of a Compton or photoelectron is linearly converted to the energy deposited in the detector material. The generation of a pair of charge carriers in silicon requires an energy of 3.62 eV [42]. Multiplying this value with the number of electrons dislodged in the sensor yields the deposited energy (top X-axis in fig. 3.15). The detector resolution was not taken into account in the simulation. In sec. 5.2, the spectra characteristics are discussed in detail after detector resolution is added.

First energy (keV)	Last energy (keV)	Step size (keV)
10	120	1
122	200	2
205	695	5
700	1100	100
1400	1400	—

Table 3.1: Photon energies of the simulated charge deposition spectra. The rows list different energy intervals. The first column denotes the first energy, the second column the last energy and the third column the step size in an energy interval. The simulations are performed in the frame of a PhD thesis [39].

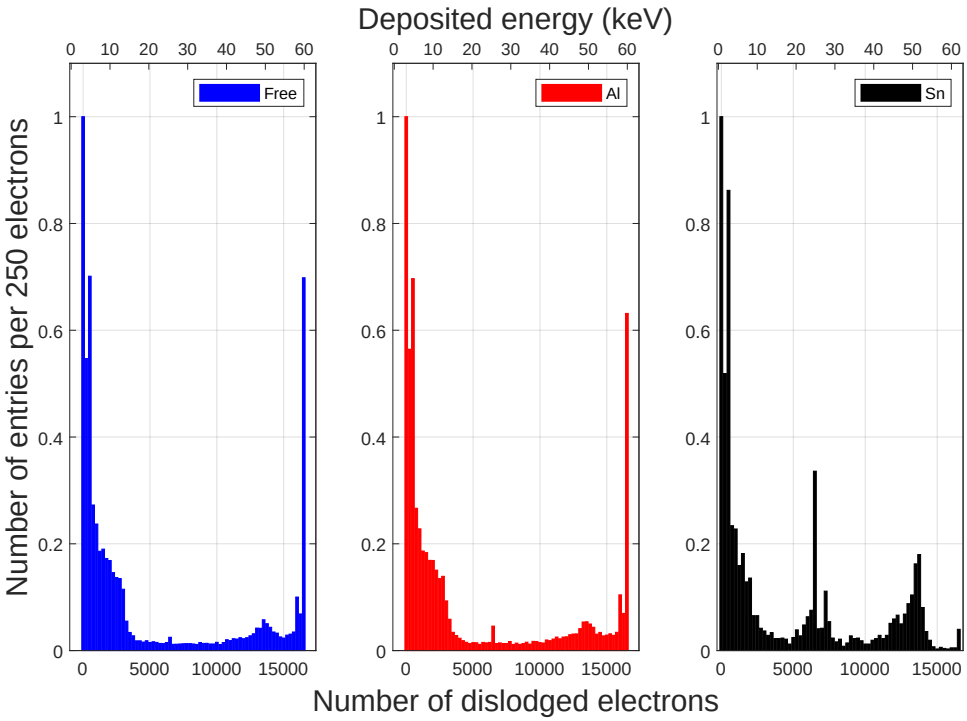

Figure 3.15 Simulated charge deposition spectra for an initial photon energy of 60 keV for the unfiltered detector (blue), with aluminum filter (red), and with tin filter (black). The spectra are each normalized to the highest value. The lower X-axis denotes the number of created electron-hole pairs in the pixel, and the upper X-axis the corresponding deposited energy. The simulations were performed in the frame of a PhD thesis [39].

3.8 Simulated photon detection efficiency

The photon detection efficiency $\varepsilon(c)$ (PDE) for each of the three detectors c is derived from the energy deposition spectra without the detector resolution. As outlined in sec. 2.3.1, all dose measurements were performed with the Dosepix dosemeter placed onto a slab phantom with a front area of $A^{phan} = 30\,cm \times 30\,cm$ to simulate backscattering from the human body. This phantom was taken into account in the simulations [39]. To compare the number of initial photons N^{init} irradiating the whole slab phantom, to the number of photons N^{det} detected by a single pixel, the pixel area $A^{pixel} = 220\,\mu m \times 220\,\mu m$ and the phantom front area need to be taken into account. The PDE is defined as

$$\varepsilon(c) = \frac{\frac{N^{det}(c)}{A^{pixel}}}{\frac{N^{init}(c)}{A^{phan}}} = \frac{\frac{N^{det}(c)}{A^{pixel}}}{\Phi^{phan}}. \tag{3.2}$$

Φ^{phan} denotes the photon fluence on the slab phantom. Fig. 3.15 shows the PDE for the three Dosepix detectors (first: blue, second: red, third: black) as a function of the initial photon energy. As expected, $\varepsilon(1)$ is the highest for low energies. Low energies are cut off by the filters. $\varepsilon(2)$ starts to rise at about 15 keV and $\varepsilon(3)$ at about 50 keV. At about 150 keV $\varepsilon(3)$ exceeds $\varepsilon(1)$ and $\varepsilon(2)$. This is due to the tin filter, which emits fluorescence photons at about 25 keV and 28 keV in close proximity to the third detector. These secondary photons contribute to the number of detected photons in the detector.

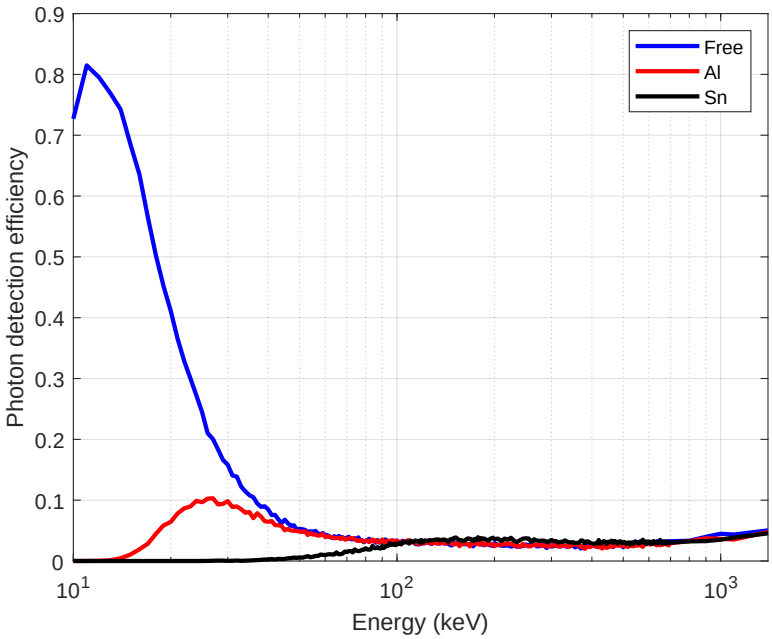

Figure 3.16 Photon detection efficiency for the three Dosepix detectors as a function of the initial photon energy. The data is based on a simulation in [39].

Chapter 4

Calibration and characterization measurements

Contents

This chapter presents an overview of the preparatory steps that need to be performed to conduct energy resolving measurements with the Dosepix detector. The equalization of the individual thresholds of each pixel is motivated and explained. Setup and procedure of measurements necessary for an energy calibration are introduced. The simulation outlined in sec. 3.7 is used to determine the deposition energy, which is used to perform an energy calibration. Two different models for the energy calibration are compared to each other. The measurements that were conducted for calibration purposes are used to determine the energy resolution.

4.1 Threshold equalization

The analogue threshold level is chosen globally for all pixels. However, the individual pixels, which are designed identically for big and small ones respectively, show differences in the energy response. This is due to process variations that cause mismatches in the electronics [32]. Therefore, the analogue threshold level THL can be adjusted for each pixel individually to compensate for these differences. This is performed using a 6-bit deep digital to analogue converter, so-called *pixel-DACs*. First, the actual threshold level of each individual pixel is determined using the *noise edge* method [43]. Here, the detector operates in photon counting-mode. The adjustable pixel-DAC value is set to its maximum (63) for all pixels. Then, the global threshold is decreased within a preset interval. At some point, the threshold reaches the signal baseline where noise exceeds the threshold and produces signals. The noise edge is reached at the momentarily adjusted threshold level if a pixel counts a certain number of signals. In this thesis, the noise limit is chosen to be 3. Fig. 4.1 shows the number of pixels that reached the noise edge for each THL value. The threshold level is given in its digital code on the X-axis.

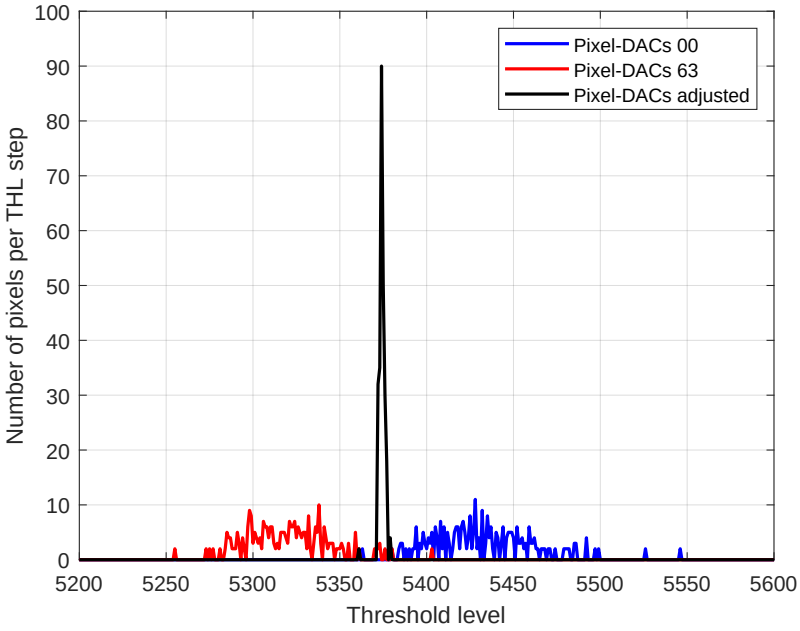

Figure 4.1 Distribution of the pixels that reached the noise edge with the minimum pixel-DAC value (blue) and the maximum value (red). The black curve shows the distribution after the adjustment of the pixel-DACs.

Fig. 4.1 (blue) shows the threshold level distribution for all pixels for a descending scan. The same procedure is performed with the adjustable pixel-DAC values set to the minimum (00) and an increasing global threshold. Fig. 4.1 (red) shows this threshold level distribution. The center of mass of both distributions is calculated. The threshold levels are adjusted in a way that they match the mean ($\mathrm{THL_{target}}$) of the two centers of the two distributions. The corresponding value $\mathrm{THL_{pixel}}$ that is set for each pixel, is calculated via [36]

$$\mathrm{THL_{pixel}} = (\mathrm{THL_{pixel}^{noise}}(00) - \mathrm{THL_{target}}) \cdot \frac{63}{\mathrm{THL_{pixel}^{noise}}(00) - \mathrm{THL_{pixel}^{noise}}(63)}, \tag{4.1}$$

where $\mathrm{THL_{pixel}^{noise}}(0)$ is the value at which a pixel reaches the noise edge when the pixel-DAC is set to 0 and $\mathrm{THL_{pixel}^{noise}}(63)$ the value when the pixel-DAC is set to 63. This procedure yields a new distribution for the number of pixels that reach the noise edge level (black in fig. 4.1). The value for the global threshold is estimated conservatively by subtracting a certain value $\mathrm{THL_{sub}}$ from the smallest threshold value in the distribution of the adjusted pixels. In the measurements, $\mathrm{THL_{sub}}$ was varied between 20 and 60. The threshold equalization needs to be performed for each adjusted I_{Krum}.

4.2 Energy calibration

4.2.1 Calibration setup

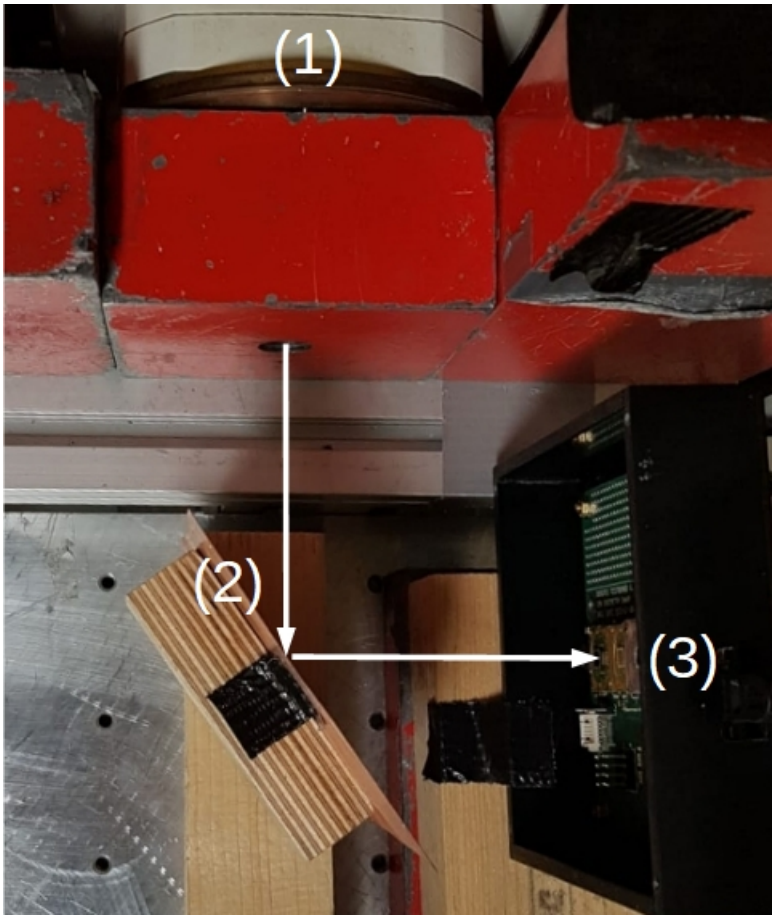

Figure 4.2 Energy calibration setup. A fluorescence target (2) is irradiated by the X-ray tube (1) [44]. The Dosepix detectors (3) measure the fluorescence photons.

An energy calibration is performed to convert measured ToT to deposited energy. Monoenergetic radiation and a high photon flux to decrease the measurement time is desirable. For this purpose, X-ray fluorescence lines from various elements are used. An X-ray tube of the type *MEGALIX CAT 125/15/40/80* [44] is used to excite fluorescence in the target materials. The measurements are performed in ToT-mode without the filter caps above the three Dosepix detectors. Fig. 4.2 shows an image of the setup. The X-rays emitted by the X-ray tube (1) are collimated using an aperture made of lead. Additional lead blocks are placed around the X-ray tube. The aperture and the blocks shield the Dosepix detectors (3) from direct or scattered irradiation from the X-ray tube. The collimated X-ray radiation excites the target material (2), which emits fluorescence photons with discrete energies. Then, the Dosepix detectors detect the fluorescence radiation. The distance between the X-ray tube and the target material and the distance between the target material and Dosepix detectors is kept as short as possible to maximize the flux of fluorescence photons on the Dosepix detectors. The distances are in the range of 10 cm to 20 cm. The X-ray tube voltage U_t is chosen so that

$$U_\mathrm{t} \cdot \mathrm{e} > E_\mathrm{f} \tag{4.2}$$

with e the elementary charge and E_f the energy of the fluorescence lines of the material that is to be excited. The X-ray tube current is set between 10 mA and 15 mA.

4.2.2 Calibration proceeding

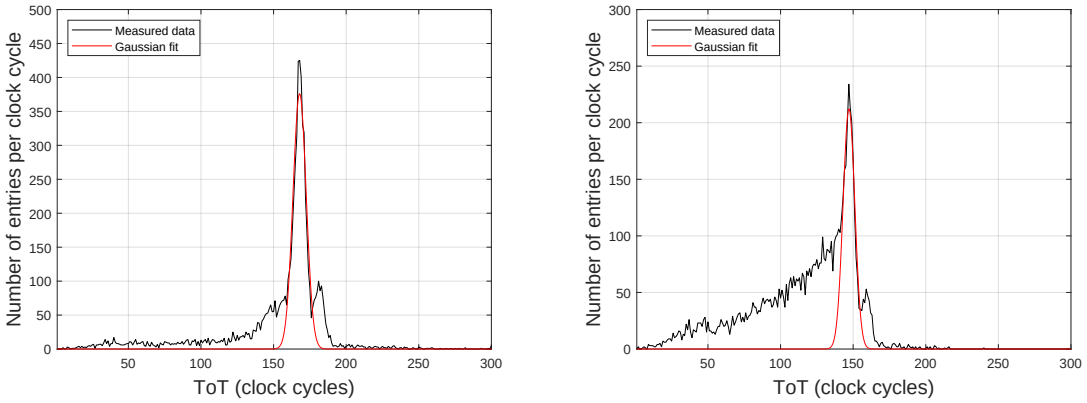

(a) Big pixel **(b)** Small pixel

Figure 4.3 (a): ToT spectra of a barium fluorescence (black) for a single big pixel and (b): for a single small pixel. The red curves denote Gaussian fits that are applied to the most prominent peak.

A ToT spectrum is acquired for all 256 individual pixels for all three Dosepix detectors for different fluorescence materials and one γ-spectrum. Fig. 4.3a shows a ToT spectrum of a big pixel, and fig. 4.3b the one of a small pixel. Here, the target material is barium. Fig. 4.3a shows three peaks that originate from the total absorption of the fluorescence lines. The most prominent one at about 165 clock cycles corresponds to the $K_{\alpha 1}$ emission, the one at about 180 clock cycles to an overlap of the $K_{\beta 1}$ and $K_{\beta 3}$ emission and the one at about 150 clock cycles to the $K_{\alpha 2}$ emission. Due to the smaller pixel volume, the deposition of the whole photon energy is less probable in small pixels than in big ones. Therefore, the peaks in fig. 4.3b are not as prominent as in fig. 4.3a. A Gaussian function (red) of the form

$$G(x, A, B, C) = A \cdot \mathrm{e}^{-(\frac{x-B}{C})^2} \tag{4.3}$$

is fitted to the peaks. Here, A, B, C denote the fit parameters. The center position B of the Gaussian function corresponds to the energy $E(B)$ deposited in the detector material. Due to the imperfect detector resolution, the peaks from the different emission lines usually overlap with each other and with the part of the spectrum that originates from Compton scattering and charge sharing. B is therefore shifted towards small ToT values and is not equal to the mean energy of the initial fluorescence photons. The fluorescence spectra need to be simulated to balance this shift. This way, a value for $E(B)$ is determined for every fluorescence material. The values of the deposited energy for the fluorescence of Cu, Pb, Sn, Gd and the γ-spectrum of ^{241}Am are taken from [35]. The value of the deposited energy for the Ba fluorescence was simulated by [45]. Tab. 4.1 lists these utilized fluorescence materials and the corresponding deposition energies for both pixel sizes.

Radioactive material	Fluorescence material	E_{big} (keV)	E_{small} (keV)
	Cu	8.00	7.33
	Pb	11.13	10.12
	Sn	25.12	24.45
	Ba	31.98	31.49
	Gd	42.37	41.72
^{241}Am		59.18	58.41

Table 4.1: Fluorescence materials and their simulated energy deposition in small and big pixels. Cu, Pb, Sn, Gd and Am according to [35] and Ba according to [45].

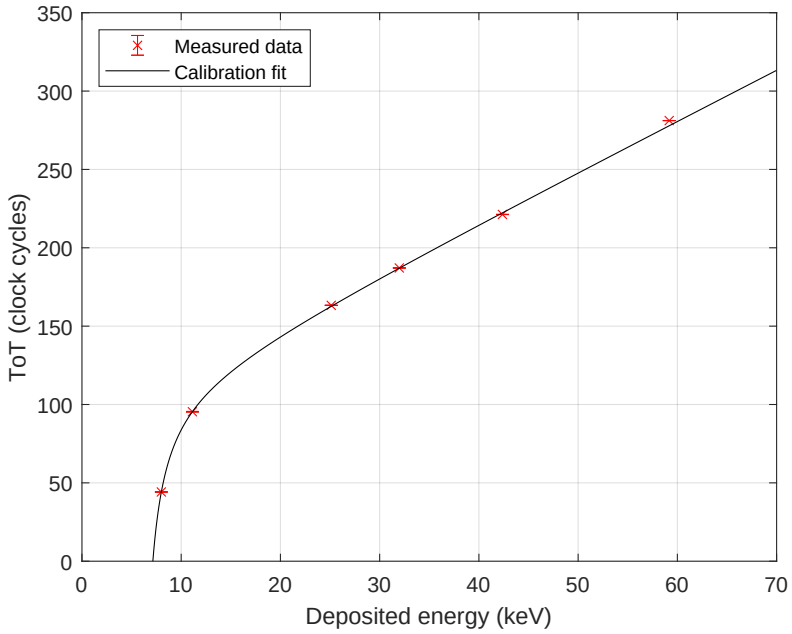

Figure 4.4 Fitted calibration curve of an individual big pixel (black) to fluorescence data (red).

Fig. 4.4 shows the measured ToT data (red) for the fluorescence materials as a function of the deposited energy for a single big pixel. The error bars denote the standard uncertainty of the mean position B of the Gaussian function that is fitted to the ToT spectrum. A fit with a function of the form [46]

$$f(x) = a + b \cdot x + \frac{c}{x - t} \tag{4.4}$$

is applied to the data. This function is further referred to as *traditional model*. This calibration is performed for all individual pixels of all three Dosepix detectors.

Additional energies $E(B)$ are required to perform a finer energy calibration. Therefore, the fluorescences of further target materials are measured with the Dosepix detectors. The simulated energy deposition spectra introduced in sec. 3.7 are used to compose fluorescence spectra as these target materials emit them.

For this purpose, the four most prominent fluorescence lines ($K_{\alpha 1}$, $K_{\alpha 2}$, $K_{\beta 1}$, $K_{\beta 3}$) of the additional materials are taken into account. The values for the emitted photon energies and their relative abundance are taken from [37]. The filter caps are taken off during the calibration measurements. Therefore, only the simulated energy deposition spectra for the first Dosepix detector are used. Since the simulated energy deposition spectra are only available for the big pixels, the small pixels are not considered in the following. The simulated energy deposition spectra are only available in steps of 1 keV for the initial photon energy. Therefore, the peaks that originate from total energy depositions in a composed response spectrum are separated in steps of at least 1 keV. However, the energy difference between the $K_{\alpha 1}$ and the $K_{\alpha 2}$ fluorescence emission lines, which lies between 0.1 keV and 0.7 keV for the utilized target materials, is essential to determine the deposited energy that corresponds to the measured ToT. Therefore, the energy deposition spectra are shifted in steps of 0.1 keV so that the energies of the total absorption peaks are equal to the energies of the fluorescence emission lines. The energy deposition spectra that are shifted are chosen so that the difference between the total absorption peak and the fluorescence emission line is minimal. Here, the assumption is made that the form of the spectra does not change within the small energy range that they are shifted. Since the detection efficiency of the Dosepix detectors is energy-dependent, each fluorescence emission energy is multiplied with the efficiency of the shifted response spectrum. Fig. 4.5 shows the detector response spectrum to an iodine fluorescence without added detector resolution. The spectra are broadened in order to take the detector resolution into account. This procedure aims to determine the deposited energy of fluorescence lines from certain target materials.

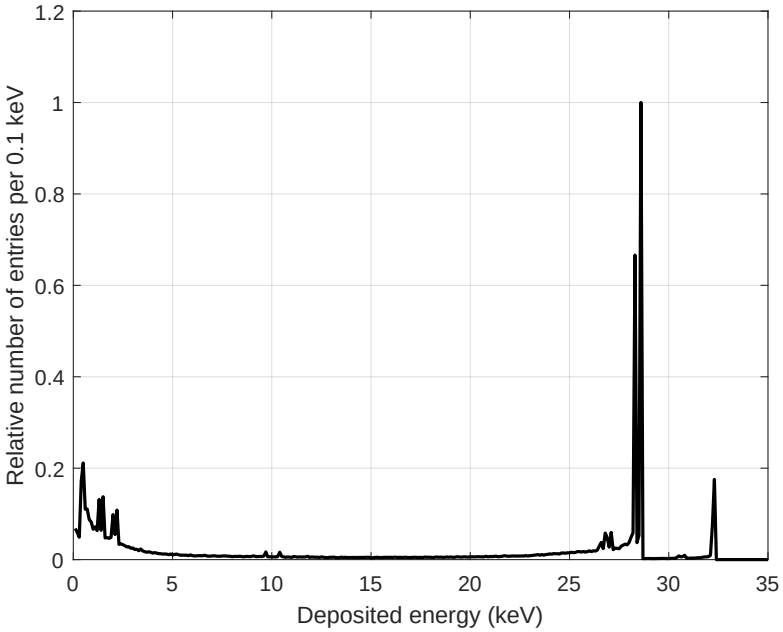

Figure 4.5 Simulated iodine fluorescence spectrum. The spectrum is composed of four monoenergetic response spectra that represent the four most prominent fluorescence lines of iodine.

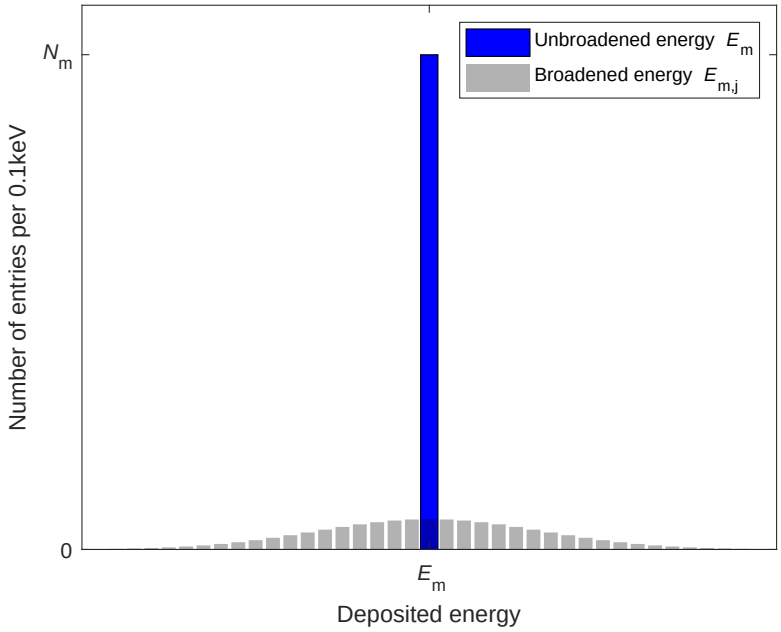

Figure 4.6 Broadening of one energy bin E_m (blue) from the unbroadened fluorescence spectrum. The number of entries N_m in E_m is spread along a Gaussian distribution to the energy bins $E_{m,j}$ (gray).

Fig. 4.6 shows the broadening procedure for an energy bin E_m in the unbroadened spectrum. The number of entries N_m in the energy bin E_m (blue in fig. 4.6) are distributed over the energy bins $E_{m,j}$ along a Gaussian distribution with a mean of E_m and a standard deviation of $\sigma(E_m)$ (gray in fig. 4.6). This is performed for all energy bins E_m in the unbroadened spectrum. After broadening an energy bin E_m, the number of entries in the energy bin $E_{m,j}$ is denoted with $N_{m,j}$. To gain the broadened spectrum, the sum over all entries $N_{m,j}$ in the energy bins $E_{m,j}$ is calculated via

$$N_j^{'} = \sum_m N_{m,j}. \tag{4.5}$$

A low level of noise is added to the broadened spectrum. A Gaussian distribution

$$G'(x, A', B', C') = A' \cdot e^{-(\frac{x-B'}{C'})^2} \tag{4.6}$$

equal to the one that is used in the calibration measurements is fitted to the fluorescence lines of the broadened spectrum. In the following, C' denotes the standard deviation of the Gaussian function that is fitted to the simulated broadened fluorescence spectra and C denotes the standard deviation of the Gaussian function that is fitted to the measured fluorescence spectra. Since C' is fitted to an energy spectrum and C to a ToT spectrum, one parameter needs to be converted using the energy calibration function outlined in equ. 4.4 to make C and C' comparable. Using this calibration a condition is formulated on $\sigma(E_m)$, where $f^{-1}(x)$ denotes the inverse function of $f(x)$. The broadening process is repeated where $\sigma(E_m)$ is varied until

$$\left| \frac{f^{-1}(C)}{C'} - 1 \right| < 0.001. \tag{4.7}$$

The corresponding center of the Gaussian fit B' is considered to be the simulated deposited energy E_{dep}. This procedure is repeated for all 192 big pixels of all three detectors.

Fig. 4.7a shows the result for a broadened response spectrum for the iodine fluorescence for a single pixel (black) compared to a measurement (red). The measurement is converted from ToT to energy using the energy calibration outlined in equ. 4.4. The peak at about 48 keV originates from scattered radiation from the primary beam of the X-ray tube. Most simulations of the broadened spectra are in good accordance with the corresponding measurements. However, some simulated spectra deviate from the measurements due to variances between the fitted energy calibration model and the actual data points. Fig. 4.7b shows the result for a broadened response spectrum for a tin fluorescence for a single pixel (black) compared to a measurement (red). This deviation between the simulated and measured spectra is further discussed in sec. 4.2.3. Generally, the deposited energy E_{dep} deviates from the initial energy.

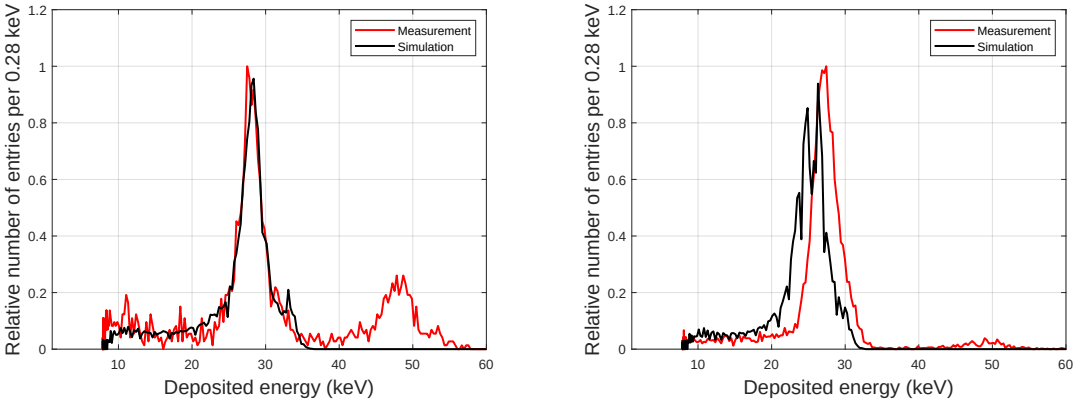

(a) Iodine fluorescence **(b)** Tin fluorescence

Figure 4.7 Simulated (black) and measured (red) detector response for (a): an iodine fluorescence lines and (b): for an tin fluorescence lines.

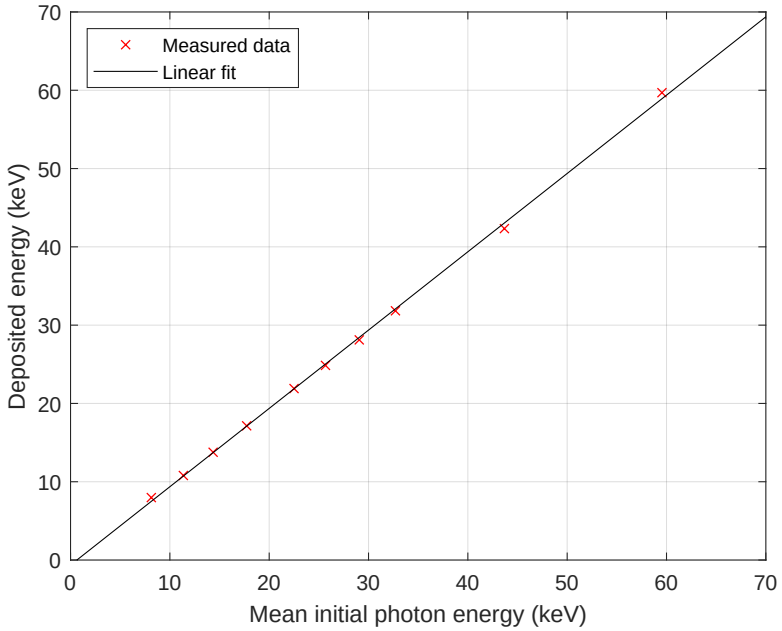

Figure 4.8 Simulated deposited energy as a function of the mean initial photon energy. The black curve denotes a linear fit.

Fig. 4.8 shows E_{dep} for one detector for all examined fluorescence materials (red) as a function of the weighted mean photon energies E_{in} of the four most prominent fluorescence lines n. E_{in} is calculated via

$$E_{\mathrm{in}} = \frac{\sum_{\mathrm{n}=1}^{4} E_{\mathrm{n}} \cdot w_{\mathrm{n}}}{\sum_{\mathrm{n}=1}^{4} w_{\mathrm{n}}}, \tag{4.8}$$

where E_{n} denotes the energy of the fluorescence line and w_{n} the relative emission abundance [37]. A linear fit (black) is applied, where the slope is very close to one for most pixels. However, an offset occurs for all pixels. Linear fits to the mean ToT data of all pixels of each detector respectively yield the functions

$$E_{\mathrm{dep}}(\mathrm{Free}) = 1.001 \cdot E_{\mathrm{in}}(\mathrm{Free}) - 0.669\,\mathrm{keV} \tag{4.9}$$

$$E_{\mathrm{dep}}(\mathrm{Al}) = 1.000 \cdot E_{\mathrm{in}}(\mathrm{Al}) - 0.639\,\mathrm{keV} \tag{4.10}$$

$$E_{\mathrm{dep}}(\mathrm{Sn}) = 1.000 \cdot E_{\mathrm{in}}(\mathrm{Sn}) - 0.584\,\mathrm{keV}. \tag{4.11}$$

The offset is not negligible, especially for low energies. Therefore, E_{dep} is used for further calibration. The data depicted in fig. 4.8 is listed in tab. A.1 with the corresponding fluorescence element.
Different settings of measurement parameters alter the measured ToT (see sec. 3.4). Therefore, an energy calibration needs to be performed for every combination of $\mathrm{THL_{sub}}$ and I_{Krum} measurements are conducted with. Six different energy calibrations for three different $\mathrm{THL_{sub}}$ (20, 30, 40) and two different I_{Krum} (2.2 nA, 11 nA) are performed. Here, small pixels are only considered for the adjustment $\mathrm{THL_{sub}} = 20$ and $I_{\mathrm{Krum}} = 2.2\,\mathrm{nA}$. Fig. 4.9 shows the calibration curves of one big pixel for all six adjustments. As expected, the calibration curves are shifted towards lower ToT values for higher $\mathrm{THL_{sub}}$. A higher I_{Krum} results in a smaller slope in the linear part of the traditional calibration model, and the zero point tends to shift towards higher energies.

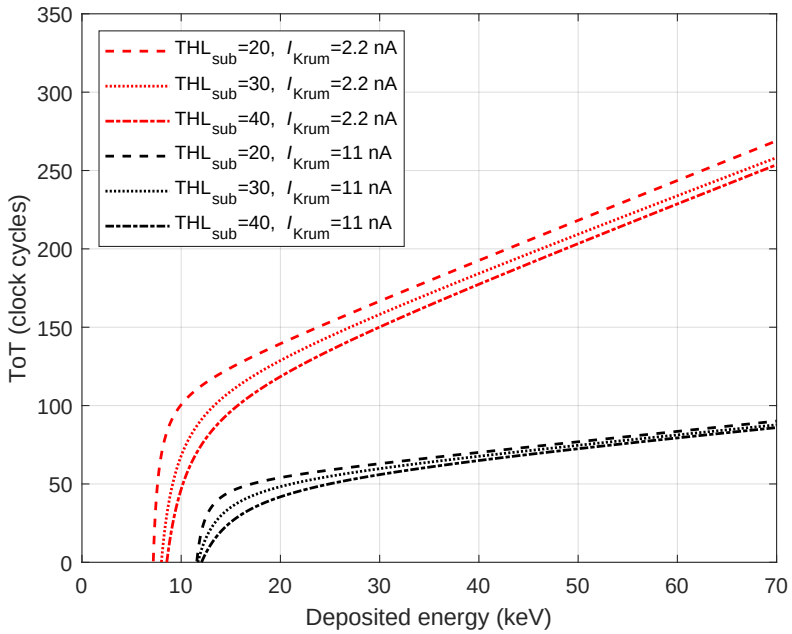

Figure 4.9 Different energy calibration curves for a single big pixel according to the traditional model defined in equ. 4.4. The red curves are calculated with an I_{Krum} of 2.2 nA, the black ones with an I_{Krum} of 11 nA. For each I_{Krum} calibrations with three different $\mathrm{THL_{sub}}$ are performed.

4.2.3 Calibration model evaluation

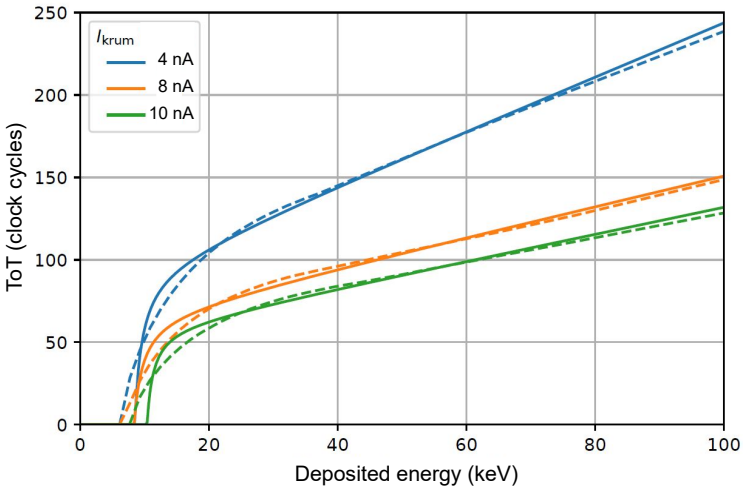

Figure 4.10 Average calibration curves of all big pixels of one Dosepix detector. The solid lines denote calibrations using the traditional calibration function (see equ. 4.4) and the dashed lines denote the optimized energy calibrations. The image is taken and modified from [39].

A fairly precise energy calibration curve is acquired using the fluorescence data from sec. 4.2.2. However, for most pixels, the fluorescence data seems to deviate from the fitted calibration curve. This is not a statistical effect. In [39] it was shown that this deviation from the calibration curve originates from the pixel electronics. Fig. 4.10 shows the mean calibration curves of all big pixels of one Dosepix detector for different settings of I_{Krum}. The solid lines denote the calibration curves for the traditional model as calculated in equ. 4.4, and the dashed lines the corresponding optimized energy calibration. Such a deviation from the traditional fit function is observed in direct measurements with the fluorescence data outlined in sec. 4.2.2. Fig. 4.11 shows an example of the calibration for a single pixel. The fluorescence data is depicted in red, and the curve that is fitted according to equ. 4.4 is depicted in black. In order to determine whether a deviation from the traditional model affects the dose calculation, a calibration curve based on interpolation between the measured fluorescence data is defined (blue). The interpolation is performed using cubic splines [22, 23] from the first to the second to last data point. From the second to last data point to the last data point, linear interpolation is applied. The behavior of the Dosepix detector is assumed to be steady. An additional linear interpolation between the last data point and a point (green) on the traditional curve is applied to inhibit discontinuity in the calibration curve. Fig. 4.12 shows how this point of intersection is determined. The line h (gray) denotes the perpendicular to the traditional calibration curve through the last data point. α denotes the angle between the line from the second to last to the last data point and h. The point of intersection is chosen so that α' is equal to α.

To compare the traditional to the interpolated calibration curve to each other, the ratio

$$F = \frac{\mathrm{ToT}_{\mathrm{inter}}(E)}{\mathrm{ToT}_{\mathrm{trad}}(E)} \tag{4.12}$$

is defined. $\mathrm{ToT}_{\mathrm{inter}}(E)$ denotes the ToT values calculated via the interpolation curve and $\mathrm{ToT}_{\mathrm{trad}}(E)$ the ToT values calculated via the traditional model.

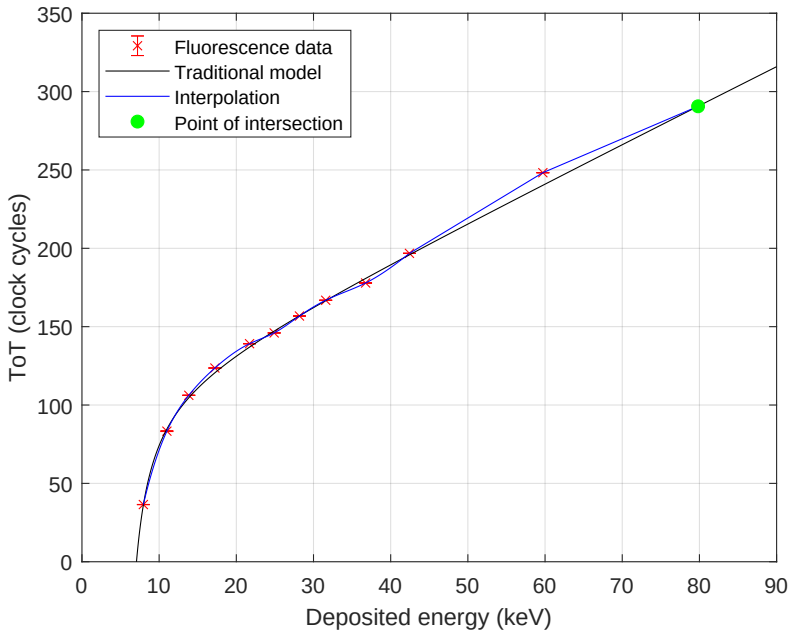

Figure 4.11 Energy calibration for a single pixel using fluorescence data (red) with an applied fit function according to equ. 4.4 (black) and an interpolated function (blue).

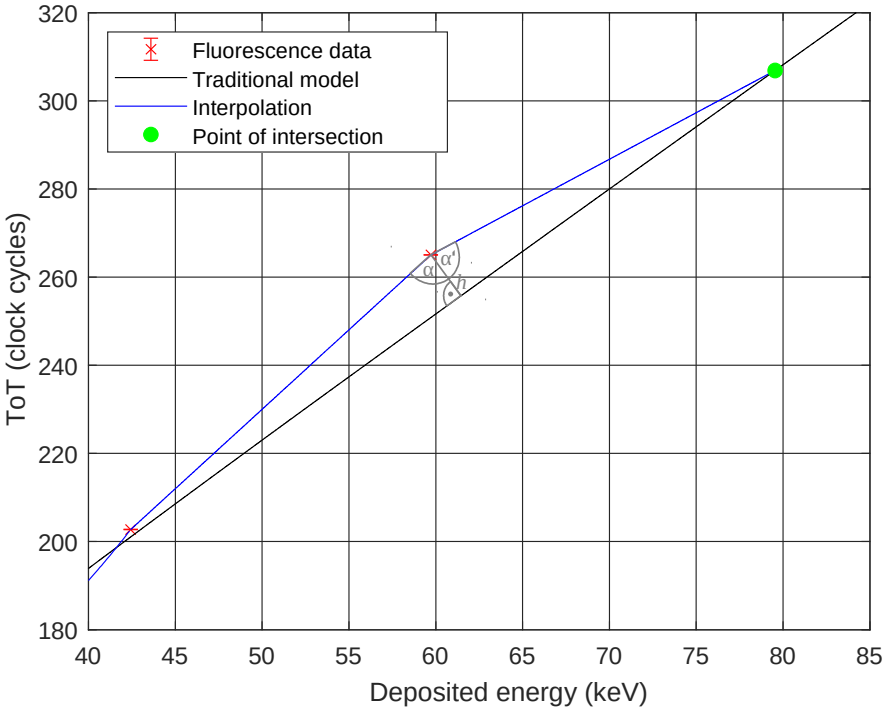

Figure 4.12 Determination of the point of intersection (green) between the traditional model (black) and the interpolation model (blue). The red data points denote the measured fluorescence data.

Fig. 4.13a shows F as a function of the deposited energy E_{dep} for the data shown in fig. 4.11. It can be seen that for this pixel, the deviation reaches over 5 % at an energy of about 60 keV. This pixel is not an individual case. The interpolated calibration curves of all pixels of all three detectors show a very similar deviation from the traditional calibration curve. Fig. 4.13b shows the ratio F averaged over all pixels for each of the three detectors, respectively. The mean deviation of F from 1 reaches over 4 % and might have an effect on the dose reconstruction in the energy region below the point of intersection. This is further investigated in sec. 7.1.
The data acquisition necessary to determine an energy calibration via interpolation is significantly more extensive than with the traditional model. Therefore, the influence on the dose reconstruction is investigated only for one setting of THL_{sub} (20) and I_{Krum} (2.2 nA).

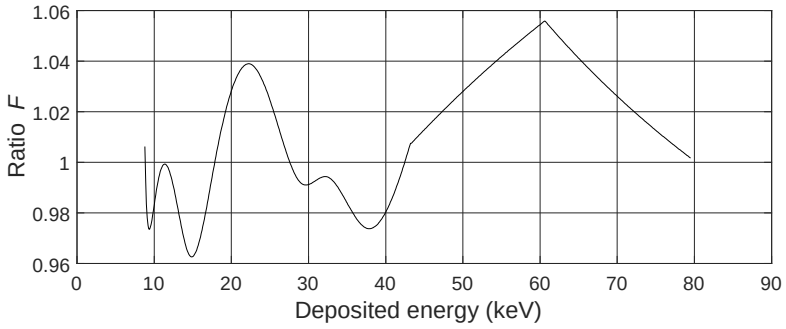

(a) F for a single pixel

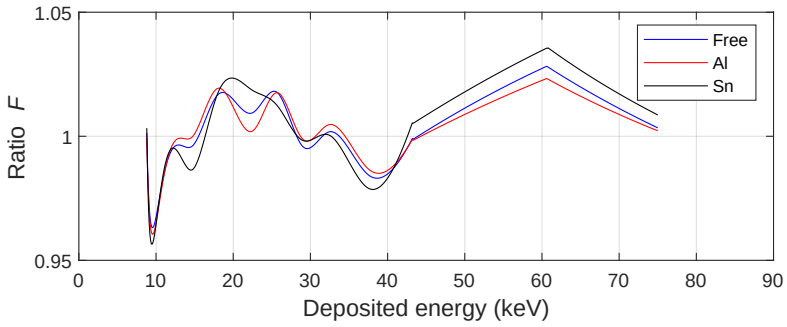

(b) Mean F for each detector

Figure 4.13 Ratio F between the interpolated and the traditional calibration curve as a function of the deposited energy. (a): F for the data of a single pixel shown in 4.11 and (b): average ratio F over all big pixels for each detector respectively.

4.3 Energy resolution

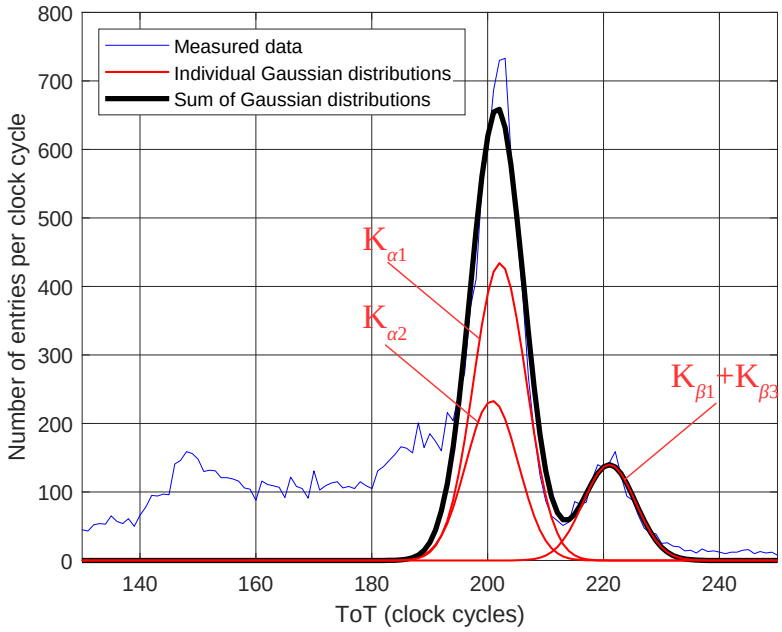

Figure 4.14 Example of a multi-Gaussian fit (black) according to equ. 4.13 to gadolinium fluorescence data (blue). The individual terms of the multi-Gaussian function are depicted in red and labeled with the fluorescence line they represent.

The data outlined in sec. 4.2.2 is used to determine the energy resolution of the detector. Here, the energy resolution $\frac{\sigma(E)}{E}$ is defined as the standard deviation of the total absorption peak of monoenergetic radiation with the energy E divided by the mean energy of the total absorption peak. Since the materials emit multiple fluorescence energy lines, the measured energy cannot be assumed to be monoenergetic. A single Gaussian distribution that is fitted to the data, as it is performed in sec. 4.2.2, can be used to calculate a good estimate on an upper limit of the energy resolution. This is performed in [47] for various fluorescence materials. However, a multi-Gaussian fit applied to the most prominent fluorescence lines yields a more accurate result. For this purpose, a function of the form

$$G^{\text{mult}}(x, A1, A2, B1, B2, C) = \underbrace{A1 \cdot \mathrm{e}^{(\frac{-(x-B1)}{C})^2}}_{\mathrm{K}_{\alpha1}} + \underbrace{A1 \cdot \Delta h \cdot \mathrm{e}^{(\frac{-(x-\Delta E \cdot B1)}{C})^2}}_{\mathrm{K}_{\alpha2}} + \underbrace{A2 \cdot \mathrm{e}^{(\frac{-(x-B2)}{C})^2}}_{\mathrm{K}_{\beta1}\,+\,\mathrm{K}_{\beta3}} \tag{4.13}$$

is applied to fit the sum of three Gaussian distributions to the data. The curly brackets indicate the fluorescence line each term corresponds to. $A1, A2, B1, B2, C$ denote the fit parameters. Δh denotes the ratio between the relative abundance and ΔE the ratio between the energies of the $\mathrm{K}_{\alpha2}$ and the $\mathrm{K}_{\alpha1}$ fluorescence lines. To calculate ΔE the energies of the fluorescence lines are converted to ToT using the energy calibration outlined in sec. 4.2.2. The data to determine Δh and ΔE is taken from [37]. $A1, B1$ and C denote the height, the mean and the standard deviation of the measured $\mathrm{K}_{\alpha1}$ fluorescence line. The height and the mean of the measured $\mathrm{K}_{\alpha2}$ fluorescence line is set to be dependent on $A1$ and $B1$. The $\mathrm{K}_{\beta1}$ and the $\mathrm{K}_{\beta3}$ fluorescence lines contribute significantly to the measured spectrum. Yet, for most of the used fluorescence materials, their energy differences are too small ($< 0.1\,\mathrm{keV}$) to be resolved individually. Therefore, the Gaussian distribution in equ. 4.13 with parameters $A2, B2$ and C fits both fluorescence lines together.

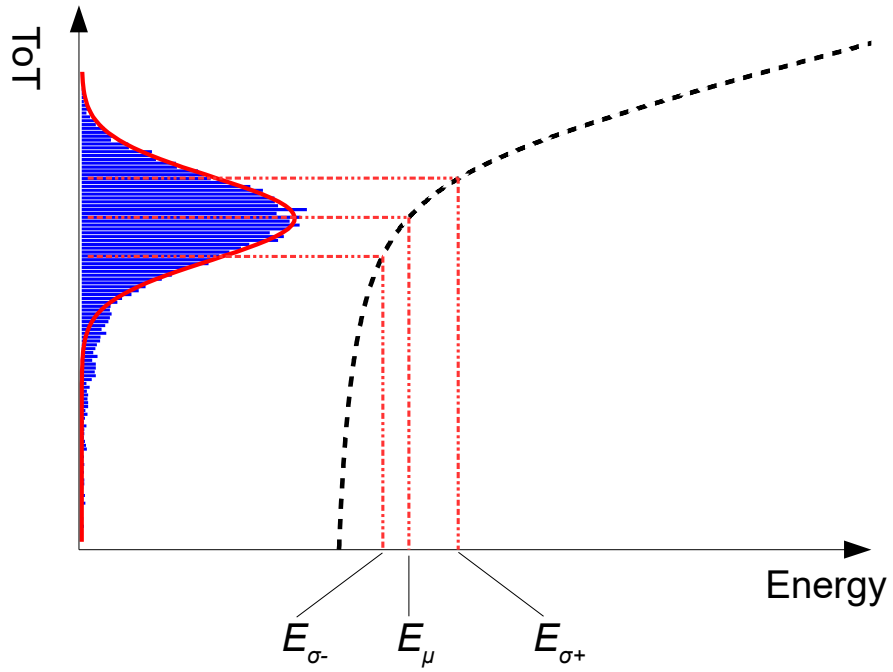

Figure 4.15 Explanation of how the width of a Gaussian distribution (red) changes when the distribution is converted from ToT to energy. The distribution is fitted to a copper fluorescence (blue).

Fig. 4.14 shows a measurement with gadolinium as fluorescence material. The terms of equ. 4.13 and their corresponding fluorescence lines are shown individually (red) and summed (blue). To determine the energy resolution, the parameters $B1$ and C are converted from ToT to energy. For $B1$, this is performed using the inverse $f^{-1}(x)$ of the energy calibration function shown in equ. 4.4

$$E(B1) = f^{-1}(B1). \tag{4.14}$$

Since equ. 4.4 is not linear, $E(C)$ cannot be calculated the same way. A symmetric function, like a Gaussian function, that is converted from ToT to energy results in a non-symmetric function. Fig. 4.15 shows how the width of a Gaussian function (red) that is fitted to a ToT spectrum (blue) changes when converted from ToT to energy. The half-width $E_{\sigma-}$ towards lower energies is smaller than the half-width $E_{\sigma+}$ towards higher energies. An energy resolution Z is calculated for both half-widths, providing an upper and a lower limit on the energy resolution. The lower limit is calculated via

$$Z^{\mathrm{Low}} = \frac{E_{\mu} - E_{\sigma-}}{E_{\mu}} \tag{4.15}$$

and the upper limit via

$$Z^{\mathrm{Up}} = \frac{E_{\sigma+} - E_{\mu}}{E_{\mu}} \tag{4.16}$$

Here, $E_{\mu} = E(B1)$. $E_{\sigma-}$ is calculated via

$$E_{\sigma-} = f^{-1}(C - B1) \tag{4.17}$$

and $E_{\sigma+}$ via

$$E_{\sigma+} = f^{-1}(B1 + C). \tag{4.18}$$

Fig. 4.16a, 4.16b, and 4.16c show the energy resolution for the three Dosepix detectors as a function of the energy of the $K_{\alpha 1}$ fluorescence lines. The data points denote the mean energy resolutions of all big pixels per Dosepix detector, and the error bars denote the corresponding standard uncertainties of the means. The solid black line indicates the energy resolution as calculated in equ. 4.16 and the black dashed line indicates the energy resolution as calculated in equ. 4.15. For low energies, it makes a major difference, which half-width is used to calculate the energy resolution. As outlined in fig. 4.15, the difference results from the non-linear part of the energy calibration function. With increasing energy, the linear part of the calibration function becomes dominant, and the two different half-widths reach the same value at about 20 keV. Therefore, the difference between the limits of the energy response decreases with increasing energy. In general, the energy resolution of all three detectors shows the same descending behavior, although there are clear differences between the absolute energy resolution. The low value for the resolution of the copper fluorescence at about 9 keV occurs because the photopeak is partially cut off on one side by the threshold. This leads to lower values of E_{σ^+} and E_{σ^-} and, therefore, a lower energy resolution.

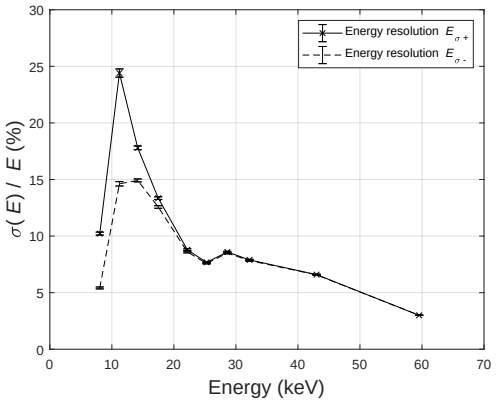

(a) First detector (Free)

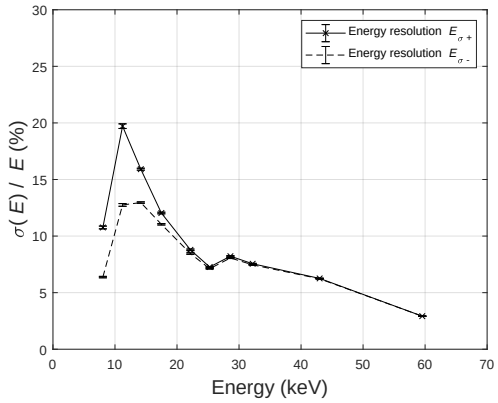

(b) Second detector (Al)

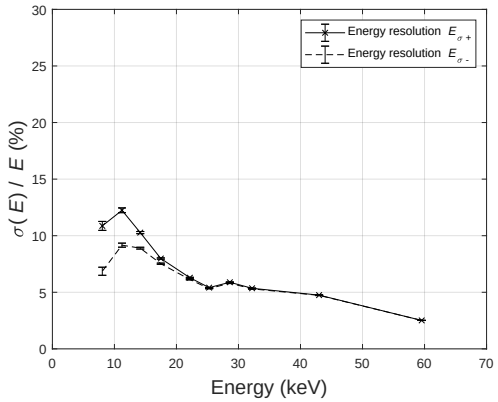

(c) Third detector (Sn)

Figure 4.16 Energy resolution for three different Dosepix detectors. The solid black line denotes the resolution as calculated in equ. 4.16, the dashed black line the resolution as calculated in equ. 4.15.

4.4 Conclusion

The main objective in this chapter was to prepare the Dosepix dosemeter to perform spectroscopic measurements, which form the basis of the determination of dose quantities in X-ray radiation fields. For this purpose, a threshold equalization for different settings of measurements parameters was performed. An energy calibration with fluorescence emissions that were already simulated [35, 45] using the traditional model was performed for different measurement parameters. Additional measurements with further fluorescence materials were used to determine the deposited energy of the corresponding fluorescence emission lines. Here, the simulated energy deposition spectra outlined in sec. 3.7 were used. The additional fluorescence data was used to establish an energy calibration model based on an interpolation method. This model is evaluated and compared to the traditional model in sec. 7.1 concerning energy-dependent dose measurements. The measured data was further used to determine an upper and a lower limit on the energy resolution.

Chapter 5

Simulation of the detector response in total pile-up case

Contents

Various measurements outlined in this thesis are conducted in photon fields that cause total pile-up. Therefore, the maximum effect that total pile-up (see sec. 3.5) can have on measurements in integration-mode is estimated in this chapter. Further, energy resolution is added to the simulated monoenergetic deposition spectra outlined in sec. 3.7. The individual steps performed to simulate the detector response for initial photon fields that cause total pile-up are explained. Properties of the simulated data are discussed.

5.1 Comparison of ToT generation in total pile-up and non-pile-up case

Pile-up alters the measured ToT output of the Dosepix detector since multiple signals are processed as a single one (see sec. 3.5). This leads to a modification of the measured ToT spectrum and, therefore, the measured energy deposition spectrum. An energy deposition spectrum can only be acquired in ToT-mode or Dosi-mode. When the Dosepix detector is operated in integration-mode, all measured ToT values are summed up regardless of pile-up. However, pile-up alters the detector output in integration-mode as well. The maximum effect total pile-up can have on measurements in integration-mode is estimated in the following.

Assuming a photon field that generates N signals in the detector, each with a deposited energy of E, the detector output $\mathrm{ToT}^{\mathrm{NP}}$ in non-pile-up case is calculated via

$$\mathrm{ToT}^{\mathrm{NP}} = \sum_{i=1}^{N}(a + bE + \frac{c}{t-E}) = N \cdot (a + bE + \frac{c}{t-E}). \tag{5.1}$$

Here, the traditional model (see equ. 4.4) is used to convert the deposited energy to ToT. The detector output $\mathrm{ToT}^{\mathrm{TP}}$ in total pile-up case is calculated via

$$\mathrm{ToT}^{\mathrm{TP}} = a + b \cdot (\sum_{i=1}^{N} E) + \frac{c}{t - (\sum_{i=1}^{N} E)} = a + NbE + \frac{c}{t - NE}. \tag{5.2}$$

Further, the assumption is made that the maximum effect pile-up can have occurs in the case of total pile-up. Then the maximum difference between $\mathrm{ToT}^{\mathrm{NP}}$ and $\mathrm{ToT}^{\mathrm{TP}}$ is determined in the limit $N \to \infty$

$$\lim_{N\to\infty} \frac{\mathrm{ToT}^{\mathrm{NP}}}{\mathrm{ToT}^{\mathrm{TP}}} = \lim_{N\to\infty} \frac{N(a + bE + \frac{c}{t-E})}{a + bNE + \frac{c}{t-NE}} = \frac{a + bE + \frac{c}{t-E}}{bE}. \tag{5.3}$$

The expression converges towards a constant non-zero value. Fig. 5.1 shows the ratio $\frac{\mathrm{ToT}^{\mathrm{NP}}}{\mathrm{ToT}^{\mathrm{TP}}}$ as a function of the number of detected signals up to $N = 100$. The color code denotes different deposited energies from 15 keV to 150 keV. Here, the mean parameters a, b, c, t of all big pixels of the three detectors are used. Convergence is reached at higher N for lower energies. For a mean deposited energy of 50 keV, the difference converges at about 2.34. However, a mean deposited energy of 50 keV can hardly be reached.

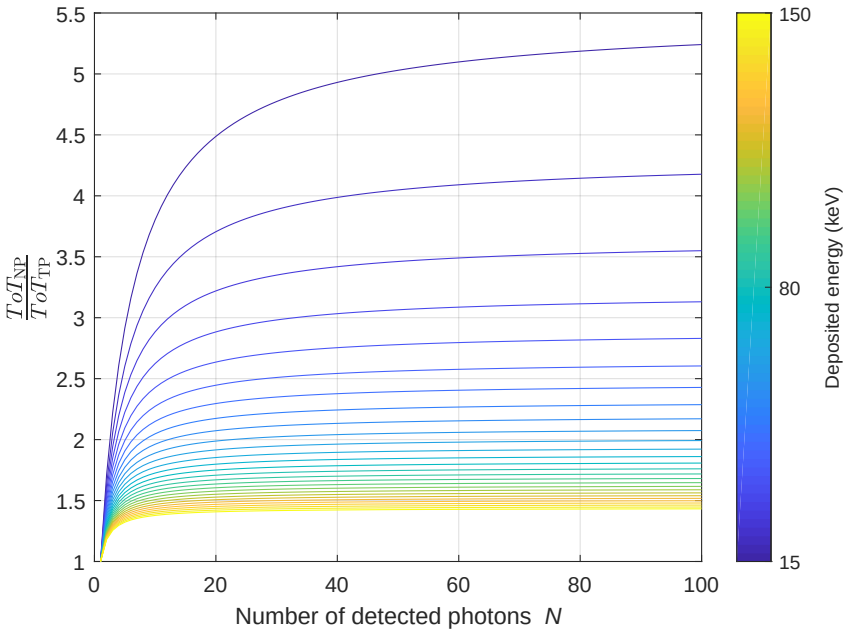

Figure 5.1 Difference between the ToT outputs in integration-mode in non-pile-up case and total pile-up case as a function of the number of detected photons for various energies.

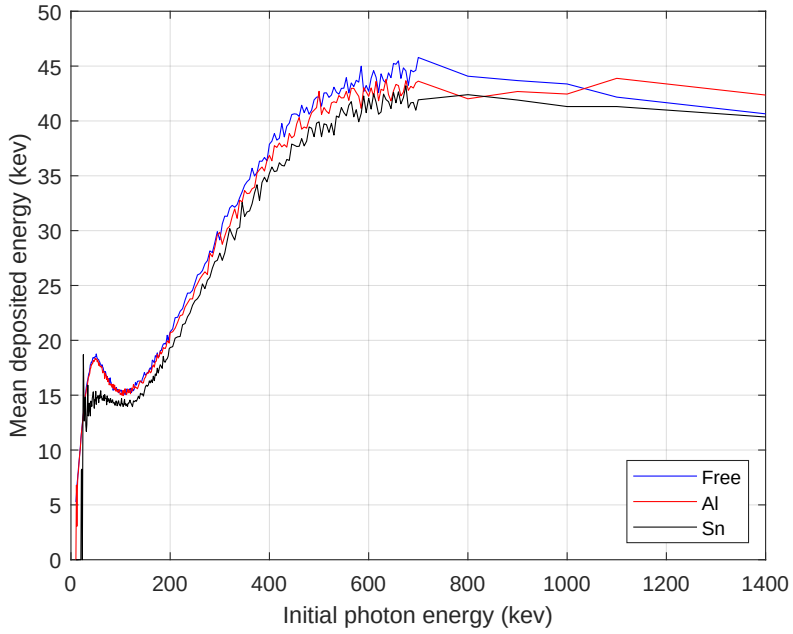

Figure 5.2 Mean deposited energies as a function of the initial photon energy for all three detectors. Here, the energy deposition spectra [39] without additional energy resolution are used.

Fig. 5.2 shows the mean deposited energies $\bar{E}_{\mathrm{dep}}$ as a function of the initial photon energy E_{ini}. Here, the simulated energy deposition spectra without energy resolution are used. $\bar{E}_{\mathrm{dep}}$ rises with E_{ini} until Compton scattering becomes dominant over photoelectric absorption. When the photopeak is not measurable anymore, only the Compton spectrum and charge sharing contribute to the deposited energy, and $\bar{E}_{\mathrm{dep}}$ rises again. The difference between the ToT response in photon fields that cause total pile-up and such that cause no pile-up is too significant to be neglected for dosimetric measurements. Therefore, a simulation that takes total pile-up into account is required.

5.2 Broadening of the energy deposition spectra

In sec. 4.2.2, measured data was used to add energy resolution to fluorescence spectra composed of simulated monoenergetic energy deposition spectra (see sec. 3.7). A broadening coefficient C', which is the standard deviation of a Gaussian distribution that is fitted to the data (see equ. 4.6), and the corresponding mean deposited energy B' was determined. The measured energy deposition E depends linearly on the number N of charge carriers that are liberated in a pixel. The variation of N and, therefore, the variation of E is governed by Poisson statistics. Therefore, the width of a peak in a measured energy spectrum is expected to increase proportionally to $\sqrt{E}$ with increasing energy. Fig. 5.3a shows the broadening coefficient C' for all big pixels of one detector as a function of the mean energy of the corresponding fluorescence spectra as calculated in equ. 4.8 (black dots). Other than expected, the data does not increase but saturate or even decrease. The data point at 60 keV arises from the γ-signature of an ^{241}Am source. In contrast to the fluorescence data, this radiation source is monoenergetic. A smaller broadening coefficient than for fluorescence data is therefore expected. The saturating trend of the data can be explained with an electronic noise in the detector.

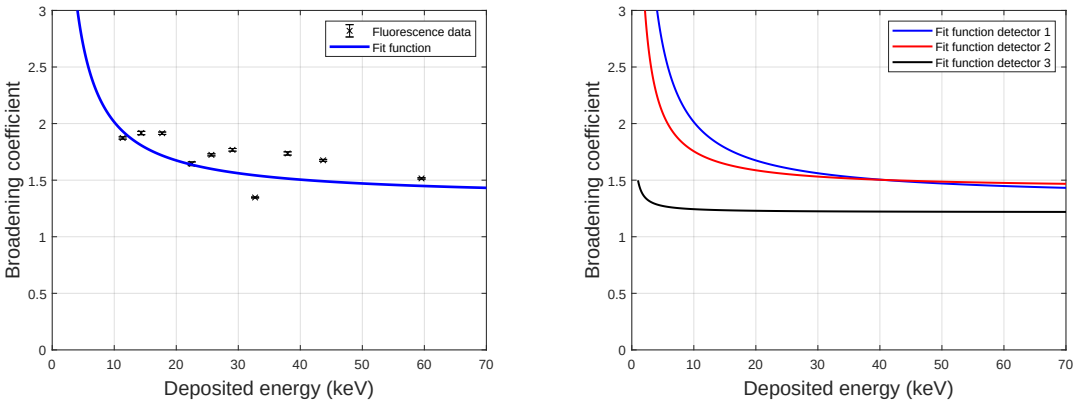

(a) Broadening coefficient for first detector **(b)** Broadening coefficient for all detectors

Figure 5.3 Broadening coefficient as a function of the deposited energy. (a): Broadening coefficient for a single Dosepix detector. The black data points denote the fluorescence data and the blue curve the corresponding fit. (b): Fit for the broadening coefficient for the three Dosepix detectors.

The variation σ_{el}^2 that arises from this noise contributes, among other effects, to the variation from the number of detected charge carriers. The observed variation σ_{obs}^2, which corresponds to the measured width of the peak in an energy spectrum, can be expressed as [48]

$$\sigma_{\text{obs}}^2 = \sigma_{\text{det}}^2 + \sigma_{\text{el}}^2 \tag{5.4}$$

where σ_{det}^2 denotes the variation from the number of created charge carriers with $\sigma_{\text{det}}^2 = N \cdot F$, with N the number of created charges and F the Fano factor in silicon. A value of $F = 0.13$ is assumed [48]. For an energy deposition of 10 keV, the number of created charges can be calculated via

$$N = \frac{10\,\text{keV}}{3.62\,\text{eV}} \approx 2762 \tag{5.5}$$

with a required energy of 3.62 eV [42] for every created electron-hole pair. This results in a variation of $\sigma_{\text{det}}^2 = 359$ charge carriers. In [32], the equivalent noise charge (ENC) was simulated for the Dosepix detector. At an I_{Krum} of about 2.2 nA, which was used in the measurements for the broadening coefficient, an ENC of about 150 charge carriers (derived from a figure in [32]) was determined. This results in $\sigma_{\text{el}}^2 = 22500$, which dominates the observed variation. The electronic noise affects the analogue charge signal that exceeds the threshold and therefore changes the measured ToT, which is converted to energy using the energy calibration. How the measured ToT, and therefore the measured energy, depends on this noise could not be quantified. In sec. 4.2.3 a deviation of the behavior of the pixel electronics from the calibration model has already been discussed. This deviation might also contribute to the course of the broadening coefficient with the deposited energy. However, a model that makes predictions from the measurements is required to add energy resolution to the simulated monoenergetic energy deposition spectra. For low energies, the broadening coefficient cannot be determined because measurements are limited by the analogue threshold. Therefore, a simple converging model is chosen heuristically where the function follows the course of the data towards higher values of C' with decreasing energy. A fit function of the form

$$f(x) = \frac{a}{x} + b \tag{5.6}$$

is applied to the data, where a and b denote the fit parameters.

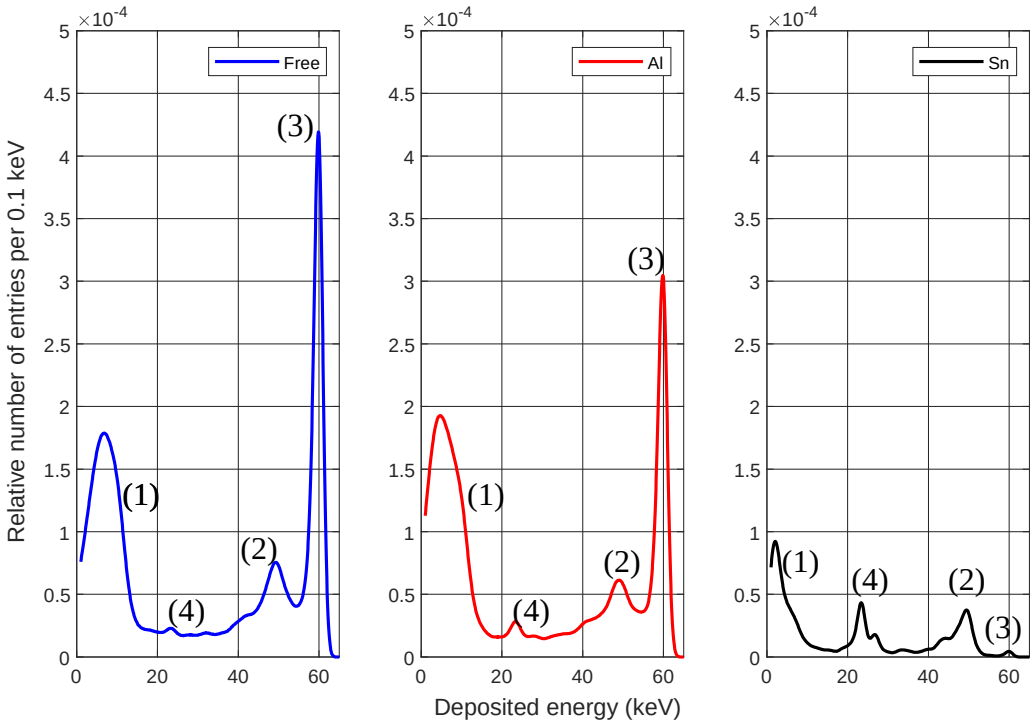

Figure 5.4 Energy deposition spectra for the uncovered detector (blue), the detector with aluminum cap (red) and the detector with tin cap (black). (1) and (2) denote the Compton edges, (3) denotes the total absorption peak and (4) denotes the total absorption from the tin fluorescence that originates from the tin filter on the third detector. The spectra are normalized to their integral and their PDE.

This is performed for all three detectors (see fig. 5.3b). Equ. 5.6 provides values for the broadening coefficients for all deposited energies. Each energy bin in an energy deposition spectrum is broadened individually and with respect to the broadening coefficient, as explained in sec. 4.2.2 (see fig. 4.6). The broadened energy deposition spectra are calculated by summing over all individually broadened energy bins as outlined in equ. 4.5. Fig. 5.4 shows the energy deposition spectra for an initial energy of 60 keV for all three detectors after the broadening was applied. The spectra are normalized to their integral and with their respective PDE. The main characteristics of the spectra are marked. (3) denotes the total absorption peak at 60 keV. While it is dominantly present in the spectra of the first and second detector, it is almost not visible in the spectrum of the tin-covered detector. Due to absorption, Compton scattering, and fluorescence excitation in the filter cap, deposited energies below 60 keV are more prominent. (1) and (2) denote the Compton edges. (4) denotes the total absorption peak of the tin fluorescence at about 25 keV. Since the tin filter cap is close to the third detector, this peak is prominent here. It is, however, also visible in the other spectra. Towards energies below 7 keV, the spectra decline. This results from the broadening procedure with the model introduced in equ. 5.6. Energies below 7 keV are usually not measurable since, for most pixels, signals that result from such low energies do not exceed the threshold. Therefore, only assumptions about the broadening coefficient at these low energies can be made. The main characteristics outlined in fig. 5.4 can be found in all energy deposition spectra.

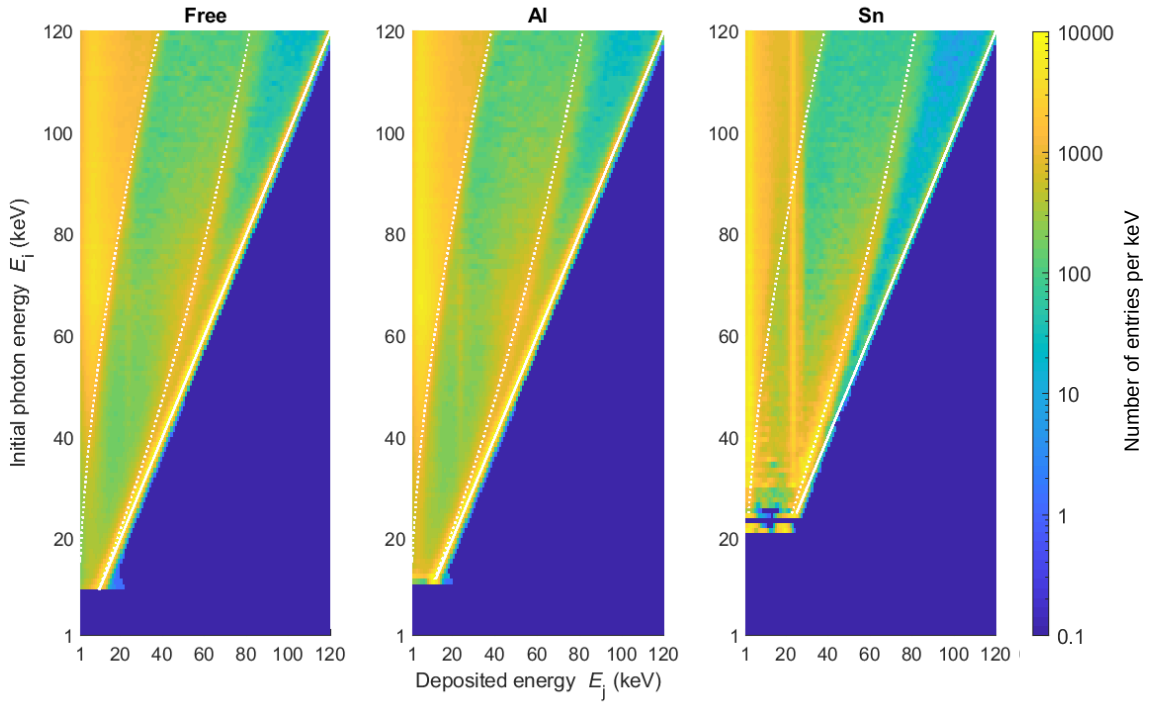

Figure 5.5 Energy deposition spectra for initial photon energies up to 120 keV. The color code denotes the number of entries in the energy deposition spectrum per keV. The solid white line indicates the total absorption peak. The dashed white lines indicate the Compton edges according to equ. 5.8 and equ. 5.9.

Fig. 5.5 shows a scatter matrix where all response spectra for initial energies E_i between 10 keV and 120 keV are plotted for all three detectors. The Y-axis denotes the initial photon energy, and the X-axis denotes the corresponding deposition E_j. The color code denotes the number of entries in the energy deposition spectrum per 1 keV. In addition, three lines that represent the characteristics of the spectra are shown. The straight line represents the full absorption peak in every deposition spectrum. Since the initial photon energy is fully absorbed, the line follows the equation

$$E_j = E_i. \tag{5.7}$$

The dotted lines represent the Compton edges in every spectrum. They follow the equations (see sec. 2.1.2)

$$E_j = \frac{E_i}{1 + \frac{m_e c^2}{2E_i}} \tag{5.8}$$

and

$$E_j = E_i - \frac{E_i}{1 + \frac{m_e c^2}{2E_i}}. \tag{5.9}$$

For each Dosepix detector, all energy deposition spectra are expressed as matrix $M_{i,j}$, where the energy distribution of the deposited energy E_j occurs for photons with initial energy E_i.

5.3 Simulation procedure

The simulation is required to find an analytical method to determine the applied dose from measurements in high dose rate photon fields, where only total pile-up occurs. This simulation needs to provide information about the applied dose and the detector response for the incident photon field. For the simulation, the software *Matlab* [49] is used. Fig. 5.6 shows a scheme where the main steps of the simulation are pointed out. The part encased in green denotes the calculation of the applied dose, and the part encased in blue denotes the determination of the detector response.

Applied dose

As explained in sec. 2.3.1, the dose per fluence $\frac{H_\mathrm{p}(d)}{\Phi}(E)$ can be determined depending on the photon energy E. For clarity, the values $\frac{H_\mathrm{p}(d)}{\Phi}(E)$ are substituted with $D_\Phi(E)$ in the following. Fig. 2.6 shows this dependence for a slab phantom for $H_\mathrm{p}(0.07)$ and $H_\mathrm{p}(10)$. The slab phantom has a front area of $\mathrm{A_{phan}} = 30\,\mathrm{cm} \times 30\,\mathrm{cm}$. For a certain number of photons N with the energy E, the applied dose $H_\mathrm{p}(d, E)$ can therefore be calculated via

$$H_\mathrm{p}(d, E) = D_\Phi(E) \cdot \frac{N}{\mathrm{A_{phan}}}. \tag{5.10}$$

The applied dose $H_\mathrm{p}(d)$ for a photon spectrum with photon energies E_i (fig. 5.6(a)) and associated number of photons N_i can therefore be calculated via

$$H_\mathrm{p}(d) = \sum_\mathrm{i} D_\Phi(E_\mathrm{i}) \cdot \frac{N_\mathrm{i}}{\mathrm{A_{phan}}}. \tag{5.11}$$

The relative amount of photons n_i for each occurring energy E_i is determined by scaling each N_i with the total number of photons N. By replacing N_i with n_i in equ. 5.11, the mean dose that a single photon from the photon spectrum applies is calculated via

$$H_\mathrm{p}^\gamma(d) = \sum_i D_\Phi(E_\mathrm{i}) \cdot \frac{n_\mathrm{i}}{\mathrm{A_{phan}}}. \tag{5.12}$$

$H_\mathrm{p}^\gamma(d)$ is characteristic for each X-ray spectrum and is used in the simulations to calculate the applied dose. To do so, $H_\mathrm{p}^\gamma(d)$ is multiplied with a certain number of photons N that impinge on the slab phantom.

$$H_\mathrm{p}(d) = H_\mathrm{p}^\gamma(d) \cdot N. \tag{5.13}$$

Here, N needs to be large enough so that statistical variations in the applied spectrum can be neglected. This is given since the smallest value for N chosen in the simulations is 10^7.

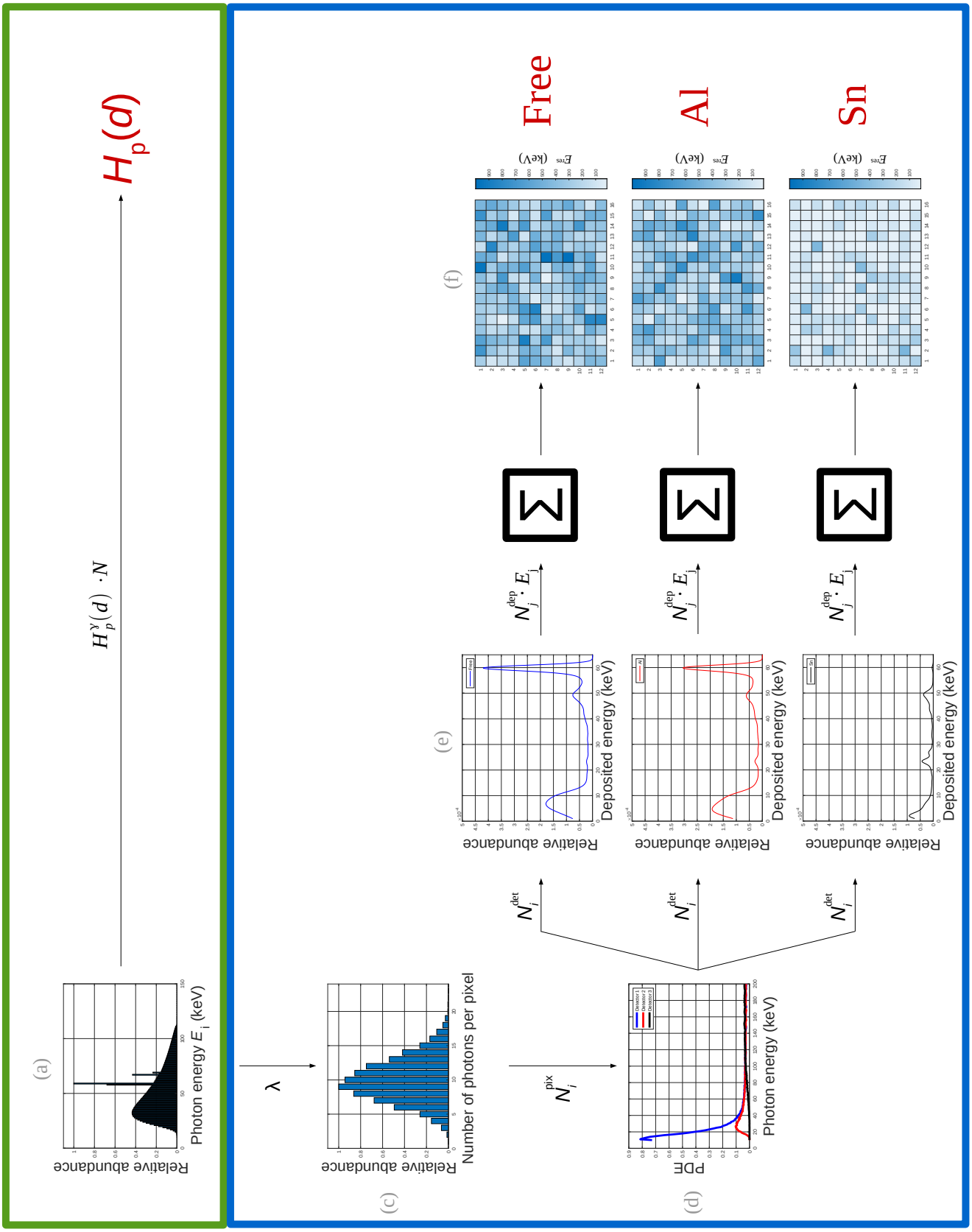

Figure 5.6 Schematic of the simulation procedure in the case of total pile-up. The calculation of the applied dose is encased in green. The determination of the detector response is encased in blue. Detailed information on the procedure is given in the text.

Detector response

To simulate the detector response for an incident spectrum, the mean number of photons λ that impinge onto a single big pixel with an active area of $A_{pix} = 220\,\mu m \times 220\,\mu m$ is calculated from the number of incident photons N on the whole slab phantom

$$\lambda = \frac{A_{pix}}{A_{phan}} \cdot N. \tag{5.14}$$

The number of photons N^{pix} that impinge on an individual pixel is randomly determined from a Poisson distribution with λ as expected value (fig. 5.6(c)). To determine the number of photons N_i^{det} with the energy E_i that produce a signal in a pixel, the number of photons with the energy E_i that impinge on a pixel N_i^{pix} is multiplied with the photon detection efficiency $\varepsilon(E_i)$ (fig. 5.6(d))

$$N_i^{det} = N_i^{pix} \cdot \varepsilon(E_i). \tag{5.15}$$

The energy E_j that a photon with the energy E_i deposits in one pixel, is obtained randomly from the energy deposition spectra $M_{i,j}$ (fig. 5.6(e)). Here, the relative abundances of the energies in the deposition spectra serve as weights for the random selection. This step is performed for all N_i^{det} resulting in an energy deposition spectrum with N_j^{dep} recorded events with deposited energies E_j. These events represent the energy deposited by ionizing the sensor material and creating charge carriers in a pixel. Since total pile-up is assumed, all charge carriers accumulate. This accumulated charge represents the total deposited energy in one pixel. Therefore, the energies of all recorded events are summed up to gain the total deposited energy E^{res} in one pixel

$$E^{res} = \sum_j N_j^{dep} \cdot E_j^{dep}. \tag{5.16}$$

E^{res} is the output of one pixel. The simulation differs in $\varepsilon(E_i)$ and $M_{i,j}$ for each detector. Therefore, the simulation is repeated 192 times for all three detectors for every incident spectrum and an initial number of photons N. Fig. 5.6(f) shows an example of the output pixel matrix for all big pixels of the three detectors. The color code denotes the total deposited energy in each pixel.

5.4 Simulation properties

The initial spectra are simulated using the python package *Xpecgen* [50]. 7599 different initial photon spectra are simulated. The X-ray tube voltage is varied between 19 keV and 400 keV. Different sets of filters are applied. Fig. 5.7a shows the distribution of the adjusted tube voltages and fig. 5.7b shows the corresponding distribution of the mean energy of the photon spectra. The initial number of photons N is randomly (uniformly) chosen in an interval between 10^7 and 10^{10}. This way, 106140 different photon fields are simulated. The lowest and highest simulated $H_p(10)$ is 7.5 nSv and 22.3 µSv, and the lowest and highest simulated $H_p(0.07)$ is 6.9 nSv and 50.2 µSv. Fig. 5.8a and fig. 5.8b show the dose distribution for both dose quantities.

All distributions depend on each other. Selecting simulated photon fields such that all quantities are, for example, equally distributed would decrease the variety of photon fields drastically. The applied doses are in good approximation equally distributed up to a dose of about 6 µSv. Most measurements are performed in the region of a few µSv. Therefore, no selection that alters the dose distribution is applied.

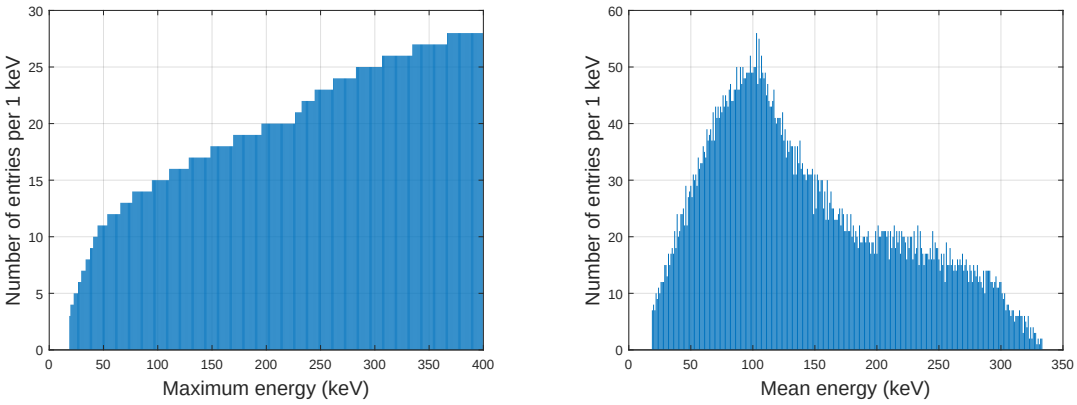

(a) Maximum spectrum energies **(b)** Mean spectrum energies

Figure 5.7 (a): Distribution of the maximum energy of the simulated photon spectra. (b): Distribution of the mean energy of the simulated photon spectra.

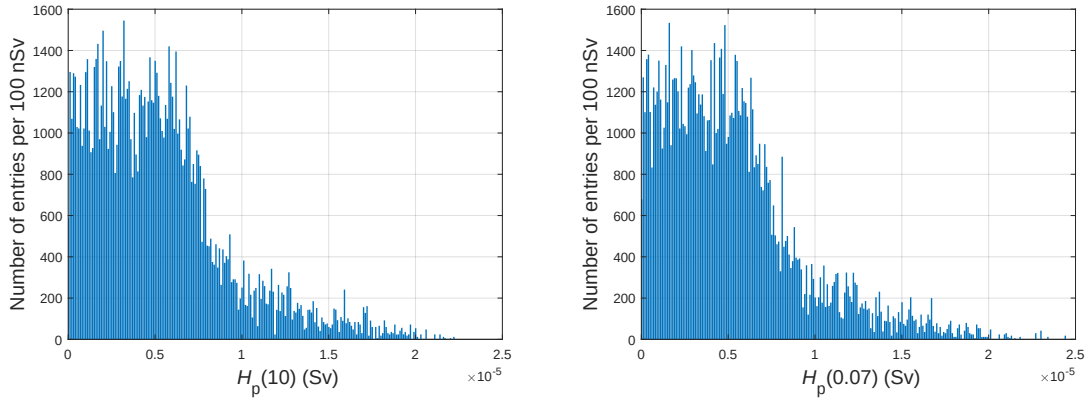

(a) Simulated $H_\mathrm{p}(10)$ **(b)** Simulated $H_\mathrm{p}(0.07)$

Figure 5.8 Distribution of the doses of the simulated spectra for (a): $H_\mathrm{p}(10)$ and (b): $H_\mathrm{p}(0.07)$ in total pile-up case.

5.5 Conclusion

It was shown that the maximum effect total pile-up can have in integration-mode is not negligible compared to measurements conducted in photon fields that cause no pile-up. Therefore, a simulation of the data output in integration-mode for measurements in photon fields that cause total pile-up was established. For this purpose, the monoenergetic energy spectra that were generated in the frame of a PhD thesis [39] were broadened to add energy resolution to the spectra using the data outlined in sec. 4.2. The simulation procedure for the applied dose and the detector response was explained. For every simulated applied photon spectrum the dose quantities $H_\mathrm{p}(10)$ and $H_\mathrm{p}(0.07)$ are calculated. 106140 different photon fields with doses between 6.9 nSv and 50.2 µSv were simulated.

Chapter 6

Dosimetry with pixel detectors

Contents

This chapter introduces the analytical methods to estimate the dose from measurements. The already approved method [30, 31] using the Dosi-mode is outlined. The determination of the conversion factors that are necessary to calculate the dose in Dosi-mode is explained. The neural network analysis for predicting the dose from measurements in integration-mode is introduced. The neural network architecture, the training parameters, and an evaluation based on validation data are outlined.

6.1 Dosimetry with the Dosi-mode

6.1.1 Dose reconstruction method

According to [35], the dose H corresponding to an incoming photon field of spectral distribution $N_\gamma(E)$ can be expressed as

$$H = \int_0^\infty \omega(E) \cdot N_\gamma(R)\, dE, \tag{6.1}$$

with dose conversion factors $\omega(E)$. These conversion factors assign an individual detected photon to a specific dose. According to [35], the energy response $M(E')$, which is the distribution of the detected energies, can be written as

$$M(E') = \int_0^\infty A(E', E) \cdot N_\gamma(E)\, dE, \tag{6.2}$$

with $A(E', E)$ the detector response function. $A(E', E)$ matches the energy E of incoming photons to a distribution of detected energies E'.

To estimate the dose with the Dosi-mode, the number of entries in the energy response spectra that are within certain energy intervals $[E_\mathrm{i}, E_{\mathrm{i}+1}]$ are determined [35]

$$\begin{aligned} N_\mathrm{i} &= \int_{E_\mathrm{i}}^{E_{\mathrm{i}+1}} M(E')\, dE' \\ &= \int_{E_\mathrm{i}}^{E_{\mathrm{i}+1}} \left(\int_0^\infty A(E', E) \cdot N_\gamma(E) \right) dE'. \end{aligned} \tag{6.3}$$

These energy intervals $[E_\mathrm{i}, E_{\mathrm{i}+1}]$ are equivalent to the energy bins of the Dosi-mode introduced in sec. 3.3. Here, E_i denotes the lower edge of each energy bin. The number of entries within the interval $[E_\mathrm{i}, E_{\mathrm{i}+1}]$ in the energy response spectrum is linearly dependent on the total number of initial photons N_γ with the spectral distribution $N_\gamma(E)$. Therefore, the applied dose H can be assumed to be proportional to the measured number of entries within each interval $[E_\mathrm{i}, E_{\mathrm{i}+1}]$ [35]

$$H \propto N_\mathrm{i}. \tag{6.4}$$

Using α_i as constant of proportionality, H is expressed as

$$H = \alpha_\mathrm{i} \cdot N_\mathrm{i}. \tag{6.5}$$

Here, the number of entries in each individual interval is put in relation to the applied dose. By summing over all energy intervals, equ. 6.5 is extended to

$$\sum_\mathrm{i}^{\mathrm{i_{max}}} H = \sum_\mathrm{i}^{\mathrm{i_{max}}} \alpha_\mathrm{i} \cdot N_\mathrm{i}\ , \tag{6.6}$$

where $\mathrm{i_{max}}$ denotes the total number of energy bins. Equ. 6.6 can further be simplified and solved for H

$$\mathrm{i_{max}} \cdot H = \sum_\mathrm{i}^{\mathrm{i_{max}}} \alpha_\mathrm{i} \cdot N_\mathrm{i} \tag{6.7}$$

$$H = \sum_\mathrm{i}^{\mathrm{i_{max}}} \frac{\alpha_\mathrm{i}}{\mathrm{i_{max}}} \cdot N_\mathrm{i} \tag{6.8}$$

New conversion factors $k_\mathrm{i} \overset{!}{=} \frac{\alpha_\mathrm{i}}{\mathrm{i_{max}}}$ are defined, which changes H to (see also [51])

$$H_\mathrm{reco} = \sum_\mathrm{i}^{\mathrm{i_{max}}} k_\mathrm{i} \cdot N_\mathrm{i}. \tag{6.9}$$

The standard uncertainty of the mean ΔH_stat depends on fluctuations of the entries in each energy bin. A Poisson distribution is assumed for these fluctuations and the statistical deviation ΔN_i is calculated via $\Delta N_\mathrm{i} = \sqrt{N_\mathrm{i}}$. Therefore, ΔH_stat can be expressed as

$$\Delta H_\mathrm{stat} = \sqrt{\sum_\mathrm{i}^{\mathrm{i_{max}}} (\Delta N_\mathrm{i}(E) \cdot k_\mathrm{i})^2} = \sqrt{\sum_\mathrm{i}^{\mathrm{i_{max}}} N_\mathrm{i}(E) \cdot k_\mathrm{i}^2}. \tag{6.10}$$

The standard uncertainty of the mean ΔR of the response (see sec. 2.3.2) is expressed as

$$\Delta R = \frac{\Delta H_\mathrm{stat}}{H_0}, \tag{6.11}$$

with the reference dose H_0.

Equ. 6.9 forms the basis of the dose reconstruction and is applied using the data output of three Dosepix detectors when operated in Dosi-mode. The data output of the Dosi-mode consists of vectors with 16 entries i for every pixel p in each of the three Dosepix detectors, as described in sec. 3.3. Each entry in a vector denotes the number of energy depositions $N_{\mathrm{i,p}}$ in the energy bins, respectively. The entries of each energy bin are summarized for big and small pixels separately

$$N_{\mathrm{i}}^{\mathrm{mes}} = \sum_{\mathrm{p}} N_{\mathrm{i,p}}. \tag{6.12}$$

The registered number of entries in the energy bins $N_{\mathrm{i}}^{\mathrm{mes}}$ are further used to estimate the applied dose using equ. 6.9. The energy bin edges are adjustable and are set before the measurements. Since the detector output is not given in units of energy but in ToT, the energy values of the bin edges need to be converted to the corresponding ToT. This is performed for each pixel individually. Tab. 6.1 lists the lower edges of the used energy bins for big and small pixels for the three detectors. The values for the bin edges of the small pixels were optimized [39] during the making of this thesis. The focus in this work, however, lies on the big pixels. Therefore, measurements performed with the old bin edges of the small pixels are not corrected. Since the different filters of the three detectors modify the incoming spectrum for each detector differently, individual conversion factors (k_{i} in equ. 6.9) are used. The factors also differ for big and small pixels.

Index i	Big pixels			Small pixels		
	Free (keV)	Al (keV)	Sn (keV)	Free (keV)	Al (keV)	Sn (keV)
1	12.0	12.0	32.0	11	10	22
2	18.0	17.0	37.0	16	15.5	40
3	21.0	31.0	47.0	26.0	23.0	47.5
4	24.5	40.0	57.5	36.0	31.5	55.5
5	33.5	45.5	68.5	46.5	42.0	64
6	43.0	50.5	80.0	57.0	53.5	74.0
7	53.5	60.5	91.5	70.5	66.5	84.5
8	66.5	68.0	104.0	84.5	79.5	98.0
9	81.5	91.0	117.0	99.5	94.5	113.0
10	97.0	102.5	131.0	115.0	109.5	128.5
11	113.0	133.0	145.0	131.0	126.0	144.5
12	131.5	148.0	163.5	148.5	142.5	161.5
13	151.5	163.0	183.5	167.0	160.5	182.5
14	173.0	196.0	207.5	194.0	180.0	203.5
15	200.5	220.0	234.5	223.0	200.0	232.0
16	236.0	257.0	269.5	260.0	221.5	264.5

Table 6.1: Lower bin edges for the big and small pixels of the Dosepix dosemeter operated in Dosi-mode. The rows denote the corresponding Dosepix detector for big / small pixels.

6.1.2 Determination of the conversion factors

The conversion factors k_i in equ. 6.9 are determined to measure the dose in [39]. This is achieved using simulated data, where the detector response for an initial photon field and the corresponding personal dose equivalent $H_p^{ref}(d)$ is known. Energy deposition spectra of various photon fields are simulated in [39]. Since the detector output of the simulation has to be the same as the detector output of a measurement performed in Dosi-mode, the simulated energy deposition spectra are binned to the 16 lower energy bin edges listed in tab. 6.1. The number N_i of detected energy depositions in each energy bin is determined for each of the three Dosepix detectors. The reconstructed dose $H_p^{DPX}(d)$ can be calculated by applying the simulated data of the bin entries to equ. 6.9

$$H_p^{DPX}(d) = \sum_i N_i^{sim} \cdot k_i. \tag{6.13}$$

A function $\mathscr{L}$ is defined to optimize k_i [39]

$$\mathscr{L} = \sqrt{\sum_s \left(\frac{H_p^{DPX}(d)_s}{H_p^{ref}(d)_s} - 1 \right)^2}, \tag{6.14}$$

where s iterates over data of different simulated photon energies. k_i is optimized by minimizing $\mathscr{L}$. This way, k_i are determined to calculate $H_p(10)$ and $H_p(0.07)$ for the big pixels. Fig. 6.1a and fig. 6.1b show these conversion factors as a function of the deposited energy that is binned to the lower edges of the energy bins. The unfiltered detector is depicted in blue, the detector with aluminum filter in red and the detector with tin filter in black. Fig. 6.1c shows the conversion factors for $H_p(10)$ for the small pixels. $H_p(0.07)$ is not evaluated for the small pixels since this work focuses on the big pixels. The values of the factors are listed in the appendix (A.2, A.3, A.4).

6.2 Dosimetry with the integration-mode

The method described in the following is primarily designed to estimate the dose in photon fields with high dose rates that cause total pile-up (see sec. 3.5) in the pixel electronics. Pile-up can lead to a high energy deposition in the detector and a high corresponding ToT. Therefore, the integration-mode with its 24-bit register is chosen over the ToT-mode with its 12-bit register for these measurements. In the following, the python package *Keras* [52] is used for the training and evaluation of the neural network.

The Dosepix detector returns the ToT accumulated in each pixel during the measurement time when operated in integration-mode. The output consists of 192 ToT values from the big pixels and 64 ToT values from the small pixels for each of the three Dosepix detectors. Since the simulation of total pile-up (see sec. 5.3) only considers big pixels, the small pixels are not discussed in the following. The 576 values that correspond to the big pixels of all three detectors are used as input for a neural network. Unlike raw data from measurements, which is given in ToT, the data from the simulation is given in units of energy. These deposited energy values from the simulation are used to train and evaluate the neural network. The measured data needs to be converted from ToT to deposited energy later to make predictions from measurements.

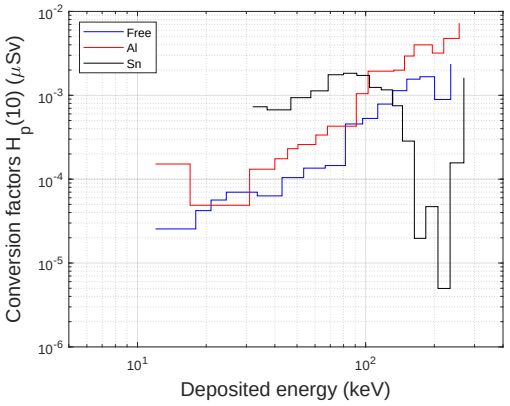

(a) $H_\mathrm{p}(10)$ big pixels

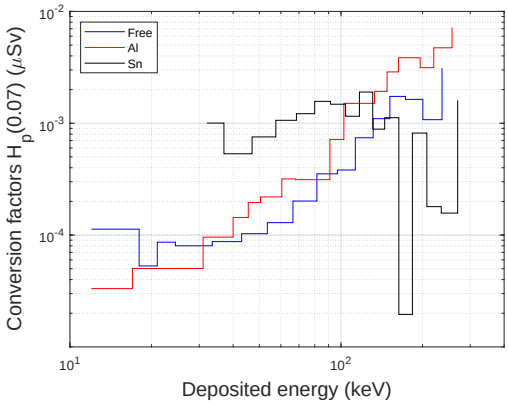

(b) $H_\mathrm{p}(0.07)$ big pixels

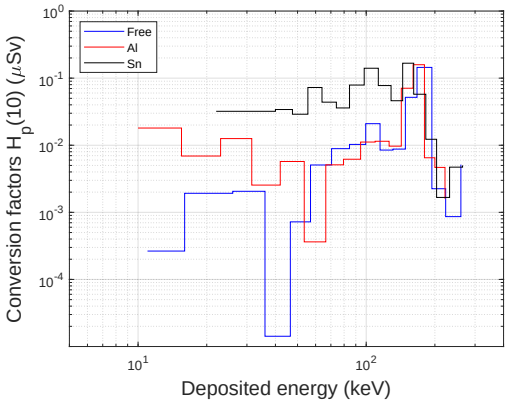

(c) $H_\mathrm{p}(10)$ small pixels

Figure 6.1 Conversion factors for the three Dosepix detectors for the big pixels for (a): $H_\mathrm{p}(10)$ and (b): $H_\mathrm{p}(0.07)$. (c): Coefficients for the small pixels for $H_\mathrm{p}(10)$. The data for the unfiltered detector is depicted in blue, the data for the detector with aluminum filter in red and the data for the detector with tin filter in black. The data was simulated in the frame of PhD thesis [39].

The pixels of each detector are assumed to have the same detection efficiency. Therefore, the specific location of a single pixel on the sensor is irrelevant, and the spatial distribution of the pixels does not need to be taken into account. The registered energy values are used as input vector with 576 entries for the neural network. Here, the first 192 entries denote the deposited energies in the first detector, the entries 193 to 374 the deposited energies in the second detector, and the entries 375 to 576 the deposited energies in the third detector. The input is propagated through the network as explained in sec. 2.2 and generates two output values. These outputs denote the predicted personal dose equivalents $H_\mathrm{p}(10)$ and $H_\mathrm{p}(0.07)$. From a total of 106140 data samples, 10% are chosen randomly to serve as validation data. The remaining data samples are used for training. The training of the network is stopped when the validation loss does not improve for 100 epochs. The quality of the network is graded with the validation loss. Various combinations of numbers of hidden layers and numbers of neurons in each hidden layer are investigated to determine a suitable network architecture.

Tab. 6.2 lists the investigated architectures, which are sorted by the number of hidden layers denoted by the rows. The columns represent the interval of the number of neurons implemented in each hidden layer. The intervals are of the form (A, B), where A denotes the first number and B denotes the last number of the interval. The step size is equal to A. For each number of hidden layers, all possible combinations of the intervals are investigated. This way 729 different networks are trained until the training is aborted by the criterion outlined above. Some architectures did not improve the loss at all and ended up at a loss of 100 % or converged at slightly over 50 %. These architectures are excluded from the analysis by setting a cutoff at 50 % of the validation loss. This results in a total number of 695 trained networks. For all networks, the loss function (see sec. 2.2.2) is mean absolute percentage error σ_{MAPE} [53]

$$\sigma_{\mathrm{MAPE}} = 100 \left| \frac{y - y_{\mathrm{k}}}{y} \right|, \tag{6.15}$$

where y denotes the labels and y_{k} the predicted outputs. Here, y_{k} corresponds to the measured dose H^{mes} and y to the reference dose H_0 in measurements. The response (see equ. 2.38) reaches its optimum at $H^{\mathrm{mes}} = H_0$. Therefore, σ_{MAPE} is chosen as loss function since the minimization of this function optimizes the response. All network architectures are composed of rectifying linear units as activation functions. Fig. 6.2a shows a box plot of the resulting validation loss depending on the number of hidden layers. The red line denotes the median, the lower and upper sides of the box denote the 25^{th} and 75^{th} percentile, and the lower and upper extensions of the box (so-called *whiskers*) denote the minimum and the maximum values of the validation loss distribution. The maximum length of the whiskers is set to 1.5 times of the interquartile range (range between the 25^{th} and the 75^{th} percentile). All data points outside this range are depicted as individual data points (blues crosses). The mean validation loss converges for networks with more than four hidden layers. The network architecture with the lowest validation loss is selected in the following. This applies to a network with four hidden layers. This choice is supported by the fact that the mean validation loss of all networks with the same number of hidden layers is the lowest for four hidden layers. The chosen network architecture is depicted in fig. 6.2b. Each rectangle corresponds to a layer, its activation function, and the number of neurons within the layer. This network has a total number of 571112 parameters. Since the initial values for weights and biases in a network are chosen randomly, the training process and the final set of parameters differ if the same network is trained multiple times. This also changes the output of the multiple trained network for the same input data. However, this variation of the data output provides information about the accuracy of the network to simulated data. Therefore, 10-fold cross-validation (see sec. 2.2.3) is performed. Here, the training is aborted after the validation loss has not improved for 150 epochs. Fig. 6.3a shows one of the learning curves for the cross-validation analysis. The black curve denotes the training loss, and the red curve the validation loss. The losses converge with increasing number of epochs. Overfitting does not take place.

Number of hidden layers	Number of neurons in layer						
	2	3	4	5	6	7	8
2	100,1000	20,200					
3	200,1000	40,200	5,25				
4	250,100	150,450	50,150	10,30			
5	330,990	250,500	150,450	100,200	30,90		
6	330,990	300,600	200,400	100,200	50,100	20,40	
7	330,990	300,600	200,400	100,200	50,100	20,40	10,20

Table 6.2: Architectures of the trained neural networks. The intervals of neurons in each layer (columns) are listed for the total number of hidden layers in the network (rows). The intervals are of the form (A, B), where A denotes the first number and the step size and B denotes the last number.

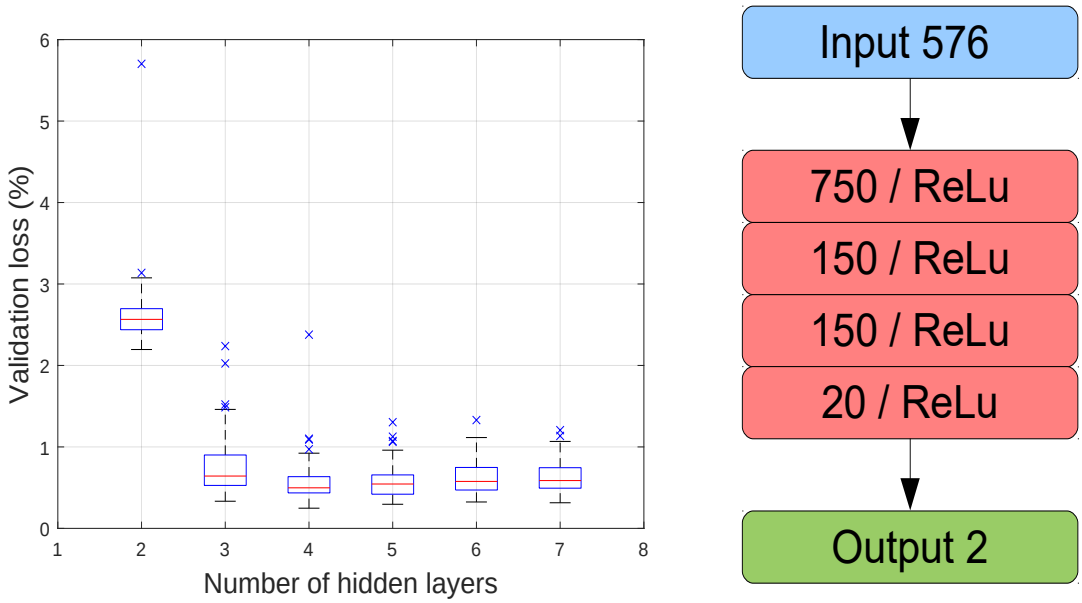

(a) Validation loss distributions

(b) Network architecture

Figure 6.2 (a): Validation loss distribution depending on the total number of hidden layers within the evaluated networks. The red line denotes the median, the the upper and lower side of the box the 25^{th} and 75^{th} percentile, the whiskers the maximum and minimum value of the distribution. The blue data points denote outliers that do not contribute to the whiskers. The total number of networks is 695. (b): Network architecture with the lowest resulting validation loss. Each rectangle denotes a layer and its numbers of neurons within the layers. All activation functions are rectifying linear units.

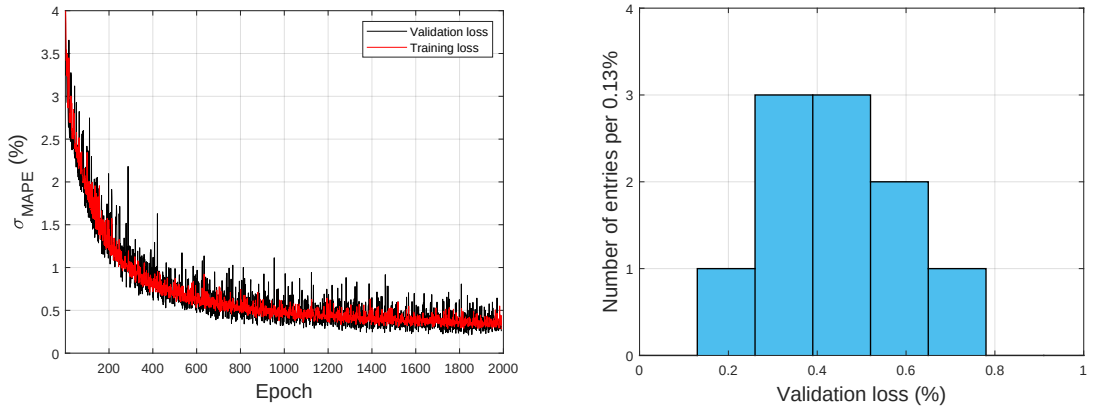

(a) Mean absolute percentage loss σ_{MAPE} **(b)** Cross-validation loss distribution

Figure 6.3 (a): Learning curve. The mean average percentage error σ_{MAPE} is shown as a function of the training epoch. The red curve denotes the training loss, the black curve depicts the validation loss. (b): Distribution of the final validation losses from the cross-validation analysis.

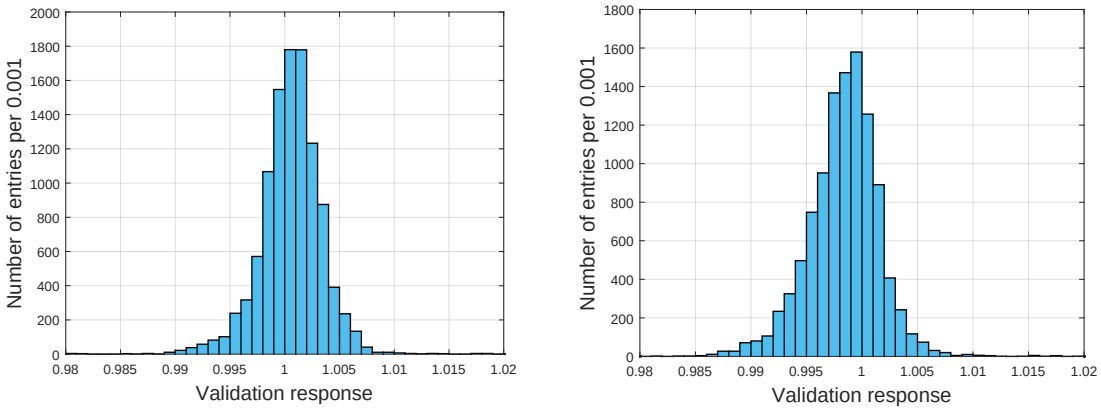

(a) $H_{\mathrm{p}}(10)$ **(b)** $H_{\mathrm{p}}(0.07)$

Figure 6.4 (a): Validation response of $H_{\mathrm{p}}(10)$. (b): Validation response of $H_{\mathrm{p}}(0.07)$. The total number of validation data samples is 10614.

Fig. 6.3b shows the distribution of all ten final validation losses from the cross-validation analysis. The mean validation loss is 0.44 % with a standard deviation of 0.15 %. This trained network returns the lowest validation loss in the cross-validation analysis and is therefore used for further analysis. The responses for a validation data set for $H_{\mathrm{p}}(10)$ and $H_{\mathrm{p}}(0.07)$ are depicted in Fig. 6.4a and fig. 6.4b. The responses R are calculated via

$$R = \frac{H_{\mathrm{pred}}}{H_0}, \tag{6.16}$$

where H_{pred} denotes the dose predicted by the neural network and H_0 the simulated dose for $H_{\mathrm{p}}(10)$ and $H_{\mathrm{p}}(0.07)$ respectively. Here, the validation data set has 10614 samples. The means and standard deviations are $\mu(H_{\mathrm{p}}(10)) = 1.001$, $\sigma(H_{\mathrm{p}}(10)) = 0.004$ and $\mu(H_{\mathrm{p}}(0.07)) = 0.998$, $\sigma(H_{\mathrm{p}}(0.07)) = 0.004$, which is a good result on simulated data.

6.3 Conclusion

In this chapter, the method to perform dosimetry measurements using photon-counting was explained. The bin edges and the conversion coefficients that assign a measured signal to a certain dose value were outlined. The simulation introduced in sec. 5.3 was used to train several neural networks with different architectures. The best performing network was further investigated and chosen to be used for dosimetry measurements in photon fields that cause total pile-up in the pixel electronics. The chosen network yields very good and stable results on simulated data. Here, $H_\mathrm{p}(10)$ and $H_\mathrm{p}(0.07)$ were investigated. The response this network yields was investigated on simulated data for $H_\mathrm{p}(10)$ and $H_\mathrm{p}(0.07)$.

Chapter 7

Measurements with the Dosi-mode

Contents

The dose reconstruction method introduced in chap. 6.1 is applied to measurements in continuous and pulsed photon fields in this chapter. The two different energy calibration methods outlined in sec. 4.2.3 are evaluated. Measurements with the two calibration methods are compared, and the effect on the estimated dose is investigated. Characteristics relevant for a type test for new dosemeter systems are examined. Further investigations concerning the energy dependence in photon fields with high dose rates are discussed. Dose measurements in high dose rate photon fields with two different settings of I_{Krum} are performed.

7.1 Measurements at PTB

7.1.1 Setup

The measurements are performed following the requirements for new personal dosemeters outlined in sec. 2.3.2 [25, 26]. They are conducted at PTB to ensure that the measurement conditions meet these required standards. Different irradiation facilities are utilized to investigate a broad energy and dose rate range using the standard spectra outlined in tab. 2.4. Fig. 7.1 shows photographs of the four facilities the measurements are taken at. A-series spectra with lower mean photon energies are examined at (a) and spectra with higher energies at (b). The measurements with high dose rates are carried out at (c) (further referred to as GeSa). (d) shows an image of the facility containing the radioactive sources ^{137}Cs and ^{60}Co. All X-ray tubes are equipped with adjustable filters and an ionization chamber to measure the reference dose.

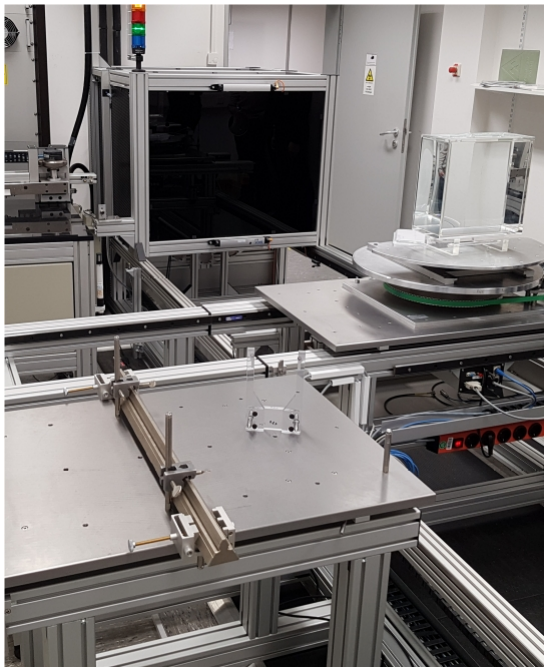

(a) 15 kV - 120 kV

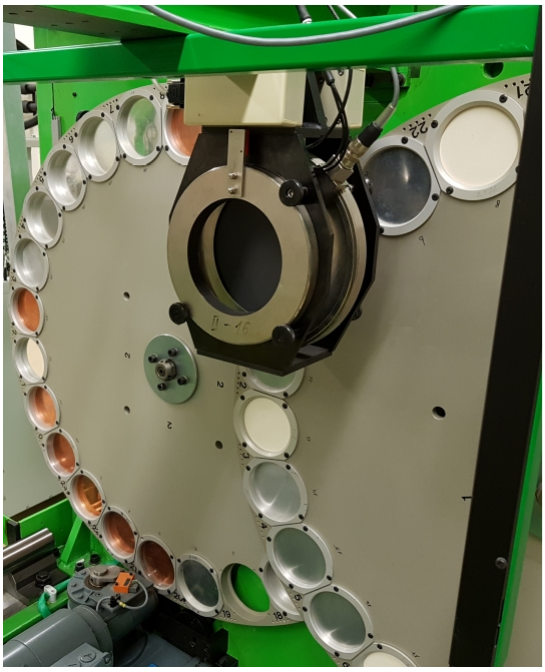

(b) 120 kV - 400 kV

(c) High dose rates

(d) ^{137}Cs and ^{60}Co

Figure 7.1 Photographs of the irradiation facilities used for type tests for new personal dosemeters at PTB with X-ray tube voltages between (a): 12 kV and 150 kV and (b): between 120 kV and 400 kV (b). (c): Facility for measurements to investigate the response in high dose rate photon fields. (d):Facility for measurements with ^{137}Cs and ^{60}Co.

The measurement parameters set for each facility are outlined in the following.

150 kV facility (7.1a)

The Dosepix dosemeter resides on a slab phantom placed onto a table perpendicular to the X-ray tube at a distance of 2.50 m. The table can be rotated. The spectra A-15 to A-60 are investigated here. The irradiation time is set to 60 s or 120 s. A nominal dose of about 15 mSv is applied and monitored with an ionization chamber. The dose rates are varied between 5.3 $\frac{\text{mSv}}{\text{h}}$ and 9.7 $\frac{\text{mSv}}{\text{h}}$. Additional to the perpendicular irradiation, photon fields under angles of $\pm 30°$ for the A-20 spectrum and angles of $\pm 60°$ for the A-20 and A-60 spectrum are applied. The A-series spectra are strongly filtered and cover, therefore, a narrow energy region. The C-60 spectrum, which is broader than the A-spectra, is evaluated as well. Measurements with both calibration methods are performed here.

400 kV facility (7.1b)

Setup, irradiation time, and nominal dose are the same as for the 150 kV facility. The investigated spectra are A-80 to A-300, where additional irradiations under angles of $\pm 60°$ are applied for the A-150 and the A-250 spectrum. Measurements with both calibration methods are performed here.

GeSa facility (7.1c)

Since the main objective here is to increase the dose rate of the applied photon fields, the facility is set up to maximize the photon flux. Therefore, the Dosepix dosemeter and the slab phantom are placed as close as possible to the X-ray tube, ensuring the Dosepix dosemeter is fully illuminated. This is achieved at a distance of 0.5 m. Since the slab phantom contributes to the measured dose via backscattering, the effect of the slab phantom is determined for both applied spectra RQR 8 and RQR 9. For this purpose, two identical measurements, one with and one without slab phantom, are performed at a distance of 2.50 m. The measured responses are compared, and a correction factor for measurements without slab phantom is derived. This correction factor is determined to be 1.12 for the RQR 8 and the RQR 9 spectrum. Measurements, where a complete illumination of the slab phantom cannot be ensured, are performed without it. Furthermore, the irradiation angle alters when the Dosepix dosemeter is moved towards the X-ray tube. Two measurements with the same dose rates are performed in a distance of 0.5 m and 2.5 m without slab phantom to derive a correction factor for this effect as well. This correction factor is determined to be 1.02 for the RQR 8 and the RQR 9 spectrum. The pulse duration is varied between 10 ms and 10 s. Dose rates between 0.062 $\frac{\text{Sv}}{\text{h}}$ and 1209 $\frac{\text{Sv}}{\text{h}}$ are achieved. Here, the maximum applied dose is 3.35 mSv. Only measurements with the calibration method based on interpolation are performed here.

Radioactive sources facility (7.1d)

Various radioactive sources of the same isotopes (^{137}Cs and ^{60}Co) and different activities are available at this facility. The dose rate of the applied photon field is altered by either changing the radioactive source or the distance between the source and the Dosepix dosemeter. An additional PMMA plate is placed directly in front of the Dosepix dosemeter. This practice is applied to shield tested dosemeters from secondary electrons that are generated by the γ-radiation in the air between the radioactive source and the dosemeter. The plate ensures that secondary electron equilibrium is achieved for the dosemeter. The

applied dose rates ranged from $10^{-6}\,\frac{\mathrm{Sv}}{\mathrm{h}}$ to $30\,\frac{\mathrm{Sv}}{\mathrm{h}}$. Additional to the type test evaluation, this data is used to compare the Dosepix dosemeter to other dosemeters introduced in sec. 2.3.3. These results are presented in sec. 7.1.5. The exposure time is set between 25 s and 100 s. The exposure time is constrained. The lower limit is 25 s due to the mechanical mechanism of the safety container the radioactive sources are stored in. The applied dose ranged from $2.78 \cdot 10^{-8}$ Sv to 0.206 Sv. The measurement with an applied dose rate of $30\,\frac{\mathrm{Sv}}{\mathrm{h}}$ with the ^{60}Co source is performed in a distance, where the phantom is not fully illuminated. The influence of the phantom is determined to be so small that it can be neglected.

7.1.2 General settings and data acquisition

Energy calibrations using fluorescence targets were performed in two different ways (see sec. 4.2.3). The traditional model according to equ. 4.4 and an interpolation method using cubic splines (see fig. 4.11). For both methods, the dose reconstruction using the Dosi-mode is investigated. The energy bin edges (see sec. 6.1) are converted to ToT for both calibration methods. For both methods, the traditional model is used for energies higher than about 80 keV since the interpolation method does not return a calibration for these energies. All measurements are performed with an I_{Krum} of 2.2 nA and $\mathrm{THL}_{\mathrm{sub}}$ set to 20.
Here, the utilized conversion factors originate from a simulation of the Dosepix dosemeter with a plastic lid made of PMMA with a thickness of 1 mm. However, the measurements are performed with a plastic lid made of ABS with a thickness of 1.5 mm. Although thickness and material are different, the attenuation of the photon flux is almost identical, even for low energies. The energy-dependent total transmission T is calculated by rearranging equ. 2.4 to

$$T(E) = \frac{I(E)}{I_0(E)} = \mathrm{e}^{-\mu(E)\rho \mathrm{l}}, \tag{7.1}$$

where $\mu(E)$ denotes the energy dependent mass attenuation coefficient, ρ the density of the material and l its thickness. Fig. 7.2a shows the total absorption for the PMMA lid (blue) and the ABS lid (black) as a function of the energy of the incoming photon field. A density of $1.04\,\frac{\mathrm{g}}{\mathrm{cm}^3}$ [54] was used for ABS and $1.18\,\frac{\mathrm{g}}{\mathrm{cm}^3}$ [54] for PMMA. The mass attenuation coefficients are taken from [15]. The deviation of both transmissions from another is expressed as the ratio

$$K = \frac{T_{\mathrm{PMMA}}}{T_{\mathrm{ABS}}}, \tag{7.2}$$

where T_{PMMA} denotes the transmission for the PMMA lid and T_{ABS} the transmission for the ABS lid. Fig. 7.2b shows the ratio K as a function of the photon energy. The deviation drops below 1 % for energies over 13.5 keV and converges after a local minimum at about 50 keV towards 1 with increasing energy. The absolute deviation at the local minimum is about 0.7 %. This value denotes the maximum possible deviation for energies higher than about 14.5 keV. All utilized spectra, except the A-15 spectrum, have mean energies higher than 14.5 keV (See tab. 2.4). Therefore, the effect of the different lid is further neglected.

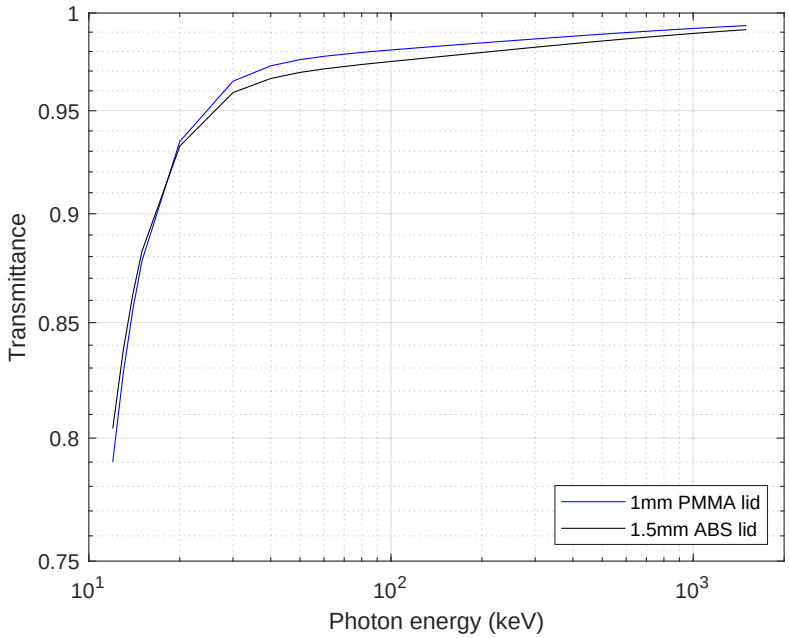

(a) Transmittance of plastic lids

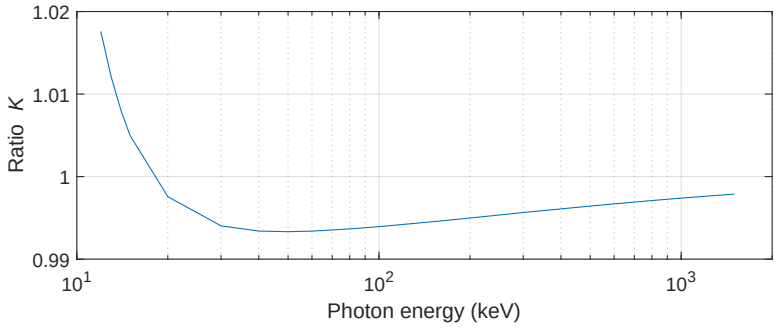

(b) Ratio of transmittances

Figure 7.2 (a): Transmittance of the ABS (black) and PMMA lid (blue) as a function of the photon energy. (b): Ratio K between the transmittances of both plastic lids as a function of the photon energy.

To protect the first Dosepix detector from dust, an adhesive tape made of PMMA and a thickness of 55 µm is taped on top of the opening of the first Dosepix detector. This tape is not implemented in the simulation. However, the effects of this tape are assumed to be negligible since the absolute attenuation drops under 1 % for energies above 13 keV and decreases further with increasing energy (based on data taken from [15]).

All differences between simulation and measurements apply to both investigated calibration methods. Therefore, the comparison of the methods is only affected in a minor way.

7.1.3 Comparison of the methods for the big pixels

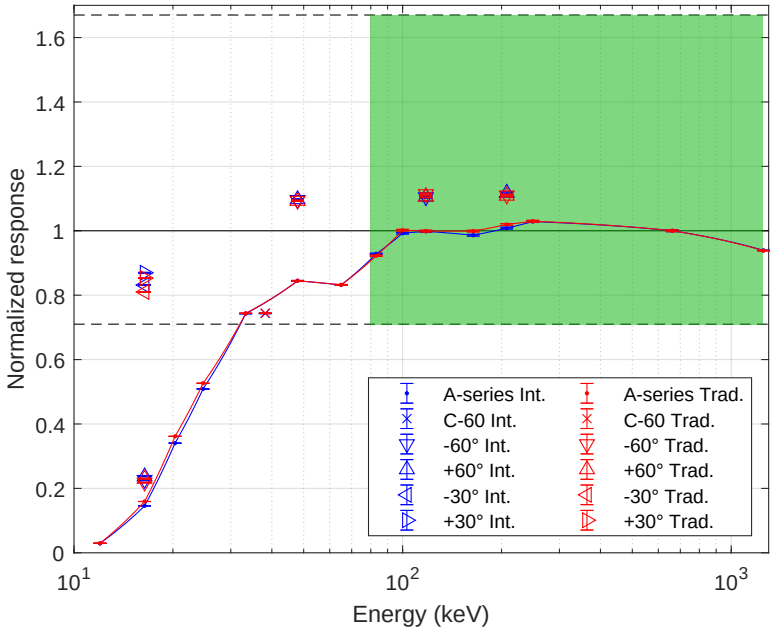

(a) $H_p(10)$ big pixels

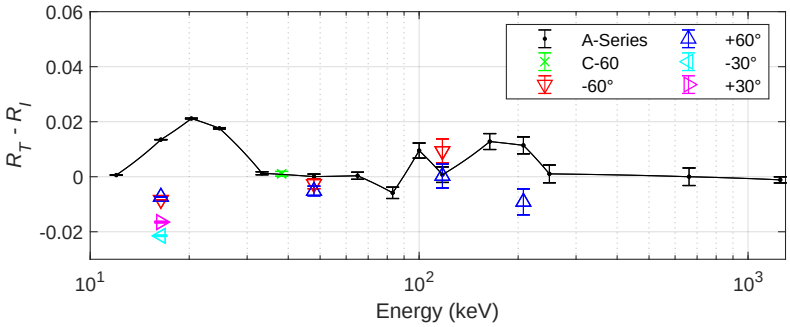

(b) Difference between methods

Figure 7.3 (a): Normalized responses for $H_p(10)$ for the big pixels as a function of the mean energy of the applied spectra for perpendicular irradiation (solid lines), irradiation under angles of $\pm 60°$ and $\pm 30°$ and a C-60 spectrum. The response calculated with the energy calibration with the interpolation method is depicted in blue, the response calculated with the traditional model in red. The black dashed lines indicate the upper and lower PTB limits (see sec. 2.3.2) on the normalized response and the green area the required energy range within this allowed response range. (b): Difference between the normalized responses of both calibration methods.

Fig. 7.3a shows the normalized response of the Dosepix dosemeter for $H_p(10)$ as a function of the mean energy of the applied spectra. The colored lines represent the A-series and the ^{137}Cs and ^{60}Co γ-spectra, the crosses the C-60 spectrum, and the triangular data points the response under certain irradiation angles according to the legend. The dashed black lines denote the PTB limits on the normalized response and the green shaded area the required energy range within these response limits outlined in tab. 2.1. The required energy range is 80 keV to 1250 keV. The solid black line denotes a perfect response of 1.

The blue data indicate the measurements where the energy bin edges are calculated using the interpolation method, and the data in red shows the measurements with the energy bin edges set using the traditional model. The responses are calculated via equ. 2.38 and the uncertainties of the means using equ. 6.11 and equ. 6.10. Following the requirements from tab. 2.1, the responses of the C-60 spectrum, the A-series, and the radioactive sources are normalized to the response at 662 keV (^{137}Cs). The responses under angular irradiation are normalized to the responses of measurements taken for the same photon field at an irradiation angle of 0°. Both methods yield normalized responses that are in accordance with the requirements of PTB. The results of the different methods are almost identical. In the following, any response that corresponds to measurements performed using the interpolation method is referred to as R_{Int}, and any response that corresponds to measurements performed using the traditional model is referred to as R_{Trad}.

Perpendicular irradiation for $H_{\mathrm{p}}(10)$

The maximum deviation from 1 occurs for the A-15 spectrum with a normalized response of $R_{\mathrm{Int}} = 0.02919 \pm 0.00008$, $R_{\mathrm{Trad}} = 0.02978 \pm 0.00008$ at a mean energy of 12 keV. The response rises and exceeds the lower PTB limit at an energy of about $E_{\mathrm{Int}} = 32.1$ keV, $E_{\mathrm{Trad}} = 32.0$ keV. The required energy range (green area) is reached with a normalized response of $R_{\mathrm{Int}} = 0.91$, $R_{\mathrm{Trad}} = 0.91$. This response value also denotes the maximum deviation from 1 within the required energy range. The average absolute deviation $\bar{W}^{\mathrm{en}}$ from the perfect response of 1 for all data points within the required energy range is $\bar{W}^{\mathrm{en}}_{\mathrm{Int}} = 0.0275 \pm 0.0009$, $\bar{W}^{\mathrm{en}}_{\mathrm{Trad}} = 0.0275 \pm 0.0009$. The uncertainties are determined via Gaussian error propagation. The average absolute deviation from 1 $\bar{W}^{\mathrm{req}}$ that resides within the PTB limits on the normalized response is $\bar{W}^{\mathrm{req}}_{\mathrm{Int}} = 0.0773 \pm 0.0007$, $\bar{W}^{\mathrm{req}}_{\mathrm{Trad}} = 0.0772 \pm 0.0007$. The data point for ^{137}Cs is not included in this calculation since all data points are normalized to it. The normalized response for the C-60 spectrum is $R_{\mathrm{Int}} = 0.7433 \pm 0.0008$, $R_{\mathrm{Trad}} = 0.7443 \pm 0.0008$.

Angular irradiation for $H_{\mathrm{p}}(10)$

The accordance with the PTB requirements on the normalized response also accounts for measurements with an irradiation under angles. All data points, except the ones for the A-20 spectrum, reside within the PTB limits. The maximum deviation from $R = 1$ occurs for the A-250 spectrum with $R_{\mathrm{Int}} = 1.118 \pm 0.003$, $R_{\mathrm{Trad}} = 1.132 \pm 0.003$ for an irradiation angle of 60°. Although an irradiation under angles of 0° and ± 60° lead to strong underestimations of the dose for the A-20 spectrum, the normalized response measured for the same spectrum with a ± 30° irradiation angle fits the PTB requirements. The maximum deviation from $R = 1$ occurs at an angle of −30° with a normalized response of $R_{\mathrm{Int}} = 0.832 \pm 0.002$, $R_{\mathrm{Trad}} = 0.8101 \pm 0.0012$.

Comparison of methods for $H_{\mathrm{p}}(10)$

Fig. 7.3b shows the difference between the normalized responses calculated with the interpolation method and the traditional model ($R_{\mathrm{Trad}} - R_{\mathrm{Int}}$) as a function of the mean energy of the applied spectra. The error bars are calculated from the standard uncertainties of the means using Gaussian error propagation. The data points of the A-series and the radioactive sources, the irradiation under angles and the C-60 spectrum are depicted according to the legend. The absolute difference tends to be higher for lower energies with the largest difference for the A-25 spectrum of $R_{\mathrm{Trad}} - R_{\mathrm{Int}} = 0.0212 \pm 0.0002$. The average absolute difference of all data except the data point for the γ-spectrum of ^{137}Cs is $R_{\mathrm{Trad}} - R_{\mathrm{Int}} = 0.0069 \pm 0.0007$. The measurements under irradiation angles different from 0° show a maximum absolute difference of $R_{\mathrm{Trad}} - R_{\mathrm{Int}} = -0.0215 \pm 0.0003$ at an irradiation angle of −30°. The difference for the C-60 spectrum is 0.0011 ± 0.0009.

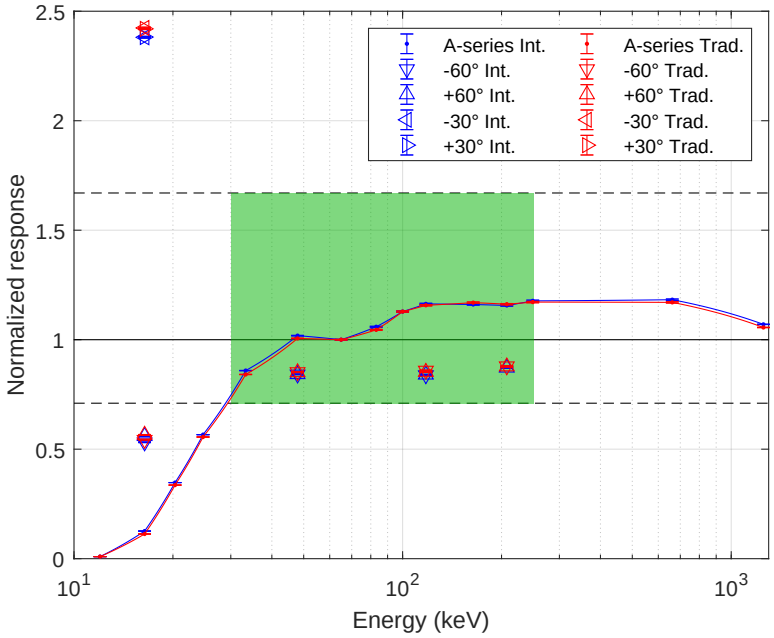

(a) $H_p(0.07)$ big pixels

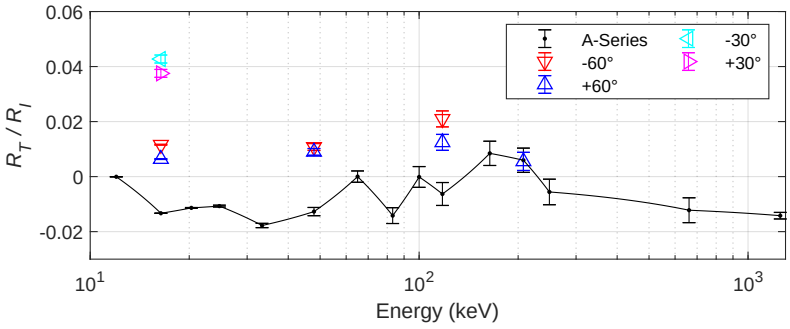

(b) Difference between methods

Figure 7.4 (a): Normalized responses for $H_p(0.07)$ for the big pixels as a function of the mean energy of the applied spectra for perpendicular irradiation (solid lines), irradiation under angles of $\pm 60°$ and $\pm 30°$. The response calculated with the energy calibration with the interpolation method is depicted in blue, the response calculated with the traditional model in red. The black dashed lines indicate the upper and lower PTB limits (see sec. 2.3.2) on the normalized response and the green area the required energy range within this allowed response range. (b): Difference between the normalized responses of both calibration methods.

Fig. 7.4a shows the normalized response of the Dosepix dosemeter for $H_p(0.07)$ as a function of the applied spectra. The data is depicted the same way as in fig. 7.3a. The C-60 spectrum is not shown. The dashed black lines denote the PTB limits on the normalized response, and the green area indicates the required energy range within these limits. The required energy range is 30 keV to 250 keV. As for the measurements for $H_p(10)$, the mean responses and the standard uncertainties of the means are calculated using 2.38, equ. 6.11 and equ. 6.10. Following the requirements from tab. 2.2, the responses of the A-series and the radioactive sources are normalized to the response at 65 keV (A-80). The responses under angular irradiation are normalized to the responses of measurements taken for the same photon field at an irradiation angle of 0°. As for the measurements for $H_p(10)$, both methods yield normalized responses that are in accordance with the requirements of PTB.

Perpendicular irradiation for $H_p(0.07)$

The normalized response for the A-15 spectrum is almost zero for the A-spectrum and rises towards increasing energies. The lower PTB limit is exceeded at $E_{Int} = 28.9\,keV$, $E_{Trad} = 29.4\,keV$. The required energy range is entered with a normalized response of $R_{Int} = 0.75$, $R_{Trad} = 0.73$ for an energy of 30 keV. This response also denotes the maximum deviation from 1 within the required energy range. The average absolute deviation from 1 within the required energy range is $R_{Int} = 0.1256 \pm 0.0009$, $R_{Trad} = 0.1248 \pm 0.0009$. The average absolute deviation from 1 within the required normalized response range is $R_{Int} = 0.1258 \pm 0.0008$, $R_{Trad} = 0.1225 \pm 0.0008$. The data point of the A-80 spectrum is not included in this calculation since all data points are normalized to it. After the required energy range is exceeded, the normalized response stays within the PTB limits.

Angular irradiation for $H_p(0.07)$

All measurements performed under an irradiation angle of $\pm 60°$, except the one for the A-20 spectrum, reside within the PTB requirements. As for the measurements of the A-series and the radioactive sources, the normalized responses of the interpolation method and the traditional model are almost identical. The minimum normalized response occurs for 16.4 keV (A-20 spectrum) with $R_{Int} = 0.532 \pm 0.002$, $R_{Trad} = 0.543 \pm 0.002$ and an irradiation angle of −60°. The normalized response for measurements under an angle of $\pm 30°$ exceeds the maximum PTB limit. The maximum normalized response occurs for the A-20 spectrum under an angle of 30° with $R_{Int} = 2.382 \pm 0.004$, $R_{Trad} = 2.423 \pm 0.004$.

Comparison of methods for $H_p(0.07)$

Fig. 7.4b shows the difference of the two methods for $H_p(0.07)$ as calculated in fig. 7.3b as a function of the mean energy of the applied spectra. The highest absolute difference from 0 occurs for the A-40 spectrum with $R_{Trad} - R_{Int} = -0.0177 \pm 0.0008$. The average absolute difference of all data points, except the one for the A-80 spectrum, is 0.0109 ± 0.0008. The measurements under irradiation angles different from 0° show a maximum difference of $R_{Trad} - R_{Int} = 0.043 \pm 0.002$ at an irradiation angle of −30°.

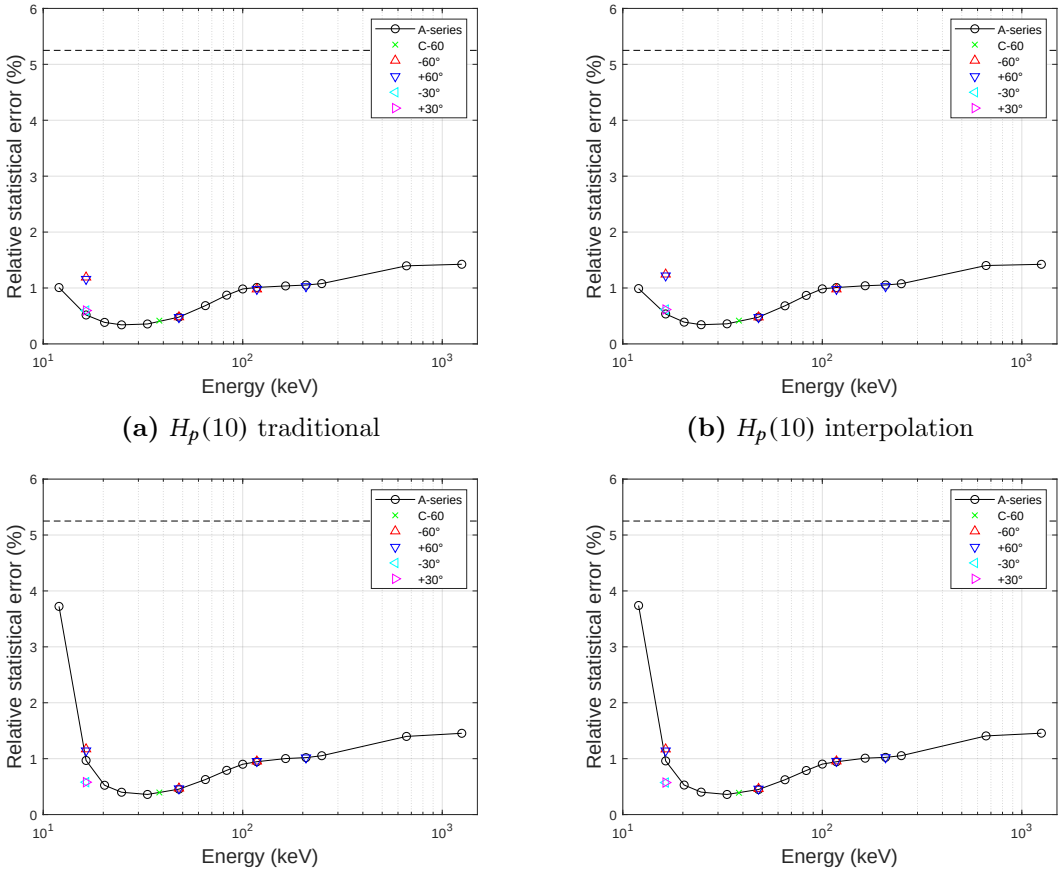

(a) $H_p(10)$ traditional

(b) $H_p(10)$ interpolation

(c) $H_p(0.07)$ traditional

(d) $H_p(0.07)$ interpolation

Figure 7.5 Relative statistical error as a function of the mean energy of the applied spectra for (a): the traditional model and $H_\mathrm{p}(10)$ (b): the interpolation method and $H_\mathrm{p}(10)$ (c): the traditional model and $H_\mathrm{p}(0.07)$ (d): the interpolation method and $H_\mathrm{p}(0.07)$.

Fig. 7.5 shows the relative statistical error (see sec. 2.3.2) for the measurements of $H_\mathrm{p}(10)$ and $H_\mathrm{p}(0.07)$ with the interpolation method and the traditional model. The individual data points are depicted according to the legend. The measurements with the different models are almost identical. Both dose quantities are measured without exceeding the limit of 5.25 % (black dashed line) as it is used in [55].

Fig. 7.6 shows the relative dose of each individual Dosepix detector as a function of the mean energy of the applied spectra for the measurements of $H_\mathrm{p}(10)$ ((a) and (b)) and $H_\mathrm{p}(0.07)$ ((c) and (d)) with the interpolation method and the traditional model. Only the A-series and the radioactive sources are depicted. Again, the measurements for the interpolation method and traditional model are almost identical. Only the first detector contributes to the total dose at low energies. This is expected since low energies do not penetrate the filter caps that cover the other two detectors. The contribution of the second detector rises with increasing energy and exceeds the contribution of the first detector. The aluminum filter becomes lesser effective with rising energy, and the number of detected events in the second detector approaches the number of detected events in the first one.

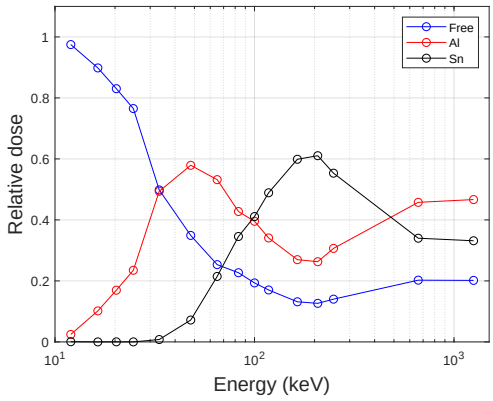

(a) $H_p(10)$ traditional

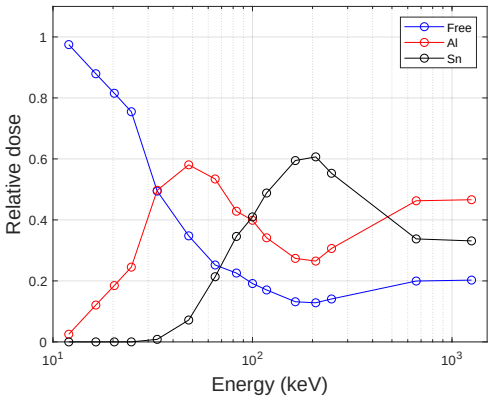

(b) $H_p(10)$ interpolation

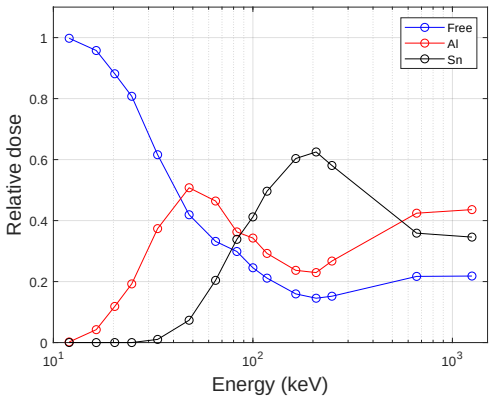

(c) $H_p(0.07)$ traditional

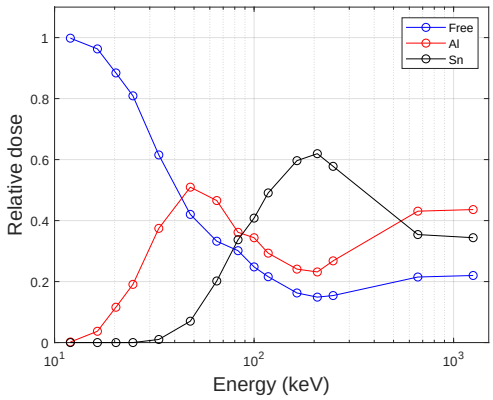

(d) $H_p(0.07)$ interpolation

Figure 7.6 Relative dose contributions of the individual Dosepix detectors as a function of the mean energy of the applied spectra for (a): the traditional model and $H_\mathrm{p}(10)$ (b): the interpolation method and $H_\mathrm{p}(10)$ (c): the traditional model and $H_\mathrm{p}(0.07)$ (d): the interpolation method and $H_\mathrm{p}(0.07)$.

However, the conversion factors of the second detector generate a higher dose contribution than the ones of the first detector. The third detector does not measure any dose for energies lower than 33.3 keV. This is because the first bin edge of the third detector is set to 32.0 keV. The third detector dominates the dose contribution at an energy of about 100 keV. Towards higher energies, the detection efficiency of all three detectors is about the same since the filters become more and more transparent. Therefore, the order of the dose contribution is analogue to the order of the dose contribution of the conversion factors.

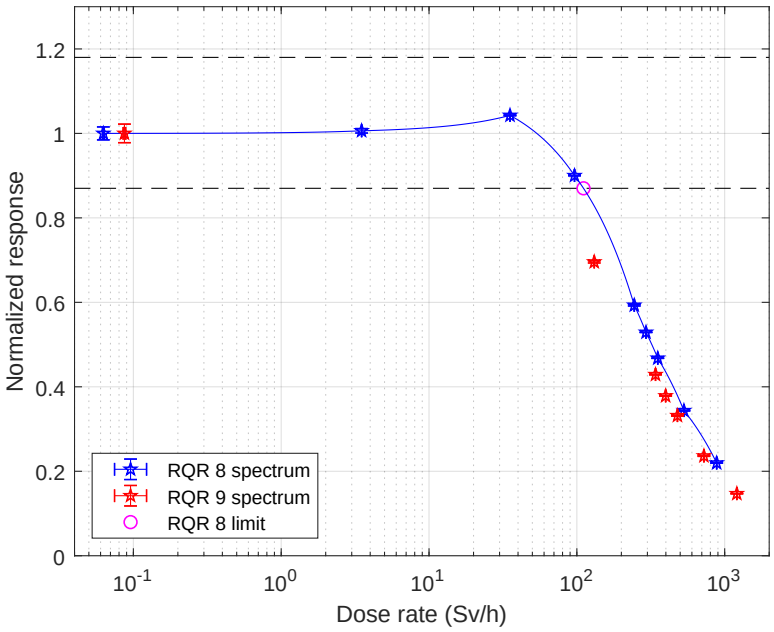

(a) Whole dose rate range

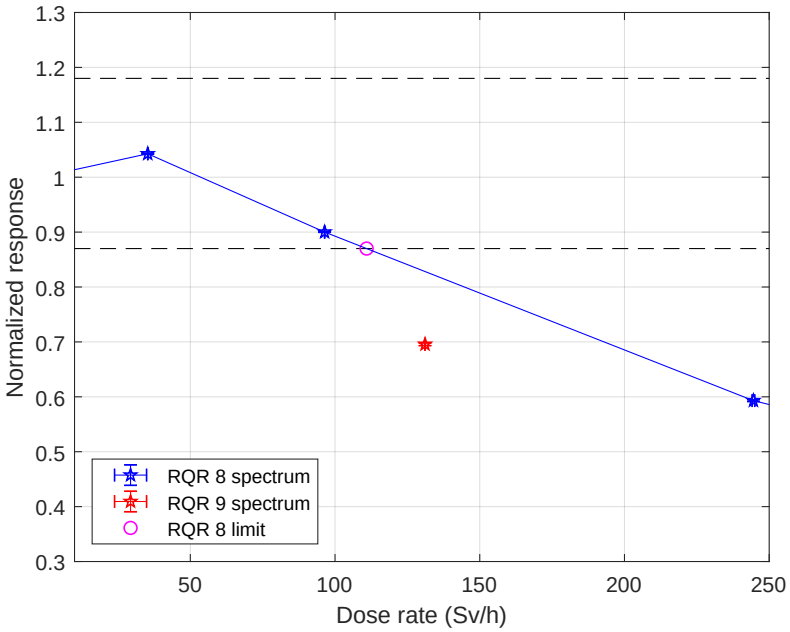

(b) Break-up point

Figure 7.7 (a): Normalized response for $H_p(10)$ for big pixels as a function of the dose rate. The red data points denote measurements with an RQR 9 spectrum, the blue data points denote measurements with an RQR 8 spectrum. The blue data is interpolated linearly. (b): Section from the data shown in (a) with the break-up point that denotes the point, where the normalized response for $H_p(10)$ undercuts the PTB limits (magenta circle) for an RQR 8 spectrum. The measurements are performed using the calibration method based on interpolation.

Fig. 7.7a shows the results for the big pixels for the measurements performed at the GeSa facility. The normalized $H_p(10)$ response is depicted as a function of the dose rate. Three measurements are performed for each adjusted dose rate for the RQR 8 spectrum and two measurements for the RQR 9 spectrum. The responses are calculated according to equ. 2.38. The data points denote the mean values, and the error bars represent the standard uncertainties of the means. Means and uncertainties are calculated from the responses measured at each adjusted dose rate. The blue data indicates measurements with the RQR 8 spectrum, and the red data measurements with the RQR 9 spectrum. Since there is a wide dose rate interval where no data for the RQR 9 spectrum is acquired, the red data points are not depicted with connecting lines. According to [25], the required dose rate value that is to be used for normalization is 1 $\frac{\mathrm{mSv}}{\mathrm{h}}$. Since measurements are not performed at this dose rate, the lowest mean dose rate at 0.063 $\frac{\mathrm{Sv}}{\mathrm{h}}$ for the RQR 8 spectrum and 0.087 $\frac{\mathrm{Sv}}{\mathrm{h}}$ for the RQR 9 spectrum are used for normalization. The normalized response remains stable for low dose rates and then rises up to a dose rate of about 35 $\frac{\mathrm{Sv}}{\mathrm{h}}$. After that, the normalized response declines. Both effects, the small increase and continuous decline towards higher dose rates of the normalized response, occur due to pile-up. Pile-up leads to an overlap of multiple individual charge signals in the pixel electronics that are interpreted as a single signal (see sec. 3.5). Instead of, for example, two single ToT values, only one with a higher value than the two individual ones is measured. This leads to measurements of false and also unrealistically high energies. Fig. 7.8 shows the number of counts in each energy bin for the first detector (blue), the second detector (red), and the third detector (black) for different dose rates applied with the RQR 8 spectrum. Since the RQR 8 spectrum is generated with a tube voltage of 100 kV, the photon energy is limited to 100 keV. Fig. 7.8a shows the distribution for a dose rate of 0.064 $\frac{\mathrm{Sv}}{\mathrm{h}}$. The maximum energy is not exceeded. This changes at a dose rate of 3.5 $\frac{\mathrm{Sv}}{\mathrm{h}}$ (see fig. 7.8c). The number of entries below 100 keV does not change significantly for all three detectors. However, the first and the second detector measure some entries in energy bins greater 100 keV. This effect increases with the dose rate until pile-up events dominate the measured spectrum. Since the energy bins correspond to individual conversion factors, the measured dose alters when the measured spectrum is changed by pile-up. This changes the response of the Dosepix dosemeter as well. The first data point that clearly shows such a change of the response is measured at a dose rate of about 35 $\frac{\mathrm{Sv}}{\mathrm{h}}$ (see fig. 7.7a). The point where the normalized response for the RQR 8 spectrum undercuts the lower PTB limit (further referred to as break-up point) is estimated using linear interpolation. Fig. 7.7b shows the section of fig. 7.7a with the break-up point (magenta circle). The break-up point is determined to be about 110.9 $\frac{\mathrm{Sv}}{\mathrm{h}}$. The measurements with the RQR 9 spectrum are mainly performed in a dose rate interval greater than the point where the normalized response undercuts the PTB limit. Therefore, an accurate determination of the break-up point for the RQR 9 spectrum is not possible. Compared to the RQR 8 spectrum, the data points of the RQR 9 spectrum seem to be shifted towards lower response values. A possible reason for this tendency is that pile-up is energy-dependent, and the applied spectra differ. The energy dependence of the break-up point is further investigated in sec. 7.2.

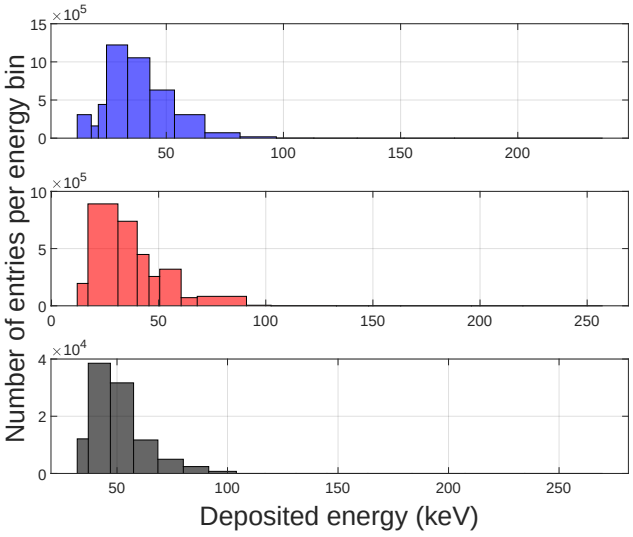

(a) $0.064\ \frac{\mathrm{Sv}}{\mathrm{h}}$

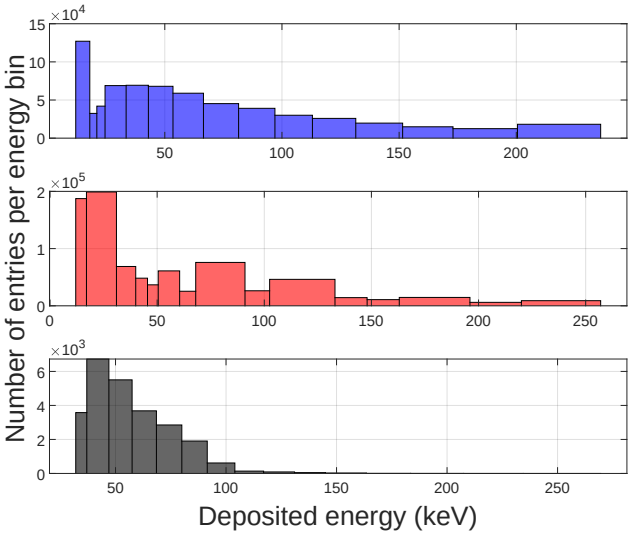

(b) $96\ \frac{\mathrm{Sv}}{\mathrm{h}}$

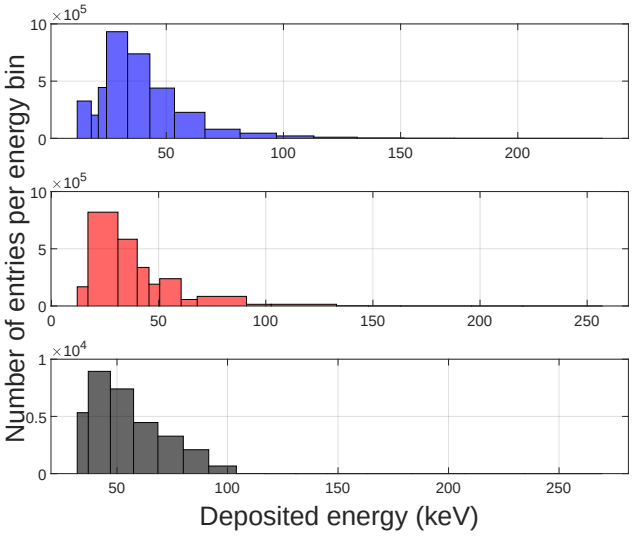

(c) $3.5\ \frac{\mathrm{Sv}}{\mathrm{h}}$

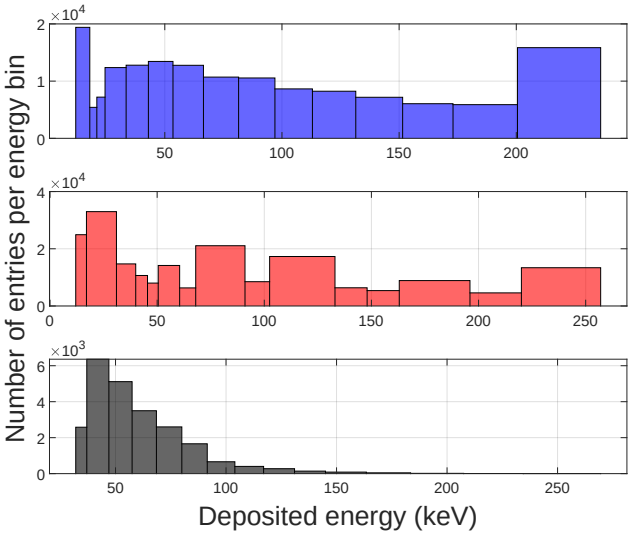

(d) $352\ \frac{\mathrm{Sv}}{\mathrm{h}}$

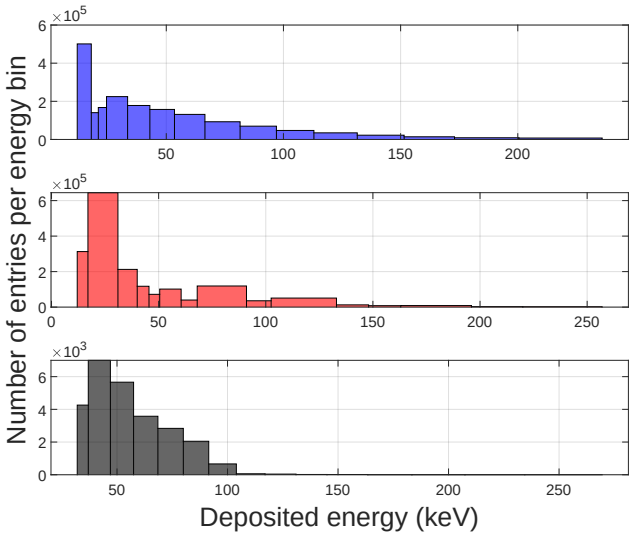

(e) $35\ \frac{\mathrm{Sv}}{\mathrm{h}}$

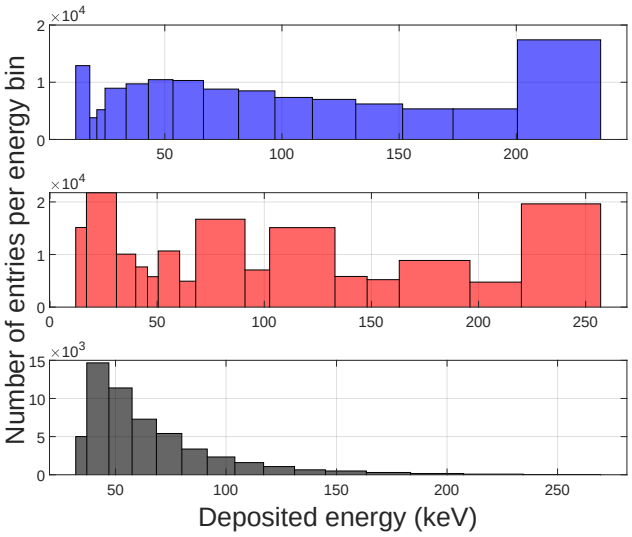

(f) $882\ \frac{\mathrm{Sv}}{\mathrm{h}}$

Figure 7.8 Energy response of the big pixels for the three detectors in Dosi-mode of measurements with an RQR 8 spectrum. Depicted are the number of entries per energy bin for the first (blue), second (red) and third (black) Dosepix detector as a function of the deposited energy for different dose rates. (a): $0.064\ \frac{\mathrm{Sv}}{\mathrm{h}}$, (b): $96\ \frac{\mathrm{Sv}}{\mathrm{h}}$, (c): $3\ \frac{\mathrm{Sv}}{\mathrm{h}}$, (d): $352\ \frac{\mathrm{Sv}}{\mathrm{h}}$, (e): $35\ \frac{\mathrm{Sv}}{\mathrm{h}}$, (f): $882\ \frac{\mathrm{Sv}}{\mathrm{h}}$. The measurements are performed using the calibration method based on interpolation.

A further effect caused by pile-up can be observed. Fig. 7.8e, fig. 7.8b and fig. 7.8d show an increased number of entries in the first two energy bins of the first and second Dosepix detectors, compared to fig. 7.8a. Here, charge signals that are too small to exceed the first energy bin edge or even the analogue threshold level accumulate. These pile-up signals can now exceed the first or even the second energy bin edge and contribute to the number of detected events in the lower energy bins. This effect is so significant because a large part of the deposited energy spectrum is located below the lowest energy bin edge of 12 keV.

7.1.4 Results for the small pixels

In the following, the performance of the small pixels is briefly evaluated as well. Since the small pixels are not calibrated with the interpolation method, only the energy calibration for the traditional model is used. Fig. 7.9 shows the normalized response for $H_p(10)$ for the small pixels as a function of the mean energy of the applied spectra for the A-series, the radioactive sources, measurements performed under certain irradiation angles, and the C-60 spectrum. Similar to the measurements with the big pixels, the means and standard uncertainties of the means are calculated using equ. 2.38, equ. 6.11 and equ. 6.10. The data for the A-series and the radioactive sources are normalized to the response of ^{137}Cs. The data for the measurements under irradiation angles is normalized to the responses measured for the same spectrum under an angle of incidence of 0°. The variation is larger than for the big pixels since the number of detected photons decreases with a smaller active pixel area. This results in a smaller measurement statistics and, therefore, a higher uncertainty of the mean.

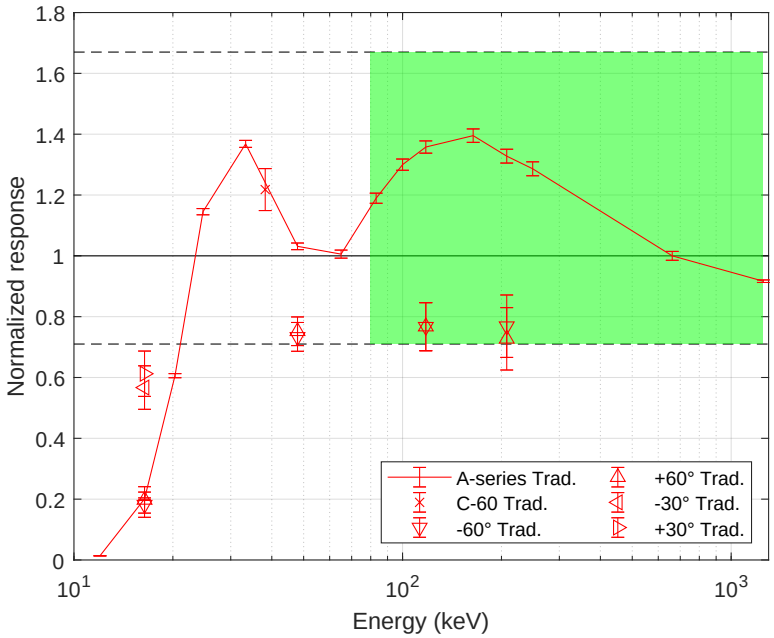

Figure 7.9 (a): Normalized response for $H_p(10)$ for the small pixels as a function of the mean energy of the applied spectra for perpendicular irradiation (solid lines) and irradiation under angles of ± 30° and ± 60°. The black dashed lines indicate the upper and lower PTB limit on the normalized response and the green area the required energy range within this allowed response range. The measurements are performed using the traditional calibration model.

However, the PTB requirements are fulfilled for perpendicular irradiation and angles of $\pm 60°$. The normalized response for low energies tends towards zero and rises with increasing energy. The normalized response enters the PTB limits and stays within them for energies higher than about $E = 21.1\,\mathrm{keV}$. This lowest response value that resides within the allowed limits is even lower than the one measured for the big pixels for $H_\mathrm{p}(10)$. The dose reconstruction with the small pixels is also tested in pulsed radiation fields. Fig. 7.10 shows the normalized $H_\mathrm{p}(10)$ response of the small pixels for the RQR 8 spectrum (blue) and the RQR 9 spectrum (red) as a function of the applied dose rate. The data for the RQR 8 spectrum is normalized to the response value acquired at a dose rate of $0.063\,\frac{\mathrm{Sv}}{\mathrm{h}}$ and the data for the RQR 9 spectrum to the response value acquired at $0.087\,\frac{\mathrm{Sv}}{\mathrm{h}}$. The magenta circle denotes the break-up point where the normalized response for the RQR 8 undercuts the allowed PTB limits (black dashed lines). This point is calculated the same way as for the data for the big pixels shown in fig. 7.7. The break-up point is determined to be $184.9\,\frac{\mathrm{Sv}}{\mathrm{h}}$. Here, similar to the data of the big pixels, the RQR 9 spectrum is shifted towards lower response values.

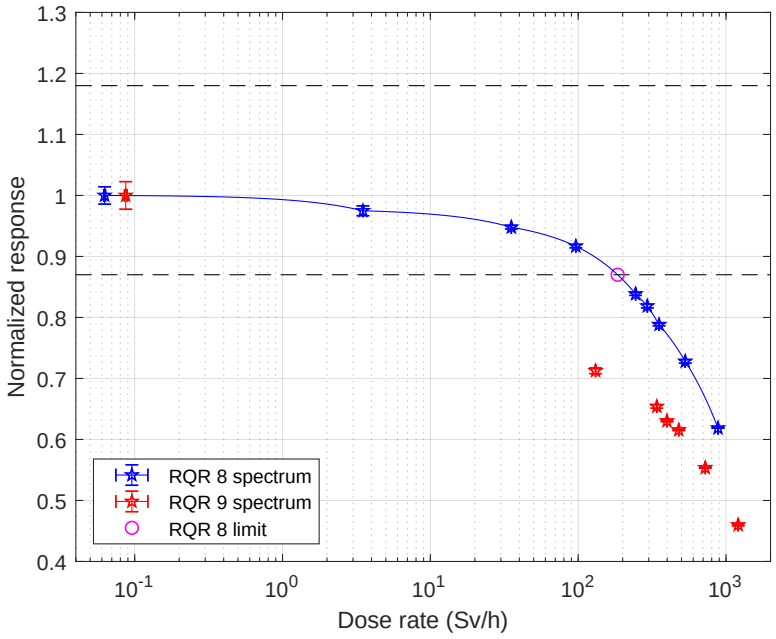

Figure 7.10 Normalized $H_\mathrm{p}(10)$ response for small pixels as a function of the dose rate. The red data points denote measurements with an RQR 9 spectrum, the blue data points measurements with an RQR 8 spectrum. The blue data is interpolated linearly. The break-up point, where the normalized response undercuts the lower PTB limit is depicted in magenta.

7.1.5 Conclusion

The Dosepix dosemeter was investigated concerning its performance with different energy calibrations. The main goal was to examine if the performance of the Dosepix dosemeter can be significantly improved by using an energy calibration method that describes the transformation from ToT to energy more accurately than the traditionally used model. It was shown that a dose determination within the PTB limits on the normalized response and the energy is possible for both methods, the traditional one and the one based on interpolation, for energies between abour 32 keV and 1250 keV for $H_\mathrm{p}(10)$ and between about 29 keV and 1250 keV for $H_\mathrm{p}(0.07)$ for the big pixels.

Both methods show very similar results. The big pixels show a good performance concerning the A-series, irradiation under angles of $\pm 60°$, a C-60 spectrum, and the relative statistical error. All tested PTB requirements are fulfilled. It was shown that variations in the energy calibration do not play a major role concerning the measured response. Even though the calibration curves deviate over 5 % for some pixels (see fig. 4.13a), the energy-dependent response remains stable. The performance of the small pixels shows a stronger variation. However, the mean normalized responses stay within the allowed limits in an energy range of about 21 keV to 1250 keV for $H_\mathrm{p}(10)$. The data taken at GeSa show that the normalized response for an RQR 8 spectrum does not undercut the PTB limit up to about 111 $\frac{\mathrm{Sv}}{\mathrm{h}}$ for the big pixels and about 185 $\frac{\mathrm{Sv}}{\mathrm{h}}$ for the small pixels, which is a good result in comparison to the other active personal dosemeters outlined in sec. 2.3.3. Here, the highest upper limit on the dose rate as given by the manufacturers is 12 $\frac{\mathrm{Sv}}{\mathrm{h}}$ (see tab. 2.5). Additionally, the performance of the Dosepix dosemeter for increased dose rates with high energies is better as well. Fig. 7.11 shows the normalized response for a ^{60}Co radiation source as a function of the dose rate for the big pixels (black) and the small pixels (red). The means and standard uncertainties of the means are calculated using equ. 2.38, equ. 6.11 and equ. 6.10. The data is normalized to the response value with the smallest applied dose rate for both pixel sizes. The normalized response starts to decline at about 10 $\frac{\mathrm{Sv}}{\mathrm{h}}$ and does not undercut the allowed limits at a maximum tested dose rate of about 30 $\frac{\mathrm{Sv}}{\mathrm{h}}$. Higher dose rates could not be achieved with the used ^{60}Co source since the Dosepix dosemeter could not be placed any closer to the source. However, all test measurements conducted in this chapter show that the Dosepix dosemeter is suited for active personal dosimetry in continuous and pulsed radiation fields. During the making of this thesis, further data that show the good performance of the Dosepix dosemeter in continuous radiation fields [30] and pulsed radiation fields [31] was published by the Dosepix workgroup.

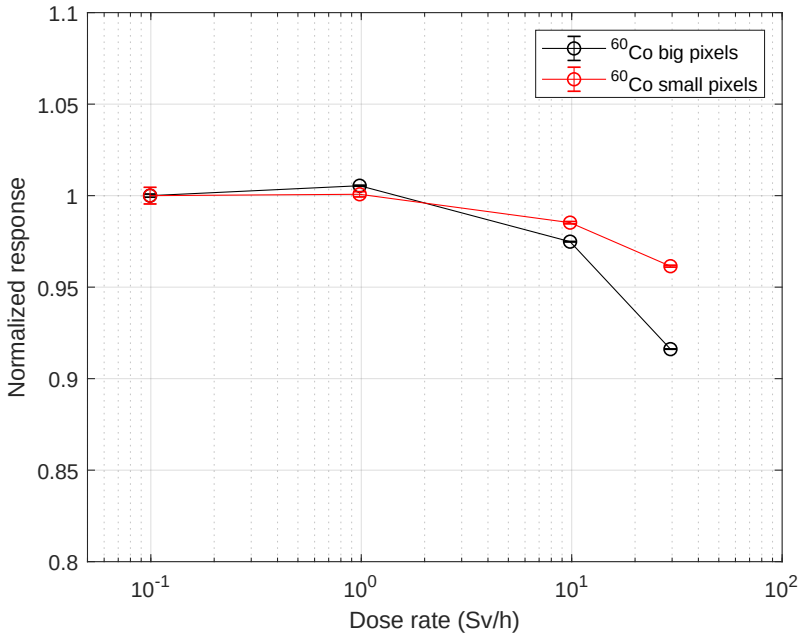

Figure 7.11 Normalized $H_\mathrm{p}(10)$ response for a ^{60}Co source as a function of the dose rate for the big (black) and the small (red) pixels.

7.2 Energy dependence of the break-up point

As mentioned above, the data in fig. 7.7a and fig. 7.10 for the RQR 9 spectrum is shifted towards lower response values compared to the response for the RQR 8 spectrum. This shift alters the point of intersection of the normalized response curve with the PTB limits (break-up point). In the following, the dependence of this point on the energy of the applied spectrum is investigated. This dependence is motivated by the correlation of pile-up with the deposited energy. Pile-up increases the deposited energy additively and, therefore, linearly with the number of detected monoenergetic photons. However, the measured dose does not increase linearly with the deposited energy. It is possible that multiple photons with low energies that cause pile-up in the Dosepix electronics deposit the same energy as a single photon with a higher energy. Therefore, the measured doses in the pile-up case deviate from the measured doses in the non-pile-up case. Additional measurements are performed at Erlangen University to investigate a possible energy dependence of the applied photon spectra and the break-up point. Here, two different settings of I_{Krum} are investigated. The instance that a higher I_{Krum} might decrease the effects of pile-up is motivated by the lower width of the analogue signals in the pixel electronics. A higher I_{Krum} leads to a shorter decay time of the falling edge of the charge signal. The probability that multiple signals overlap correlates to the signal duration. Therefore, a higher I_{Krum} should reduce pile-up and might increase the dose rate at which the normalized response undercuts the PTB limit.

The measurements were performed together with a bachelor's student, whom I have supervised during her work on her thesis [56]. Only the big pixels and $H_{\mathrm{p}}(10)$ as dose quantity are considered in the following.

7.2.1 Preparatory measurements

In this experiment, the response is investigated for different applied dose rates and different energy spectra. The setup and procedure of the experiment are designed to maximize the applied dose rate. Here, the dose rate is varied by changing the current I of the utilized X-ray tube [44] or by changing the distance d between the Dosepix dosemeter and the X-ray tube. The photon flux Φ is assumed to increase linearly with the tube current. Therefore, the applied dose H and the applied dose rate $\dot{H}$ are assumed to increase linearly with the current as well

$$\Phi \propto I \Rightarrow H, \dot{H} \propto I. \tag{7.3}$$

The photon flux, the dose and the dose rate are assumed to increase with decreasing distance d via the inverse square law

$$\Phi \propto \frac{1}{d^2} \Rightarrow H, \dot{H} \propto \frac{1}{d^2}. \tag{7.4}$$

The minimum distance between the Dosepix dosemeter and the X-ray tube is the distance where all three Dosepix detectors are still fully illuminated. The radiation profile of the X-ray tube is scanned to calculate this distance. Fig. 7.12 show schematics of the setup used to examine the radiation profile in the horizontal (a) and vertical (b) direction. A semiconductor sensor (further referred to as RQX-sensor [57]) is used to measure the dose rate (air kerma per time) under varying angles α in horizontal and α' in vertical direction. This dose rate is not measured with a slab phantom and is only used to scan the radiation profile of the X-ray tube.

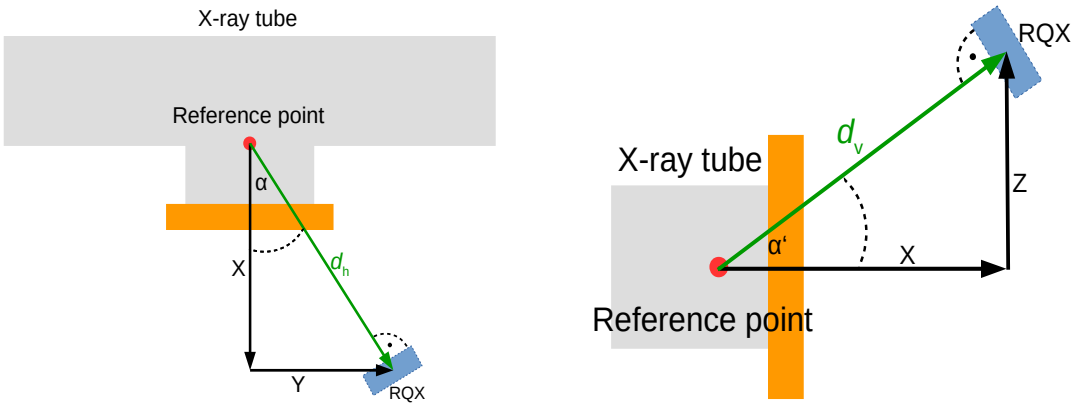

(a) Horizontal setup **(b)** Vertical setup

Figure 7.12 (a): Top view of the setup. (b): Side view of the setup. The RQX-sensor [57] is moved along the Y- / Z-axis to scan the radiation profile of the X-ray tube.

The angle is varied by changing Y (Z in vertical direction) for a fixed X. Since the distance changes according to

$$d_{\mathrm{h}} = \sqrt{\mathrm{X}^2 + \mathrm{Y}^2} \tag{7.5}$$

in horizontal and

$$d_{\mathrm{v}} = \sqrt{\mathrm{X}^2 + \mathrm{Z}^2} \tag{7.6}$$

in vertical direction, the measured dose rate is weighted with a factor of $\frac{1}{d^2}$. X is chosen to be 54 cm for the horizontal measurements and 49 cm for the vertical measurements. α and α' are determined via

$$\alpha(\mathrm{X}, \mathrm{Y}) = \arctan\left(\frac{\mathrm{Y}}{\mathrm{X}}\right) \tag{7.7}$$

in horizontal and

$$\alpha'(\mathrm{X}, \mathrm{Z}) = \arctan\left(\frac{\mathrm{Z}}{\mathrm{X}}\right) \tag{7.8}$$

in the vertical direction. α' ranges from about $-17°$ to $17°$ and α from $-25°$ to $25°$. All measurements are performed five times in horizontal and three times in vertical direction for every angle and for two tube voltages of 40 kV and 120 kV. Fig. 7.13a and fig. 7.13b show the relative dose rates as a function of α and α'. The data is normalized to the dose rate measured at angles of $\alpha = 0°$ and $\alpha' = 0°$ for 40 kV and 120 kV, respectively. The error bars denote the standard uncertainties of the means. A scan of the tube profile shows deviations between the applied voltages in the horizontal direction. It can also be seen that the opening angle in the vertical direction is larger than in the horizontal direction. Therefore, in later experiments, the Dosepix dosemeter is placed in front of the X-ray tube such that the detectors are arranged in vertical direction. A fine scanning of the tube profile in vertical direction is performed. Here, at about $-11°$ and $10°$, the dose rate decreases rapidly. This is due to internal shielding and collimation of the X-ray tube. A conservative estimate of the opening angle of $18°$ (from $-9°$ to $9°$) is used for further analysis. The Dosepix detectors are arranged over a distance of 6.0 cm on the readout-board (see fig. 3.3). The minimum distance d_{min} the Dosepix dosemeter can be placed in front of the X-ray tube such that the Dosepix detectors are still fully illuminated is calculated via

$$d_{\mathrm{min}} = \frac{\frac{6\,\mathrm{cm}}{2}}{\tan\left(\frac{18°}{2}\right)} \approx 19\,\mathrm{cm}. \tag{7.9}$$

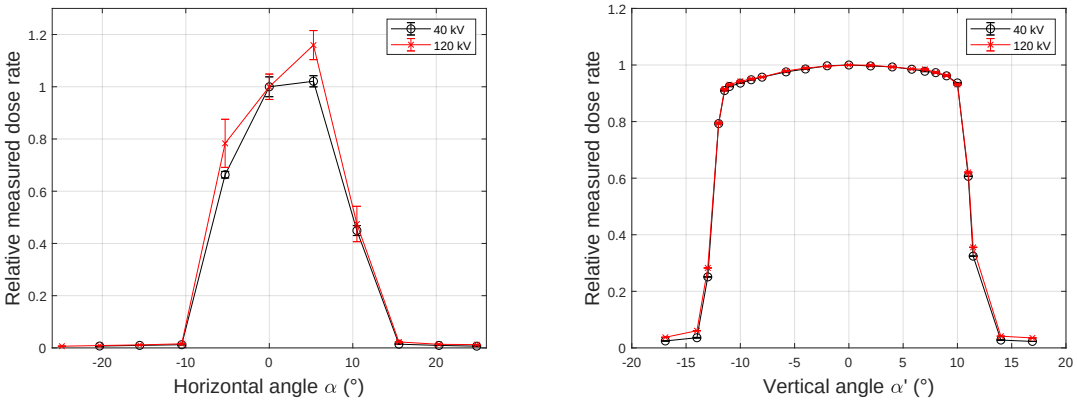

(a) Horizontal radiation profile

(b) Vertical radiation profile

Figure 7.13 Relative measured dose rates as a function of the horizontal (a) and vertical (b) angle. The error bars denote the standard uncertainties of the means. The curves are normalized to the dose rates measured at 0° respectively. The black curves show the measurements for a tube voltage of 40 kV and the red curves for a tube voltage of 120 kV.

For practical reasons, the smallest adjusted distance is 22.5 cm. Fig. 7.13b further shows that the radiation intensity is not equally distributed over the opening angle. For example, the measured dose rate at an angle of −9° drops to about 94.8 % compared to an angle of 0°. Since the individual Dosepix detectors are spatially distributed over the Dosepix dosemeter and are illuminated under different angles, the radiation profile is used to correct the intensity of the incoming radiation per detector. No correction needs to be applied to the second detector since it always resides in the center of the beam. The irradiation angles under which the center of the two outer Dosepix detectors are illuminated are calculated depending on the distance between the Dosepix dosemeter and the X-ray tube. The distance between the centers of two neighboring detectors is 1.9 cm. The angles $\alpha_{1(3)}$, under which the centers are illuminated, are expressed as

$$\alpha_{1(3)} = \pm \arctan\left(\frac{1.9\,\mathrm{cm}}{\mathrm{X}}\right), \tag{7.10}$$

where X denotes the distance from the Dosepix dosemeter to the X-ray tube. Two correction factors, $C_1(\mathrm{X})$ and $C_3(\mathrm{X})$, are derived for the first and the third detector. The data shown in fig. 7.13b is linearly interpolated and provides relative dose rates for α_1 and α_3 that correspond to X. These relative dose rates denote the fraction of maximum radiation intensity. The total number of measured entries in all energy bins N_1 and N_3 of the first detector and the third detector is divided by the factors respectively to gain the corrected number of entries N_1^{corr} and N_3^{corr}

$$N_{1(3)}^{\mathrm{corr}} = \frac{N_{1(3)}}{C_{1(3)}}. \tag{7.11}$$

Only the data for 120 kV is used for the correction since there is no significant difference between the relative dose rates measured with a tube voltage of 40 kV and 120 kV within an angle interval of ± 9°.

7.2.2 Reference dose determination

X-ray tube voltage (kV)	Mean energy (keV)	Normalized Response
40	25.97	1.050
50	30.12	1.064
60	33.90	1.073
70	37.34	1.080
80	40.80	1.084
90	43.91	1.087
100	46.67	1.087
110	49.19	1.085
120	51.52	1.080

Table 7.1: Normalized $H_p(10)$ responses of the used reference dosemeter (column 3) for the mean energies (column 2) determined from simulations of the used X-ray spectra [58]. Column 1 lists the corresponding X-ray tube voltages.

A reference dose is necessary to calculate the response of the Dosepix dosemeter for the applied dose of an initial photon field. Therefore, a second Dosepix dosemeter that has already been evaluated in a type test at PTB is used to measure the reference dose [59]. This dosemeter is placed onto a slab phantom at a fixed distance of 186.9 cm. The dose is measured for an irradiation time of 20 s. The time is not measured automatically. Instead, a program is used to switch the X-ray tube on and, after a waiting time of 20 s, off again. This method might include uncertainties due to delays in the data transfer to the X-ray tube. Therefore an uncertainty of 0.1 s on the time measurement is assumed. The tube voltage is varied from 40 kV to 120 kV in steps of 10 kV. The tube current is varied between 1 mA and 16 mA. The measured dose and its standard uncertainties of the means are calculated according to equ. 6.9 and equ. 6.10. Here, the deviation that arises from angular irradiation of the two outer Dosepix detectors is corrected as explained in sec. 7.2.1. In addition, the calculated dose is further corrected using the normalized response R_{ref} from the type test evaluation that was performed with the reference dosemeter. The mean energy of each applied spectrum is calculated since the response is energy-dependent. The energy spectra of the utilized X-ray tube are simulated with [58]. The mean energy and the corresponding normalized responses are listed in tab. 7.1. The corrected reference dose H_0 is calculated via

$$H_0 = \frac{H_{\mathrm{meas}}}{R_{\mathrm{ref}}} \tag{7.12}$$

for each energy spectrum respectively.

Fig. 7.14 shows the dose rates of the individual measurements as a function of the X-ray tube current for all applied tube voltages. The dose rate is calculated according to equ. 2.37. The standard uncertainty of the mean dose rate is calculated using error propagation. The lines denote linear functions calculated from the data point at 1 mA and the origin for each voltage, respectively. The dose rate increases linearly with the tube current as well, assuming proportionality between the tube current and the number of emitted photons. This is only valid for currents up to 6 mA for most voltages. As outlined in sec. 7.1.3, pile-up leads to an underestimation of the dose and, therefore, the dose rate as well. At a tube current of 1 mA pile-up has the smallest effect on the measured dose. Therefore, the calculated reference dose is based on this measurement for each applied voltage. The two assumptions outlined in equ. 7.3 and equ. 7.4 are made to calculate the dose rate that is applied with a certain tube voltage U and a tube current I in a certain distance d.

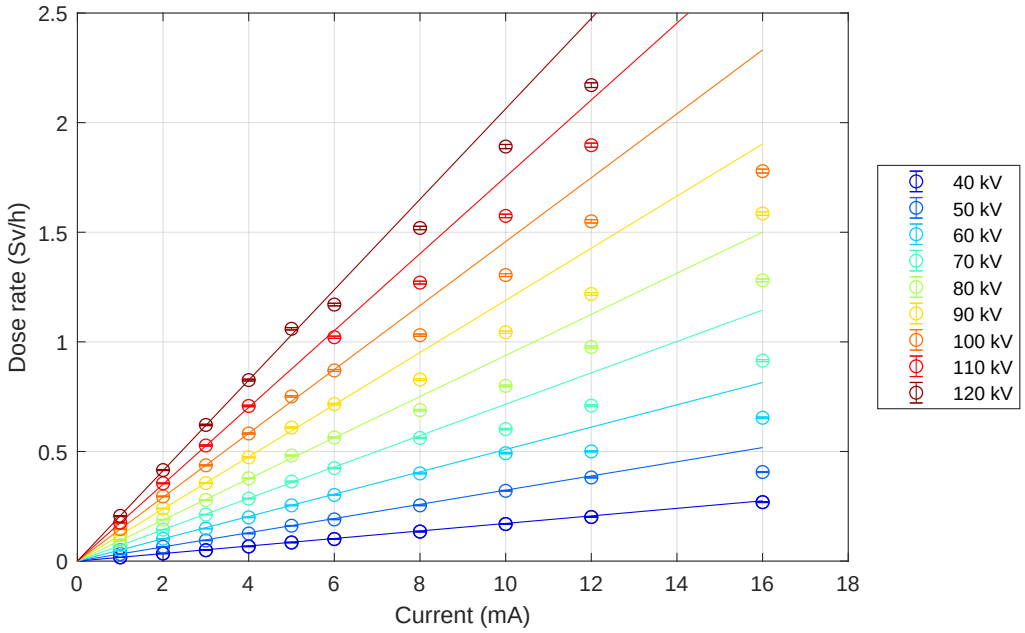

Figure 7.14 Measured dose rate as a function of the adjusted X-ray tube current for different X-ray tube voltages. The lines denote linear extrapolations between the origin and the first data point of each voltage.

The dose rate $\dot{H}_0(U, I, d)$ for arbitrary I and d is calculated for each U via

$$\dot{H}_0(U, I, d) = \dot{H}_0(U) \cdot \left(\frac{186.9\,\text{cm}}{d} \right)^2 \cdot I. \tag{7.13}$$

from the reference dose rate $\dot{H}_0(U)$ that is measured in a distance of 186.9 cm with a tube current of 1 mA.

7.2.3 Pile-up measurements

The pile-up measurements are performed without a slab phantom since it could not be fully illuminated at small distances. However, the influence of the slab phantom does not need to be taken into account since the data is later normalized in the analysis. The measurements are conducted in 28 different distances ranging from 22.5 cm to 257.5 cm. Measurements with a tube current of 1 mA are conducted at all distances. A systematic uncertainty of 0.3 cm is assumed for the measurements on the distance. Additionally, 21 different tube currents that range from 1 mA up to 60 mA are applied at a distance of 22.5 cm. The highest tube currents are only applied for the lowest tube voltages. The irradiation time cannot be set to 20 s as it is done for the reference dose measurements. An exposure this long would cause a total appliance of about 3.2 Sv for the highest measured dose rate. At these high doses, a possible damage of the Dosepix dosemeter cannot be ruled out. Therefore, the irradiation time is set to 0.5 s to prevent damage and to create equal conditions for all measurements. This is done using the program as described in sec. 7.2.2. The uncertainty of the measurement time (0.1 s) at this short exposure is too high to be neglected. Therefore, the time is measured in parallel to the dose using the RQX-sensor. During the measurements, the sensor is placed within the radiation field. Fig. 7.15 shows the measured times as a function of the distance between the Dosepix dosemeter and the X-ray tube for the applied tube voltages.

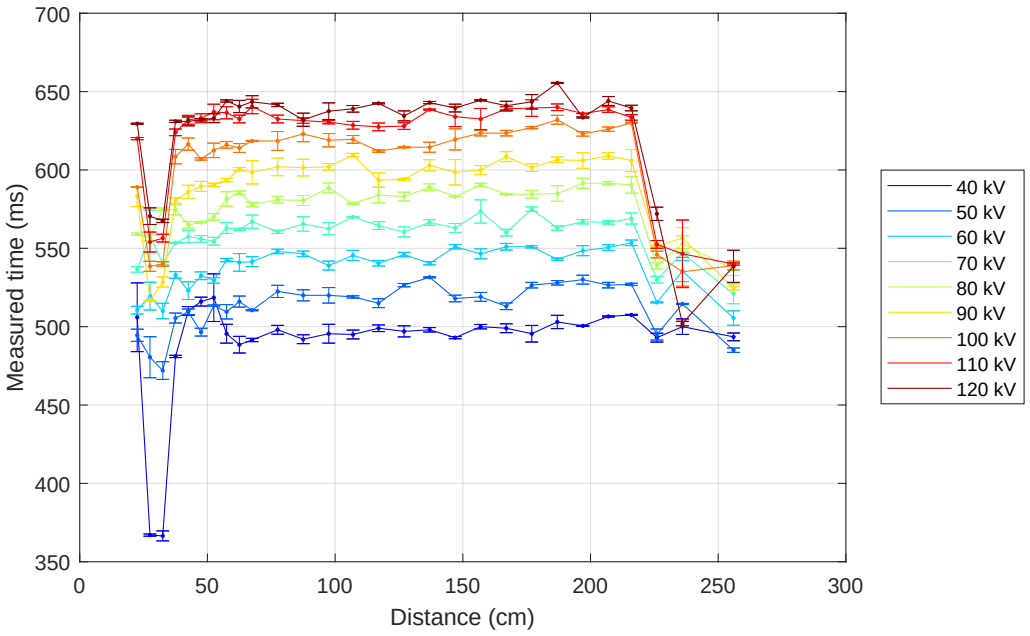

Figure 7.15 Irradiation times measured with the RQX-sensor as a function of the distance between the Dosepix dosemeter and the X-ray tube for different tube voltages.

Each measurement is performed with two different settings of I_{Krum}. Therefore, two time measurements with the RQX-sensor are performed for each distance and applied X-ray tube voltage. The error bars denote the standard deviations. The time measurement depends on the applied tube voltage. The discontinuity for small distances occurs because the RQX-sensor could not be properly placed in the radiation field without being blocked by the Dosepix dosemeter. The discontinuity for large distances can be explained by misplacement of the RQX-sensor as it probably did not face the X-ray tube perpendicularly. In additional measurements, the anode current of the tube is recorded using an oscilloscope to investigate whether the voltage dependence is caused by the RQX-sensor or the X-ray tube. Fig. 7.16 shows the measured anode signal for pulses with a nominal duration of 0.5 s. The anode signal stays above zero for longer than the set 0.5 s. This indicates that the radiation time is voltage-dependent. Therefore, the time measured by the RQX-sensor is used for further evaluation. Since the time measurements for small and large distances are not reliable, the mean time for each applied voltage in a range between 50 cm and 210 cm is used for all other distances. Generally, the time measurement is not very important as long as it is consistent for one applied voltage since the response is normalized to the same value for each voltage. The dose and its standard uncertainty of the mean are calculated according to equ. 6.9 and equ. 6.10. Some pixels could not be calibrated for an I_{Krum} of 11 nA and are excluded in the analysis. Therefore, the sum of the entries in each energy bin in the remaining pixels is scaled to 192 for the big pixels. Since the measurement durations t_{i}^{0} of the reference doses H_{i}^{0} and the measurement durations t_{i} of the test doses H_{i} are different, the calculated responses are scaled with the ratio of the measurement times. The response is then calculated by dividing the measured dose rates

$$R = \frac{H_{\mathrm{i}}}{H_{\mathrm{i}}^{0}} \cdot \frac{t_{\mathrm{i}}^{0}}{t_{\mathrm{i}}} = \frac{\frac{H_{\mathrm{i}}}{t_{\mathrm{i}}}}{\frac{H0_{\mathrm{i}}}{t_{\mathrm{i}}^{0}}} = \frac{\dot{H}_{\mathrm{i}}}{\dot{H}_{\mathrm{i}}^{0}}. \tag{7.14}$$

According to [25], the response in pulsed radiation fields is supposed to be normalized to the response measured at 1 $\frac{\mathrm{mSv}}{\mathrm{h}}$. No measurements at a dose rate this low are performed.

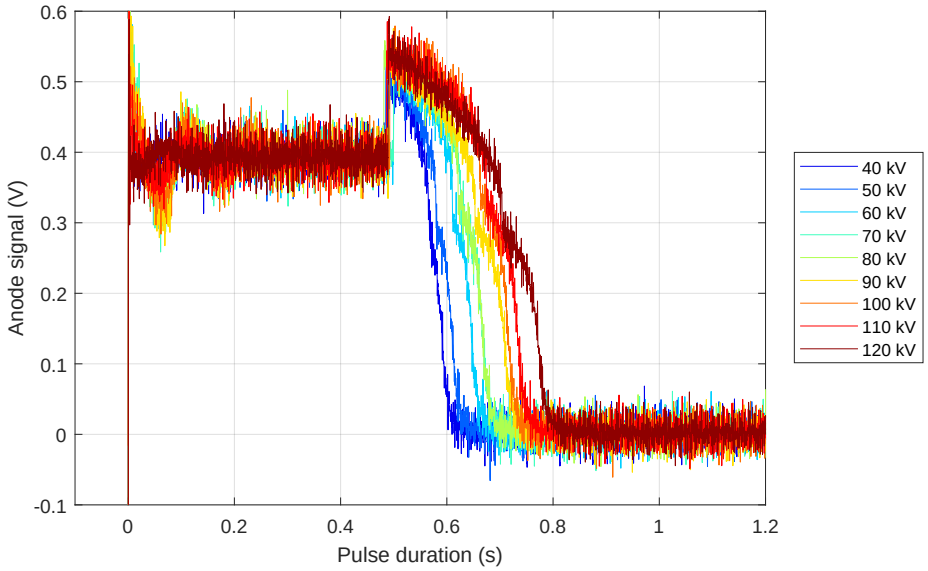

Figure 7.16 Time-dependent anode signal of the X-ray tube for different tube voltages and a nominal pulse duration of 0.5 s.

Instead, all responses are normalized to the mean response of the five lowest measured dose rates for each applied voltage, respectively.

7.2.4 Results

Fig. 7.17 shows the normalized responses of measurements with an I_{Krum} of 2.2 nA. The error bars denote the standard uncertainties of the means, and the error bands represent the systematic uncertainties of the measurement of the distance between the Dosepix dosemeter and the X-ray tube. Here, the systematical uncertainty is calculated assuming the maximum deviation from the measured distance. The upper limit on the reference dose rate is, therefore, calculated using

$$d^{\mathrm{up}} = d + 0.3\,\mathrm{cm} \tag{7.15}$$

as distance and the lower limit on the reference dose rate using

$$d^{\mathrm{low}} = d - 0.3\,\mathrm{cm} \tag{7.16}$$

in equ. 7.13. However, the error bars and the error band are too small to be visualized. All curves rise a little before they decline with increasing dose rate. As explained in sec. 7.1.3, the decline at higher dose rates originates from pile-up. The initial rise is also explained by pile-up but might partially originate from scattering from the walls and other equipment placed on the same lab table as the Dosepix dosemeter. As the distance between the Dosepix dosemeter and the X-ray tube varies, the contribution of scattered photons varies as well. The black dashed lines denote the PTB limits on the normalized response for pulsed radiation (0.87 and 1.18 [25]). The magenta circle denotes the point where each response curve undercuts the lower PTB limit on the normalized response (introduced as break-up point in sec. 7.1.3). The break-up point is determined via linear interpolation between the last data points. Both, the standard uncertainty of the mean and the systematical uncertainty originate from linear interpolation between the standard uncertainties on the means of the data points and their systematic uncertainties.

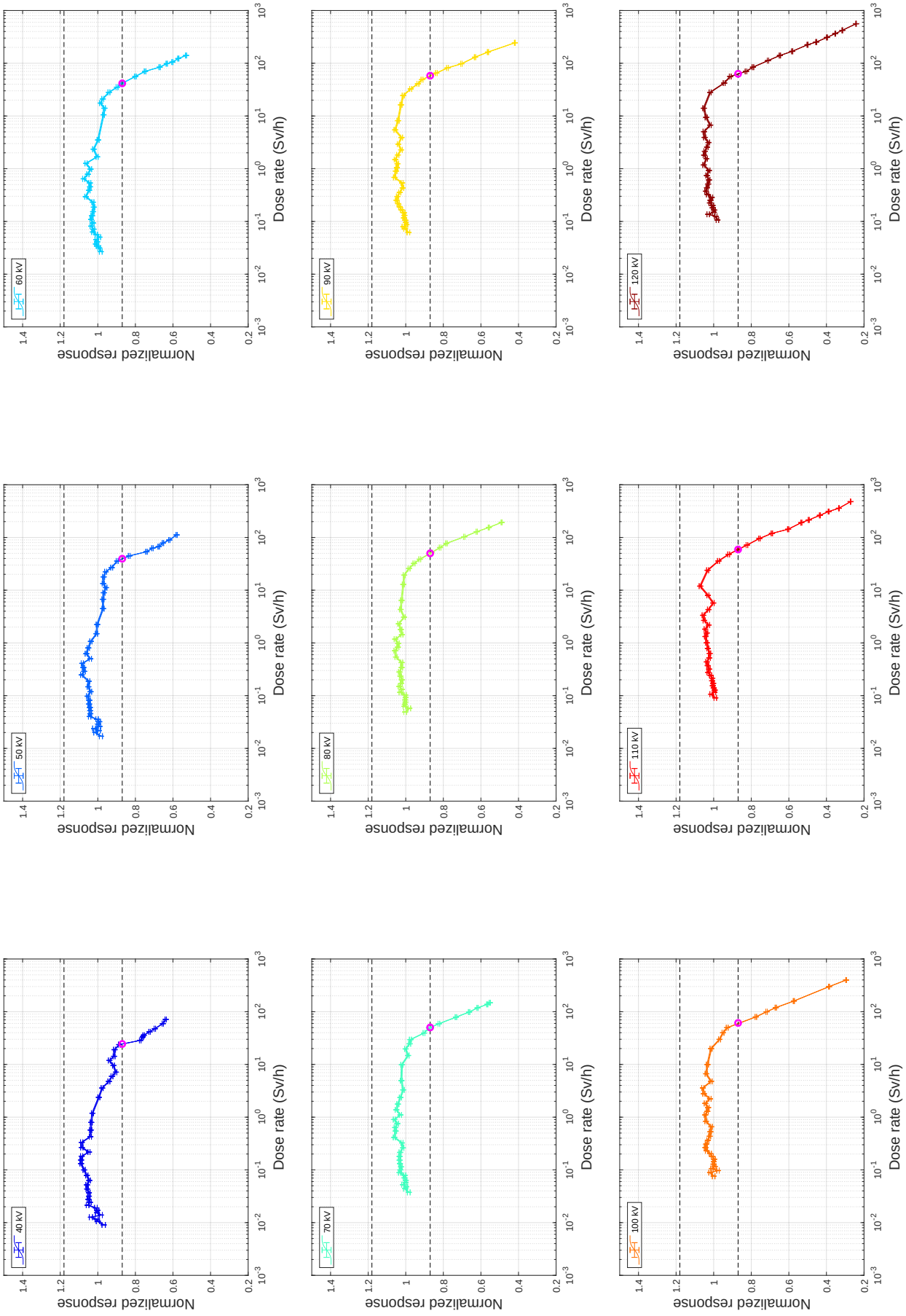

Figure 7.17 Normalized response for the big pixels and measurements with an I_{Krum} of 2.2 nA as a function of the dose rate for different X-ray tube voltages. The black dashed lines indicate the PTB limits on the normalized response. The magenta circles denote the points, where the response curves undercut the lower limit (break-up point).

Fig. 7.18 shows the break-up dose rates for the measurements with an I_{Krum} of 2.2 nA as a function of the mean energy of the applied spectra. The error bars denote the standard uncertainties of the means. The systematic uncertainty is depicted via the band around the mean values. The red data point denotes the break-up dose rate from measurements at PTB with an RQR 8 spectrum (see sec. 7.1.3). As presumed, the break-up dose rate changes with the applied tube voltage. However, there is a large difference between the measurements taken in Erlangen and the RQR 8 spectrum. The main reason for this deviation is the difference in the applied spectra. The RQR 8 spectrum is filtered with 3.32 mm aluminum, while the experiments in Erlangen are conducted without additional filters. This leads to a difference in the low-energy parts of the spectra. Especially low energies play an important role for pile-up since the PDE of the first and second Dosepix detectors rise with decreasing energy (see fig. 3.16). A further contribution could be an inaccurate reference dose for the measurements in Erlangen. The response values that are used to correct the measured reference dose (see tab. 7.1) are derived from measurements with A-series spectra at PTB [59]. The A-series spectra are strongly filtered and very narrow, unlike the spectra that are applied here in the measurements. This difference can have an impact on the calculated reference dose.

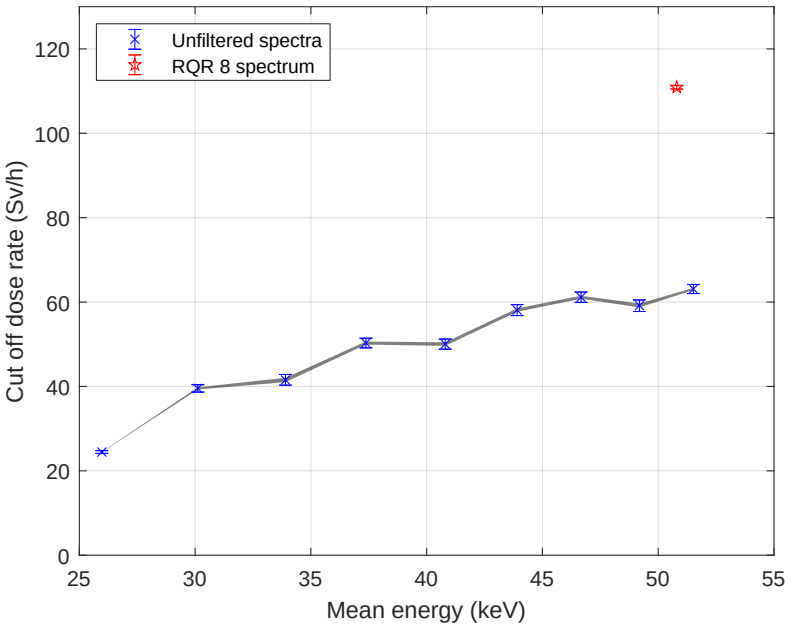

Figure 7.18 Break-up dose rates of the measurements with unfiltered spectra (blue) and an RQR 8 spectrum (red) as a function of the mean energy of the applied spectra. The error bars denote the standard uncertainties of the means and the error band the systematic uncertainties that originate from the measurement of the distance between the Dosepix dosemeter and the X-ray tube. I_{Krum} is set to 2.2 nA.

Fig. 7.19 shows the count rate per pixel for each Dosepix detector as a function of the applied dose rate for the measurements at PTB with the RQR 8 spectrum in blue, the RQR 9 spectrum in red, and the Erlangen measurements (see color bar). The RQR 8 spectrum (kVp = 100 kV) follows the same course as the unfiltered spectrum with an applied voltage of 100 kV in good accordance for the Dosepix detector filtered with the tin cap (fig. 7.19(c)). This is because the difference of the aluminum filtrations from the X-ray tubes play a minor role in comparison to the 1 mm thick tin filter. In contrast to the tin-filtered Dosepix detector, the count rate for the unfiltered detector (fig. 7.19(a)) and the Dosepix detector with aluminum filter (fig. 7.19(b)) decreases with increasing X-ray tube voltage because low energies are more dominant. As expected, this effect is stronger in fig. 7.19(a) than in fig. 7.19(b). The RQR 9 spectrum (kVp = 120 kVp) is only measured for two dose rates below 132 $\frac{\mathrm{Sv}}{\mathrm{h}}$. The count rate as a function of the applied dose rate is therefore insufficiently resolved, and a valid comparison to the other spectra cannot be performed.

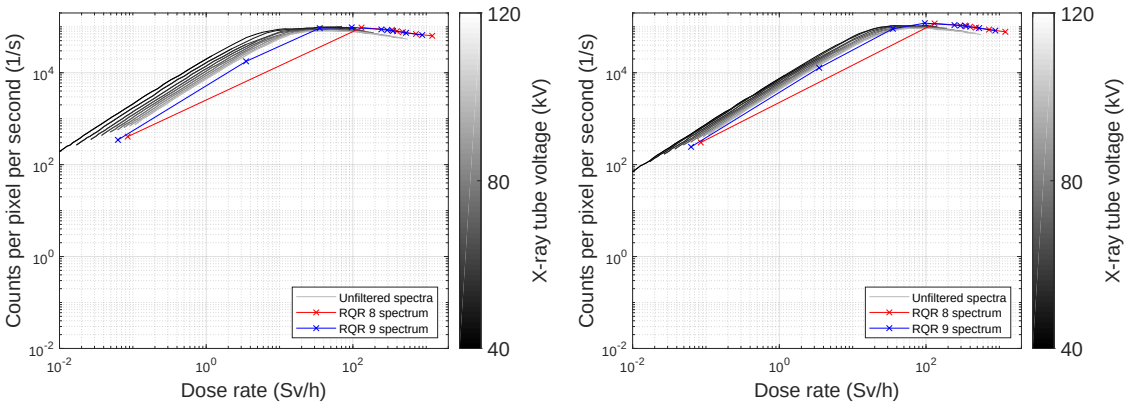

(a) First detector (Free) **(b)** Second detector (Al)

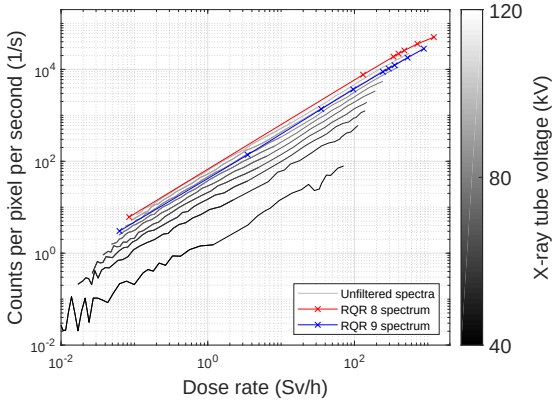

(c) Third detector (Sn)

Figure 7.19 Count rate per pixel as a function of the applied dose rate. The gray lines denote the measurements with unfiltered spectra (see color code), the red data points measurements with the RQR 9 spectrum and the blue data points measurements with the RQR 8 spectrum. (a): First detector, (b): Second detector, (c): Third detector.

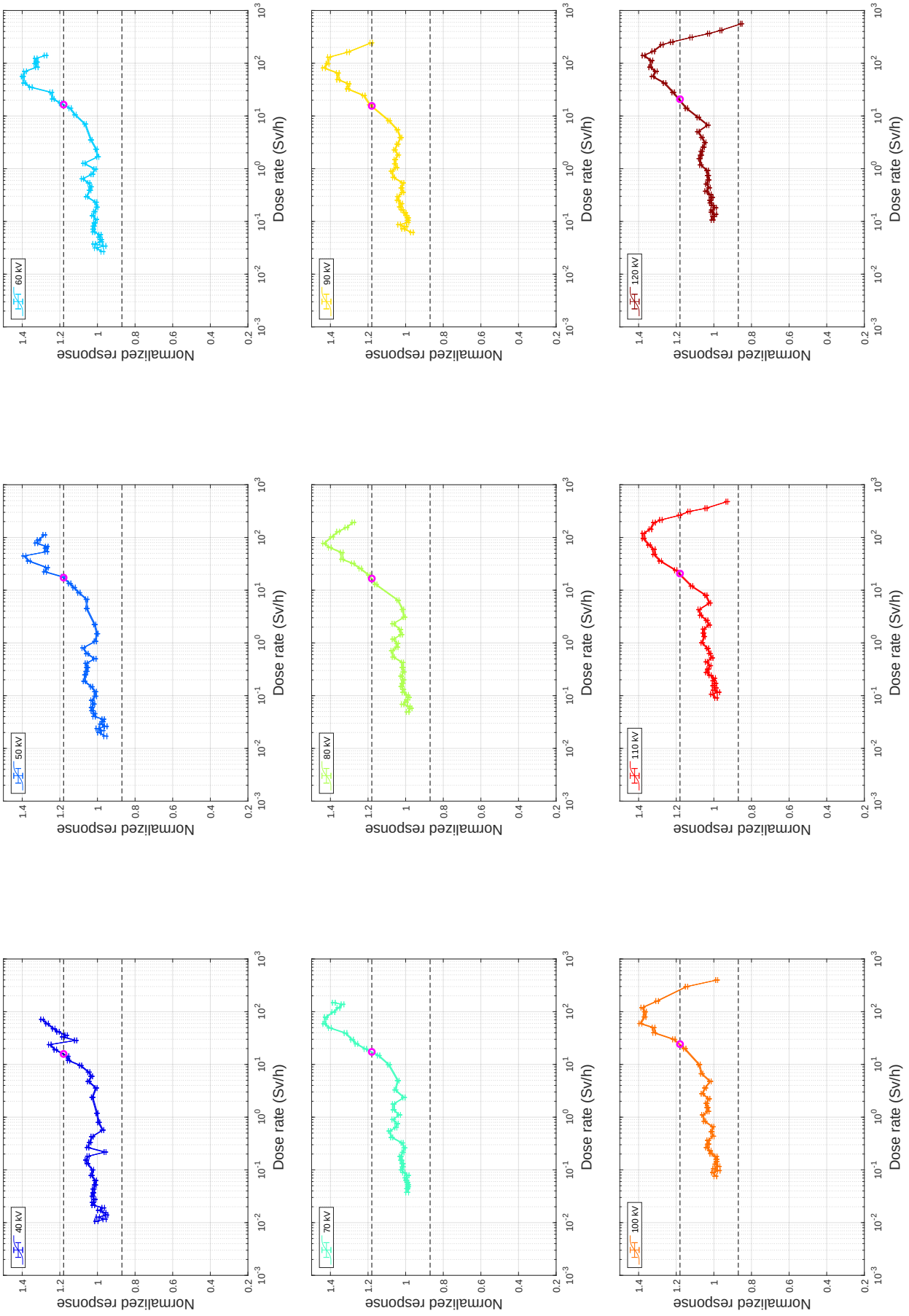

Figure 7.20 Normalized response for the big pixels and measurements with an I_{Krum} of 11 nA as a function of the dose rate for different X-ray tube voltages. The black dashed lines indicate the PTB limits on the normalized response. The magenta circles denote the points, where the response curves exceed the upper limit (break-up point).

Fig. 7.20 shows the normalized responses of measurements with an I_{Krum} of 11 nA. All uncertainties are calculated as outlined for the data in fig. 7.17. The trend of the response is similar for all applied spectra but differs from the trend of the curves shown in fig. 7.17. The higher I_{Krum} leads to lower ToT values. Since the probability for pile-up depends on the ToT of the individual signals that overlap, I_{Krum} can have a major effect on the pile-up behavior. At first, all curves in fig. 7.20 show no or only a slight tendency to rise like the data for an I_{Krum} of 2.2 nA. In this region, pile-up has no significant effect on the normalized response. Then, the normalized response rises and does not decline in contrast to the measurements with an I_{Krum} of 2.2 nA. The normalized response for an applied voltage of 40 kV shows a shift towards lower response values at about 30 $\frac{\mathrm{Sv}}{\mathrm{h}}$. The origin of this shift could not be determined by the time writing this thesis. The required upper PTB limit (black dashed line) on the normalized response is exceeded (magenta circle) for all applied spectra. This break-up dose rate for the upper limit of the normalized response and its uncertainties are determined as outlined for the data shown in fig. 7.17. The normalized response reaches a maximum and declines again. The data taken for spectra with applied voltages of 90 kV and higher enter the region within the limits on the normalized response again and decline further.

Fig. 7.21 shows the break-up dose rate for the measurements with an I_{Krum} of 11 nA as a function of the mean energy of the applied spectra. The uncertainties are calculated as for the data in fig. 7.18. As outlined above, the normalized response shows a different behavior than for the measurements with an I_{Krum} of 2.2 nA. The break-up dose rate stays stable at about 17 $\frac{\mathrm{Sv}}{\mathrm{h}}$ for applied voltages up to 90 kV and rises for the last three voltages. This stable behavior at a lower dose rate than for the measurements with an I_{Krum} of 2.2 nA occurs because the upper PTB limit on the normalized response is exceeded before the lower limit can be undercut.

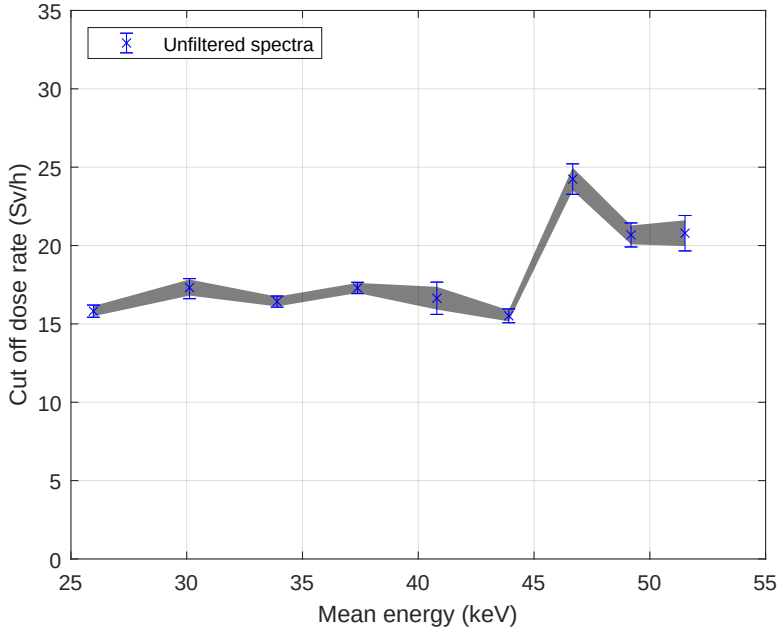

Figure 7.21 Break-up dose rate of the measurements with unfiltered spectra as a function of the mean energy of the applied spectra. The error bars denote the standard uncertainties of the means and the error band the systematic uncertainties that originate from the measurement of the distance between the Dosepix dosemeter and the X-ray tube. I_{Krum} is set to 2.2 nA.

7.2.5 Conclusion

In this chapter, the energy dependence of the break-up dose rate was investigated. The measurements shown in fig. 7.18 confirm the hypothesis of the energy dependence for the investigated unfiltered spectra. The break-up dose rate increases with the applied X-ray tube voltage. In the measurements, no saturation was observed up to a tube voltage of 120 kV. Additionally, the comparison between the RQR 8 spectrum, and the unfiltered spectra indicates that the break-up dose rate is influenced by the X-ray tube voltage and the shape of the energy spectrum (for example, altered via different filters). The low-energy part seems to have a significant effect on the pile-up behavior.

Furthermore, the pile-up measurements were conducted with two different I_{Krum}. As presumed, I_{Krum} altered the pile-up behavior of the responses. In contrast to lower values of I_{Krum}, higher values of I_{Krum} gave rise to the response so that the upper limit was exceeded first. This makes it hard to compare the dependences of the break-up dose rate on the applied voltage for different I_{Krum}. For an I_{Krum} of 11 nA, the measured dose rates were not high enough to measure the break-up dose rate for the lower limit. This could only be achieved for 120 kV, where the break-up dose rate of the lower limit is about 538 $\frac{\mathrm{Sv}}{\mathrm{h}}$.

Chapter 8

Measurements with the integration-mode in total pile-up case

Contents

Measurements in different photon fields that cause total pile-up are performed to evaluate the general behavior of the Dosepix dosemeter in such extreme conditions. Setup and parameters are outlined for measurements conducted at PTB and at *GSI Helmholtzzentrum für Schwerionenforschung* in the following chapter. Certain characteristics that differ from measurements with continuous radiation are pointed out. The dose of short X-ray pulses from two portable X-ray generators and a laser driven X-ray source is determined using the neural network analysis outlined in sec. 6.2.

8.1 Measurements at PTB

8.1.1 Setup

	X-ray tube voltage (kV)	Mean energy (keV)	Pulse duration (ns)	Opening angle (°)
XR200	150 (see [61])	54.6 ± 0.4 (see [62])	115 (see [63])	40 (see [61])
XRS4	370 (see [60])	88.0 ± 1.5 (see [62])	10 (see [60])	40 (see [60])

Table 8.1: Key properties of the X-ray generators of the experiments.

To test the dose reconstruction method for total pile-up introduced in 6.2, a XR200 [61] (see fig. 8.1 right) and a XRS4 [60] (see fig. 8.1 left) X-ray generator are used. These mobile X-ray generators apply very short and intense pulses with pulse durations of 115 ns (XR200) [63] and 10 ns (XRS4) [60].

Figure 8.1 Photograph of the two X-ray generators the measurements are performed with. Left: XRS4 [60], right: XR200 [61].

The pulse length that is applied by the utilized XR200 was measured by [64] using a set of diodes. The applied X-ray tube voltages of the generators cannot be changed. Therefore, measurements with two X-ray generators with different key features are conducted. Both devices can apply single pulses or multiple pulses repeatably with a frequency of about 10 Hz. The relevant features of both X-ray generators are listed in tab. 8.1. Fig. 8.2 shows a photograph of the measurement setup. As in previous experiments, the Dosepix dosemeter is attached to an ISO slab phantom (3) facing the X-ray generator (here, an XR200) (1). An ionization chamber (2) (further referred to as primary ionization chamber [65]) resides in a fixed distance of 10 cm in front of the X-ray generator and is used to determine the reference dose. The XR200 can be replaced with the XRS4. For measurements performed in May 2021, the slab phantom with the Dosepix dosemeter can be replaced with an additional ionization chamber [66] (further referred to as secondary ionization chamber) via a moving table. The distance between the Dosepix dosemeter and the X-ray generators is adjustable to change the applied dose rate. During this thesis, several measurement series are conducted. The detector settings and the setup adjustments are outlined for each measurement series in the following. Each series is labeled with the month and the year it was conducted in. The corresponding results (see sec. 8.1.4) are discussed chronologically since the results build upon each other.

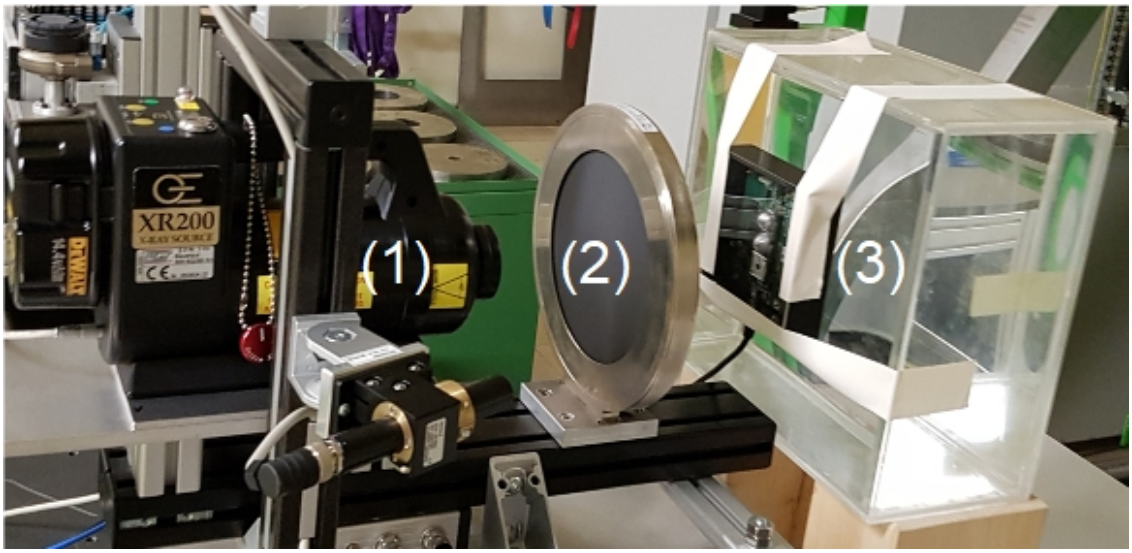

Figure 8.2 Photograph of the measurement setup with an XR200 X-ray generator (here, XR200 [61]) at PTB. (1): X-ray source. (2): Ionization chamber [65] in a fixed distance of 10 cm in front of the X-ray source for reference dose determination. (3): Dosepix dosemeter on a slab phantom. The distance between the Dosepix dosemeter and the X-ray generator is variable.

August 2018

The first dose measurements are carried out with the XR200. The main goal is to investigate the behavior of the Dosepix detectors under total pile-up conditions and to test the neural network approach to determine the dose. Here, only single pulses are applied at a distance between 300 cm and 772 cm. Five to eleven individual pulses are measured per distance. Preparatory measurements are performed in ToT-mode and dose measurements in integration-mode. Additional dose measurements are performed with the Dosepix dosemeter operated in Dosi-mode to compare the performance of the neural network analysis to the dose reconstruction method with the Dosi-mode. Here, three to seven individual pulses are measured per adjusted distance. All measurements are conducted with an I_{Krum} of 2.2 nA and a threshold level of $\mathrm{THL_{sub}} = 20$. The filter caps without edges (see fig. 3.4) are used. An adhesive tape made of 55 µm thick PMMA covered the opening of the cap in front of the first detector to protect the sensor from dust and damage. This tape is not included in the simulations. However, as outlined in sec. 7.1.2, at an energy of already about 13 keV, 99 % of the radiation passes through 55 µm of PMMA (calculated with data taken from [15]). Therefore, the adhesive tape is further neglected in the analysis. As mentioned in sec. 7.1.2, the plastic lid of the Dosepix dosemeter is changed throughout the making of this thesis. Here, the lid made of ABS is used. The difference in absorption between the ABS and the PMMA lid is neglected (see sec. 7.1.2).

November 2019

This measurement series is performed with the XR200 to investigate the optimal detector setting. The measurements are conducted with an I_{Krum} varying between 2.2 nA and 11 nA and a $\mathrm{THL_{sub}}$ varying between 20 and 60. The measurements are performed in ToT-mode and integration-mode. The filter caps with edges (see fig. 3.4) are used. The adhesive tape in front of the first detector mentioned above is applied. The lid made of PMMA is used. The distance is varied between 24 cm and 738 cm, and only single pulses are applied.

May 2021

This measurement series is performed with the XR200 and the XRS4 to reevaluate measurements performed in November 2019. Some of the earlier measurements showed unexpectedly low charges measured by the primary ionization chamber for pulses with the XR200. Therefore, the secondary ionization chamber is placed at the same location where the Dosepix dosemeter would be in the measurements, and a calibration is performed. For this calibration, the primary and secondary ionization chamber measured three times between 20 and 50 pulses. This calibration is conducted to examine what charge signal is to be expected from the primary ionization chamber (see sec. 8.1.2). This procedure is necessary since the secondary ionization chamber and the Dosepix dosemeter could not be placed in the center of the radiation field at the same time without influencing each other. The calibration is performed for both X-ray generators and every adjusted distance. The dose measurements with the Dosepix dosemeter are carried out with single pulses, an adjusted I_{Krum} of 11 nA, and a $\mathrm{THL_{sub}}$ of 20. The measurements are performed in integration-mode. Here, the adhesive tape mentioned above is not applied. The filter caps with edges (see fig. 3.4) are used. The lid made of PMMA is used. The distance is varied between 100 cm and 755 cm.

8.1.2 Reference dose determination

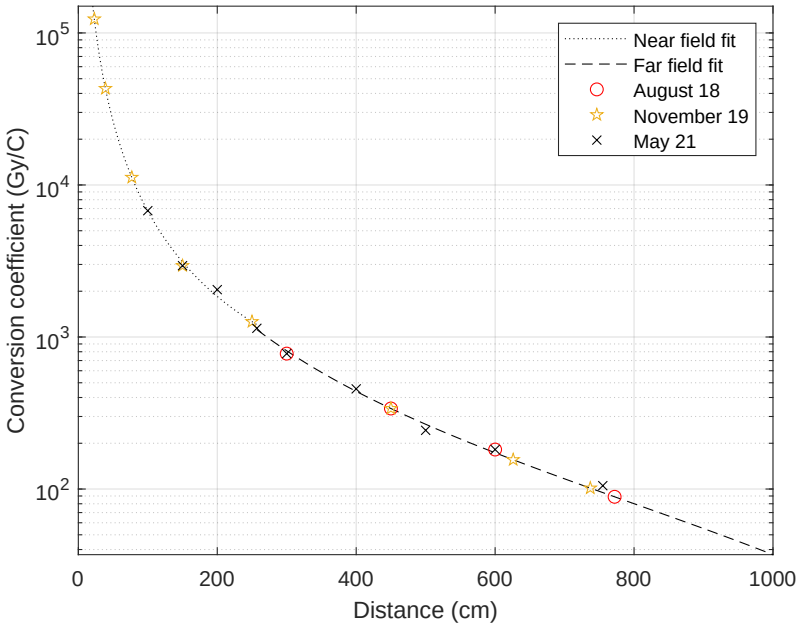

Figure 8.3 Conversion coefficient that maps the measured charge from the primary ionization chamber to air kerma as a function of the distance. The black crosses denote the measurements performed in May 2021. Two inverse square fits are applied to this data. The dotted line denotes a near-field fit to the first four data points, and the dashed line denotes a far-field fit for the remaining data points. The coefficients for the measurements taken in August 2018 (red circles) and November 2019 (yellow stars) are extracted from the fit functions.

The measurements with the two ionization chambers performed in May 2021 are used to determine the reference dose. Using the measured charge from the primary ionization chamber and the measured air kerma K_a from the secondary ionization chamber, a conversion coefficient $C(d)$ is determined for each adjusted distance d. This coefficient can directly be used to calculate $H_p(10)$ and $H_p(0.07)$ for all measurements performed in May 2021. For all other measurements that are not necessarily conducted in the same distances as the measurements in May 2021, the conversion coefficient is extracted using two fit functions of the form

$$C(d) = \frac{A}{d^2} + B, \tag{8.1}$$

where A and B denote fit parameters. This model is based on the assumption of a quadratic dependence between the photon fluence and the distance. This model, however, is not entirely accurate since absorption in air depends on the photon energy and the applied spectrum alters with the distance. Therefore, the applied spectrum alters with the distance. A fit function is determined for photon fields with small distances ($< 250\,\text{cm}$) and another for large distances ($> 250\,\text{cm}$). Fig. 8.3 shows the conversion coefficients for May 2021 (black crosses) as a function of the distance. The black dotted line denotes the near-field fit, and the black dashed line the far-field fit. The data from August 2018 (red circles) and November 2019 (yellow stars) are extracted from the fit functions. This procedure only needs to be performed for the XR200 since measurements with the XRS4 are only performed in May 2021. To calculate the dose quantities $H_p(10)$ and $H_p(0.07)$, factors β that are unique for each spectrum and dose quantity are multiplied with $C(d)$.

	$\frac{H_\mathrm{p}(10)}{K_\mathrm{a}}$ $(\frac{\mathrm{Sv}}{\mathrm{Gy}})$	$\frac{H_\mathrm{p}(0.07)}{K_\mathrm{a}}$ $(\frac{\mathrm{Sv}}{\mathrm{Gy}})$
β(XR200)	1.38 ± 0.03	1.43 ± 0.01
β(XRS4)	1.49 ± 0.05	1.48 ± 0.02

Table 8.2: Coefficients to convert air kerma to $H_\mathrm{p}(10)$ and $H_\mathrm{p}(0.07)$ for both X-ray generators. Data taken from [62].

These factors (see tab. 8.2) are taken from [62] for the utilized X-ray generators. The uncertainties denote the standard uncertainties of the means. In the following, the dose rate is calculated according to equ. 2.37 using the measured reference doses and the pulse durations listed in tab. 8.1.

8.1.3 Preparatory measurements

The energy deposition spectrum of the XR200 is measured for different photon fluences to investigate the effects of total pile-up. Therefore, several single pulses are acquired in ToT-mode. The photon fluence is varied by adjusting the distance between the Dosepix dosemeter and the XR200 in a range of 3.0 m to 7.7 m. For each distance, 48 to 94 single measurements are performed. The figures in 8.4 show the measured ToT spectra (left column) and the corresponding energy deposition spectra (right column) for the big pixels of the three Dosepix detectors at four distances. Two major characteristics that only occur in measurements with high dose rate photon fields appear in the ToT spectra of the first two Dosepix detectors. A prominent peak below 30 clock cycles and a periodic structure in the measurements at a distance of 7.7 m and 6.0 m occur. The origin of both characteristics could not be fully clarified. A possible explanation of this behavior is a correlation between the analogue threshold level and the photon flux. Fig. 8.5a shows the measured ToT of all big pixels of the first Dosepix detector for measurements with an I_Krum of 2.2 nA and different settings of $\mathrm{THL_{sub}}$. The measurements are performed in ToT-mode at a distance of 4.5 m. 25 single pulses are recorded for each adjusted set of parameters. The height of the peak decreases with an increasing threshold level $\mathrm{THL_{sub}}$. This behavior suggests that the dominant peak arises from a lowering of the analogue threshold so that it runs into the noise edge. By presetting $\mathrm{THL_{sub}}$ to a higher value, the effect that causes the dominant peak can partially be compensated. The hypothesis that a high photon flux causes a decrease of the analogue threshold level, however, contradicts results on measurements that were performed in [39]. It was shown that measured energy spectra shift towards lower energy values with increasing photon flux. This effect is traced to a rise in the difference between the analogue threshold level and the baseline of the charge signal. This spectrum shift can also be observed in the data for the third Dosepix detector (see fig. 8.4f). For distances down to 4.5 m, a peak at about 23 keV is visible. This peak originates from fluorescence photons from the tin filter that covers this detector. With decreasing distance and therefore increasing photon flux, this peak shifts towards lower energy values.

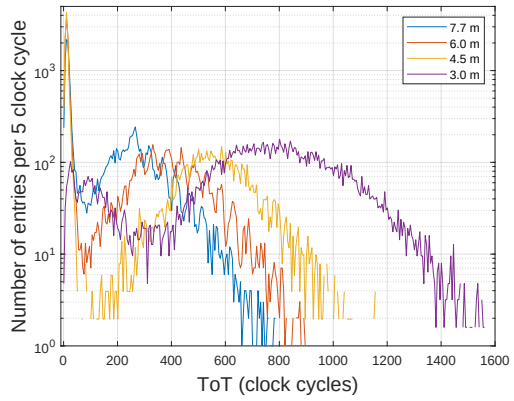

(a) ToT spectrum first detector (Free)

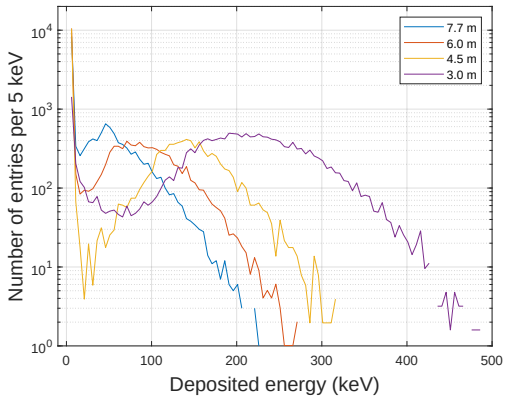

(b) Energy spectrum first detector (Free)

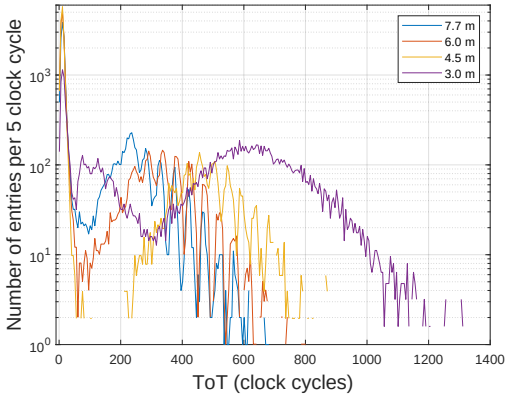

(c) ToT spectrum second detector (Al)

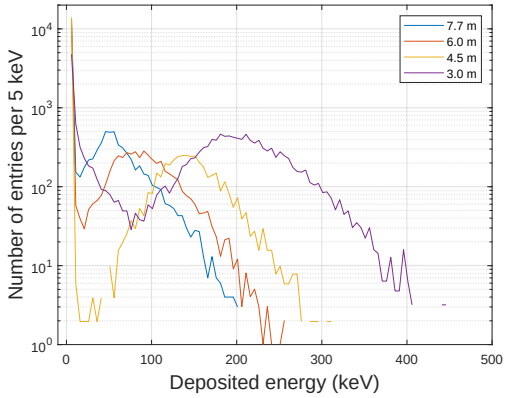

(d) Energy spectrum second detector (Al)

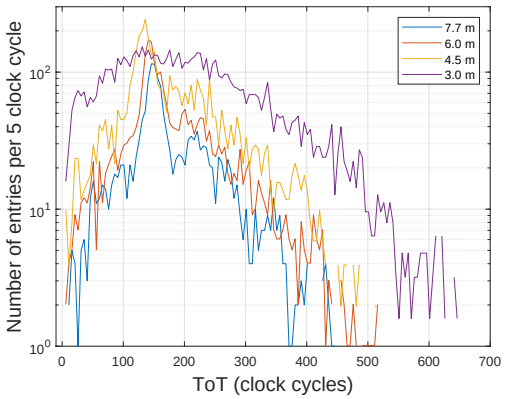

(e) ToT spectrum Third detector (Sn)

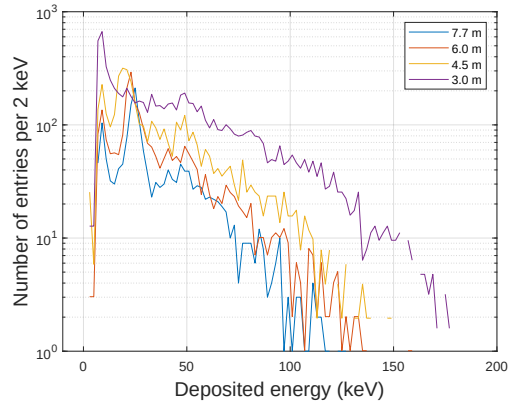

(f) Energy spectrum third detector (Sn)

Figure 8.4 ToT spectra (left column) of the three Dosepix detectors for different distances. The corresponding energy spectra are shown in the right column.

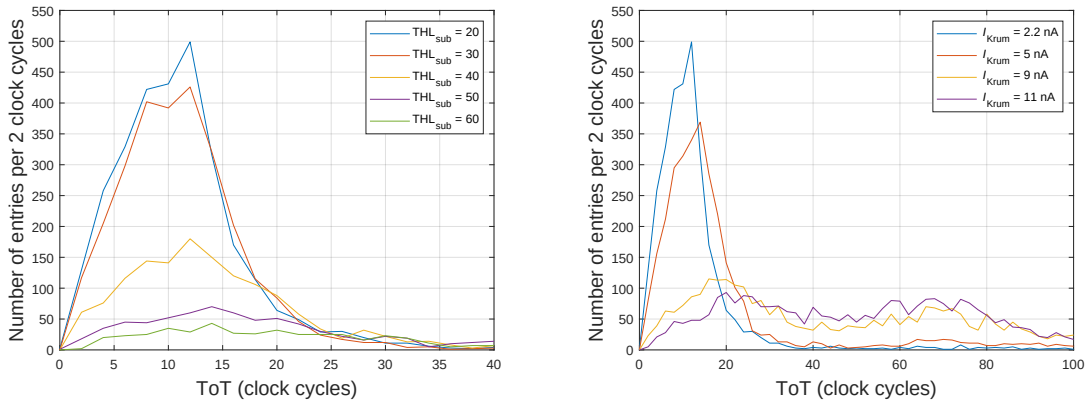

(a) Constant I_{Krum} **(b)** Constant $\mathrm{THL}_{\mathrm{sub}}$

Figure 8.5 (a): ToT spectra with fixed I_{Krum} and different settings of $\mathrm{THL}_{\mathrm{sub}}$. (b): ToT spectra with fixed $\mathrm{THL}_{\mathrm{sub}}$ and different settings of I_{Krum}.

Fig. 8.6a shows the section with the tin fluorescence from fig. 8.4f in detail. A Gaussian function is fitted to the data to determine the center of the peaks $\mu(E)$ (vertical lines). The energy shift $\Delta\mu(E)$ is calculated by subtracting $\mu(E)$ from a reference energy E_0. The energy at which the tin fluorescence occurs in the calibration measurements (see sec. 4.2) is chosen to be E_0. The correlation of $\mu(E)$ with the photon flux Φ can be determined qualitatively. The inverse square of the distance d between the Dosepix dosemeter and the X-ray generator is used as a measure for the photon flux since Φ scales quadratically with the distance

$$\Phi \propto \frac{1}{d^2}. \tag{8.2}$$

Fig. 8.6b shows this relation. In [39] it was shown that $\mu(E)$ depends linearly on the applied photon flux. It was further shown that $\mu(E)$ decreases with increasing I_{Krum}. The effects of a higher I_{Krum} on the disturbance can be seen in fig. 8.5b. The measurements are taken with $\mathrm{THL}_{\mathrm{sub}}$ set to 20 for four different settings of I_{Krum} between 2.2 nA and 11 nA. The dominant peak at low ToT values decreases with increasing I_{Krum}. This compensating effect might occur because the leakage current compensation depends on the adjusted I_{Krum}.

The occurrence of a dominant peak and a periodic structure, as well as the energy shift of the spectrum, could disturb the dose measurements. Since the dominant peak and the energy shift of the spectrum are influenced by the settings of $\mathrm{THL}_{\mathrm{sub}}$ and I_{Krum}, measurements with different settings of those parameters were carried out in November 2019 (see sec. 8.1.4).

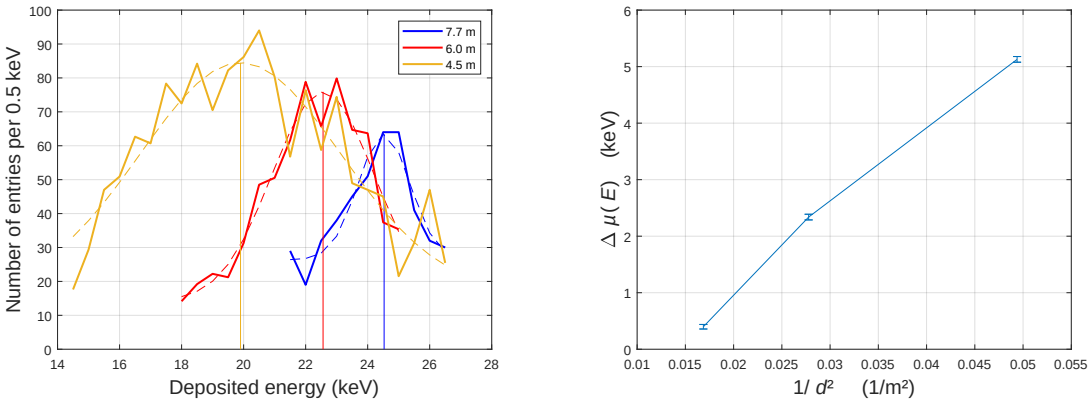

(a) Tin fluorescence lines **(b)** Energy shift

Figure 8.6 (a): Energy deposition spectra of the third Dosepix detector for different distances. The section containing the tin fluorescence is depicted. A Gaussian function (dashed lines) is fitted to the data to determine the center positions (vertical lines) of the fluorescence. (b): Energy shift of the tin fluorescence as a function of the inverse square of the distance between the Dosepix dosemeter and the XR200.

8.1.4 Results

Measurements were conducted in August 2018 to investigate if reasonable results can be achieved in the case of total pile-up when the Dosepix dosemeter is operated in Dosi-mode. Fig. 8.7 shows the response in Dosi-mode as a function of the applied dose rate. The dose of each individual measurement is calculated according to equ. 6.9 and the responses according to equ. 2.38. The error bars denote the standard uncertainties of the means of the measured responses. The dose is generally overestimated, even for low dose rates. Additionally, the response is not stable and increases with increasing dose rate.

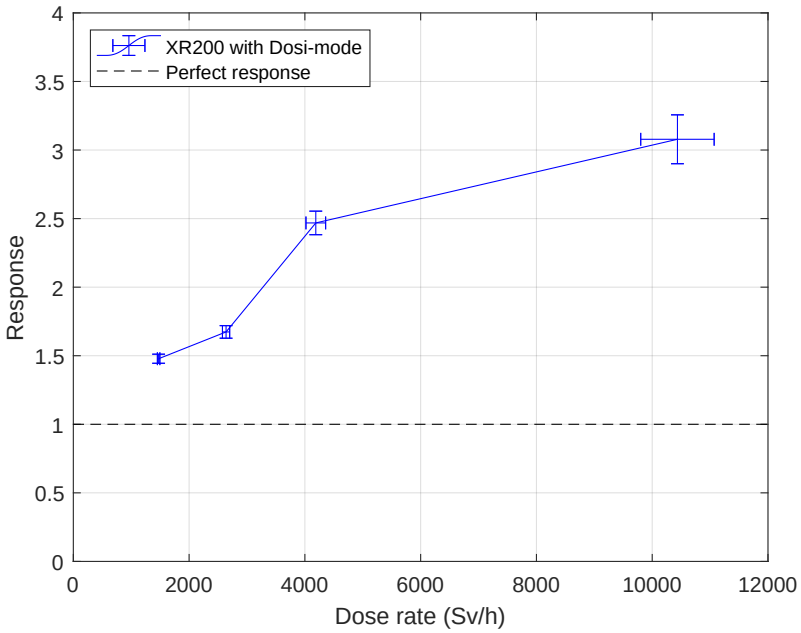

Figure 8.7 $H_p(10)$ response as a function of the dose rate for measurements in Dosi-mode with the XR200 (blue). The black dashed line denotes the perfect response.

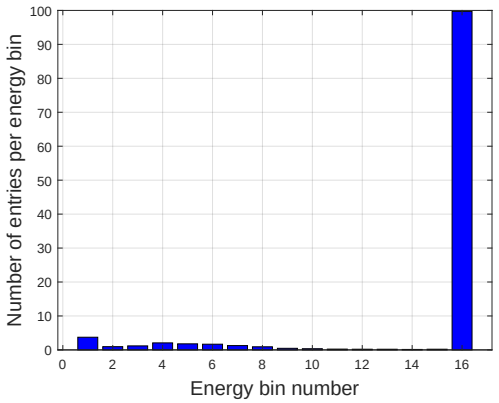

(a) First detector (Free)

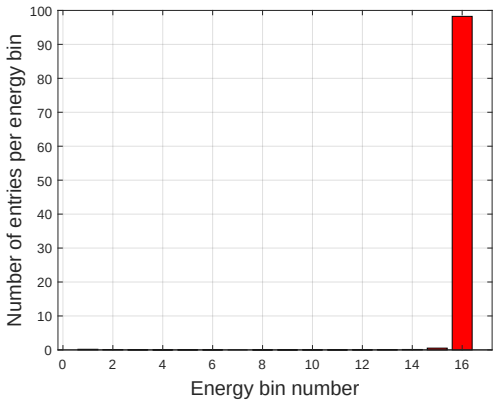

(b) Second detector (Al)

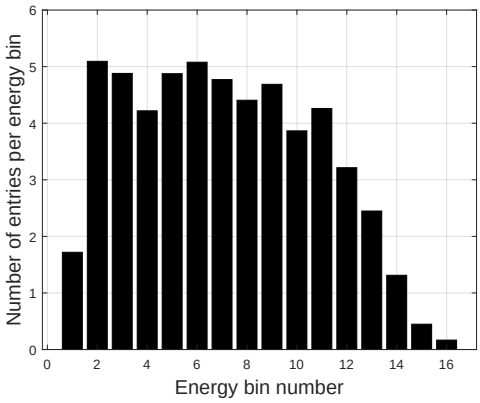

(c) Third detector (Sn)

Figure 8.8 Mean number of entries in the energy bins for the big pixels of the three detectors. 99 Pulses are applied.

This behavior results from the fact that only a single signal is produced in each pixel per pulse. The individual photons that contribute to this signal cannot be resolved, and spectroscopic photon counting is not possible. Only one entry in one of the energy bins is counted. To further investigate this effect, 99 X-ray pulses from the XR200 are applied to the Dosepix dosemeter that is operated in Dosi-mode. The dosemeter is placed onto the slab phantom at a distance of 1.5 m from the X-ray generator. I_{Krum} is set to 2.2 nA and $\mathrm{THL}_{\mathrm{sub}}$ to 20. A reference dose measurement is not performed. However, the entries in the energy bins provide information about measurement limits of the Dosi-mode in the case of total pile-up. Fig. 8.8 shows the mean number of entries in the energy bins for the big pixels of the three Dosepix detectors. Most entries are measured in the last energy bin of the first and the second detector. Each of the 99 applied pulses generates a signal high enough to exceed the last bin edge. Since the last energy bin has no upper limit, all signals that exceed the last bin edge accumulate regardless of their energy or number of detected photons. This limit is not yet reached in the tin-covered detector. Here, pile-up distorts the measurements similar to the measurements shown in fig. 7.8. For higher doses, the signals in the tin-covered detector exceed the last bin edge as well. When all pulses generate a single entry in the last energy bin of every pixel of all three detectors, the maximum measurable dose is reached.

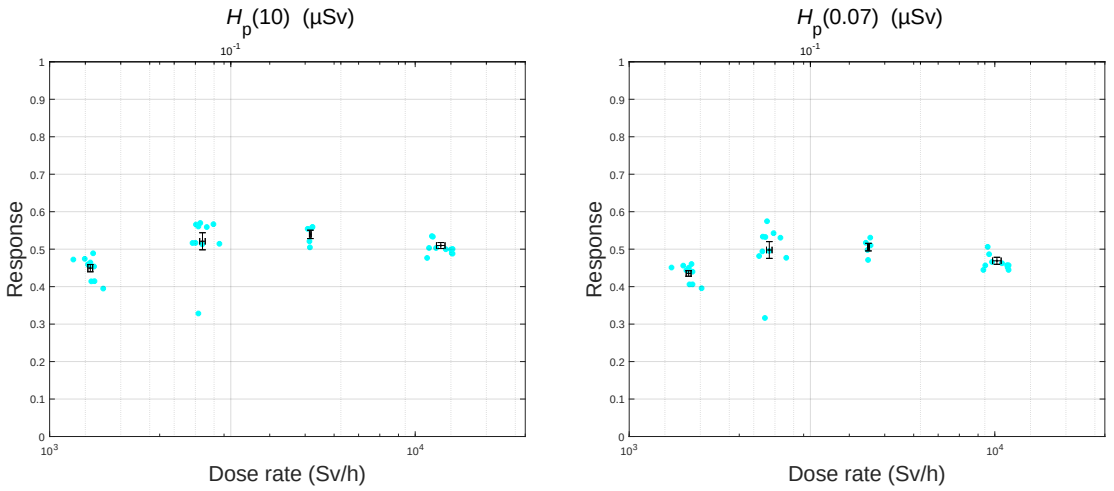

(a) Response for $H_p(10)$ **(b)** Response for $H_p(0.07)$

Figure 8.9 Response of the Dosepix dosemeter in integration-mode calculated with data taken in August 2018 as a function of the dose rate (lower X-axis) and the dose (upper X-axis). The individual measurements are depicted in blue, the means and the standard uncertainties of the means for each adjusted distance are depicted in black. (a): Response for $H_p(10)$ and (b): Response for $H_p(0.07)$.

Dose measurements in integration-mode were performed in August 2018 as well. The measurements are evaluated with the neural network as outlined in sec 6.2. Fig. 8.9a and 8.9b show the response for $H_p(10)$ and $H_p(0.07)$ as a function of the applied dose rate (bottom X-axis) and the applied dose (top X-axis). The cyan-colored dots denote the individually measured response values, and the black data points denote the means and the standard uncertainties of the means. The response shows that the neural network generally underestimates the applied doses, yet stays stable at about 0.52 for $H_p(10)$ and 0.49 for $H_p(0.07)$. There are multiple reasons for this underestimation. One contribution can be discrepancies between the simulation of the detector response and the real Dosepix dosemeter. As shown in sec. 4.7, the deposited energy spectra of simulated and measured fluorescence spectra are mostly in good accordance with another. A discrepancy between simulation and reality is more likely to be found in the photon detection efficiency. An overestimation of the PDE leads to a lower measured dose and, therefore, to a lower response as well. A further reason for the underestimation can be that the process of total pile-up in the pixel electronics differs from the assumptions made in the simulation that is used to generate the training data for the neural network. This presumption is supported by the unexpected behavior of the Dosepix detectors in the case of total pile-up, especially the dominant peak at low ToT values. Here, the contribution of a malfunction in the Dosepix electronics is not quantifiable.

Since the disturbance as a possible reason for the underestimated response seems to be dependent on the adjusted $\mathrm{THL_{sub}}$ and I_{Krum} (see fig. 8.5a and 8.5b), these parameters are varied to investigate if and how the threshold level and I_{Krum} settings balance effects of the disturbance. Fig. 8.10a and 8.10b show the responses of the data taken in November 2019 as a function of $H_p(10)$ and $H_p(0.07)$. The individual responses are depicted in yellow. The mean responses per distance and the standard uncertainties are depicted in black. The measured responses vary significantly from pulse to pulse. This variability in the response can be traced back to variations in the charge, which is measured by the primary ionization chamber used to determine the reference dose (see sec. 8.1.2).

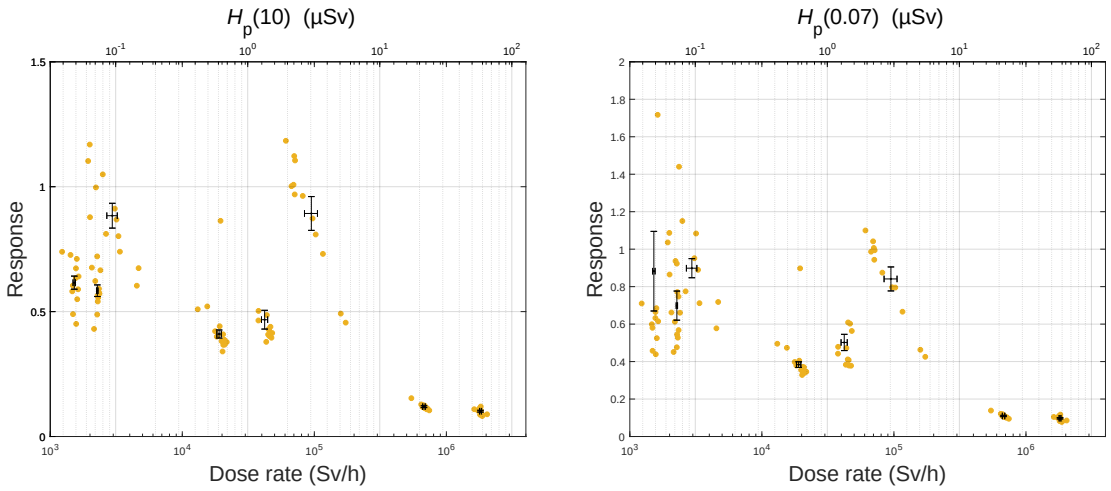

(a) Response for $H_p(10)$ **(b)** Response for $H_p(0.07)$

Figure 8.10 Response of the Dosepix dosemeter in integration-mode calculated with data taken in November 2019 as a function of the dose rate (lower X-axis) and the dose (upper X-axis). The individual measurements are depicted in yellow, the means and the standard uncertainties of the means for each adjusted distance are depicted in black. (a): Response for $H_p(10)$ and (b): Response for $H_p(0.07)$.

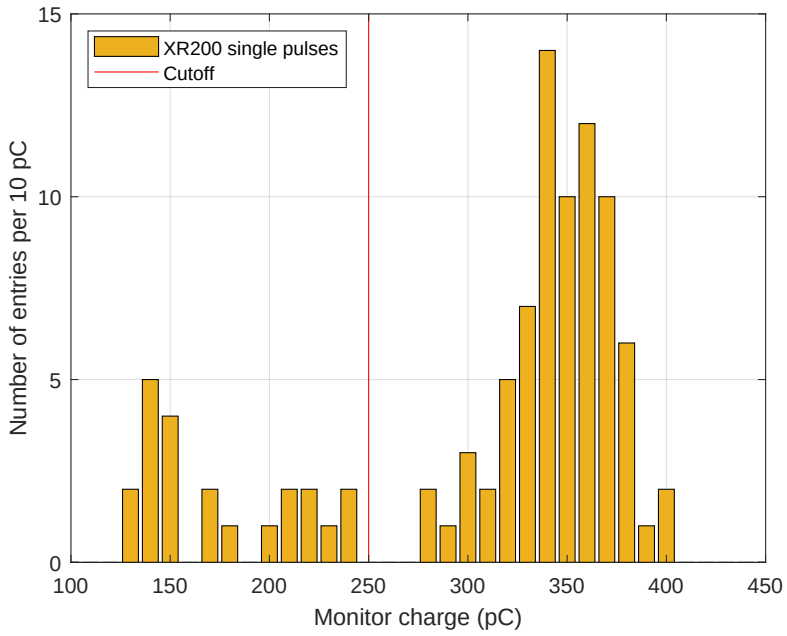

Figure 8.11 Histogram of the charge released by individual X-ray pulses in the primary ionization chamber in front of the XR200 (yellow). The cutoff is depicted as vertical red line at a charge of 250 pC.

As mentioned above, the primary ionization chamber is placed at a fixed distance in front of the X-ray generator. Therefore, the generated charge per pulse should not change for equal pulses. Fig. 8.11 shows the charge distribution of the dose measurements in November 2019. The measurements show an accumulation at about 350 pC. However, charge signals that significantly deviate from this main distribution are measured for many pulses. The photon field from the XR200 may alter due to malfunctioning or a low battery state.

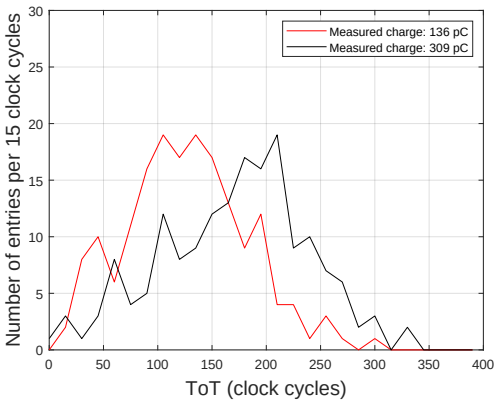

(a) First detector (Free)

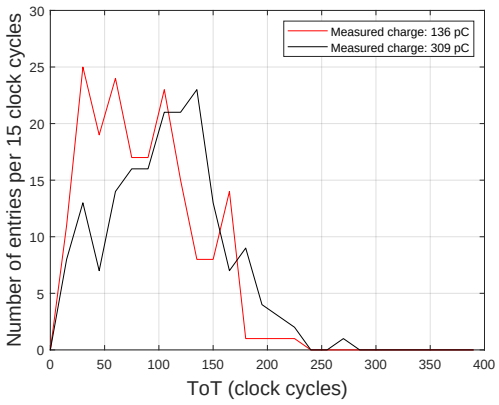

(b) Second detector (Al)

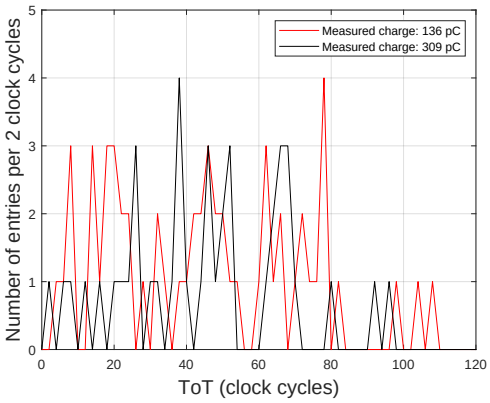

(c) Third detector (Sn)

Figure 8.12 ToT spectra for the first (a), the second (b) and the third (c) Dosepix detector. The red spectrum corresponds to an X-ray pulse measured with a charge of 136 pC in the ionization chamber and the black ToT spectrum to a pulse measured with a charge of 309 pC in the ionization chamber. Only non-zero entries are depicted.

This is not problematic if only the photon fluence changes but not the energy spectrum of the photon field. This, however, cannot be ruled out. The measurements with the Dosepix dosemeter indicate that the photon fluence did not change linearly with the charge of the primary ionization chamber. Fig. 8.12 shows the ToT spectra for the three Dosepix detectors for the big pixels. The red curve depicts the data for a pulse, where the primary ionization chamber measured a charge of 136 pC, and the black curve shows the data for a pulse, where the primary ionization chamber measured a charge of 309 pC. Both pulses are measured with the same settings of measurement parameters ($I_{\mathrm{Krum}} = 11\,\mathrm{nA}$, $\mathrm{THL}_{\mathrm{sub}} = 20$) in a distance of 4.5 m and right after another. The ratio of the mean ToTs between the low charge pulse and the high charge pulse is 0.7875 for the first detector, 0.8067 for the second detector, and 0.8132 for the third detector. Here, only non-zero values are taken into account. The ratio between the two measured charges of the primary ionization chamber is 0.4401. It is expected that the charge of the ionization chamber depends linearly on the photon fluence. In the case of total pile-up, the measured ToT in the Dosepix detectors is in good approximation linearly dependent on the photon fluence. The data indicates that a malfunctioning of the primary ionization chamber for some of the measured pulses cannot be excluded.

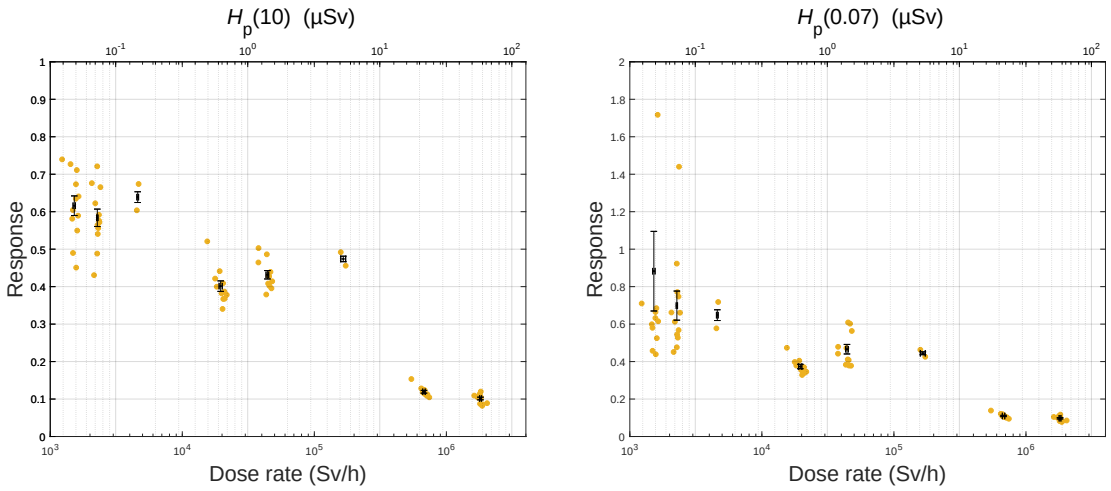

(a) Response for $H_p(10)$ **(b)** Response for $H_p(0.07)$

Figure 8.13 Data shown in fig. 8.10 with applied cutoff. (a): Response for $H_p(10)$ and (b): Response for $H_p(0.07)$.

However, the primary objective of these measurements is to evaluate if the response could be improved by adjusting the measurement parameters of the Dosepix dosemeter. Therefore, the distribution around 350 pC is assumed to be the true charge distribution, and all measurements with charges above 250 pC are assumed to be comparable to each other. The red line in fig. 8.11 denotes this cutoff. Fig. 8.13 shows the response of the data taken in November 19 with the cutoff applied. Most of the deviating data points are excluded, especially between 2 µSv and 3 µSv. For low doses, the variance of the data points is still significantly higher than for the data taken in August 2018. The response for $H_p(10)$ and $H_p(0.07)$ is very similar except for two outlying data points at low doses. It generally declines towards higher dose rates. The measurements with applied doses above 10 µSv are conducted in distances of 23 cm and 39 cm, where the slab phantom is not fully illuminated due to the limited opening angle of the XR200. This contributes to an underestimation of the dose and, therefore, to a decrease in the response. However, the partial illumination of the slab phantom alone cannot cause this significant drop. It is more probable that the function of the Dosepix electronics depends on the photon flux, which leads to a change in the detector output for high photon fluxes. In addition, the distances in which the drop of the response is observed are unrealistically small. A realistic distance in the use case is assumed to be not smaller than 1 m. Fig. 8.14 shows the response of the data taken in November 2019 as a function of the dose rate sorted by the adjusted parameters. There is no set of parameters that yields the best results over the whole dose rate range. Therefore, a suitable set of parameters is chosen for further investigation based on pragmatical reasons. As outlined in sec. 3.6 the temperature dependence of the Dosepix detector decreases with increasing I_{Krum}. Therefore, an I_{Krum} of 11 nA is adjusted in further experiments with the X-ray generators. $\mathrm{THL}_{\mathrm{sub}}$ is chosen to be 20 and therefore minimal since the smallest measurable energy increases with $\mathrm{THL}_{\mathrm{sub}}$.

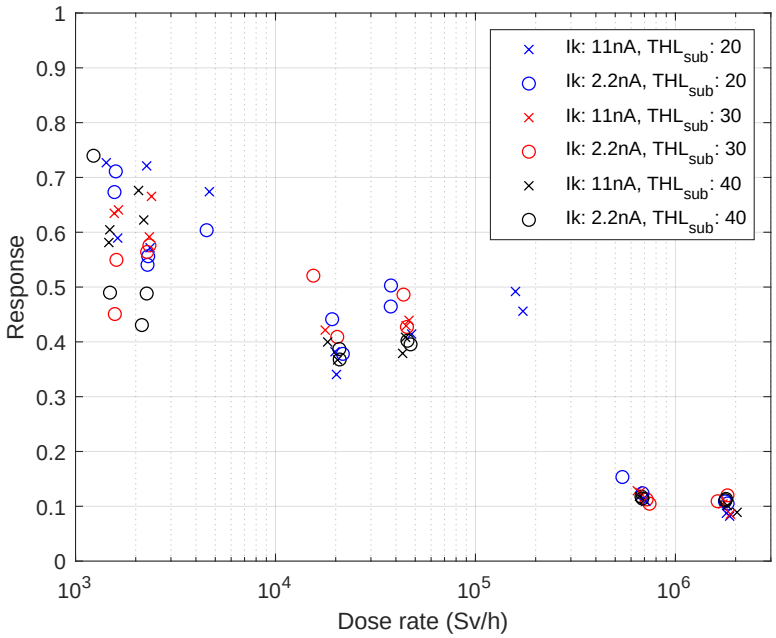

Figure 8.14 $H_p(10)$ response of the data taken in November 2019 as a function of the applied dose rate. The individual settings of measurement parameters are depicted according to the legend. The cutoff on the measured charge of the primary ionization chamber is applied.

As outlined in sec. 8.1.1, a second ionization chamber is used in May 2021 to calibrate the primary ionization chamber and to determine the conversion coefficients that are used to determine the reference dose. This way, strongly deviating data is identified during the measurements. These measurements (in total three single dose measurements) are repeated. Fig. 8.15 shows the response that is calculated from measurements taken in May 2021 as a function of the dose and the dose rate for $H_p(10)$ and $H_p(0.07)$. The data taken with the XR200 is shown in red and the data acquired with the XRS4 is shown in black. The error bars denote the standard uncertainties of the means. In contrast to the data taken in November 2019, there is no apparent descending trend. The response of both X-ray generators stays stable over the whole measured dose range. Again, the response for $H_p(10)$ and $H_p(0.07)$ show a similar behavior. The mean response for the XR200 for all data points is $\mu(R(H_p(10))) = 0.57$ with a standard deviation of $\sigma(R(H_p(10))) = 0.07$ and $\mu(R(H_p(0.07))) = 0.57$ with a standard deviation of $\sigma(R(H_p(0.07))) = 0.10$. The mean response for the XRS4 for all data points is $\mu(R(H_p(10))) = 0.55$ with a standard deviation of $\sigma(R(H_p(10))) = 0.03$ and $\mu(R(H_p(0.07))) = 0.51$ with a standard deviation of $\sigma(R(H_p(0.07))) = 0.04$. The response for the XR200 for the highest dose rate seems to be exceptionally high compared to the other data points. Although it is unlikely, it could be a statistical effect. Another possible systematical reason could be an inhomogeneity of the radiation field of the XR200. The dose rate is increased in the measurements by decreasing the distance between the Dosepix dosemeter and the X-ray generators. The field of view of the dosemeter increases with decreasing distance as well. Therefore, an inhomogeneity in the radiation field could have a greater effect on the measurement when the Dosepix dosemeter is placed closer to the XR200.

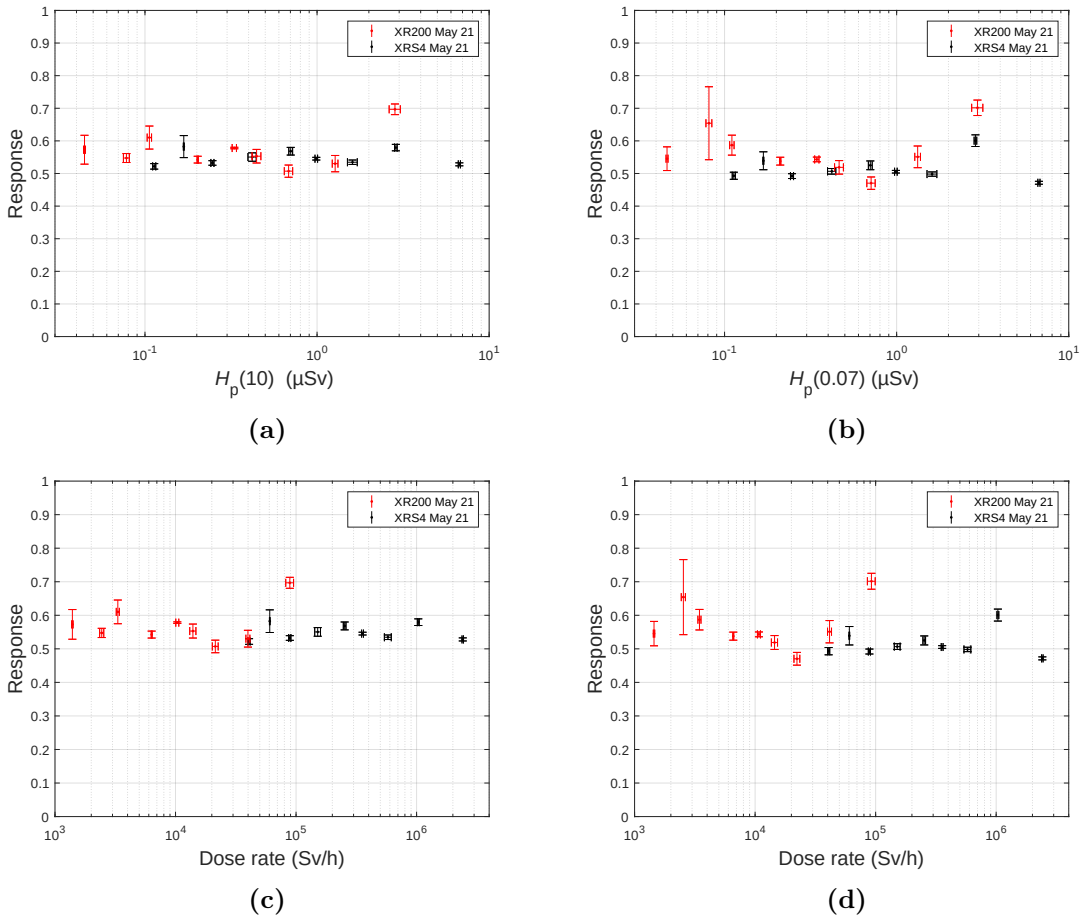

Figure 8.15 Response of the data taken in May 2021 as a function of (a) the dose for $H_p(10)$ and (b) the dose for $H_p(0.07)$. The dependence of the response on the dose rate is depicted in (c) for $H_p(10)$ and in (d) for $H_p(0.07)$. The red data denotes measurements performed with the XR200 and the black data denotes measurements performed with the XRS4.

The mean values for both X-ray generators are very similar. The offset by which the response is shifted does not seem to depend on the spectra, the dose, or the dose rate of the two applied photon fields. Normalization is applied to eliminate this offset. As outlined in sec 2.3.2, such a normalization to specified data points is also applied when evaluating the energy dependence and the dose rate dependence of tested dosemeters. No requirements exist for measurements in photon fields with dose rates as high as the X-ray generators produce them. The value the data is normalized to is chosen to be the mean response value of the XR200 data.

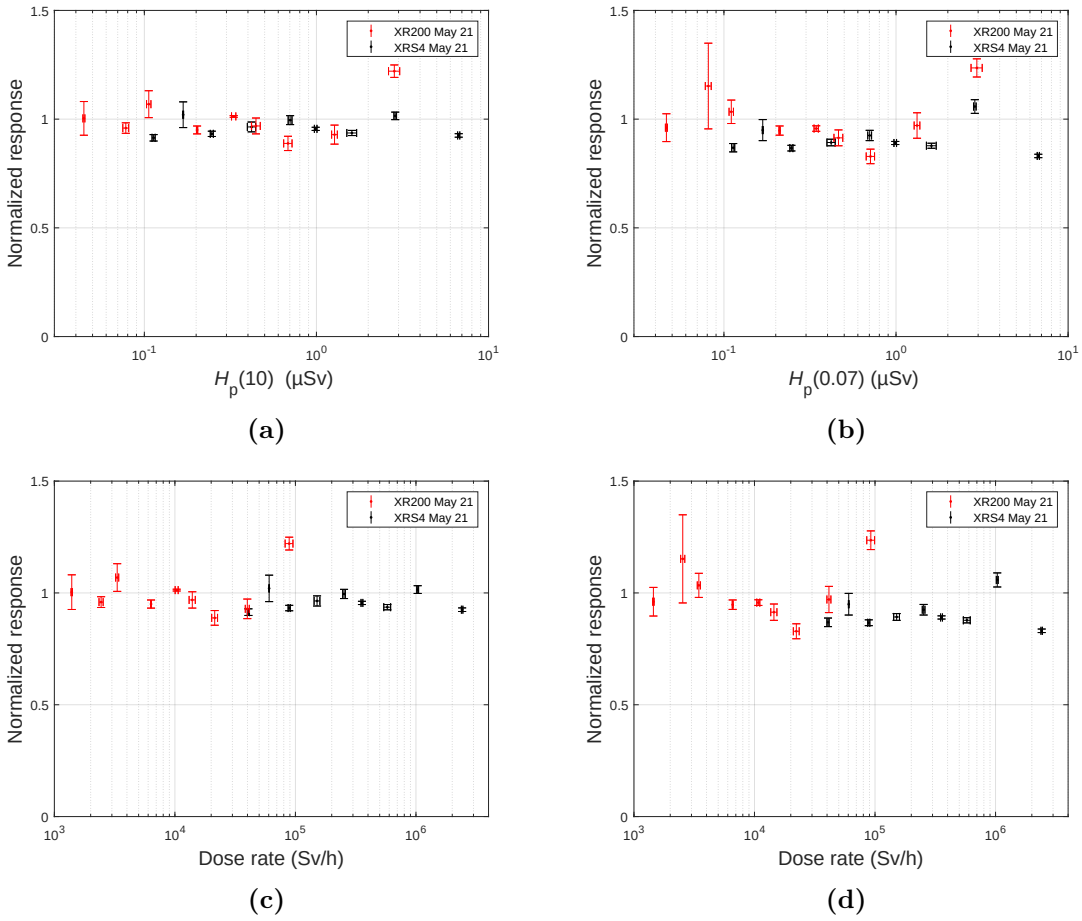

Figure 8.16 Data as shown in fig. 8.15. A normalization factor is applied to all data points for Hp10 and Hp007 respectively.

Fig. 8.16 shows the same data as in 8.15 with normalization applied. The mean normalized response for the XR200 is, therefore, $\mu(R(H_p(10))) = 1$ with a standard deviation of $\sigma(R(H_p(10))) = 0.11$ and $\mu(R(H_p(0.07))) = 1$ with a standard deviation of $\sigma(R(H_p(0.07))) = 0.13$. The mean normalized response for the XRS4 is $\mu(R(H_p(10))) = 0.97$ with a standard deviation of $\sigma(R(H_p(10))) = 0.05$ and $\mu(R(H_p(0.07))) = 0.91$ with a standard deviation of $\sigma(R(H_p(0.07))) = 0.08$.

8.2 Measurements with picosecond pulses

In addition to measurements with portable X-ray generators, another X-ray radiation source is used to determine the personal dose in very short-pulsed photon fields that cause total pile-up. The ***P**etawatt **H**och- **E**nergie **L**aser für Schwer**I**onene**X**perimente* (PHELIX) at the *GSI Helmholtzzentrum für Schwerionenforschung* (GSI) is a high power laser system with maximum laser powers up to 0.5 PW [67] that can be used to produce laser induced X-ray radiation when shot onto a target (see sec. 2.1.1). Detailed information on the PHELIX facility is given in [68]. The measurements are conducted within the course of an experiment performed by another workgroup of the Physics Department at Erlangen University. For this work, only the parts of the experiment relevant to the measurements with the Dosepix dosemeter are outlined.

8.2.1 Setup

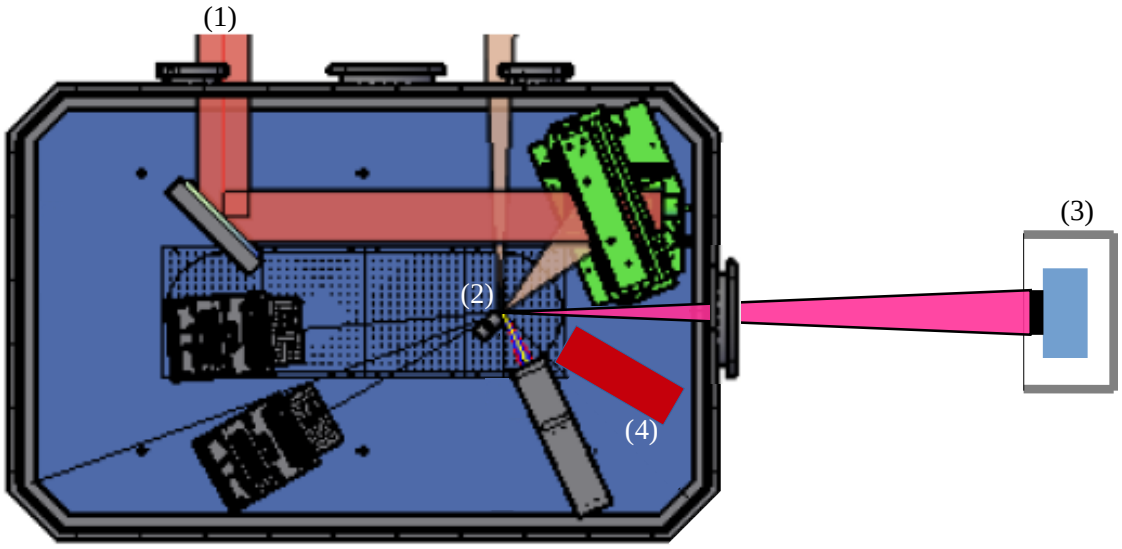

Figure 8.17 Setup at the laser facility. In an evacuated chamber, the laser (1) is focused onto a target (2). The Dosepix dosemeter (3) is placed on a slab phantom within an aluminum box. This box is placed outside the vacuum chamber. A TLD-based spectrometer (4) is placed by PTB inside the chamber for additional dose measurements and spectrum reconstruction.

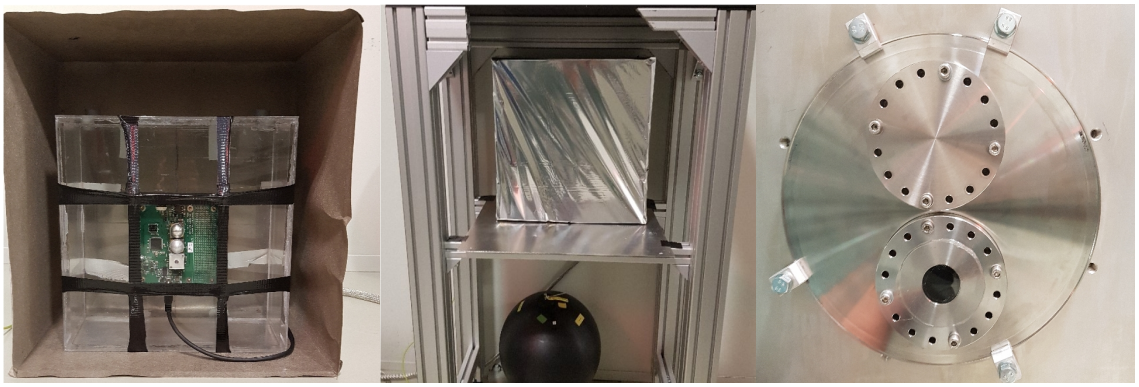

(a) **(b)** **(c)**

Figure 8.18 (a): Dosepix dosemeter placed on slab phantom inside aluminum box. The inside of the box is coated with a shielding wire fabric. (b): Grounded aluminum box with Dosepix dosemeter inside. The box is covered with a conductive plastic foil. (c): Vacuum seal with PMMA window.

Fig. 8.17 shows a schematic of the experimental setup. A pulsed laser beam (1) with a pulse duration of 0.7 ps enters an evacuated chamber. The laser is focused onto a tungsten wire (2), the so-called backlighter wire, with a diameter of either 5 µm or 10 µm. The energy of the laser pulse varied between 19.5 J and 37.9 J. The Dosepix dosemeter is placed onto a slab phantom outside the evacuated chamber. Dosemeter and phantom reside in a grounded aluminum box (3) that is coated inside with a wire fabric [69] to shield the Dosepix dosemeter from electromagnetic disturbances (see fig. 8.18a).

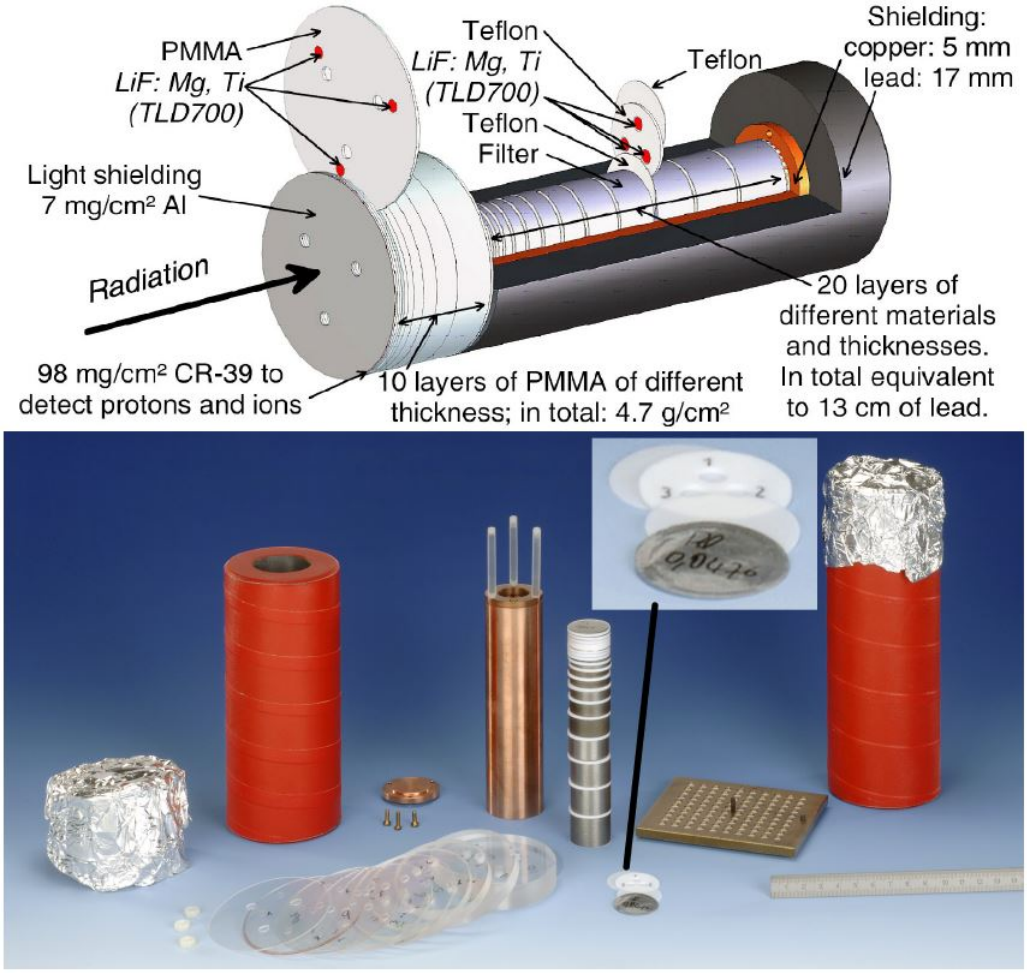

Figure 8.19 Schematic of the assembly of the TLD-based spectrometer (top) and photograph of its components (bottom). The spectrometer was developed by PTB. It is placed in the vacuum chamber to determine the reference dose. The image is taken from [70].

The front side of the aluminum box is covered with a 12 µm thick plastic foil that is electrically conductive on one side (see fig. 8.18b). The foil is conducted to the aluminum box. The Dosepix dosemeter is positioned facing the backlighter wire perpendicularly through a 0.5 mm thick PMMA window of the vacuum chamber (see fig. 8.18c). The distance between the PMMA window and the Dosepix dosemeter is 297 cm, and the distance between the backlighter wire and the PMMA window is 70 cm. The PMMA window had a diameter of 4.5 cm. Therefore, the slab phantom is not fully illuminated since the projection of the window onto the slab phantom is only about 23.5 cm in diameter. In addition, a spectrometer consisting of thermoluminescence detectors (TLDs) (4) is placed inside the vacuum chamber 20 cm away from the backlighter wire to measure the applied spectrum and the corresponding dose separately. Fig. 8.19 shows a schematic of the composition of the individual components and a corresponding photograph of the spectrometer [70]. The spectrometer is composed of filters with different sizes and TLDs to measure incoming radiation. Filters and TLDs are arranged alternately. The assembly of filters and TLDs are placed in a tube made of lead and copper to shield the TLDs from lateral irradiation. The amount of detected radiation in the individually filtered TLDs provides information about the spectrum and the applied dose. Detailed information on the spectrometer is given in [70]. The measurements with the spectrometer are conducted by [64] and evaluated by [71].

The measurements with the Dosepix dosemeter are conducted in integration-mode with $\mathrm{THL_{sub}}$ set to 20 and an I_{Krum} of 2.2 nA. 46 pulses are recorded. The time between two pulses is between 20 minutes and two hours on every measurement day. 15 pulses are performed with slab phantom and 9 without. The remaining pulses are recorded with lead shielding from other experiments between the Dosepix dosemeter and the PMMA window or an additional cover on the window. These measurements are excluded from further investigation. The TLD-based spectrometer recorded a total of 13 pulses. Due to the functioning of this spectrometer, the dose and spectrum information from the spectrometer is averaged over all acquired pulses. 4 of these 13 pulses are recorded with the Dosepix dosemeter when it is placed onto the slab phantom. All measurements are manually started and stopped after the pulse is applied. This resulted in integration times up to two hours. Therefore, a dark measurement with an integration time of 3821 s is performed beforehand to exclude noise and background. The dark measurement is performed in the absence of X-rays from the backlighter wire.

8.2.2 Results

Before the dose is determined, noise and background are subtracted from the measurements. Fig. 8.20a shows the data acquired in the dark measurement for the first Dosepix detector. Fig. 8.20b shows the same data in a smaller range. About eight pixels measured an exceptionally high ToT. This only occurs when measurements are taken for at least several minutes. This kind of noise is observed during short measurement periods, for example, with X-ray generators where the integration time is set between a few seconds and half a minute. Fortunately, always the same pixels show this noisy behavior and could be excluded from further analysis. Therefore, the pixels with the 15 highest ToT values in each detector are excluded. To estimate how much ToT is measured due to background radiation, the mean ToT of the remaining pixels is divided by the measurement time of the dark measurement (3821 s). This yields a background parameter B for each detector that is subtracted from the measurements.

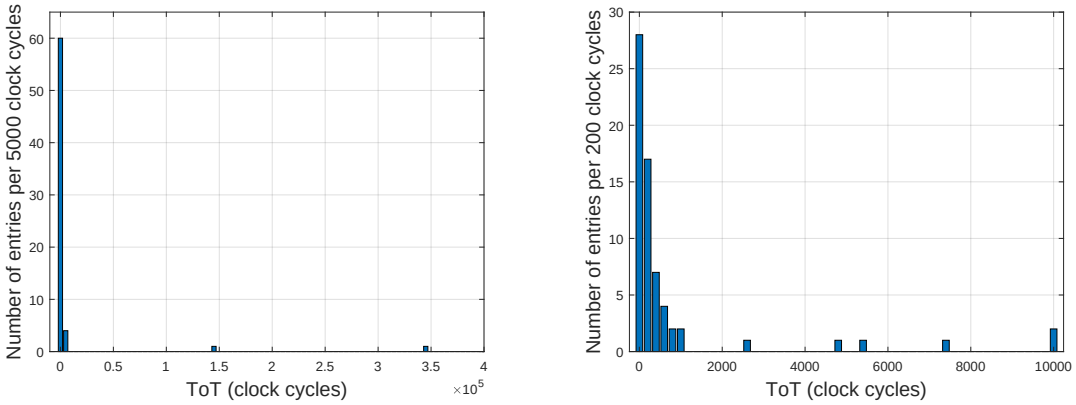

(a) Whole range **(b)** Small section

Figure 8.20 (a): Histogram of the acquired ToT by the big pixels of the first Dosepix detector in the dark measurement. (b): Data shown in (a) with a finer binning and a smaller range. Only the pixels with non-zero values are depicted.

Dosepix detector	B (clock cycles per pixel per second)
Free	$9.76 \cdot 10^{-3}$
Al	$4.84 \cdot 10^{-4}$
Sn	$1.87 \cdot 10^{-2}$

Table 8.3: Background parameter B that is derived from the dark measurement for each detector.

Tab. 8.3 lists these parameters. In the measurements with X-rays, the ToT values of the 15 excluded pixels are replaced with the mean ToT of the remaining 177 pixels. After that, B is multiplied with the measurement time of each measurement and subtracted from the measured ToT value of each pixel for each detector, respectively. The resulting ToT is converted to energy. The data is then evaluated with the neural network introduced in sec. 6.2. The resulting dose is scaled with the normalization factor that is derived in the measurements with the XR200 (see sec. 8.1.4). The mean estimated dose $H_\mathrm{p}(10)^\mathrm{DPX}$ and the corresponding standard uncertainty of the mean for all 15 measurements performed with the Dosepix dosemeter placed on the slab phantom is determined to be

$$H_\mathrm{p}(10)^\mathrm{DPX} = (1.87 \pm 0.15)\,\mu\mathrm{Sv}. \tag{8.3}$$

The mean estimated dose $H_\mathrm{p}(10)^{\mathrm{PTB}\cap\mathrm{DPX}}$ and its standard uncertainty of the mean for all four measurements recorded in the presence of the TLD spectrometer is determined to be

$$H_\mathrm{p}(10)^{\mathrm{PTB}\cap\mathrm{DPX}} = (2.6 \pm 0.3)\,\mu\mathrm{Sv}. \tag{8.4}$$

However, this dose cannot be directly compared to the dose measured with the TLD spectrometer since it is placed within the vacuum chamber and at a much smaller distance to the backlighter wire (20 cm) than the Dosepix dosemeter (367 cm). Therefore, the photon and electron fields measured with the TLD spectrometer inside the vacuum chamber are used as input for a simulation of the radiation field outside the vacuum chamber at the position of the Dosepix dosemeter [71, 72]. The simulation is performed using the software toolkit *EGSnrc* [73, 74]. The dose equivalent $H_\mathrm{p}(10)$ is calculated in two ways using the user codes *FluRZnrc* and *DosRZnrc* of EGSnrc. The user code DosRZnrc is used to directly calculate $H_\mathrm{p}(10)$ that corresponds to the simulated radiation fields at the position of the Dosepix dosemeter. According to the definition of $H_\mathrm{p}(10)$ [19], the dose equivalent is calculated in a depth of 10 mm in a slab phantom made of ICRU-tissue. The user code FluRZnrc calculates the energy-dependent fluence of the particles in a certain region of the simulated geometry. Therefore, this user code yields the energy spectrum of the particles that arrive at the position of the Dosepix dosemeter. Using the energy spectrum and the fluence, $H_\mathrm{p}(10)$ is calculated as outlined in sec. 2.3.1. The simulation is performed two times for each user code. One with the photon spectrum and one with the electron spectrum measured by the TLD spectrometer. The occurring electrons originate from the plasma that is generated from the backlighter wire. The resulting doses and particle fluences are summed up for each user code. The mean estimated dose $H_\mathrm{p}(10)^\mathrm{PTB}$ at the position of the Dosepix dosemeter and its standard uncertainty of the mean for all 13 measurements recorded with the TLD spectrometer is determined to be [71, 72]

$$H_\mathrm{p}(10)^\mathrm{PTB}(\mathrm{FluRZnrc}) = (2.83 \pm 0.14)\,\mu\mathrm{Sv} \tag{8.5}$$

and [71, 72]

$$H_\mathrm{p}(10)^\mathrm{PTB}(\mathrm{DosRZnrc}) = (2.79 \pm 0.17)\,\mu\mathrm{Sv}. \tag{8.6}$$

In both cases, the major contribution to the calculated dose arises from electrons from the plasma. The dose $H_{\mathrm{p}}^{\mathrm{e}}(10)$ that is caused by electrons at the position of the Dosepix dosemeter is [71, 72]

$$H_{\mathrm{p}}^{\mathrm{e}}(10)^{PTB}(\mathrm{FluRZnrc}) = (2.17 \pm 0.14)\mu\mathrm{Sv} \tag{8.7}$$

and [71, 72]

$$H_{\mathrm{p}}^{\mathrm{e}}(10)^{PTB}(\mathrm{DosRZnrc}) = (2.25 \pm 0.20)\mu\mathrm{Sv}. \tag{8.8}$$

The uncertainties given in the equations 8.5 to 8.8 denote the standard deviations that arise from statistical fluctuations of the simulation [71, 72]. Since the behavior of the Dosepix dosemeter is not investigated in electron fields, the difference in dose contribution cannot be taken into account. Measurements in mixed radiation fields, consisting of photons and electrons, are challenging for the Dosepix dosemeter since a photo or Compton electron cannot be distinguished from an initial electron. Nevertheless, the measurements performed with the Dosepix dosemeter and the spectrometer from PTB are in good agreement. Comparing the results yields

$$\frac{H_{\mathrm{p}}(10)^{\mathrm{PTB}\cap\mathrm{DPX}}}{H_{\mathrm{p}}(10)^{\mathrm{PTB}}(\mathrm{FluRZnrc})} = 0.9 \pm 0.1 \tag{8.9}$$

and

$$\frac{H_{\mathrm{p}}(10)^{\mathrm{PTB}\cap\mathrm{DPX}}}{H_{\mathrm{p}}(10)^{\mathrm{PTB}}(\mathrm{DosRZnrc})} = 0.9 \pm 0.1. \tag{8.10}$$

The good agreement might be coincidental. However, a mechanism that might explain the agreement qualitatively can be formulated. The minimum energy an electron needs to pass through a material can be estimated using the CSDA (continuous slowing down approximation) range given by [75]. After the electrons that are generated in the plasma pass the PMMA window in the vacuum chamber and the 3 m of air, they still need an energy of at least 370 keV [75] to penetrate the 1 mm thick PMMA lid of the Dosepix dosemeter. It can be assumed that all electrons that pass the PMMA lid and impinge onto the first detector generate a signal. Electrons that pass the PMMA lid and the aluminum filter cap of the second detector need an energy of at least 980 keV [75], and electrons that are measured by the detector with the tin cap at least 1020 keV [75]. If a majority of electrons have an energy up to 980 keV, the filtered detectors contribute only little to the electron dose. In comparison to electrons, photons with such an energy distribution would generate a higher deposited energy in the filtered detectors and a smaller in the unfiltered one. Fig. 8.21 illustrates this hypothesis qualitatively. The blue bars denote the deposited energy in each detector for an irradiation with electrons (left) and photons (right) with the same energy spectrum. The effect that the deposited energy is redistributed could lead to similar results in the dose calculation. This hypothesis can be supported by evaluating the deposited energy of the measurements. Tab. 8.4 lists the relative averaged deposited energy in each detector for measurements with both portable X-ray generators and the measurements at GSI that are carried out with a slab phantom. The measurements at GSI are sorted by the thickness of the backlighter wire. The measurements of the X-ray generators are averaged over three measurements. Here, measurements are chosen so that the applied doses match the dose measured at GSI as good as possible. The data shows that the relative amount of deposited energy in the first two detectors is very similar for the X-ray generators, even though the applied energy spectrum differs very much. The measurements at GSI show that a high fraction of the energy was deposited in the first detector, thus supporting the hypothesis outlined above.

Source	Relative energy (Free)	Relative energy (Al)	Relative energy (Sn)
XR200	58.1 %	38.2 %	4.7 %
XRS4	53.6 %	35.7 %	10.7 %
GSI(5 µm)	90.8 %	6.8 %	2.4 %
GSI(10 µm)	79.1 %	14.3 %	6.6 %

Table 8.4: Averaged relative amount of deposited energy in the three detectors for three measurements with both X-ray generators and the measurements that are carried out at GSI with slab phantom. The measurements at GSI are sorted by the backlighter wire thickness.

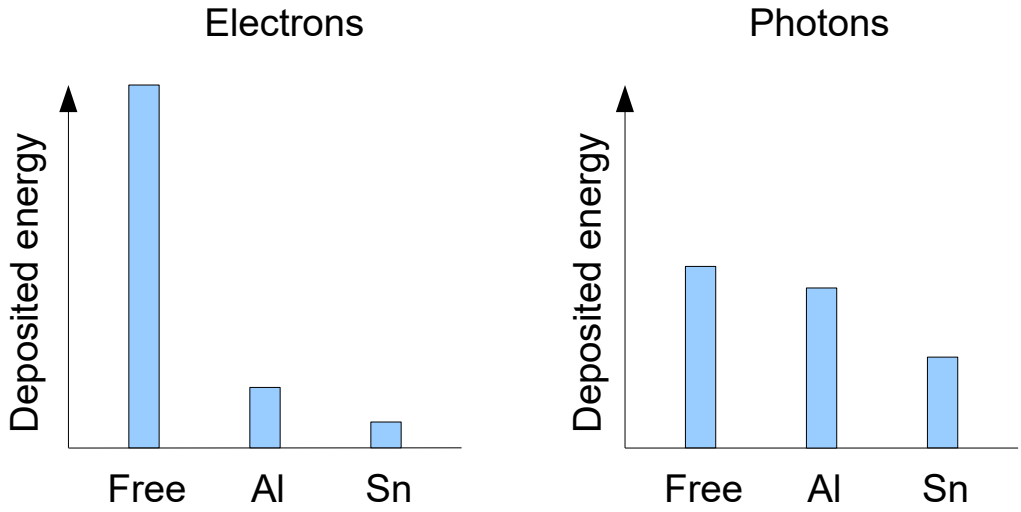

Figure 8.21 Qualitative comparison between the deposited energy in the three detectors for an initial electron field (left) and an initial photon field (right) with the same spectral distribution. This scheme does not show a general case but potentially the case for the measurements at GSI.

Besides the presence of electrons, additional circumstances can lead to inaccuracies. First, the neural network is trained with photon spectra with a maximum energy of 400 keV. However, photon energies up to several MeV are measured with the TLD spectrometer [71, 72]. At photon energies higher than 1.022 MeV nuclear pair-production can occur (see fig. 2.2). Since the maximum energy the neural network was trained with is much below 1.022 MeV, nuclear pair-production is not considered. Fortunately, most of the measured photons had energies below 400 keV [71, 72]. Another cause of inaccuracies is that both devices, the Dosepix dosemeter and the TLD spectrometer, are facing slightly different sides of the backlighter wire. If the radiation produced by the plasma is not emitted isotropically towards the two devices, they might be irradiated with different spectra and different fluences.

As outlined in sec. 2.1, the electron temperature and the power of the Bremsstrahlung that is produced in plasma correlates with the absorbed laser intensity. Therefore, the measured dose should also depend on the absorbed laser intensity. Fig. 8.22 shows the measured dose as a function of the laser energy. The red data points denote the measurements with a backlighter wire of 5 µm diameter, and the blue data points denote the measurements with a backlighter wire of 10 µm diameter.

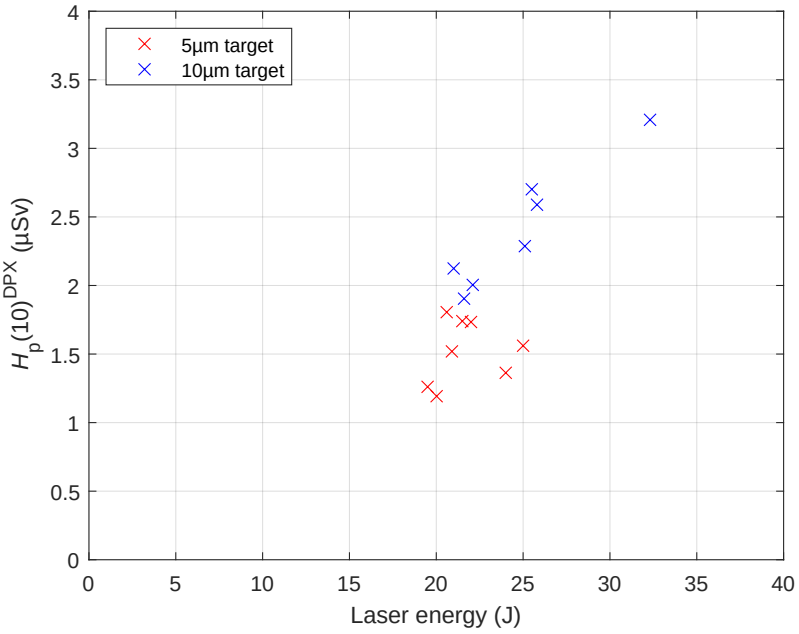

Figure 8.22 Dose measured with the Dosepix dosemeter as a function of the laser energy. The data in blue denotes measurements with a 10 µm thick target wire and the data in red the measurements with a 5 µm thick target wire.

The blue data shows a linearly increasing dependence. However, the data for the 5 µm thick target does not show such a clear dependence. A possible reason for that is the difference in size and mass of the target wire. A smaller target might lead to stronger variations of the electron temperature and the X-ray radiation intensity. In addition, the photon and electron fields for the 5 µm target wire might not be distributed as isotropic as for the 10 µm target wire.

8.3 Conclusion

It was shown that the established dose reconstruction method using the Dosi-mode outlined in sec. 6.1 overestimates the dose and provides an unstable response even for low applied doses in the range of 100 nSv in photon fields that cause total pile-up. The primary goal of this chapter was to investigate if the dose can be calculated more stable and accurately using the new neural network approach introduced in sec. 6.2.
Preparatory experiments with the XR200 indicate that the measurement behavior of the Dosepix dosemeter changes in photon fields with very high fluxes. Even pulses with doses below 100 nSv lead to a detector output that differs from what is expected in continuous radiation fields. It looks like the detector electronics behaves differently when too many pixels measure signals simultaneously. Although this disturbance is affected by the adjustments of $\mathrm{THL}_{\mathrm{sub}}$ and I_{Krum}, the measured response does not seem to be significantly influenced by the adjusted measurement parameters. Despite this disturbance, it was shown that a stable dose determination is possible. The response that was measured with the X-ray generators shows no dependence on the dose rate. Additionally, the response for both spectra shows a very similar offset even though the spectra are very different from each other. Applying normalization to balance this offset enables the Dosepix dosemeter to perform dose measurements in photon fields that cause total pile-up.

Device	$H_p(10)$		$H_p(0.07)$	
	$\mu(R)$	$\sigma(R)$	$\mu(R)$	$\sigma(R)$
XR200	1	0.11	1	0.13
XRS4	0.97	0.05	0.91	0.08

Table 8.5: Mean normalized response $\bar{R}$ and corresponding standard deviation $\sigma(R)$ of the Dosepix dosemeter to pulses from both X-ray generators and $H_p(10)$ and $H_p(0.07)$. The perfect response of 1 for the XR200 arises since the mean values for both dose quantities are used as normalization factors.

It was possible to determine the dose within a dose rate range of $(1.39 \pm 0.02) \cdot 10^3 \frac{\mathrm{Sv}}{\mathrm{h}}$ to $(8.9 \pm 0.7) \cdot 10^4 \frac{\mathrm{Sv}}{\mathrm{h}}$ for the XR200 and in a dose rate range of $(4.07 \pm 0.09) \cdot 10^4 \frac{\mathrm{Sv}}{\mathrm{h}}$ to $(2.42 \pm 0.04) \cdot 10^6 \frac{\mathrm{Sv}}{\mathrm{h}}$ for the XRS4. Tab. 8.5 lists the mean normalized responses and their standard deviations of all measurements conducted in May 2021 for both devices. The mean normalized response of 1 for the XR200 arises since this value is used for normalization. In general, the measurements with the XRS4 yield more stable results with a smaller variation compared to the XR200. A possible reason for that is the difference in age between the devices and the longer period of use of the XR200.

Additionally, the neural network approach was tested in a laser-driven X-ray backlighter experiment where pulses with a duration of 0.7 ps occurred. Here, measurements with a TLD spectrometer were carried out by [64] and evaluated by [71]. According to [71], the main contribution to the applied dose arises from electrons. Nevertheless, the Dosepix dosemeter provided very similar results. The ratio between measurements of the Dosepix dosemeter and the TLD spectrometer is 0.9 ± 0.1. However, it is unclear whether the good agreement is coincidental. The different filter caps might as well balance the presence of electrons so that a valid dose determination with the neural network approach is possible for a certain energy range of the applied mixed radiation fields. A condition on the lowest energy of the electron spectrum can be estimated for the used Dosepix dosemeter setup. Electrons need at least 370 keV to penetrate the PMMA lid of the dosemeter so the first detector can measure them. However, further measurements with electron fields need to be performed to investigate the influence of electrons on the measured dose. Radioactive sources that emit β-radiation can be used for such experiments. The mean dose ($H_p(10)$) of the pulses that are simultaneously measured with the spectrometer by PTB was determined to be (2.6 ± 0.3) µSv. Assuming that the X-ray photons and the electrons are produced in the same time as the laser pulse length, the measured dose corresponds to a dose rate of $(1.3 \pm 0.2) \cdot 10^{10} \frac{\mathrm{Sv}}{\mathrm{h}}$ or $(13 \pm 2) \frac{\mathrm{GSv}}{\mathrm{h}}$.

Chapter 9

Measurements with the integration-mode in continuous radiation fields

Contents

This chapter outlines measurements that are conducted to test the dose calculation method based on a neural network as outlined in sec. 6.2 in continuous radiation fields. Total pile-up is assumed in the simulation that is used to generate training data for the neural network. The measurements, however, are mostly performed with low dose rate photon fields, where no pile-up occurs. In the following, it is investigated if this difference can be balanced by normalization as it is applied in a type test. The general performance is investigated. For this purpose, the energy dependence, the dependence on the dose rate, and the coefficient of variation are determined. In addition, the linearity of the response for a wide range of applied dose is outlined.

9.1 Setup

The measurements are performed at the radiation facilities (see fig. 7.1) at PTB introduced in sec. 7.1. As in the former measurements, standard radiation fields that are applied in type tests for new dosemeter systems are used to investigate the energy dependence and the dose rate dependence. In the following, the measurement parameters set at each facility are outlined. At all facilities, the Dosepix dosemeter is placed on a slab phantom. All measurements are performed in integration-mode with an I_{Krum} of 11 nA and a $\mathrm{THL}_{\mathrm{sub}}$ of 20.

150 kV facility (7.1a)

The Dosepix dosemeter is placed at a distance of 2.50 m from the X-ray tube. The spectra A-20 to A-60 are applied. The irradiation time is set to 100 s, where a nominal dose of about 166 µSv is applied. The dose rate is, therefore, fixed to 6 $\frac{\mathrm{mSv}}{\mathrm{h}}$. For all spectra investigated at this facility, perpendicular irradiation is applied. Additionally, irradiation under angles of ± 30° for the A-20 spectrum and irradiation under angles of ± 60° for the A-20 and A-60 spectrum is investigated. Each measurement is performed three times.

In addition to the energy dependence, a dependence on the applied dose is investigated as well. Therefore, the exposure time is varied between 10 s, and 150 s for the A-40 spectrum. The applied dose rate is kept at 6 $\frac{\text{mSv}}{\text{h}}$. This results in applied doses between 16.7 µSv and 251 µSv.

400 kV facility (7.1b)

Set up, irradiation time, and nominal dose are the same as at the 150 kV facility. The investigated spectra are A-80 to A-300, where additional irradiation under angles of ± 60° is applied for the A-150 and the A-250 spectrum. Here, each measurement is conducted three times as well. Additionally, a dependence on the applied dose is investigated for the A-250 spectrum. Therefore, the exposure time is varied between 10 s and 150 s with a dose rate of 6 $\frac{\text{mSv}}{\text{h}}$. This resulted in applied doses between 17.1 µSv and 251 µSv.

GeSa facility (7.1c)

At this facility, the dose rate dependence is investigated. Therefore, the Dosepix dosemeter and the slab phantom are placed at a distance of 0.5 m as close as possible to the X-ray tube, but where the Dosepix dosemeter is still fully illuminated. However, since the slab phantom contributes to the measured dose via backscattering, the effect of the slab phantom is determined for the applied RQR 8 spectrum. For this purpose, two similar measurements, one with and one without slab phantom, are performed at a distance of 2.50 m, where the slab phantom is fully illuminated. Measurements in which the slab phantom could not be fully illuminated are performed without it. A correction is applied later. Furthermore, the irradiation angle alters slightly when the Dosepix dosemeter is moved towards the X-ray tube. Two measurements are performed at a distance of 0.5 m, and 2.5 m without slab phantom to correct for this effect. The dose rate is kept constant. The pulse duration is varied between 10 ms and 10 s. Dose rates between 0.062 $\frac{\text{Sv}}{\text{h}}$ and 685 $\frac{\text{Sv}}{\text{h}}$ are achieved. The measurements are repeated three times for each adjusted dose rate. The maximum applied dose is 5.5 mSv.

Radioactive sources facility (7.1d)

At this facility, the coefficient of variation (see sec. 2.3.2) is determined for both radiation sources ^{137}Cs and ^{60}Co. Therefore, ten measurements for each radiation source are performed with an exposure time of 100 s. The nominal applied dose per measurement is set to 166 µSv for ^{137}Cs and 75 µSv for ^{60}Co. The dose rate is set in accordance with the other parameters by adjusting the distance between the Dosepix dosemeter and the radiation sources. An additional PMMA plate is placed directly in front of the Dosepix dosemeter. This practice is applied to shield tested dosemeters from secondary electrons that are generated by the γ-radiation in the air between the radioactive source and the dosemeter. The plate also ensures that secondary electron equilibrium is achieved for the dosemeter. In addition, a dependence of the response on the applied dose is investigated as well. For this purpose, the exposure time is varied between 60 s and 600 s with two different dose rates of 1 $\frac{\text{Sv}}{\text{h}}$ and 36 $\frac{\text{mSv}}{\text{h}}$ for ^{60}Co. This resulted in applied doses between 60 µSv and 82 mSv.

9.2 Results

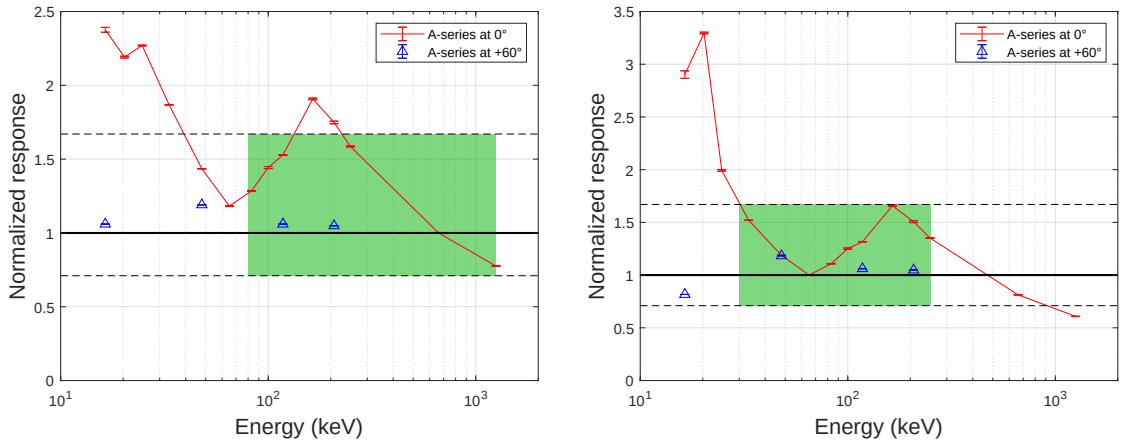

(a) $H_p(10)$ **(b)** $H_p(0.07)$

Figure 9.1 Normalized response as a function of the mean energy of the A-series and the radioactive sources for perpendicular irradiation (red) and under angels of +60° (blue) for (a) $H_p(10)$ and (b) $H_p(0.07)$. The black dashed lines indicate the upper and lower PTB limits on the normalized response. The green area shows the required energy range within this allowed response range. The error bars denote the standard uncertainties of the mean normalized responses.

All measurements are evaluated with the neural network described in sec. 6.2. Fig. 9.1a and 9.1b show the normalized response as a function of the mean energy of the applied spectra for $H_p(10)$ and $H_p(0.07)$. The red data points denote the A-series at 0°, and the blue data points denote the measurements under an angle of +60°. All measurements are performed three times. The error bars denote the standard uncertainties of the mean normalized responses. The data of the A-series is normalized to the response of ^{137}Cs for $H_p(10)$ and to the response of the A-80 spectrum for $H_p(0.07)$. The black dashed lines denote the PTB limits on the normalized response. The green area denotes the minimum required energy range. The data of the angle measurements is normalized to the response of the corresponding measurement for an irradiation angle of 0°. $H_p(10)$ is overestimated for low energies and declines towards a local minimum at about 65 keV. Within the minimum energy range of 65 keV to 1250 keV, the data for the A-200 spectrum at an energy of 166.5 keV exceeds the upper PTB limit of 1.68 with a normalized response of 1.908 ± 0.006. Like $H_p(10)$, $H_p(0.07)$ is overestimated for energies below 30 keV. The upper PTB limit is undercut at an energy of about 30.3 keV. From here on, the course of the normalized response is very similar to the one of $H_p(10)$ with a local minimum at 65 keV, which denotes the response value the data is normalized to. The normalized response stays within the PTB limits and undercuts them only for the data point of the ^{60}Co source. The measurements under angles of +60° reside within the required limits for $H_p(10)$ and $H_p(0.07)$.

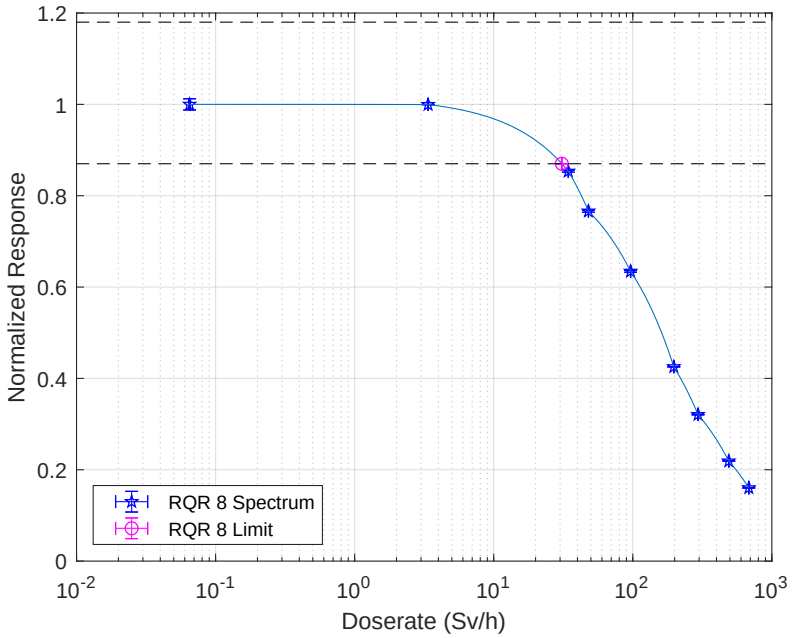

Figure 9.2 Normalized response for $H_p(10)$ of a RQR 8 spectrum as a function of the dose rate (blue). The magenta circle denotes the break-up point.

Fig. 9.2 shows the results of the measurements with the RQR 8 spectrum at the GeSa facility. The normalized response is depicted as a function of the applied dose rate (blue). The data is normalized to the data point at 0.064 $\frac{\text{Sv}}{\text{h}}$ and is linearly interpolated. The black dashed lines denote the PTB limits on the normalized response. After the data point at about 3.7 $\frac{\text{Sv}}{\text{h}}$ the normalized response starts to decline and undercuts the limit at a dose rate of about 31 $\frac{\text{Sv}}{\text{h}}$ (magenta circle). The applied doses range from 1 mSv to 5.5 mSv and are therefore two orders of magnitude higher than the maximum dose simulated for the training data of the neural network. The higher dose alone, however, does not explain the declining course. Fig. 9.3a and 9.3b show the response for an A-40 spectrum (blue), an A-250 spectrum (red) and the ^{60}Co source for $H_p(10)$ and $H_p(0.07)$. The response is depicted as a function of the applied dose. As mentioned above, the dose rates are set very low. No declining trend occurs for any of the investigated spectra. The response for the A-250 spectrum even seems to rise a little. The maximum measurable dose is limited by the storing capacity of the integration-mode (24 bit). If the ToT counter exceeds 2^{24}, it is set to zero and continues to measure the ToT.

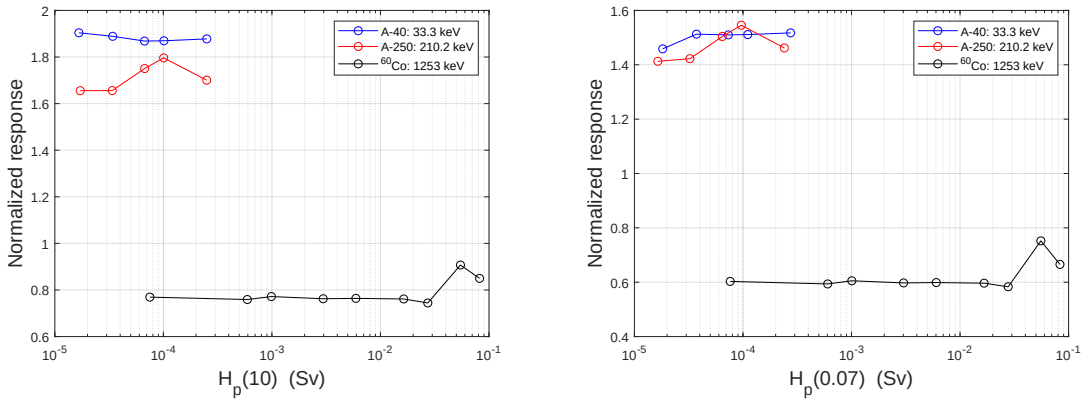

(a) Dose linearity $H_p(10)$ **(b)** Dose linearity $H_p(0.07)$

Figure 9.3 Response for an A-40 spectrum (blue), an A-250 spectrum (red) and a ^{60}Co source (black) as a function of (a): $H_p(10)$ and (b): $H_p(0.07)$.

Dose range	v_{max} (%)	$v^{Cs}(H_p(10))$(%)	$v^{Co}(H_p(10))$ (%)
$H_{ref} < 0.1$ mSv	15	/	0.8
0.1 mSv $\leq H_{ref} <$ 1.1 mSv	14.3	1.0	/
1.1 mSv $\leq H_{ref}$	5	/	/

Table 9.1: Limits on the coefficient of variation for $H_p(10)$.

Dose range	v_{max} (%)	$v^{Cs}(H_p(0.07))$ (%)	$v^{Co}(H_p(0.07))$ (%)
$H_{ref} < 1$ mSv	15	1.1	0.9
1 mSv $\leq H_{ref} <$ 11 mSv	14.3	/	/
11 mSv $\leq H_{ref}$	5	/	/

Table 9.2: Limits on the coefficient of variation for $H_p(0.07)$.

The coefficient of variation is calculated using equ. 2.41 for two different applied doses. v^{Cs} corresponds to the coefficient of variation that is measured with the ^{137}Cs source and v^{Co} to the one measured with the ^{60}Co source. The limits on the coefficient of variation v_{max} are determined according tab. 2.3. The applied reference doses are listed in tab. 9.3. The references doses do not exceed 1 mSv. Therefore, only two dose ranges are covered for $H_p(10)$ and only one for $H_p(0.07)$. Tab. 9.1 lists v_{max}, v^{Cs} and v^{Co} for the corresponding dose ranges for $H_p(10)$. Tab. 9.2 lists these values for $H_p(0.07)$. Within the tested ranges, the maximum coefficient of variation is not exceeded.

	$H_p(10)$ (mSv)	$H_p(0.07)$ (mSv)
^{137}Cs	0.167	0.167
^{60}Co	0.075	0.075

Table 9.3: Applied reference doses H_{ref} for the radioactive sources.

9.3 Conclusion

The main goal of this chapter was to investigate if reliable dose measurements can be performed with continuous radiation using the neural network analysis for total pile-up. The possibility that normalization might balance deviations that arise from the difference between measurements in total pile-up and non-pile-up photon fields was the motivation for this measurement series.

The PTB requirements on the energy dependence is almost fulfilled for both $H_\mathrm{p}(10)$ and $H_\mathrm{p}(0.07)$. Only very slight deviations from the allowed range occurred for $H_\mathrm{p}(0.07)$. The coefficients of variation for the tested dose ranges also showed sufficient results. The measurements for different dose rates show the same descending course as for the measurements in Dosi-mode. The dose rate, at which the lower PTB limit is undercut, however, is lower with a break-up dose rate of about 31.2 $\frac{\mathrm{Sv}}{\mathrm{h}}$. Here, the break-up dose rate is far lower than the dose rates measured with the X-ray generators. As outlined in sec. 5.1 a difference between very low dose rates (no pile-up) and very high dose rates (total pile-up) is expected. The mean energy of the RQR 8 spectrum is about 51 keV. The mean energy deposited in the first detector when it is irradiated with monoenergetic X-rays with an energy of 51 keV is about 18.76 keV. The ratio

$$\lim_{N\to\infty} \frac{\mathrm{ToT}^{\mathrm{NP}}}{\mathrm{ToT}^{\mathrm{TP}}}$$

as calculated in equ. 5.3 for a deposited energy of 18.76 keV is about 4.84. Although this is just a rough estimate for the maximum effect pile-up can have, this change in ToT contributes to the descending of the response. The dependence of the response with the applied dose was tested as well. Three different spectra were investigated and showed that the neural network yields a stable response, even for applied doses that are several times higher than the maximum simulated dose in the training data of the neural network. The results of this measurement series are unexpectedly positive. However, the unsteady response that slightly exceeds the allowed regions in the energy dependence is still a problem.

Chapter 10

Summary and outlook

The Dosepix detector was designed for dosimetric measurements in photon fields with dose rates of several hundreds $\frac{\mathrm{Sv}}{\mathrm{h}}$, as they occur in the medical sector. The functionality of a dosemeter based on three Dosepix detectors operated in Dosi-mode was proven and already published during the making of this thesis [30, 31]. This marks a major step in personal dosimetry since active personal dosemeters are enabled to measure the dose, or at least give a warning signal to the exposed person, in high dose rate photon fields. Concerning the dose rate, only $H_\mathrm{p}(10)$ was investigated here in detail. However, the required energy dependence of the normalized response was achieved for $H_\mathrm{p}(10)$ and $H_\mathrm{p}(0.07)$.

Advanced characteristics of the Dosepix detector were investigated. Here, measurements were conducted that show an oscillation-like course of the energy-ToT calibration curve that was investigated theoretically in [39]. Two calibration models, one that is commonly used and one that takes these oscillations into account, were investigated in this thesis. The influence of a change of the energy calibration model on the dose determination was evaluated in measurements. It was shown that the deviation between the two calibration curves, which can reach more than 5 % for individual pixels, has no major effect on the dose calculation. Here, the difference is smaller than 2 % within the tested energy ranges for $H_\mathrm{p}(10)$ and $H_\mathrm{p}(0.07)$. The PTB requirements on the normalized response and energy range in continuous radiation fields are fulfilled for both calibration methods. Furthermore, the dependence of the normalized response for an RQR 8 spectrum on the maximum dose rate that resides within the PTB limits was investigated. For the big pixels, a maximum dose rate of 111 $\frac{\mathrm{Sv}}{\mathrm{h}}$ was measured. The break-up dose rate for the small pixels was determined to be 185 $\frac{\mathrm{Sv}}{\mathrm{h}}$. The maximum dose rate that could be applied with a radioactive ^{60}Co source with a mean photon energy of 1250 keV was about 30 $\frac{\mathrm{Sv}}{\mathrm{h}}$. At this dose rate, the normalized response of the big and the small pixels stayed within the PTB requirements. It was also shown that the break-up dose rate is dependent on the applied spectrum. An analysis for spectra that differ only in the applied X-ray tube voltage shows an increasing dependence of the break-up dose rate with the mean energy of the applied spectra. However, an additional filtered spectrum yields a very different break-up dose rate. This indicates that pile-up depends on the applied spectrum. Further, a measurement series was conducted with a higher I_Krum that led to a very different behavior of pile-up as well. In future works, optimizing I_Krum might yield a break-up voltage several times larger than what was measured here.

The performance of the Dosepix dosemeter operated in Dosi-mode was tested in short-pulsed photon fields that cause total pile-up exclusively. Here, the dose reconstruction method was unstable with the increasing dose rate. Measurements in ToT-mode showed an unexpected behavior of the Dosepix detector in such photon fields.

A dependence of $\mathrm{THL_{sub}}$ and I_{Krum} on this distortion-like behavior was investigated. Despite this unexpected characteristic of the Dosepix detector, a stable dose determination over a wide dose rate range was observed. For this purpose, the detector output in integration-mode and irradiated with photon fields that cause total pile-up in the pixel electronics was simulated. This simulation was used to generate training and validation data for a neural network. Two different X-ray generators that produce pulses with lengths of 10 ns and 115 ns were used to test this method. The maximum applied dose rate in the measurements was $(2.42 \pm 0.04) \cdot 10^6 \, \frac{\mathrm{Sv}}{\mathrm{h}}$. The data for the XR200 was used to determine a normalization factor for $H_{\mathrm{p}}(10)$ and $H_{\mathrm{p}}(0.07)$ respectively. Therefore, the mean normalized response for all tested dose rates is exactly 1. The standard deviation on the normalized response for this device was determined to be $\sigma(R(H_{\mathrm{p}}(10))) = 0.11$ and $\sigma(R(H_{\mathrm{p}}(0.07))) = 0.13$. The response of the XRS4 X-ray generator does not contribute to the normalization factor. Here, the mean and the standard deviation of the normalized response for all tested dose rates were determined to be $\mu(R(H_{\mathrm{p}}(10))) = 0.97$, $\sigma(R(H_{\mathrm{p}}(10))) = 0.05$ and $\mu(R(H_{\mathrm{p}}(0.07))) = 0.91$, $\sigma(R(H_{\mathrm{p}}(0.07))) = 0.08$. In addition to commonly used X-ray generators, X-ray pulses from a laser-induced plasma source (X-ray backlighter) were used to test the neural network analysis. Here, the mean hypothetical dose rate was $(13 \pm 2) \, \frac{\mathrm{GSv}}{\mathrm{h}}$. Additional dose measurements with a well-established spectrometer system were performed by PTB. The dose measured with this spectrometer and the dose measured with the Dosepix dosemeter are in good agreement even though a mixed photon field consisting of photons and electrons occurred [71, 72]. Here, the ratio between the dose measured by the Dosepix dosemeter and the spectrometer was determined to be 0.9 ± 0.1. Since the analytical method that was used on data from the Dosepix dosemeter was not designed to measure the dose in mixed radiation fields, the good agreement with the measurements from PTB is unexpected. The good agreement might be coincidental. However, it might be that the different filters balance the effect that an additional electron contribution has on the dose measurement for a certain energy range of the applied electron spectrum. Here, further investigations need to be performed. Radioactive reference sources that emit β-radiation (for example, at PTB) can be used as reference. This way, the neural network analysis can be tested in different electron fields, and the influence electrons have on the dose measurement could be estimated.

The performance of the neural network analysis was investigated in regular photon fields as they occur in a type test that is performed at PTB. Although the simulation used to generate the training data for the neural network only includes photon fields where total pile-up occurs, the results are good. The energy dependence, yet unstable, almost fulfills the requirements given by PTB. The dependence of the response on the applied dose shows a stable course before starting to decline. A break-up dose rate of about 31 $\frac{\mathrm{Sv}}{\mathrm{h}}$, which is far below the occurring dose rates in the medical sector, was measured. This value, however, fulfills the current requirement on the dose rate given by PTB. The positive results that were achieved with a neural network that has not even been trained for the tested tasks indicate that it is possible to perform a stable dose determination with the integration-mode. For this purpose, a more complex simulation that allows different levels of pile-up is required. This, however, could change the performance of the network on measurements in total pile-up. Here, more investigations need to be done if the dose in pulsed and non-pulsed radiation with and without the occurrence of total pile-up is to be determined using a single method. The maximum measurable dose with the integration-mode is limited. The storing capacity for ToT in a single pixel is 24 bit in integration-mode. If the ToT counter exceeds 2^{24}, it is set to zero and continues to measure the ToT. The Dosepix detector, when operated in this mode, cannot be read out continuously without dead time. A rolling shutter, as it is implemented for the Dosi-mode would be required.

In this work, certain characteristics of the Dosepix detector and its behavior in extreme conditions were investigated. The measurements and analytical methods show that the Dosepix dosemeter is suited for various tasks in dosimetry. Here, only two dosimetric quantities, $H_\mathrm{p}(10)$ and $H_\mathrm{p}(0.07)$ were looked at. Using simulated data, information about the maximum applied energy could be derived in future work. Such a kVp-meter provides information about the applied X-ray tube voltage and could be realized for X-ray radiation in the case of total pile-up. Additionally, mainly the big pixels were considered. Even higher dose rates and more stable results can be achieved with the small pixels, which are more robust in photon fields with high dose rates due to their smaller sensitive area. Although many practical problems still need to be solved and further experiments need to be conducted, the dosemeter harbors the potential to extend the limits on the measurability of dose quantities in active personal dosimetry.

Appendix A

Appendix

Element	Mean initial energy (keV)	Mean deposited energy (keV)
Cu	8.133	7.99
Se	11.359	10.86
Sr	14.355	13.89
Mo	17.731	17.22
Ag	22.500	21.93
Sn	25.667	24.94
I	29.067	28.18
Ba	32.710	31.80
Nd	37.953	36.76
Gd	43.681	42.43
^{241}Am	59.541	59.74

Table A.1: Fluorescence materials and their characteristic mean energies as calculated in equ. 4.8 and their simulated deposited energy.

Index i	k_i^{Free} (keV)	$H_p(10)$ (µSv)	k_i^{Al} (keV)	$H_p(10)$ (µSv)	k_i^{Sn} (keV)	$H_p(10)$ (µSv)
1	12.0	$2.550958 \cdot 10^{-5}$	12.0	0.000151	32.0	0.000729
2	18.0	$4.217108 \cdot 10^{-5}$	17.0	$4.885910 \cdot 10^{-5}$	37.0	0.000670
3	21.0	$5.638798 \cdot 10^{-5}$	31.0	0.000131	47.0	0.000937
4	24.5	$6.995226 \cdot 10^{-5}$	40.0	0.000175	57.5	0.001129
5	33.5	$6.319448 \cdot 10^{-5}$	45.5	0.000230	68.5	0.001757
6	43.0	0.000104	50.5	0.000258	80.0	0.001830
7	53.5	0.000135	60.5	0.000335	91.5	0.001725
8	66.5	0.000145	68.0	0.000428	104.0	0.001241
9	81.5	0.000455	91.0	0.001045	117.0	0.001161
10	97.0	0.000529	102.5	0.001938	131.0	0.000750
11	113.0	0.000785	133.0	0.001993	145.0	0.000284
12	131.5	0.001135	148.0	0.002938	163.5	$1.969764 \cdot 10^{-5}$
13	151.5	0.001556	163.0	0.003994	183.5	$4.704539 \cdot 10^{-5}$
14	173.0	0.001664	196.0	0.003186	207.5	$4.975624 \cdot 10^{-6}$
15	200.5	0.000891	220.0	0.004766	234.5	0.000156
16	236.0	0.002358	257.0	0.007243	269.5	0.001618

Table A.2: Used conversion factors for the big pixels of the three Dosepix detectors that convert the number of registered events to $H_p(10)$. The factors were simulated in the frame of a PhD thesis [39].

Index i	k_i^{Free} (keV)	$H_p(10)$ (µSv)	k_i^{Al} (keV)	$H_p(10)$ (µSv)	k_i^{Sn} (keV)	$H_p(10)$ (µSv)
1	11.0	0.000264	10.0	0.018048	22.0	0.032049
2	16.0	0.001922	15.5	0.006908	40	0.034066
3	26.0	0.002058	23.0	0.012566	47.5	0.028994
4	36.0	$1.422462 \cdot 10^{-5}$	31.5	55.5	0.002547	0.072572
5	46.5	0.000721	42.0	0.005724	64.0	0.043864
6	57.0	0.005078	53.5	0.000362	74.0	0.035969
7	70.5	0.008893	66.5	0.005105	84.5	0.078893
8	84.5	0.010286	79.5	0.006187	98.0	0.140491
9	99.5	0.020962	94.5	0.011157	113.0	0.077536
10	115.0	0.008471	109.0	0.011462	128.5	0.046069
11	131.0	0.008759	126.0	0.009690	144.5	0.166983
12	148.5	0.051790	142.5	0.070735	161.5	0.057551
13	167.0	0.144565	160.5	0.158539	182.5	0.012269
14	194.0	0.002248	180.0	0.006506	203.5	0.001667
15	223.0	0.000863	200.0	0.004674	232.0	0.004715
16	260.0	0.005143	221.5	0.001592	264.5	0.005005

Table A.3: Used conversion factors for the small pixels of the three Dosepix detectors that convert the number of registered events to $H_p(10)$. The factors were simulated in the frame of a PhD thesis [39].

Index i	k_i^{Free} (keV)	$H_p(0.07)$ (µSv)	k_i^{Al} (keV)	$H_p(0.07)$ (µSv)	k_i^{Sn} (keV)	$H_p(0.07)$ (µSv)
1	12.0	0.003104	12.0	0.007169	32.0	0.001601
2	18.0	0.001076	17.0	0.004728	37.0	0.000157
3	21.0	0.001634	31.0	0.003142	47.0	0.000179
4	24.5	0.001738	40.0	0.003853	57.5	0.000817
5	33.5	0.001098	45.5	0.002877	68.5	$1.952808 \cdot 10^{-5}$
6	43.0	0.000741	50.5	0.001929	80.0	0.001121
7	53.5	0.000381	60.5	0.001505	91.5	0.000885
8	66.5	0.000352	68.0	0.000717	104.0	0.001900
9	81.5	0.000201	91.0	0.000313	117.0	0.001155
10	97.0	0.000129	102.5	0.000317	131.0	0.001479
11	113.0	0.000102	133.0	0.000219	145.0	0.001569
12	131.5	$8.739615 \cdot 10^{-5}$	148.0	0.000195	163.5	0.001217
13	151.5	$8.020446 \cdot 10^{-5}$	163.0	0.000143	183.5	0.001062
14	173.0	$8.638210 \cdot 10^{-5}$	196.0	$9.585715 \cdot 10^{-5}$	207.5	0.000754
15	200.5	$5.299497 \cdot 10^{-5}$	220.0	$5.022166 \cdot 10^{-5}$	234.5	0.000533
16	236.0	0.000112	257.0	$3.322555 \cdot 10^{-5}$	269.5	0.001003

Table A.4: Used conversion factors for the big pixels of the three Dosepix detectors that convert the number of registered events to $H_p(0.07)$. The factors were simulated in the frame of a PhD thesis [39].

List of Figures

List of Tables

References

[1] Wilhelm Conrad Röntgen. "Ueber eine neue Art von Strahlen". In: *Sitzungsberichte der Würzburger physik.-med. Gesellschaft Würzburg* (1895). URL: http://posner.library.cmu.edu/Posner/books/pages.cgi?call=548_R77N_VOL._1&layout=vol0/part0/copy0&file=0004.

[2] Bundesamt für Strahlenschutz. *Grenzwerte für beruflich exponierte Personen*. [Online], https://www.bfs.de/DE/themen/ion/strahlenschutz/beruf/grenzwerte/grenzwerte.html, [accessed on 08.11.2021].

[3] Physikalisch-Technische Bundeanstalt Braunschweig und Berlin. *Problematik bei Messungen in gepulsten Photonen-Strahlungsfeldern*. September 2009. URL: https://www.ptb.de/cms/fileadmin/internet/fachabteilungen/abteilung_6/6.3/bap/gepstrl.pdf.

[4] Oliver Hupe, Hayo Zutz, and Jana Klammer. *Radiation Protection Dosimetry in Pulsed Radiation Fields*. [Online], https://www.irpa.net/members/TS2f.3.pdf, [accessed on 08.11.2021].

[5] F. Vanhavere et al. *EURADOS Report 2012-02, ORAMED: Optimization of Radiation Protection of Medical Staff*. 2012. URL: https://eurados.sck.hosted-temp.com/sites/eurados/files/uploads/Report-Publications/Reports/2012/EURADOS%5C%20Report%5C%202012-02.pdf.

[6] Golden Engineering Inc. Portable X-ray technology. *Non-Destructive Testing (NDT)*. [Online], http://www.goldenengineering.com/applications/non-destructive-testing-ndt/, [accessed on 08.11.2021].

[7] OR Technology. *Portable monoblock X-ray machines in small animal practices and equine clinics*. [Online], https://www.or-technology.com/en/products/vet/amadeo-p-systems.html, [accessed on 08.11.2021].

[8] Golden Engineering Inc. Portable X-ray technology. *Pulsed X-Ray Technology*. [Online], http://www.goldenengineering.com/home/products/, [accessed on 08.11.2021].

[9] W. Demtröder. *Experimentalphysik 3: Atome, Moleküle und Festkörper*. Springer-Lehrbuch. Springer-Verlag Berlin Heidelberg New York, 2000. ISBN: 3-540-66790-3.

[10] Hanno Krieger. *Grundlagen der Strahlungsphysik und des Strahlenschutzes*. Vieweg + Teubner Verlag, 2012. ISBN: 978-3-8348-2238-3.

[11] Horst Aichinger et al. *Radiation Exposure and Image Quality in X-Ray Diagnostic Radiology*. Springer-Verlag Berlin Heidelberg New York, 2004. ISBN: 3-540-44287-1.

[12] Björn Borm, Dimitri Khaghani, and Paul Neumayer. "Properties of laser-driven hard x-ray sources over a wide range of laser intensities". In: *Physics of Plasmas* 26.2 (2019), p. 023109. DOI: 10.1063/1.5081800. eprint: https://doi.org/10.1063/1.5081800. URL: https://doi.org/10.1063/1.5081800.

[13] Danilo Giulietti and Leonida Gizzi. "X-ray emission from laser-produced plasmas". In: *La Rivista del Nuovo Cimento* 21 (October 1998). DOI: 10.1007/BF02874624.

[14] Ervin B. Podgoršak. *Radiation Physics for Medical Physicists*. e-isbn: 978-3-642-008745-7. Springer-Verlag Berlin Heidelberg, 2010.

[15] Martin Berger et al. *XCOM: Photon Cross Section Database (version 1.2)*. [Online], http://physics.nist.gov/xcom, [accessed on 11.10.2020]. January 1999.

[16] Ian Goodfellow, Yoshua Bengio, and Aaron Courville. *Deep Learning*. http://www.deeplearningbook.org. MIT Press, 2016.

[17] C.M. Bishop. *Neural networks for pattern recognition*. Oxford University Press, USA, 1995. ISBN: 0198538642.

[18] Diederik P. Kingma and Jimmy Ba. *Adam: A Method for Stochastic Optimization*. 2017. arXiv: 1412.6980 [cs.LG].

[19] ICRU. "Report 57: Conversion Coefficients for use in Radiological Protection against External Radiation". In: *Journal of the International Commission on Radiation Units and Measurements* (August 1998).

[20] Peter Ambrosi et al Wolfgang G. Alberts. *PTB-Dos-23e, New dose quantities in radiation protection*. 1995. ISBN: 3-89429-932-0.

[21] International Organization for Standardization. *ISO 4037-3: X and gamma reference radiation for calibrating dosemeters and dose rate meters and for determining their response as a function of photon energy - Part 3: Calibration of area and personal dosemeters and the measurement of their response as a function of energy and angle of incidence*. ISO 4037-3:1999(E), First edition 1999-06-15.

[22] Hiroshi Akima. "A New Method of Interpolation and Smooth Curve Fitting Based on Local Procedures". In: *J. ACM* 17.4 (October 1970), pp. 589–602. ISSN: 0004-5411. DOI: 10.1145/321607.321609. URL: https://doi.org/10.1145/321607.321609.

[23] Hiroshi Akima. "A Method of Bivariate Interpolation and Smooth Surface Fitting Based on Local Procedures". In: *Commun. ACM* 17.1 (January 1974), pp. 18–20. ISSN: 0001-0782. DOI: 10.1145/360767.360779. URL: https://doi.org/10.1145/360767.360779.

[24] *Physikalisch-Technische Bundesanstalt (PTB)*. [Online], https://www.ptb.de/cms/, [accessed on 19.01.2022].

[25] Physikalisch-Technische Bundeanstalt Braunschweig und Berlin. *PTB-Anforderungen für Strahlenschutzmessgeräte, Personendosimeter zur Messung der Tiefe- und Oberflächen-Personendosis*. November 2013. URL: https://oar.ptb.de/files/download/56d6a9e6ab9f3f76468b4627.

[26] Physikalisch-Technische Bundesanstalt Braunschweig und Berlin. *Ergänzung der PTB-Anforderungen PTB-A 23.2: Strahlenschutzmessgeräte; Personendosimeter zur Messung der Tiefen- und Oberflächen-Personendosis*. November 2018. URL: https://doi.org/10.7795/510.20181129A.

[27] Physikalisch-Technische Bundesanstalt Braunschweig und Berlin. *Radiation qualities used for studies in radiation protection*. [Online], https://www.ptb.de/cms/fileadmin/internet/fachabteilungen/abteilung_6/6.2/6.25/ptb_rad_qual_2015_01_07.pdf, [accessed on 05.10.2019], Last update: 01.07.2015.

[28] International Organization for Standardization. *ISO 4037-1: X and gamma reference radiation for calibrating dosemeters and dose rate meters and for determining their response as a function of photon energy - Part 1: Radiation characteristics and production methods*. ISO 4037-1:1996(E).

[29] Oliver Hupe et al. “Determining the dose rate dependence of different active personal dosemeters in standardized pulsed and continuous radiation fields”. In: *Radiation protection dosimetry* 187 (September 2019). DOI: 10.1093/rpd/ncz173.

[30] Dennis Haag et al. “Personal Dosimetry in Continuous Photon Radiation Fields With the Dosepix Detector”. In: *IEEE Transactions on Nuclear Science* PP (March 2021), pp. 1–1. DOI: 10.1109/TNS.2021.3068832.

[31] Dennis Haag et al. “Personal Dosimetry in Pulsed Photon Fields with the Dosepix Detector”. In: (June 2021). arXiv: 2106.06714 [physics.med-ph].

[32] Winnie Sze-Wing Wong. “A Hybrid Pixel Detector ASIC with Energy Binning for Real-Time, Spectroscopic Dose Measurements”. PhD thesis. Electronics Design Division, in the Department of Information Technology and Media Mid Sweden University SE-851 70 Sundsvall, Sweden, 2012.

[33] [Online], https://www.iba-dosimetry.com/, [accessed on 10.11.2020].

[34] [Online], http://medipix.web.cern.ch/, [accessed on 10.11.2020].

[35] Michael Böhnel. “Evaluierung und Entwicklung von Röntgendetektoren für die Dosimetrie”. Friedrich-Alexander-Universität Erlangen-Nürnberg, 2012.

[36] Thomas Gabor. “Simulation und Experimente zur Anwendung eines neuartigen spektroskopischen Pixeldetektors in der Personendosimetrie”. Diplomarbeit. Friedrich-Alexander Universität, Erlangen-Nürnberg, 2012.

[37] S.Y.F. Chu, L.P. Ekström, and R.B. Firestone. *The Lund / LBNL Nuclear Data Search*. [Online], http://nucleardata.nuclear.lu.se/toi/, [accessed on 10.11.2021]. 1999.

[38] Florian Beißer. “Temperature Dependence of the Hybrid Pixel Detector Dosepix with respect to IKrum variation”. Friedrich-Alexander Universität Erlangen-Nürnberg, 2019.

[39] Sebastian Schmidt. “Dosimetry and X-ray spectroscopy with the photon counting pixel detector Dosepix”. PhD thesis. Friedrich-Alexander-Universität Erlangen-Nürnberg, November 2021.

[40] S. Spannagel et al. “Allpix2: A modular simulation framework for silicon detectors”. In: *Nuclear Instruments and Methods in Physics Research Section A: Accelerators, Spectrometers, Detectors and Associated Equipment* 901 (2018), pp. 164–172. ISSN: 0168-9002. DOI: https://doi.org/10.1016/j.nima.2018.06.020. URL: https://www.sciencedirect.com/science/article/pii/S0168900218307411.

[41] S. Agostinelli et al. “Geant4—a simulation toolkit”. In: *Nuclear Instruments and Methods in Physics Research Section A: Accelerators, Spectrometers, Detectors and Associated Equipment* 506.3 (2003), pp. 250–303. ISSN: 0168-9002. DOI: https://doi.org/10.1016/S0168-9002(03)01368-8. URL: https://www.sciencedirect.com/science/article/pii/S0168900203013688.

[42] William R. Leo. “Semiconductor Detectors”. In: *Techniques for Nuclear and Particle Physics Experiments: A How-to Approach*. Berlin, Heidelberg: Springer Berlin Heidelberg, 1994, pp. 215–247. ISBN: 978-3-642-57920-2. DOI: 10.1007/978-3-642-57920-2_10. URL: https://doi.org/10.1007/978-3-642-57920-2_10.

[43] Xavier Llopart Cudie. “Design and Characterization of 64K Pixels Chips Working in Single Photon Processing Mode”. Presented on 25 May 2007. 2007. URL: http://cds.cern.ch/record/1056683.

[44] Siemens Healthineers. *X-ray tubes & x-ray tube assemblies*. [Online] https://www.oem-products.siemens-healthineers.com/x-ray-tube, [19.10.2021].

[45] *Personal discussion and consultation with PD Dr. Thilo Michel.* Friedrich-Alexander Universität Erlangen-Nürnberg.

[46] Jan Jakubek. "Precise energy calibration of pixel detector working in time-over-threshold mode". In: *Nuclear Instruments and Methods in Physics Research Section A: Accelerators, Spectrometers, Detectors and Associated Equipment* 633 (2011). 11th International Workshop on Radiation Imaging Detectors (IWORID), S262–S266. ISSN: 0168-9002. DOI: https://doi.org/10.1016/j.nima.2010.06.183. URL: https://www.sciencedirect.com/science/article/pii/S0168900210013732.

[47] Ina Ritter et al. "Characterization of the Dosepix detector with XRF and analog testpulses". In: *Journal of Instrumentation* 9.5 (2014). DOI: doi:10.1088/1748-0221/9/05/C05069.

[48] Ivan Kotov, H. Neal, and P. O'Connor. "Pair creation energy and Fano factor of silicon measured at 185 K using 55Fe X-rays". In: *Nuclear Instruments and Methods in Physics Research, Section A: Accelerators, Spectrometers, Detectors and Associated Equipment* 901 (September 2018), pp. 126–132. DOI: 10.1016/j.nima.2018.06.022.

[49] MATLAB. *9.4.0.902940 (R2018a), Update 4.* Natick, Massachusetts: The MathWorks Inc., 2018.

[50] Guillermo Hernández and Francisco Fernández. "xpecgen: A program to calculate x-ray spectra generated in tungsten anodes". In: *Journal of Open Source Software* 1.7 (2016), p. 62. DOI: 10.21105/joss.00062. URL: https://doi.org/10.21105/joss.00062.

[51] et. al Thilo Michel. "Anordnungen und Verfahren zur Bestimmung von Dosismessgrößen und zur Ermittlung von Energieinformation einfallender Strahlung aus Photonen oder geladenen Teilchen mit zählenden Detektoreinheiten (DE102006006411A1)". Friedrich-Alexander-Universität Erlangen-Nürnberg (FAU), [Online], https://patents.google.com/patent/DE102006006411A1/un, [accessed on 15.11.2021]. 2007.

[52] Francois Chollet et al. *Keras.* https://keras.io. 2015.

[53] URL: https://www.tensorflow.org/api_docs/python/tf/keras/losses/MeanAbsolutePercentageError.

[54] Wolfgang Kaiser. *Kunststoffchemie für Ingenieure, Von der Synthese bis zur Anwendung.* Carl Hanser Verlag GmbH & Co. KG, 2016. ISBN: 978-3-446-44638-0.

[55] Peter Sievers. "Optimierungen und Simulationen zur Messung der Personendosis mit einem neuartigen photonenzählenden Pixeldetektor". Friedrich-Alexander-Universität Erlangen-Nürnberg, 2009.

[56] Janna Zoe Vischer. "Experimental Investigation on Dose Rate Linearity of the Dosepix Detector". Bachelors Thesis. Friedrich-Alexander Universität Erlangen-Nürnberg, 2020.

[57] iba Dosimetry. *Dosimeter DOSIMAX plus.* [Online] https://www.iba-dosimetry.com/pagable_brochures/MI-Product-Overview_D_Rev6/#30, [accessed on 26.10.2021].

[58] *Siemens Spectrum Simulator.* [online], https://health.siemens.com/booneweb/index.html [27.02.2019].

[59] Dennis Haag. "Active personal dosimetry with the hybrid pixelated DOSEPIX detector". Friedrich-Alexander-University Erlangen-Nürnberg, 2018.

[60] Golden Engineering Inc. Portable X-ray Technology. *XRS4 20V X-RAY GENERATOR 370 kVp light duty pulsed X-ray machine.* [Online], http://www.goldenengineering.com/wp-content/uploads/2017/02/XRS4_20V_SPECSHEET_FB_JUNE2018.pdf [accessed on 08.11.2021].

[61] Golden Engineering Inc. Portable X-ray Technology. *XR200 20V X-RAY GENERATOR OPERATOR'S MANUAL*. [Online], http://www.goldenengineering.com/wp-content/uploads/2018/01/XR200_20V_Operators_Manual_082017.pdf [accessed on 08.11.2021], The design of the device was changed and differs from the utilized one. The relevant parameters stayed the same.

[62] Rolf Behrens, Hayo Zutz, and Julian Busse. "Spectrometry of pulsed photon radiation". In: *Journal of Radiological Protection* (2021). URL: http://iopscience.iop.org/article/10.1088/1361-6498/ac3dd0.

[63] H. Zutz and O. Hupe. "Recent results of irradiations of DIS-1 dosemeters with an XR200 X-ray flash unit". In: *Radiation Protection Dosimetry* 154.4 (October 2012), pp. 401–404. ISSN: 0144-8420. DOI: 10.1093/rpd/ncs265. eprint: https://academic.oup.com/rpd/article-pdf/154/4/401/4537069/ncs265.pdf. URL: https://doi.org/10.1093/rpd/ncs265.

[64] *Personal discussion and consultation with Jürgen Roth*. Physikalisch-Technische Bundesanstalt, Braunschweig.

[65] THE DOSIMETRY COMPANY PTW. *Monitor Ionization Chambers, Types 34014, 786*. [Online], https://www.ptwdosimetry.com/fileadmin/user_upload/DETECTORS_Cat_en_16522900_12/blaetterkatalog/index.html#page_52, [accessed on 08.11.2021].

[66] THE DOSIMETRY COMPANY PTW. *30 cm^3 Cylinder Stem Ionization Chambers, Types 23361*. [Online], https://www.ptwdosimetry.com/fileadmin/user_upload/DETECTORS_Cat_en_16522900_12/blaetterkatalog/index.html#page_50, [accessed on 01.12.2021].

[67] GSI. *PHELIX Lasersystem*. [Online] https://www.gsi.de/work/forschung/appamml/plasmaphysikphelix/phelix [accessed on 27.10.2021].

[68] Vincent Bagnoud et al. "Commissioning and early experiments of the PHELIX facility". In: *Appl Phys B* 100 (July 2010), pp. 137–150. DOI: 10.1007/s00340-009-3855-7.

[69] *AAronia X-Dram 10 m^2 100 dB shiedling fleece*. [Online], https://downloads.aaronia.com/datasheets/shielding/Aaronia_X-Dream_Datasheet_V5_DE.pdf [accessed on 27.10.2021].

[70] Rolf Behrens. "A spectrometer for pulsed and continuous photon radiation". In: *Journal of Instrumentation* 4 (2009), p. 03027.

[71] *Personal discussion and consultation with Dr. Rolf Behrens*. Physikalisch-Technische Bundesanstalt, Braunschweig.

[72] Rolf Behrens et al. *Radiation measurements and simulations at the PHELIX laser facility, GSI*. In preparation by the time writing this thesis. Submitted to *Journal of Instrumentation* on 11.02.2022.

[73] D.W.O. Rogers et al. "NRC User Codes for EGSnrc". In: *NRCC Report PIRS-702(revC)* (2021). URL: https://nrc-cnrc.github.io/EGSnrc/doc/pirs702-egsnrc-codes.pdf.

[74] I. Kawrakow et al. "The EGSnrc Code System: Monte Carlo Simulation of Electron and Photon Transport". In: *NRCC Report PIRS-701* (2021). URL: https://nrc-cnrc.github.io/EGSnrc/doc/pirs701-egsnrc.pdf.

[75] *Appendix: Significance of Calculated Quantities*. [Online], https://physics.nist.gov/PhysRefData/Star/Text/appendix.html, [accessed on 20.01.2022].